UNIVERSITY OF
Southampton
School of Chemistry

A Study of Some Atmospherically Important Molecules and Reactions using Photoelectron Spectroscopy

By

Grant Copeland

A thesis submitted in partial fulfilment for the
Degree of Doctor of Philosophy
in the
Faculty of Engineering, Science and Mathematics
School of Chemistry

September 2011

“...a joke is a very serious thing...”

Winston Churchill

Declaration of Authorship

I, Grant Copeland, declare that this thesis entitled "A Study of Atmospherically Important Molecules and Reactions using Photoelectron Spectroscopy" and the work presented therein is my own. I confirm that:

- This work was done wholly or mainly while in candidature for a research degree at Southampton University.
- Where any part of this thesis has previously been submitted for a degree or any other qualification at Southampton University or any other institution, this has been clearly stated.
- Where I have consulted the published work of others, this is always clearly attributed.
- Where I have quoted from the work of others, the source is always given. With the exception of such quotations, this thesis is entirely my own work.
- I have acknowledged all main sources of help.
- Where the thesis is based on work done by myself and/or jointly with others, I have made clear exactly what was done by others and to what I have contributed myself.

Recent Publications

[1] G. Copeland, E. P. F. Lee, J. M. Dyke, W. K. Chow, D. K. W. Mok and F. T. Chau, *J. Phys. Chem. A*, 114, 2010, 1816.

[2] G. Copeland, E. P. F. Lee, J. M. Dyke, W. K. Chow, D. K. W. Mok and F. T. Chau, *J. Phys. Chem. A*, 114, 2010, 3540.

[3] G. Copeland, M. V. Ghosh, D. E. Shallcross, C. J. Percival and J. M. Dyke, *Phys. Chem. Chem. Phys.,* 13, 2011, 14839.

[4] G. Copeland, M. V. Ghosh, D. E. Shallcross, C. J. Percival and J. M. Dyke, *Phys. Chem. Chem. Phys.,* 13, 2011, 17461.

Signed:

Date:

Abstract

Faculty of Engineering, Science and Mathematics
School of Chemistry

Doctor of Philosophy

A Study of Some Atmospherically Important Molecules and Reactions Using Photoelectron Spectroscopy

by

Grant Copeland

The main objective of the work reported in this thesis was to investigate molecules of atmospheric importance and their reactions. This has been achieved using spectroscopic methods, notably photoelectron spectroscopy, u.v.-visible spectroscopy and infrared spectroscopy, as well as kinetics simulations, global modelling and quantum chemical calculations.

Photoelectron spectroscopy (PES) was used to investigate the pyrolysis behaviour of two hydrofluorocarbon (HFC) fire suppression agents, pentafluoroethane (CF_3CHF_2) and 2-H heptafluoropropane (CF_3CHFCF_3) to determine their thermal decomposition pathways. The thermal decomposition of flowing pentafluoroethane (CF_3CHF_2) diluted in argon was studied over the temperature range 600-1600 °C. At lower temperatures, (< 1000 °C) there is evidence of production of the thermal decomposition products C_2F_4 and HF and at higher temperatures (over 1000 °C) the decomposition products CF_2 and CF_3H are observed. The adiabatic and vertical ionisation energy (AIE and VIE) have been measured for the first band of CF_3CHF_2 from the recorded photoelectron spectrum as (12.71 ± 0.05) eV and (13.76 ± 0.02) eV respectively. The main pathways for decomposition have been established over the temperature range investigated.

Pyrolysis of 2-H heptafluoropropane (CF_3CHFCF_3), at low pressure, diluted in argon, has been studied over the temperature range 600-2000 °C. Comparison of the results

obtained has been made with results of recent electronic structure calculations of possible decomposition pathways. The most favoured reaction thermodynamically, to produce $CF_3CF=CF_2$ + HF, is found to be the main decomposition reaction at lower temperatures, 600-900 °C. At higher temperatures, 900-1200 °C, decomposition gave C_2F_4 + CF_3H and it was found that C_3F_6 decomposes to C_2F_4 + CF_2, and C_2F_4 decomposes to CF_2 at temperatures above 1400 °C.

Three ozone-alkene reactions (O_3 + ethene, O_3 + 2-methylpropene (2MP) and O_3 + 2, 3 dimethyl-2-butene (DMB)) were separately investigated, each at low pressure, using a flow-tube interfaced to a photoelectron spectrometer. Photoelectron spectra, recorded as a function of reaction time, have been used to estimate partial pressures of the reagents and products, using photoionisation cross-sections for selected photoelectron bands of the reagents and products, (which have been measured separately) for each reaction. The yields of all the main products have been determined for each reaction. For each reaction, oxygen was observed as a product for the first time and for the O_3 + ethene reaction acetaldehyde was measured as a product for the first time. Kinetics simulations were performed using reaction schemes which were developed for these reactions in order to determine the main reactions for production of the observed products.

A feasibility study was carried out on the first PE bands of four selected non-linear triatomic molecules, SF_2, HO_2, HOCl and Cl_2O in order to optimise the experimental production conditions for a threshold PES study using synchrotron radiation. Reliable methods were developed to record threshold PE spectra of SF_2, HOCl and Cl_2O consistently for upwards of 4 hours. The work on HO_2 is still ongoing and the method developed requires further optimisation.

Absorption spectroscopy was used to determine the photolysis rate coefficient, in the atmosphere, of the atmospherically important molecule monochlorodimethyl sulphide (CH_3SCH_2Cl) from u.v. photoabsorption cross-section measurements in the gas-phase.

Acknowledgements

First and foremost I must thank my supervisor Prof. John M. Dyke, firstly for giving me the opportunity to do this project and, more importantly, for his constant support, guidance and endless enthusiasm, to which I am indebted, throughout these years.

I also extend this gratitude to Dr Ed P. F. Lee and Dr Alan Morris, both of whom helped me endlessly over the last few years. I thank Ed for all of the helpful advice on quantum theory and for the quantum chemical calculations in which he performed for the investigations reported throughout this thesis. I thank Dr Alan Morris whose experimental expertise I could not have gone without.

I thank all those who I have had the privilege of working alongside; Prof. Dudley E. Shallcross, Dr Carl J. Percival, Dr David J. Kinnison and Dr Mariana V. Ghosh for all their expert advice on atmospheric chemistry, specifically atmospheric simulations, global modelling studies and reaction kinetics. I thank Dr Stefano Stranges, Prof. John B. West and Prof. George C. King for all their discussions and guidance on synchrotron radiation, threshold photoelectron spectroscopy and photoionisation cross-section measurements during my time working in Trieste.

I thank Gary Williams, Robert Mcpheat and Dr Kevin Smith at the Molecular Spectroscopy Facility in Rutherford Appleton Laboratories for all their help and expertise on u.v.-visible and infrared absorption spectroscopy and thank the National Environmental Research Council (NERC) for providing my studentship.

I must give the upmost praise to Rob Daly and Alan Glass in the mechanical workshop and Lee Mulholland and Przemyslaw “Shamack” Tyrc in the glass blowing workshop for all the help they provided me with in the design and manufacture of instrumental components and glassware, especially those required at the last minute!

I thank all my friends and colleagues in the PES group for making my time in Southampton so enjoyable, Marie Eypper, Otello M. Roscioni, Nerina Armatta, Sonya Becacecci, Fabrizio Innoccenti and Nicholas Zonias. I must also thank the Portuguese PES group, Rui M. Pinto, Mauro A. M. Guerra and to a very close friend, of which my life in Southampton would not have been the same without, Diana “Pigeon” Guimaraes, for all the good times, vacations and trips we had together. Lastly I must thank both my mum and dad for all the support they have given me throughout my Ph.D.

Table of Contents

Chapter 1

Introduction

The work described in this thesis involves the study of selected reactions of atmospheric importance using photoionisation and photoabsorption spectroscopic methods. The reactions investigated are relevant to the troposphere and the lower stratosphere. The main experimental method used in this work is photoelectron spectroscopy.

1.1 Introduction to Photoelectron Spectroscopy

Photoelectron spectroscopy (PES), first developed by Turner *et al.* [1] and Vilesov *et al.* [2] in the early 1960's, is based on Einstein's photoelectric effect. The technique is used to study electrons (photoelectrons) ejected from an occupied orbital in an atom or a molecule in the gas-phase after interaction with vacuum ultraviolet (v.u.v.) radiation [3-5]. The measured ionisation energies, abundances and angular distributions of photoelectrons are all characteristic of the individual atomic or molecular orbitals from which they originate [6]. The kinetic energy, $\left(\frac{1}{2}m\mathrm{v}^2\right)$, of an emitted photoelectron varies *linearly* with the frequency of radiation used above a certain threshold, i.e. electrons will only be ejected from an atom or molecule when the incident radiation has sufficient energy, *(hv)*, to overcome the ionisation energy, *IE*, of the atom or molecule. The electron kinetic energy, photon energy and ionisation energy are related via,

$$hv = \frac{1}{2}m\mathrm{v}^2 + IE \tag{1.1}$$

where *m* and v are the mass and velocity of the emitted photoelectron respectively. PES can provide information on the electronic structure, vibrational frequencies and bonding

character (e.g. dissociation energies) of molecules, and molecular ions. The basic principles of PES are described in the next chapter.

PES has played an important part in the study of the electronic structure of atoms and molecules over a number of years. It has developed into two separate areas of research, X-ray PES and vacuum ultraviolet PES. In X-ray PES (XPS) the photon energy is of the order of 1000 eV and is mainly used to probe core electrons in atoms or molecules. The development of XPS was largely due to Seigbahn *et al.* in the late 1950's [7] and is usually used to investigate solid state materials and surfaces. However, vacuum ultraviolet PES (as is used in this work) uses photon energies of the order of 20-40 eV to investigate valence electrons of atoms and molecules. Ultraviolet PES has been mainly applied to the study of atoms and molecules in the gas-phase. The Southampton PES group has developed this method to study short lived atoms and molecules, which are of importance in plasmas, atmospheric chemistry and combustion chemistry. This ability to study short lived atoms and molecules is used in this work to investigate a number of reactions which are relevant in atmospheric chemistry.

1.2 A Study of Reactive Intermediates using PES

Reactive intermediates are short lived species (atoms or molecules) which are formed and react quickly during a reaction process. These short lived species play an essential role in allowing a reaction to proceed using the minimum energy required to go to completion. This makes them an integral part of the reaction process and as a result, reactive intermediates are of great importance in many chemical fields including chemical kinetics, atmospheric chemistry and combustion chemistry.

The study of reactive intermediates using PES has become the main research topic of the Southampton PES group [8]. Many atomic species, such as $H(^2S)$, $O(^3P)$, $N(^4S)$ and halogen atoms have been studied with this method [8, 9, 10]. Various other atomic species have also been investigated over the years in the gas-phase using PES, such as Zn, Cd, Hg and Ba [11-13]. A number of reactive diatomic and triatomic molecules have been studied by PES, e.g. O_2, S_2, OH, ClO, SiO, BrO, BrO_2, ClO_2, Cl_2O, CF_2 and SiF_2 [14]. One of the first reactive intermediates investigated by PES was $O_2(a^1\Delta_g)$ [15, 16]. This is the first electronically excited state of O_2 and is an important species in the atmosphere. $O_2(a^1\Delta_g)$ is present in relatively high partial pressures in the troposphere

[17]. It is produced along with $O(^1D)$ on photolysis of ozone at wavelengths lower than 320 nm and it is a major contributor to airglow in the atmosphere [18]. Larger short lived molecules (polyatomic molecules) have also been investigated using PES, such as CH_3 and N_2O_5 [19, 20]. The information obtained using PES, i.e. the electronic structure of molecular reactive intermediates and their ions, is often difficult to obtain using other spectroscopic techniques. However, producing reactive species reliably using PES in sufficient number densities can impose certain problems in itself. The lifetime of the species being investigated is an important factor. This can, to some extent, be alleviated by producing high enough concentrations of the species being investigated as close as possible to the point of photoionisation in order to be successfully detected. In order to study such short lived atoms and molecules in the vapour phase a number of preparative methods have been used. These include, microwave discharge of a flowing gas mixture, use of a suitable gas-phase reaction, (typically a rapid atom-molecule reaction) and high temperature pyrolysis (these are each described in Chapter 3). Several reviews have also been published discussing each of these methods [21-24]. Atmospherically important reactive intermediates have also been studied by related techniques such as resonance enhanced multiphoton ionisation spectroscopy (REMPI) [25], photoionisation mass spectrometry (PIMS) [26] and cavity ring down spectroscopy (CRDS) [27].

1.3 Rydberg States and Autoionisation Resonances

Synchrotron radiation was used in this work to record the first bands in the threshold photoelectron (TPE) spectrum of the triatomic molecules HO_2 and SF_2 (discussed in Chapter 9). The detection of threshold electrons is achieved by using a three element lens system which focuses low energy electrons towards the analyser of the spectrometer. A TPE spectrum is then obtained by sweeping the photon energy with the lens voltages to always extract threshold electrons (described in section 3.4.3 in Chapter 3). There are two main types of ionisation, direct (see equation 2.1 in Chapter 2) and indirect ionisation. Direct ionisation occurs when an incoming photon ejects an electron from a molecule. Indirect ionisation occurs when the energy of the incoming photon matches the energy of a discrete neutral excited state above an ionisation threshold. Ionisation then occurs from this excited state to the lower ionic state via an autoionisation process. Excited neutral states can be of two types, valence or Rydberg.

In atomic systems, the valence shell consists of a set of atomic orbitals with the same principal quantum number, n, as that of the highest occupied orbital in the ground state. States obtained by promotion of electrons within the valence shell are termed valence excited states. In contrast a Rydberg state is a highly excited state obtained when an electron is promoted from the valence shell to an orbital with a higher principal quantum number. The energy of a Rydberg state, E_n, relative to the ground state, is given by the formula [28],

$$E_n = IE - \frac{R}{(n-\delta)^2} \tag{1.2}$$

where R is the Rydberg constant (13.61 eV), δ is the quantum defect, which reflects the magnitude of penetration of the Rydberg orbital into the ionic core and n is the principal quantum number. The Rydberg constant varies slightly with the reduced mass of the electron-core system [28]. Rydberg states with successively higher principal quantum numbers form a series, converging to a particular ionisation limit, *IE*. The Rydberg electrons are at a distance so large from the ionic core that the core appears as a point charge, leading to the near hydrogen-like behaviour of the Rydberg states. Threshold photoelectron (TPE) spectra provide complementary information to conventional PE spectra in that they can show evidence of indirect ionisation via Rydberg states. TPE spectra often show Franck-Condon vibrational distributions which are different from those of direct ionisation, because of indirect ionisation via autoionisation processes [29]. Autoionisation processes are discussed in more detail in Chapter 9 where TPE spectra are presented for the reactive intermediate SF_2.

1.4 Cross-Sections

A cross-section can be thought of as the probability, per unit area, of an atom or molecule to be excited or emit a photoelectron at a given energy. It is measured in megabarns (Mb), where 1Mb = 1 x 10^{-18} cm^2. A cross-section (absorption or ionisation) is a quantitative measure of the probability in which an atom or molecule will absorb or be ionised by a photon of a given energy. It can be expressed in terms of the Beer-Lambert law as,

$$I = I_0 e^{-\sigma l c} \tag{1.3}$$

where I_0 is the intensity of incident radiation, I is the intensity of radiation after absorption or ionisation, l is the path length which the radiation traverses in the sample, c is the sample concentration and σ is the cross-section. All cross-sections (absorption and ionisation) are dependent on the photon energy. Inspection of equation (1.3) shows that if the path length has units of cm and the concentration has units of molecules cm^{-3} then the cross-section has units of cm^2.

Reliable cross-sections are needed to convert absorption or photoelectron band intensities into partial pressures and this is very useful when investigating gas-phase reactions which may proceed via more than one channel. Experimental techniques such as ultraviolet laser absorption spectroscopy and electron momentum spectroscopy have been successful in measuring the absorption and photoionisation cross-sections respectively, of various atmospherically important species, e.g. CH_2O, CO_2 and O_2 [30-32]. Photoionisation cross-sections (PI-CS) at selected photon energies have also been measured using PES by groups such as Kimura *et al.*, Samson *et al.*, and Marr and West [33-35]. The experimental method used in this work to measure the PI-CS of reactants and products observed from the ozone-alkene reactions closely follows that outlined by Kimura *et al.* [33] and Samson *et al.* [34], and is described in detail in Chapters 7 and 8.

1.5 Use of PES in Kinetics Studies

PES has been used to study first-order reactions by Wang *et al.* [36-38] and second-order reactions by Dyke *et al.* [39, 40]. Wang *et al.* studied the first-order rearrangement of a number of compounds as a function of time and derived first-order rate coefficients. Examples of the reactions studied were the isomerisation of CH_3NC to CH_3CN and the isomerisation of SSF_2 to FSSF. For a reaction $[A] \rightarrow [B]$, the first-order rate coefficient, k_1 is given by,

$$Rate = k_1[A] \tag{1.4}$$

The first-order rate coefficient can be determined by the loss of [A] as a function of time; $(\log_e[A])$ is plotted against time to yield a slope of -k. Wang *et al.* reported the first-order rate coefficients of selected compounds by plotting $\log_e$[A]/[B] versus time. This resulted in the rate coefficients obtained being in error, although his published data could still be used to derive the correct rate coefficients.

Since the work of Wang, PES has been used to measure the rate coefficient of a second-order reaction. This was done by Dyke *et al.* [39, 40], where the rate coefficient for the atmospherically important reaction between molecular chlorine and dimethyl sulphide (DMS) was determined using a differentially pumped flow-tube interfaced to a PE spectrometer (described in Chapter 3). By working under pseudo first-order conditions with $[Cl_2] \gg [DMS]$, the rate coefficient was determined by measuring the relative concentration of DMS using the intensity of its first PE band, at different reaction times at fixed chlorine partial pressure. Reaction times were determined by the position of the moveable injector on the flow-tube. This was then repeated at different partial pressures of chlorine. Plotting $\log_e\left(\frac{[DMS]_0}{[DMS]_t}\right)$ against reaction time at a known concentration of chlorine gave a gradient which was equal to the pseudo first-order rate coefficient, k'. The second-order rate coefficient was then determined from the slope of the plot of k' versus [Cl_2]. During the course of this project the differentially pumped flow-tube was only used for the photoionisation cross-section (PI-CS) measurements to allow reaction branching ratios to be determined for selected ozone-alkene reactions. The determination of branching ratios for these ozone-alkene reactions is described in Chapters 7 and 8.

1.6 Project Aims and Structure of the Thesis

The main aim of this project was to study reactions of atmospheric importance in the gas-phase using PES.

First an investigation was carried out on the thermal decomposition pathways of two hydrofluorocarbon (HFC) fire suppression agents, pentafluoroethane (HFC-125) and 2-H heptafluoropropane (FM-200). These are being used as replacements for chlorine and bromine containing molecules, such as CF_2BrCl, $C_2F_4Br_2$ and the commonly used Halon 1301 (CF_3Br) which have been banned because of their high ozone depleting potentials (ODP) in the atmosphere [41]. State-of-the-art *ab initio* calculations were also carried out (by Dr E. P. F. Lee of Southampton PES group) to obtain reliable adiabatic ionisation energies (AIE) and vertical ionisation energies (VIE) in order to assist interpretation of the experimental PE spectra and also to obtain reliable enthalpies of formation for selected neutral molecules and ions in their ground electronic state.

Then, a study was made of selected ozone-alkene reactions using a flow-tube interfaced to a PE spectrometer in order to measure product branching ratios. Alkenes, produced biogenically and anthropogenically, are an important class of volatile organic compounds (VOCs) in the troposphere [42-45]. Significant experimental studies have been carried out investigating the kinetics and mechanisms of these reactions [46-58]. Rate coefficients and products have been determined for a number of ozone-alkene reactions; however no complete product branching ratio data is available for any alkene-ozone reaction. The ozone-alkene reactions chosen for study were O_3 with ethene, O_3 with 2-methylpropene (2MP) and O_3 with 2, 3 dimethyl-2-butene (DMB). For each reaction, the measured product PE band intensities were converted into product branching ratios using measured photoionisation cross-sections (PI-CS). These yields were then used (by Prof. D. E. Shallcross of Bristol University) in a global atmospheric model to estimate the annual global budgets of the observed products. Kinetics simulations were also carried out in this work for all three reactions in order to establish the main pathway for production of each observed product.

A secondary aim of this project was to study four non-linear triatomic molecules, SF_2, HO_2, HOCl and Cl_2O using TPES and study the atmospherically important species monochlorodimethyl sulphide (CH_3SCH_2Cl) using ultraviolet absorption spectroscopy.

The structure of the thesis is as follows: Chapter 2 describes the basic principles of PES. Chapter 3 describes the spectrometers that have been used throughout this project, along with the other apparatus used with descriptions of the various sampling techniques employed. Chapter 4 focuses on the theoretical methods used to perform calculations to assist in the assignment of the PE spectra obtained. Chapters 5 and 6 discuss the thermal decomposition pathways of two hydrofluorocarbon (HFC) fire suppression agents, pentafluoroethane (HFC-125) and 2-H heptafluoropropane (FM-200) respectively. Chapters 7 and 8 present results obtained for the reactions between ozone and selected alkene molecules, (ethene, 2-methylpropene and 2, 3 dimethyl-2-butene). Chapter 9 discusses attempts to record TPE spectra of four non-linear triatomic molecules and Chapter 10 describes a determination of the photolysis rate coefficient of monochlorodimethyl sulphide (CH_3SCH_2Cl) in the atmosphere. Finally, Chapter 11 concludes the thesis with a summary of the project and outlines possibilities for future work.

References

[1] D. W. Turner and M. I. Al. Joboury, *J. Chem. Phys.*, 37, 1962, 3007.

[2] F. I. Vilsov, B. L. Kurbator and A. N. Terenin, *Dokl. Akad. Nauh.*, SSR 138, 1961, 1329.

[3] J. W. Rabalais, Principles of Ultraviolet Photoelectron Spectroscopy, *John Wiley and Sons*, *New York*, 1977.

[4] D. W. Turner, C. Baker, A. D. Baker and C. Brundle, Molecular Photoelectron Spectroscopy, *Wiley Interscience*, *London*, 1970.

[5] H. Siegbahn and L. Karlsson, Photoelectron Spectroscopy, *Springer-Verlag*, *Berlin Heidelberg*, *New York*, 1982.

[6] J.H.D. Eland, Photoelectron Spectroscopy, *Butterworths*, *London*, 1974.

[7] K. Siegbahn and K. Edvarson, *Nucl. Phys.*, 1, 1956, 137.

[8] N. Jonathan, A. Morris, D. J. Smith and K. J. Ross, *Chem. Phys. Lett.*, 7, 1970, 497.

[9] N. Jonathan, K. J. Ross and D. J. Smith, *Chem. Phys. Lett.*, 9, 1971, 217.

[10] M. C. R. Cockett, J. M. Dyke and H. Zamanpour, Vacuum Ultraviolet Photoionisation and Photodissociation of Molecules and Clusters, *World Scientific Co*, *New Jersey*, 1991.

[11] T. E. H. Walker, J. Berkowitz, J. L. Dehmer and J. T. Weber, *Phys. Rev. Lett.*, 11, 1973, 678.

[12] J. L. Dehmer and J. Berkowitz, *Phys. Rev.*, A10, 1974, 484.

[13] J. Berkowitz, J. L. Dehmer, Y. K. Kim and J. P. Desclaux, *J. Chem. Phys.*, 61, 1974, 2556.

[14] J. M. Dyke, N. Jonathan and A. Morris, Electron Spectroscopy: Theory, Techniques and Applications, Vol 3, *Academic Press*, *London*, 1979.

[15] N. Jonathan, D. J. Smith and K. J. Ross, *J. Chem. Phys.*, 53, 1970, 3758.

[16] N. Jonathan, A. Morris, D. J. Smith and K. J. Ross, *J. Chem. Phys.*, 54, 1971, 4954.

[17] D. Johnson and G. Marston, *Chem. Soc. Rev.*, 37, 2008, 699.

[18] P. S. Monks, *Chem. Soc. Rev.*, 34, 2005, 376.

[19] J. M. Dyke, N. Jonathan, E. P. F. Lee and A. Morris, *J.C.S. Faraday II.*, 72, 1976, 2225.

[20] D. L. Ames and D. W. Turner, *Proc. Roy. Soc. Lond.*, A348, 1976, 175.

[21] J. M. Dyke, N. Jonathan and A. Morris, *Int. Rev. Phys. Chem.*, 2 1982, 3.

[22] P. Chen, Photoelectron Spectroscopy of Radical Intermediates, *John Wiley and Sons*, *London*, 1994.

[23] J. M. Dyke, N. Jonathan and A. Morris, *J. Elec. Spec and Rel. Phen.*, 15, 1979, 45.

[24] N. P. C. Westwood, *Chem. Soc. Rev.*, 18, 1989, 317.

[25] J. Berkowitz, *Acc. Chem. Res.*, 22, 1989, 413.

[26] M. D. Wheeler, S. M. Newman, A. J. Orr-Ewing and M. N. R. Ashfold, *J. Chem. Soc. Faraday Trans.*, 94, 1998, 337.

[27] M. N. R. Ashfold and J. D. Howie, *Ann. Rev. Phys. Chem.*, 45, 1994, 57.

[28] A. B. F. Duncan, Rydberg series in Atoms and Molecules, *Academic Press Inc.*, *London*, 1971.

[29] U. Fano, *Phys. Rev.*, 124, 1961, 1866.

[30] C.A. Smith, F.D. Pope, B. Cronin, C.B. Parkes, and A.J. Orr-Ewing, *J. Phys. Chem. A.*, 110, 2006, 11645.

[31] C. E. Brion and K. H. Tan, *J. Elec. Spect. Rel. Phen.*, 17, 1979, 101.

[32] W. H. Hancock, and J. A. R. Samson, *J. Elec. Spect. Rel. Phen.*, 9, 1976, 210.

[33] S. Katsumata, H. Shiromaru and T. Kimura, *Bull. Chem. Soc. Jpn.*, 57, 1984, 1784.

[34] J.L. Gardner and J.A.R. Samson, *J. Elec. Spec. Rel. Phen.*, 8, 1976, 469.

[35] J. B. West and G. V. Marr, *Proc. Roy. Soc. Lond. Series A.*, Mathematical and Physical Sciences, 349, 1976, 397.

[36] D. Wang and X. Qian, *J. Elec. Spec.*, 83, 1997, 41.

[37] D. Wang, X. Qian and P. Jiang, *Chem. Phys. Lett*., 258, 1996, 149.

[38] X. Cao, X. Qian, C. Qiao and D. Wang, *Chem. Phys. Lett.*, 299, 1999, 322.

[39] J.M. Dyke, M.V. Ghosh, M. Goubet, E.P.F. Lee, G. Levita, K. Miqueu and D.E. Shallcross, *Chem. Phys.*, 85, 2006, 324.

[40] J.M. Dyke, M.V. Ghosh, M. Goubet, D.J. Kinnison, G. Levita, A. Morris and D.E. Shallcross, *Phys. Chem. Chem. Phys.*, 7, 2005, 866.

[41] W.K. Chow, E.P.F. Lee, F. T. Chau and J. M. Dyke, *Architectural Science Review*, 47, 2004, 223.

[42] J. G. Calvert, R. Atkinson, J. A. Kerr, S. Madronich, G. K. Moortgat, T. J. Wallington and G. Yarwood, The Mechanisms of Atmospheric Oxidation of the Alkenes, *Oxford University Press*, *Oxford*, 2000.

[43] R. Atkinson and S. M. Aschmann, *Environ. Sci. Technol.*, 27, 1993, 1357.

[44] W. P. L. Carter, *Atmos. Environ.*, 24A, 1990, 481.

[45] R. Atkinson, *Atmos. Environ.*, 24A, 1990, 1.

[46] R. Criegee and G. Wenner, *Chem. Ber.*, 9, 1949, 564.

[47] R. Criegee, Angew. *Chem. Int. Ed.*, 14, 1975, 745.

[48] W. H. Bunnelle, *Chem. Rev.*, 91, 1991, 335.

[49] C. A. Taatjes, G. Meloni, T. M. Selby, A. J. Trevitt, D. L. Osborn, C. J. Percival and D. E. Shallcross., *J. Am. Chem. Soc.*, 130, 2008, 11883.

[50] M. Clay and B. S. Ault, *J. Phys. Chem. A*, 114, 2010, 2799.

[51] M. D. Hoops and B. S. Ault, *J. Am. Chem. Soc.*, 131, 2009, 2853.

[52] F. J. Lovas and R. D. Suenram, *Chem. Phys. Letts.*, 51, 1977, 453.

[53] R. I. Martinez, R. E. Huie and J. T. Herron, *Chem. Phys. Letts.*, 51, 1977, 457.

[54] J. M. Anglada, R. Creheut, and J. M. Bofill, *Chem. Eur. J.*, 5, 1999, 1809.

[55] P. Aplincourt and M. F. Ruiz-Lopez, *J. Am. Chem. Soc.*, 122, 2000, 8990.

[56] T. Sato, S. Nishihara, Y. Kataoka, Y. Nakanishi, Y. Kitagawa, T. Kawakami, S. Yamanaka, M. Okumura and K. Yamaguchi, *J. Phys. Chem. A*, 114, 2010, 12116.

[57] Y. Zhao, O. Tishchenko, J. R. Gour, W. Li, J. J. Lutz, P. Piecuch, and D. G. Truhlar, *J. Phys. Chem. A*, 113, 2009, 5786.

[58] R. Ponec, J. Roithova and Y. Hass, *Croatica. Chemica. Acta.*, 74, 2001, 251.

Chapter 2

Basic Principles of PES

In 1864, Maxwell first postulated that electricity, magnetism and light were all governed by the same phenomenon; the electromagnetic field. His theory stated that the energy of an electron emitted from a molecule would be directly *proportional* to the intensity of the radiation incident on the molecule (later found not to be the case) [1]. In 1887, Hertz showed that the velocity of an electromagnetic wave was equal to the velocity of light and that a charged object loses its charge more readily when illuminated by ultraviolet radiation [2].

In 1902, Lenard first observed from his experiments that cathode rays were scattered when passed through air. This discovery implied that the cathode rays were electromagnetic waves which must have particle-like qualities. These particles however had to be smaller than those which made up the surrounding air in order for the rays to travel through. From this he confirmed that cathode rays were streams of negatively charged particles and suggested that atoms, for the most part, must consist of "empty space". Lenard's most important observation, contradictory to that postulated earlier by Maxwell, was that the energy of the emitted rays or particles, on irradiation of a molecule with ultraviolet radiation, was *independent* of the intensity of the radiation, noting that the energy of the rays increased for shorter wavelengths of radiation [3].

In 1905, Einstein solved the particle-wave discrepancy by describing radiation as being composed of discrete quanta, i.e. photons, rather than radiation being described purely as continuous waves, on which all other postulates were founded. This idea was based on Planck's quantum hypothesis of black-body radiation [4]. Einstein theorised that the

energy in each quanta of radiation was equal to the frequency multiplied by a constant, (h = 6.626x10^{-34} Js) [5]. This is better known as the *photoelectric effect*, which states that when an atom or a molecule is subjected to electromagnetic radiation above a certain threshold frequency, the radiation induces the emission of an electron. This later earned Einstein the Nobel Prize for Physics in 1921. Photoelectron spectroscopy (PES) was first developed by Turner *et al.* [6] and Vilesov *et al.* [7] in the early 1960's and is based on Einstein's photoelectric effect. The technique is used to study photoelectrons and measure ionisation energies, abundances and angular distributions of the ejected photoelectrons, which are all characteristic of the molecular orbitals from which they originate [8-11].

In this chapter, the basic principles of photoelectron spectroscopy will be discussed together with a description of the ionisation process, with consideration given to the Franck-Condon principle. The fundamental principles of angular distribution will also be presented along with the determination of relative photoionisation cross-sections (PI-CS) when polarised and unpolarised radiation is used.

2.1 The Photoelectron Process

The photoelectron spectrometers used in this work use a helium discharge lamp to provide a flux of unpolarised photons, targeted towards sample molecules in the gas-phase, of sufficient energy to eject electrons occupying the valence shell of the molecules. The photoelectron process is shown below in equation 2.1.

$$M + h\nu \rightarrow M^+ + e^- \tag{2.1}$$

where M is a neutral molecule and $h\nu$ is the photon energy. A photon will remove an electron from an occupied orbital in an atom or molecule provided the energy of the photon is greater than the binding energy or ionisation energy of the electron. By conservation of energy, the photon energy is related to the electron kinetic energy *(KE)* and ionisation energy *(IE)* as follows,

$$IE = E(h\upsilon) - KE \tag{2.2}$$

Equation 2.2 assumes that no kinetic energy is imparted to the ion in the photoionisation process [12]. This is a good assumption due to the large difference in the mass of the

ion and the ejected electron. Experimentally, the photoelectrons emitted are separated according to their kinetic energies using an electron energy analyser (described in section 3.1.3 in Chapter 3). From an atom, if the energy of the photons, *hv*, is known and the kinetic energies of the emitted photoelectrons being detected are measured, then the ionisation energy, *(IE)*, to each ionic state of the atom investigated can be determined. This is shown schematically in Figure 2.1 for an atom, *A*.

When a molecule is ionised, vibrational and rotational excitation on ionisation must be considered. Equation 2.2 is then modified to,

$$KE = h\upsilon - IE - \Delta E_{vib} - \Delta E_{rot} \tag{2.3}$$

where ΔE_{vib} and ΔE_{rot} are the change in vibrational and rotational energies on ionisation respectively. Experimentally rotational structure is not normally resolved in conventional PES; however a typical photoelectron spectrum of a diatomic molecule would show vibrationally resolved structure and an example is shown for O_2 in Figure 2.2. As rotational structure is not normally resolved, equation 2.3 can be written as,

$$KE = h\upsilon - IE' - \Delta E_{vib} \tag{2.4}$$

where IE' is equal to $IE + \Delta E_{rot}$, and therefore includes a rotational average of the rotational components within a PE vibrational component. The vibrational components in each band, (e.g. in the first band of O_2 (a) seen in the ionisation energy region 12.0-13.0 eV in Figure 2.2), correspond to ionisations from the ground vibrational level in the neutral ground state, to the vibrational levels in the ionic state [11]. Figure 2.2 shows the PE spectrum of a mixture of gases; O_2, O_3 and argon, (this spectrum was recorded during the preparation of O_3 which is described in Chapters 7 and 8) and yields a lot of information about the molecules investigated.

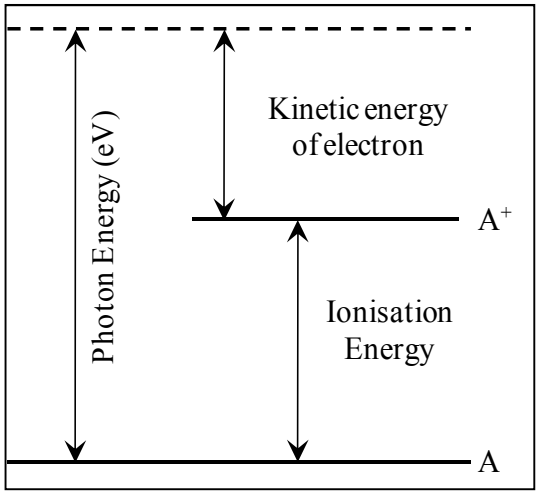

Figure 2.1: *Schematic diagram showing the relationship of the photon energy, kinetic energy and ionisation energy when ionising an atom, A.*

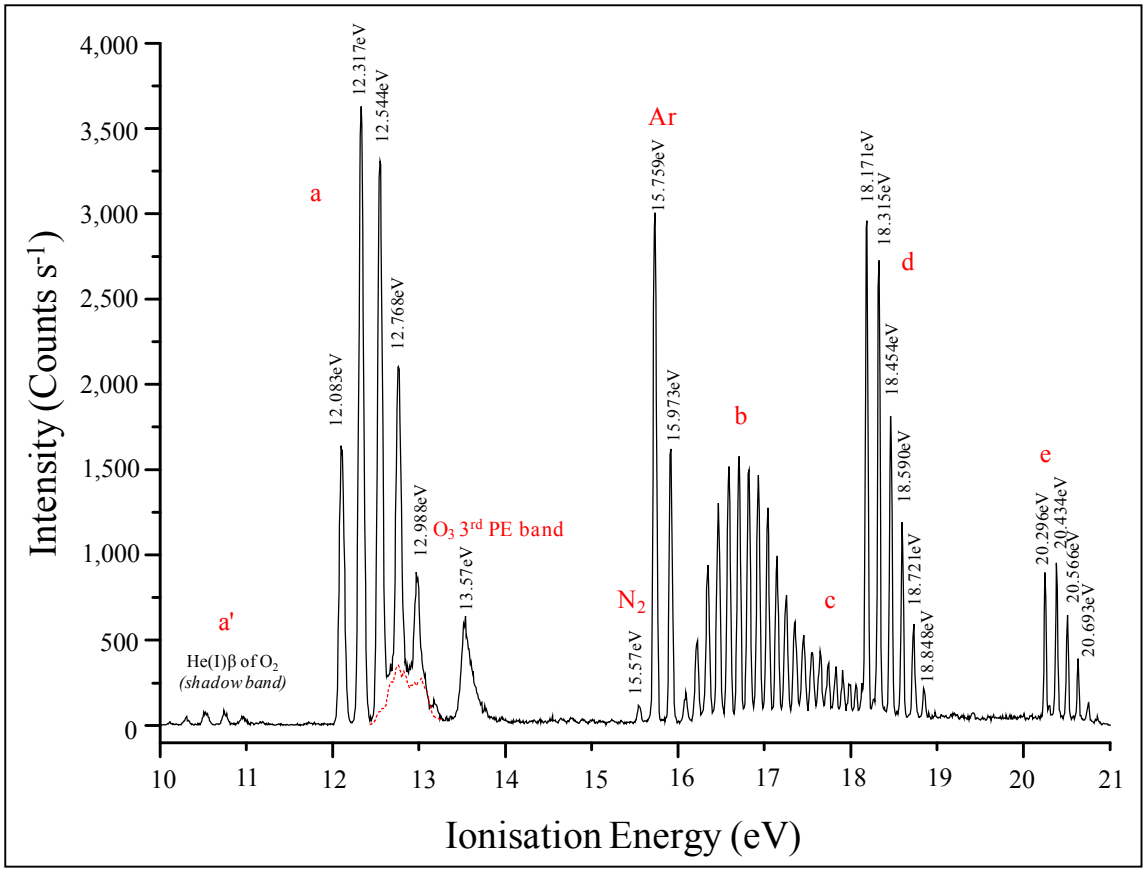

Figure 2.2: *He(I)α PE spectrum of O_2, O_3, and argon. The band labels, a, b, c, d and e, show the different PE bands associated with each ionic state of O_2 [13]. The band labelled (a') is the first band of O_2 obtained by ionisation with weaker radiation in the photon source known as He(I)β radiation. This is explained in section 3.1.1 of Chapter 3.*

There are five main types of information which can be provided from such a spectrum,

1. The adiabatic ionisation energy, (AIE) of a band, which corresponds to an ionisation from the vibrational ground state of the neutral molecule to the vibrational ground state in the ion. It is usually the first vibrational component seen in a PE band, e.g. 12.083 eV is the AIE for the first band of O_2, represented as (*a*) in Figure 2.2.
2. The vertical ionisation energy, (VIE). This corresponds to the most intense component in a photoelectron band and is seen at 12.317 eV in band (*a*) for O_2.
3. The separations in resolved vibrational components in a band. These can be used to determine vibrational constants in the ionic state (see equation 2.18).
4. The relative intensities of vibrational components within a band can be used to determine the change in equilibrium bond length on ionisation.

5. The relative intensities of bands can be used to obtain relative photoionisation cross-sections as the areas of the photoelectron bands are proportional to the relative probabilities of ionisation to different ionic states [11].

Experimental factors are also important in determining relative photoionisation cross-sections and these are discussed in section 2.2 of this chapter and in Chapters 7 and 8.

For closed-shell molecules, the VIEs measured in PES can be used to estimate the orbital energies of a molecule by use of Koopmans' theorem [6, 14]. This states, in a closed-shell molecule, that the vertical ionisation energy, IE_j, of an emitted electron is equal in magnitude to the negative of the orbital energy, $-\varepsilon_j$, from which the electron originated. This relationship is shown in equation 2.5,

$$IE_j = -\varepsilon_j \tag{2.5}$$

where, $-\varepsilon_j$, is derived from a molecular orbital calculation at the Hartree-Fock limit (described in section 4.1.4 of Chapter 4). This indicates that if a photoelectron spectrum of a closed-shell molecule is recorded, then the negative of the VIEs of the experimental bands can be used to construct a molecular orbital diagram for that molecule. However, Koopmans' theorem is only an approximation, as it does not take into consideration the effects of electron reorganisation and electron correlation upon ionisation, (see section 4.1.5 of Chapter 4 for a description of electron reorganisation and correlation). The changes in molecular geometry on ionisation can also be deduced from a PE spectrum giving an indication of the character of the orbital (bonding, anti-bonding or non-bonding) from which ionisation occurred. This information is associated with the shape and structure from the observed PE bands. Hartree-Fock theory is discussed in greater detail in section 4.1 of Chapter 4.

A photoelectron spectrum is recorded by counting emitted photoelectrons, per unit time, over a range of kinetic energies using a photon source of fixed energy. This provides a map of the ionic states of a given molecule. In a PE spectrum, each PE band, including all vibrational components, corresponds to an ionisation (removal of an electron) from a given molecular orbital (MO). There are two main types of ionisation, direct (as shown in equation 2.1) and indirect ionisation. Direct ionisation occurs when an incoming photon ejects an electron from a molecule. Indirect ionisation occurs when the energy of the incoming photon matches the energy of a discrete neutral excited state, AB^*, (a

Rydberg state) above an ionisation threshold. Once the electron has been promoted to a Rydberg orbital, then one of the following decay mechanisms in the excited neutral state can occur,

1. Re-radiation: $AB + h\nu \rightarrow AB^{*} \rightarrow AB + h\nu$
2. Predissociation: $AB + h\nu \rightarrow AB^{*} \rightarrow A + B$
3. Ion pair formation: $AB + h\nu \rightarrow AB^{*} \rightarrow A^{+} + B^{-}$
4. Autoionisation: $AB + h\nu \rightarrow AB^{*} \rightarrow AB^{+} + e^{-}$

where *AB* represents a diatomic molecule. A lot of work concerning Rydberg states of molecules has been carried out over the years in the Southampton PES group using constant ionic state (CIS) spectroscopy, (using the same photoelectron spectrometer as described in section 3.4.2 of Chapter 3); however as only direct ionisation techniques were used during the course of this work indirect ionisation processes will not be discussed further in this thesis [15-17].

Direct ionisation processes are governed by selection rules which account for the electronic and vibrational changes which occur on ionisation. The probability of ionisation, between the initial molecular ground state, Ψ'', and the final state (which includes the ion plus the electron), Ψ', is proportional to the square modulus of the transition moment integral, *M*,

$$M = \int \Psi'^{*}\, \Sigma p\, \Psi''\, d\tau \qquad (2.6)$$

where *p* is the dipole moment operator which extends over all positions for the electrons, *i* and ions *j*, (i.e. x_{ij}, y_{ij} and z_{ij}). Ψ'' and Ψ' are functions of the electron, with co-ordinates *r*, at nuclear coordinates, *R*. The Born-Oppenheimer approximation can be used to separate out the initial and final state functions, Ψ'' and Ψ' respectively, into products of the electronic, $\Psi_e(r, R)$ and nuclear (vibrational and rotational), $\Psi_n(R)$ wavefunctions to give,

$$\Psi(r, R) = \Psi_e(r, R)\Psi_n(R) \qquad (2.7)$$

This approximation is based on the large difference in mass between electrons and nuclei and assumes that the electrons move in a fixed potential generated by the nuclei (see section 4.1.2 in Chapter 4 for a more detailed description).

The dependence of Ψ_e on R retains the weak interaction between the electronic and nuclear motion [18]. Since the rotational structure of bands in a PE spectrum is usually unresolved, the nuclear wavefunction, Ψ_n can be treated as a vibrational function, neglecting rotation, i.e. $\Psi_n \equiv \Psi_v$. The electronic-nuclear separation of the wavefunction can also be applied to the dipole operator,

$$\Sigma_{i,j} p = \Sigma_i p_e + \Sigma_j p_n \tag{2.8}$$

Substituting this into equation 2.6 the transition moment integral becomes,

$$M = \iint \Psi_e''^*(r,R)\, \Psi_v''^*(R)\left(\Sigma_i p_e + \Sigma_j p_n\right)\Psi_e'(r,R)\Psi_v'(R)\,dr\,dR \tag{2.9}$$

Separating out the electronic and nuclear dipole operators in equation 2.9 gives,

$$\begin{aligned} M = &\int \Psi_v''^*(R)\Psi_v'(R)dR \int \Psi_e''^*(r,R)\,\Sigma_i p_e \Psi_e'(r,R)dr \\ &+ \int \Psi_v''^*(R)\Sigma_j p_n \Psi_v'(R)dR \int \Psi_e''^*(r,R)\,\Psi_e'(r,R)dr \end{aligned} \tag{2.10}$$

The electronic functions which belong to different states are orthogonal to one another and the second term in equation 2.10 therefore vanishes for electronic transitions. Assuming that the dependence of Ψ_e on the nuclear coordinates is neglected, equation 2.10 becomes,

$$M = \int \Psi_v''^*(R)\Psi_v'(R)dR \int \Psi_e''^*\left(r,R_{eq}\right)\Sigma_i p_e \Psi_e'\left(r,R_{eq}\right)dr \tag{2.11}$$

where R_{eq} is the equilibrium ground state configuration. Equation 2.11 now consists of one factor which depends on the nuclear motion and a second factor which depends on the electronic motion. From equation 2.11, the photoionisation transition probability (P) can be expressed as [18],

$$P \propto \left|\int \Psi_v''^*(R)\Psi_v'(R)dR\right|^2 \left|\int \Psi_e''^*\left(r,R_{eq}\right)\Sigma_i p_e \Psi_e'\left(r,R_{eq}\right)dr\right|^2 \tag{2.12}$$

This can be simplified to,

$$P \propto \left|\int \Psi_v''^*(R)\,\Psi_v'(R)dR\right|^2 \left|M_e\left(r,R_{eq}\right)\right|^2 \tag{2.13}$$

The first term is called the *Franck-Condon Factor* and it is this which controls the relative intensities of the vibrational components observed in a PE band from a PE spectrum. The second term is the square modulus of the electric dipole transition moment, M_e, and is usually assumed constant over a PE band.

2.1.1 Electronic Selection Rules

An electronic transition is allowed only when the electric dipole transition moment, M_e, shown as the second term in equation 2.13, is different from zero. Only one-electron transitions are permitted due to p_e being a one-electron operator. If the wavefunctions for the neutral and ionic states are constructed from the same set of molecular orbitals (MOs), and no reorganisation occurs on ionisation, only the electronic states which are different from those of the neutral states by one MO can be observed in PES. If spin-orbit interactions are small, the electronic wavefunctions, Ψ_e, can be expressed as a product of an orbital, Ψ_e' and as a spin function, Ψ_s [8-10],

$$\Psi_e = \Psi_{e'} \times \Psi_s \tag{2.14}$$

The spin functions corresponding to different spin values are orthogonal to one another and $M_e(r, R_e)$ is zero for states of different spin. Ionisation is allowed only between initial and final states with the same spin, i.e. $\Delta S = 0$, where the final state wavefunction is a product of both the ion and free electron wavefunctions. Closed-shell molecules with singlet neutral ground states have spin, $S_{mol} = 0$. The ejected photoelectron always has half-integral spin, $S_e = ½$. Only doublet ionic states, $S_{ion} = ½$, are therefore accessible from singlet neutral ground states.

2.1.2 Vibrational Selection Rules and Franck-Condon Factors

The relative intensity of a vibrational component in a PE band is given by the *Franck-Condon Factor* (FCF), which is written as,

$$FCF = |M_v|^2 = \left| \int \Psi_v''^*(R)\, \Psi_v'(R) dR \right|^2 \tag{2.15}$$

The Franck-Condon principle states that the intensity of a vibrational component in an electronically allowed transition (or ionisation) is proportional to the absolute square of the overlap integral of the vibrational wavefunctions of the initial and final states. These

ionisations can be represented using potential energy curves and this is shown in Figure 2.3. In a diatomic molecule the difference in energy, ΔE, between the lowest vibrational levels v″ = *0* and v″ = *1* in the electronic ground state of a molecule, *AB*, is usually large with respect to k_BT, (208cm^{-1}) at room temperature. For this reason it is therefore assumed that the lowest vibrational state v″ = *0* is significantly more populated compared to the higher levels v″ = *n*. During ionisation, a number of ionisations can take place and they will be observed in a PE spectrum for each ionic state reached. Ionic states are represented in Figure 2.3 as *X*, *A* and *B* with the three corresponding PE bands, shown in the adjacent spectrum, associated with these ionic states. The vibrational wavefunctions are shown for the vibrational levels of the neutral ground state, v″ = *0*, for molecule *AB* and for the vibrational levels of the first three ionic states, *X*, *A* and *B* respectively. The wavefunctions for the lowest vibrational levels, in both neutral and ionic states, are "bell shaped" while the wavefunctions of higher vibrational levels have broad maxima and minima near the classical turning points of the motion. It must be noted that the difference in energy, ΔE, between vibrational levels in any given state, neutral or ionic, decreases when approaching the dissociation limit and this is due to anharmonicity; however this is not represented in Figure 2.3 for illustrative purposes. In Figure 2.3, the molecular, *AB*, and ionic, AB^+X, ground states have similar equilibrium bond lengths and the shapes of their potential curves are also similar. As a result, the overlap of the v″ = *0* wavefunction with the v' = *0* wavefunction is good, giving an overlap integral close to 1.0, whereas overlap of the v″ = *0* wavefunction with the v' = *1* and v' = *2* wavefunctions give much lower overlap integrals. This would be consistent with ionisation of a *non-bonding* electron. For ionisation to the *A* state of the ion, an increase in equilibrium bond length occurs. This would be consistent with ionisation from a *bonding* electron. Overlap of the v″ = *0* wavefunction with the v' = *0* wavefunction is now much less effective. The overlap of the v″ = *0* wavefunction is greatest for the v' = *1* wavefunction and an envelope is observed in the PE spectrum shown in Figure 2.3 (shown in red). Two terms are used when considering the vibrational structure of a PE band, the adiabatic ionisation energy (AIE) and the vertical ionisation energy (VIE), which have been briefly described in the previous section of this chapter. The AIE represents the energy required to ionise the neutral molecule in the lowest vibrational level to the lowest vibrational level in the ionic state and is generally the first vibrational component seen in a PE band.

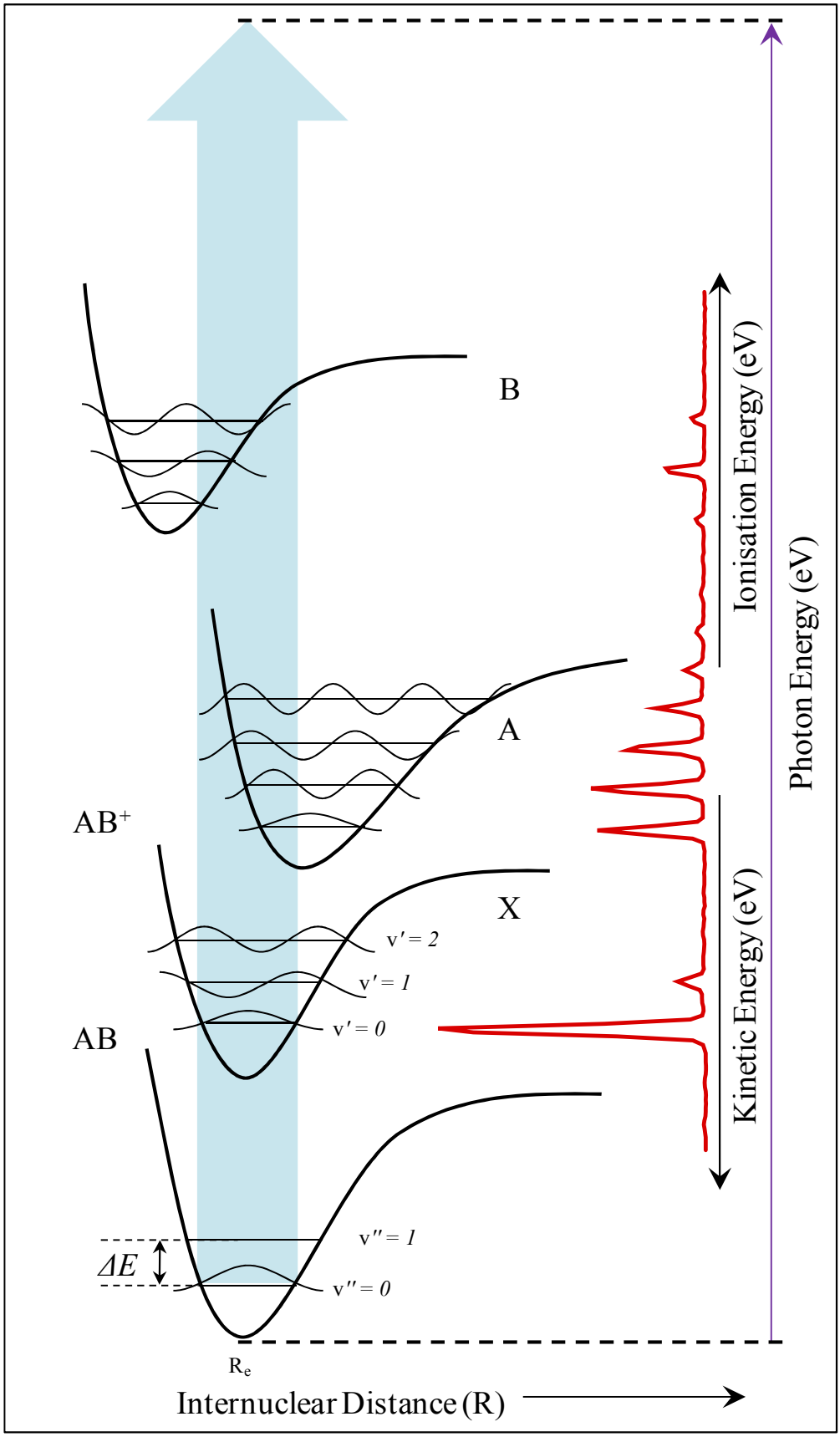

Figure 2.3: *Schematic diagram illustrating the Franck-Condon principle (for direct ionisation) showing the potential energy curves for a molecule, AB, in its ground state and for the ion, AB^+, in several ionic states, X, A and B. [8]. Schematic PE bands are shown on the right hand side.*

The VIE is the energy required to ionise from the lowest vibrational level of the neutral molecule to the vibrational level of the ionic state whose wavefunction has the largest degree of overlap with the v″ = *0* wavefunction, yielding the maximum overlap integral which is seen as the most intense component of a PE band. The AIE and VIE are only the same when the overlap integral is greatest for the ionisation v′ = *0* ← v″ = *0*. An example of this is shown for the first PE band in Figure 2.3. The energies of vibrational levels in a diatomic molecule in a given electronic state can be represented by the anharmonic oscillator expression [19],

$$E_{vib} = \omega_e\left(\mathrm{v} + {}^{1}/_{2}\right) - \omega_e\chi_e\left(\mathrm{v} + {}^{1}/_{2}\right)^2 \qquad (2.16)$$

where v is the vibrational quantum number, ω_e is the vibrational constant and χ_e is the anharmonicity constant. If the structure observed in a PE band is vibrationally resolved then the spacing between the vibrational components, ΔE_{vib}, can be determined by using equation 2.16 to give,

$$\Delta E_{vib} = E_{\mathrm{v}'+1} - E_{\mathrm{v}'} \qquad (2.17)$$

where $E_{\mathrm{v}'+1}$ and $E_{\mathrm{v}'}$ are ionisation energies from v″ = *0* to successive vibrational levels (v' + *1* and v'), in the ionic state. By measuring the separations in vibrational components seen in PE band, it is possible to determine the vibrational constants ω_e and $\omega_e\chi_e$ of the ionic state. This is shown in equation 2.18, obtained from equations 2.16 and 2.17,

$$\Delta E_{vib} = \omega_e - 2\omega_e\chi_e(\mathrm{v} + 1) \qquad (2.18)$$

Plotting the separation of vibrational components, ΔE_{vib}, as a function of (v' + *1*) will yield a line of slope $-2\omega_e\chi_e$ and intercept ω_e. A comparison of the ω_e value obtained in the ionic state with the measured value of ω_e in the molecular ground state can give an estimate of the bonding character of the orbital which the electron occupied before ionisation, e.g. if ionisation occurred from a bonding electron, the bond strength is weakened in the ionic state. The equilibrium bond length would increase and the vibrational constant ω_e of the ion will decrease. The opposite trends are expected for ionisation from an anti-bonding orbital.

In the first PE band of hexafluoropropene (C_3F_6), a product observed from the thermal decomposition of 2-H heptafluoropropane, a regular vibrational series is observed in the C=C stretching mode. This was analysed using equation 2.18 by plotting ΔE_{vib} versus (v' + *1*) to give ω_e and $\omega_e\chi_e$ in the ionic state for this vibration. This is discussed further in section 6.3.1 of Chapter 6.

2.2 Angular Distributions of Photoelectrons

The photoelectrons ejected during photoionisation are not emitted equally in all directions; also the angular distributions of such photoelectrons differ depending on the ionic state produced. As a result, the band intensities in PE spectra depend on, 1) the angle at which photoelectrons are detected with respect to either the propagating direction (for unpolarised radiation) of the incident radiation or the direction of the electric vector of polarisation of the photons (for polarised radiation) and 2) the energy of the photon beam used.

The angular dependence of the cross-section, $d\sigma/d\Omega$, where σ is the absolute angle-integrated cross-section and Ω is the solid angle collected, for *polarised* radiation in the electric dipole approximation can be expressed as [20, 21],

$$\frac{d\sigma}{d\Omega} = \frac{\sigma}{4\pi}[1 + \beta P_2(cos\theta)] \tag{2.19}$$

where θ is the angle between the direction of polarisation of the incident radiation and the detector, σ is the absolute photoionisation cross-section (PI-CS) at the photon energy used, β is the electric dipole asymmetry (anisotropy) parameter and $P_2(\cos\theta)$ is the second-order Legendre polynomial which is expressed as,

$$P_2(cos\theta) = \frac{1}{2}(3cos^2\theta - 1) \tag{2.20}$$

Equation 2.19 can be re-written as,

$$I(\theta) = \frac{\sigma}{4\pi}\left[1 + \frac{\beta}{2}(3cos^2\theta - 1)\right] \tag{2.21}$$

If the incident radiation is *unpolarised*, as is the case in the He(I) PES experiments performed in this work, then the intensity as a function of θ' can be written as [11],

$$I(\theta') = \frac{\sigma}{4\pi}\left[1 + \frac{\beta}{2}\left(\frac{3}{2}sin^2\theta' - 1\right)\right] \quad (2.22)$$

where θ' defines the angle at which the electrons are detected with respect to the propagating direction of the incident radiation.

In the dipole approximation, the β parameter is sufficient to completely describe the angular distributions of the outgoing photoelectrons emitted during ionisation and can have any value between 2 and -1. In the case of ionisation with polarised radiation, equation 2.21, $\beta = 2$ corresponds to a pure $cos^2\theta$ distribution, $\beta = 0$ corresponds to a spherical distribution and $\beta = -1$ corresponds to a pure $\sin^2\theta$ distribution.

The dipole approximation also results in the selection rule $\Delta l = \pm 1$ applying for photoionisation, where l is the angular momentum quantum number for the electron removed. As a result, ionisation from an *s* orbital, $l = 0$, a *p* photoelectron will be produced and ionisation from an atomic orbital of angular momentum $l > 0$ will give rise to two outgoing electron waves of angular momentum $(l + 1)$ and $(l - 1)$. Both waves will interfere with one another, as is manifested by the difference in phase shifts, $cos(\delta_{l+1} - \delta_{l-1})$ in the Cooper Zare formula for β [22],

$$\beta = \frac{l(l-1)R_{l-1}^2 + (l+1)(l+2)R_{l+1}^2 - 6l(l+1)R_{l+1}R_{l-1}cos(\delta_{l+1} - \delta_{l-1})}{(2l+1)(lR_{l-1}^2 + (l+1)R_{l+1}^2)} \quad (2.23)$$

where $\delta_{l\pm1}$ are the phase shifts of the *lth* partial wave and *R* is the radial matrix element, expressed as,

$$R_{l\pm1}(\varepsilon) = \int_0^\infty P_{nl}(r) r P_{\varepsilon,l\pm1}(r) dr \quad (2.24)$$

β values for the simple atomic ionisations are $\beta = 2$ for an $s \rightarrow p$ ionisation, $\beta = 0$ for a $p \rightarrow s$ ionisation and for a $p \rightarrow d$ ionisation $\beta = 1$ [23]. For a *p* ionisation, two waves (*s* and *d*) are produced and the β value at a given photon energy is determined by equation 2.23.

The asymmetry parameter, (β) depends on the character of the molecular orbital from which the photoelectron is removed and therefore is constant within a particular photoelectron band. The detection angle at which the spectra are measured is also

crucial when measuring β parameters. For linearly polarised radiation, the β values can be determined experimentally by measuring the intensity, I, of a PE band at two known detection angles, (θ), with respect to the direction of the polarisation vector of the photon beam, using equation 2.21.

If the band intensity is measured at $\theta = 0^{o}$, then equation 2.21 becomes,

$$I_0 = \frac{\sigma}{4\pi}(1 + \beta) \tag{2.25}$$

If the band intensity is measured at 54º44' (54.736º), the magic angle, with respect to the photon beam, the intensities are independent of the β parameter and therefore the intensity of a measured PE band is directly proportional to the photoionisation cross-section and equation 2.25 becomes,

$$I_{54^{\circ}44'} = \frac{\sigma}{4\pi} \tag{2.26}$$

The angular distribution parameter, β, can be determined from ratio of the intensities, given in equations 2.25 and 2.26, and can be written as,

$$\frac{I_0}{I_{54^{\circ}44'}} = (1 + \beta) \tag{2.27}$$

Equation 2.27 can be simplified to,

$$\beta = R - 1 \tag{2.28}$$

where R is ratio of the measured PE band intensities shown in equation 2.28. Therefore by recording PE spectra at two different angles, $\theta = 0^{o}$ and $\theta = 54^{o}\ 44'$, it is possible to obtain the β values [16, 20]. In this way, further information can be obtained about the photoionisation process, mainly concerning the character of the initial orbital and the nature of the free electron wavefunction.

For unpolarised radiation the β values can also be determined experimentally by measuring the intensity, I, of a PE band at different detection angles, (θ'), away from the direction of propagation of the photon beam shown in equation 2.22. If PE bands are measured at $\theta' = 90^{o}$, as is the case in this work, then equation 2.22 can be written as [24, 25],

$$I(\theta) = \frac{\sigma}{4\pi}\left(1 + \frac{\beta}{4}\right) \tag{2.29}$$

As part of this work, reaction branching ratios were determined for selected ozone plus alkenes reactions (see Chapters 7 and 8). In order to determine the reaction branching ratios for each of the alkene plus ozone reactions studied, the partial pressures of reactants and products were determined (deduced from cross-section measurements). This was done by measuring the intensities of selected PE bands observed for the reactants and products as a function of reaction time. However, in order to put these measurements on an absolute scale, the photoionisation cross-sections (PI-CS) of both reactants and reaction products were measured. The sample preparation and sampling method used to do this, described in detail in Chapter 7, were developed with the aim of measuring the photoionisation cross-sections of the reactants and products relative to argon at 90° to an unpolarised photon beam. Argon was chosen as a reference as it is inert and has a well established photoionisation cross-section at the photon energy used in this work i.e. 21.22 eV. Relative photoionisation cross-sections can then be calculated from intensity measurements at 90° to an unpolarised photon beam using,

$$\sigma_{relative} = \frac{I_{sample}}{I_{reference}} \tag{2.30}$$

for the same partial pressures of the sample and reference gas. As all photoionisation cross-section measurements were carried out using the same spectrometer in this work, absolute, angular independent intensities were not required to obtain the relative branching ratios needed and therefore the associated β parameters were not determined experimentally. However measured PI-CS were put on an absolute scale by using β values obtained from the literature purely for completeness. The experimental method used to measure the PI-CS of reactants and products observed from the ozone plus alkene reactions closely follows that outlined by Samson *et al.* [24] and Kimura *et al.* [26] and is described in greater detail in Chapters 7 and 8. The methods used rely on the characteristics of the apparatus being used, i.e. energy of the photon source, geometry and transmission efficiency of the analyser, and the photoelectron detection angle as well as the sampling preparation method and sample admission procedures. The equipment and apparatus used for all the experiments performed, which have been

reported in this thesis, are described in the following chapter, and the preparation and sampling methods are described in their respective chapters.

2.3 Summary

This chapter has focused on the basic principles of PES which are relevant to the work outlined in this thesis. The photoelectric effect has been described in order to show how it is used experimentally in PES and explained in relation to recorded PE spectra. This has included a description of the basic principles which govern direct ionisation, a discussion of the vibrational structure observed in PE bands and how the Franck-Condon principle can be used with experimental spectra to provide information on the ionic states and the character of the molecular orbitals from which ionisation has occurred. A description of photoelectron angular distribution parameters and how they can be measured experimentally along with photoionisation cross-sections was also given. These principles have been applied to the analysis of the results obtained during this work, as well as in developing some of the experimental procedures used.

References

[1] J. C. Maxwell, *Phil. Trans. Roy. Soc. Lon.*, 155, 1865, 459.

[2] H. Hertz, *Ann Phys.*, 31, 1987, 983.

[3] P. Lenard, *Ann Phys.*, 2, 287, 1894, 259.

[4] M. Planck, *Ann Phys.*, 4, 1901, 553.

[5] A. Einstein, *Ann. Phys.*, 17, 549, 1905

[6] D. W. Turner and M. I. Al. Joboury, *J. Chem. Phys.*, 37, 1962, 3007.

[7] F. I. Vilsov, B. L. Kurbator and A. N. Terenin, *Dokl. Akad. Nauh.*, SSR 138, 1961, 1329.

[8] J. W. Rabalais, Principles of Ultraviolet Photoelectron Spectroscopy, *John Wiley and Sons*, *New York*, 1977.

[9] D. W. Turner, C. Baker, A. D. Baker and C. Brundle, Molecular Photoelectron Spectroscopy, *Wiley Interscience*, *London*, 1970.

[10] H. Siegbahn and L. Karlsson, Photoelectron Spectroscopy, *Springer-Verlag*, *Berlin Heidelberg*, *New York*, 1982.

[11] J.H.D. Eland, Photoelectron Spectroscopy, *Butterworths*, *London*, 1974.

[12] A. Morris, Lecture Notes on Experimental Photoelectron Spectroscopy, *University of Southampton*, 1996.

[13] O. Edqvist, E. Lindholm, L. E. Salin and L. Åsbrink, *Physica. Scripta.*, 1, 1970, 25.

[14] P. W. Atkins, Physical Chemistry, *Oxford University Press*, *Oxford*, 1986.

[15] L. Zuin, F. Innocenti, M. L. Costa, A. A. Dias, A. Morris, A. C. S. Paiva, S. Stranges, J. B. West and J. M. Dyke, *Chem. Phys.*, 298, 2004, 213.

[16] F. Innocenti, L. Zuin, M. L. Costa, A. A. Dias, A. Morris, A. C. S. Paiva, S. Stranges, J. B. West and J. M. Dyke, *J. Elec. Spec. Rel. Phen.*, 142, 2005, 241.

[17] F. Innocenti, M. Eypper, S. Beccaceci, A. Morris, S. Stranges, J. B. West, G. C. King and J. M. Dyke, *J. Phys. Chem. A.*, 112, 2008, 6939.

[18] G. Herzberg, *Molecular Spectra and Molecular Structure.*, D. Van Nostrand Company, *Inc. Princeton N. J.*, 1, 1967, 413.

[19] M. J. Hollas, Modern Spectroscopy, *John Wiley and Sons, London*, 1987.

[20] J. A. R. Samson and A. F. Starace, *J. Phys. B. Atom. Molec. Phys.*, 8, 1975, 1806.

[21] J. A. R. Samson and J. L. Gardner, *J. Optic. Soc. Am.*, 62, 1972, 856.

[22] J. Berkowitz, Photoabsorption, Photoionisation and Photoelectron Spectroscopy, *Academic Press, London*, 1979.

[23] J. B. West, Vacuum Ultraviolet Photoionisation and Photodissociation of Molecules and Clusters*, New Jersey*, 1991.

[24] J.L. Gardner and J.A.R. Samson *J. Elec. Spec. and Rel. Phen.*, 8, 1976, 469.

[25] Y. Achiba, T. Yamazaki and K. Kimura, *J. Elec. Spec. and Rel. Phen.*, 22, 1981, 187.

[26] Y. Achiba, K. Kimura, N. Kakuta and K. Miyahara, *J. Elec. Spec. and Rel. Phen.*, 28, 1982, 139.

Chapter 3

Experimental Techniques

In this chapter experimental techniques are described which are used to study selected molecules and reactions of atmospheric importance using photoelectron spectroscopy (PES). All the work described in Chapters 5 to 9 of this thesis has been carried out using three spectrometers, all of which have been designed by Dr Alan Morris of the Southampton photoelectron spectroscopy group [1-6].

The first spectrometer consists of a 150° hemispherical electron energy analyser with a mean radius of 10 cm. It uses a helium discharge lamp to produce a flux of unpolarised photons of fixed energy (21.22eV). This spectrometer, referred to as the *small spectrometer*, was used to study the reactions, O_3 + ethene, O_3 + 2-methylpropene (2MP) and O_3 + 2, 3 dimethyl-2-butene (DMB) by recording PE spectra as a function of reaction time. This was achieved using reaction-specific inlet systems, due to the differences in the reaction rates of the three alkene plus ozone reactions studied (see section 3.2.1 of this chapter and Chapters 7 and 8 for details). The spectrometer was also used to develop a reproducible, stable method to observe and record the PE spectrum of the first 2 PE bands of the unstable intermediate hypochlorous acid (HOCl), from reactions (3.1a) and (3.1b),

$$Cl_2 + HgO_{(s)} \rightarrow Cl_2O + Hg_{(s)} \quad (3.1a)$$

$$Cl_2O + H_2O \rightarrow 2HOCl \quad (3.1b)$$

It was proposed to use this method in the future to record the threshold photoelectron (TPE) spectrum of HOCl at the synchrotron radiation facility, Elettra, in Trieste, Italy. A related objective was to record a pure PE spectrum for the first 3 PE bands of chlorine

monoxide (Cl_2O) produced from reaction (3.1a). The results of the HOCl and Cl_2O experiments are described further in Chapter 9.

The second spectrometer, referred to as the *big spectrometer*, was similar in design to that of the first (small spectrometer). It has a larger hemispherical analyser of mean radius of 20 cm. The size of the analyser is an important factor when considering the spectral resolution of the system and this is discussed in more detail in section 3.1.3. This spectrometer was used, in conjunction with the alkene-ozonolysis experiments performed on the small spectrometer, to measure the photoionisation cross-sections of the reactants and stable reaction products observed from the alkene plus ozone reactions using a differentially pumped flow-tube coupled to the ionisation region. The differentially pumped flow-tube set-up is discussed in section 3.2.2 of this chapter and the sampling procedure is described in Chapters 7 and 8. The thermal decomposition pathways of two fire suppressants, pentafluoroethane (HFC-125) and 2-H heptafluoropropane (FM-200), were studied on the big spectrometer (see Chapters 5 and 6 respectively) using a water cooled radio-frequency (RF) induction heating system coupled to the ionisation region. The RF heating system is described in section 3.3 of this chapter. Both the small and the big PE spectrometers are described in section 3.1.

The third spectrometer was used to record a well resolved first TPE band of the triatomic molecule SF_2, with reduced contributions from S_2, at the Elettra synchrotron source. The reactions used to prepare SF_2 for study by TPES were,

$$F + OCS \rightarrow SF + CO \qquad (3.2a)$$

$$SF + SF \rightarrow SF_2 + S \qquad (3.2b)$$

$$S + S + M \rightarrow S_2 + M \qquad (3.2c)$$

This spectrometer consisted of a 180° hemispherical analyser with a mean radius of 10 cm. The analyser and detector could be rotated through 75° with respect to the direction of linear polarisation of the photon source, in order to carry out angular distribution measurements as a function of photon energy. It was specifically built to be used with both polarised, tuneable synchrotron radiation and unpolarised He(I) radiation. The spectrometer utilises an electron lens system, to transmit electrons from the ionisation region towards the analyser region. By operating the analyser at fixed pass energy and

sweeping the photon energy a threshold photoelectron spectrum can be obtained. The operation of the TPE spectrometer is described in section 3.4.2.

The sampling procedures used and analysis of the experimental results obtained for each of the reactions and molecules studied are described in more detail in their respective chapters in this thesis. Only the instrumental details of the apparatus used, i.e. PE spectrometers and sampling equipment for each experiment will described in this chapter.

3.1 The Photoelectron Spectrometer

The main components of the PE spectrometers used throughout this work are a photon source, photoionisation or interaction region, an analyser region and a detector. As the designs of both the small and big PE spectrometers are essentially the same, with the only exception being the size of the analyser used, only one schematic diagram, representing both systems and showing all major components is required. This is shown in Figure 3.1.

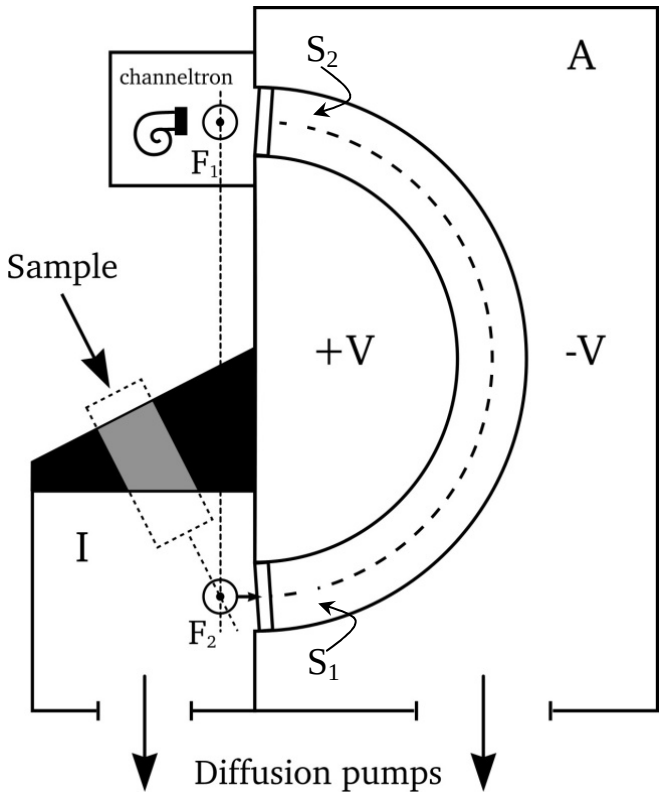

Figure 3.1: *Schematic diagram of the photoelectron spectrometer used in this work. F_1 and F_2 are the exit and entrance electron focus points. S_1 and S_2 are the entrance and exit slits respectively. I, is the ionisation chamber and A, is the analyser chamber.*

Figure 3.1 shows a cross-sectional view of the PE spectrometer with the photon source perpendicular to the vertical plane. The photon beam passes through the point labelled F_2. A helium discharge lamp is positioned on the side of the ionisation chamber. It provides a photon beam which enters the ionisation region from the side, at 90° with respect to the sample port shown in Figure 3.1. The photoionisation chamber, *I*, contains a reaction cell which is used to collimate the admitted samples. The ionisation chamber is positioned directly above a diffusion pump to ensure low pressure and good pumping efficiency are maintained within the interaction region. A gaseous sample can be introduced either from the side of the ionisation chamber through the reaction cell, coaxially aligned with the photon beam, or as shown in Figure 3.1, perpendicular to the photon source (see also Figure 3.2).

The 150º electron energy analyser, *A*, consists of two concentric hemispheres, to which equal and opposite voltages are applied [7]. This provides an electrostatic field which deflects electrons of defined energy to the detector. By sweeping the voltage difference between the hemispheres using a ramp generator, photoelectrons can be separated according to their kinetic energies [7-9]. Both ionisation and analyser chambers are maintained at low pressures, of the order of 10^{-6} torr. This reduces any collisions between the photoelectrons and residual gas-phase molecules, and ensures that the mean free path of the photoelectrons is greater than the distance travelled around the hemispheres.

The electrons are then detected using a channel electron multiplier (channeltron), which produces electrical pulses on electron impact. These pulses are amplified and counted on a ratemeter and can then be recorded using computer software.

Electron trajectories inside the spectrometer are easily perturbed by stray magnetic fields [7]. To reduce these field effects, the photoelectron spectrometer is constructed entirely of non-magnetic materials, notably Dural, an aluminium alloy, and uses three sets of mutually perpendicular Helmholtz coils [1]. The Helmholtz coils positioned around the spectrometer each have a direct current running through them to produce a field which counteracts that of the earth's magnetic field in the direction perpendicular to the coils. This current is optimised each time before any experimentation is carried out, due to changes in local magnetic fields. This is achieved by recording the He(I) PE spectrum for argon as it is intense, and well established as having two distinct bands,

$Ar^{+}(^{2}P_{3/2}, {}^{2}P_{1/2}) \leftarrow Ar(^{1}S_{0})(3p)^{-1}$, and optimising the signal intensity and resolution as the currents through the coil are changed [8].

Argon is also used to determine the resolution, $(\Delta E_{1/2})$, of the spectrometer. This is typically 20-30 meV, determined from the length, (ΔL), between the two $Ar(3p)^{-1}$ bands using equation 3.3, and the width at half height, $(\Delta E_{1/2})$, of the most intense $Ar(3p)^{-1}$ component.

$$\Delta E_{1/2} = \frac{178meV \times FWHM\left({}^{2}P_{3/2}\right)}{\Delta L} \qquad (3.3)$$

where the Full Width Half Maximum, $\Delta E_{1/2}$, is the width of the $Ar^{+}(^{2}P_{3/2}) \leftarrow Ar(^{1}S_{0})(3p)^{-1}$ band at half its total band height. ΔL represents the length separating the two bands, which is well established as 178 meV between the two ionic states, $Ar^{+}(^{2}P_{3/2}, {}^{2}P_{1/2})$ [8]. An oxygen spectrum is also recorded before each experiment to ensure that acceptable transmission can be obtained throughout the ionisation energy range.

3.1.1 The Photon Source

The u.v. photon source used in this work on both the small and the big PE spectrometers is a d.c. discharge in helium which produces an unpolarised photon emission of 58.43 nm (21.22 eV). The emission results from the transition, $^{1}S_{0}(1s^{2}) \leftarrow {}^{1}P_{1}(1s^{1}\ 2p^{1})$, in the neutral helium and is known as He(I)α radiation. It is the main photon emission from excited helium, and is sufficiently energetic to remove an electron from orbitals involved in chemical bonding, i.e. the electrons occupying the valence shell of atoms or molecules [9]. He(I)α refers to the transition between the first electronic excited state of the neutral molecule and the ground state of the neutral molecule. If a transition were to occur in the cation then the emitted radiation would be referred to as He(II) radiation. Other transitions, in neutral helium, can occur from the $^{1}P_{1}$ states with the 1s *n*p configuration, where *n = 3*, 4, 5...etc, to the $^{1}S_{0}$ ground state, and these are referred to as He(I)β, He(I)γ, He(I)δ...respectively. Small amounts of these He(I) lines are present in the discharge. However, their intensities relative to the He(I)α line are small with the most intense, He(I)β, being only *ca.* 1.3% the intensity of the He(I)α emission. In a PE spectrum, a PE band arising from He(I)β ionisation is commonly referred to as a *shadow band.* It is essentially a weaker version of the He(I)α PE band occurring 1.87eV

higher in electron kinetic energy. The He(I) emission lines including their respective energies and relative intensities are shown in Table 3.1 below.

He(I) Line	Wavelength (nm)	Energy (eV)	Excited State ($^1P_1$)	Relative Intensity
α	58.43	21.22	2p	100
β	53.73	23.09	3p	1.3
γ	52.22	23.74	4p	0.13
δ	51.56	24.04	5p	0.05
ε	51.21	24.21	6p	< 0.03

Table 3.1: *Comparison between the photons produced from the various neutral transitions which occur on discharging helium [7-9].*

Helium is admitted into the differentially pumped lamp at a pressure of ~0.5 torr through a quartz capillary where a discharge occurs between the anode and cathode. The current under operating conditions is typically 50 mA. The photons a then enter the spectrometer. Under normal operating conditions the He(I) photon flux is of the order of 10^{11} photons sec^{-1} [7]. The lamp is differentially pumped using a rotary pump and a diffusion pump which is directly connected to the ionisation chamber. By differentially pumping the lamp, excess helium, which would otherwise reach the ionisation region and reduce the partial pressures of the sample gases and hence reduce the intensity of the target signal, can be removed. By reducing the pressure of the helium gas admitted and increasing the voltage and current, the discharge in helium can be made to emit more radiation from helium ions, i.e. He(II) radiation with photon energy of 40.81 eV. However, despite being possible to obtain such a photon energy, He(II) radiation was never used during the course of this work.

3.1.2 The Ionisation Chamber and the Reaction Cell

The discharge lamp is attached, externally to the side of the ionisation chamber. A reaction cell is attached to the inside of the ionisation chamber directly in line with the emitted photons from the lamp. Sample gases can be admitted along the same line as the photon source but from the opposite direction, i.e. through the reaction cell from the opposite side, or they can be admitted perpendicular to the photon source as is seen in the schematic diagram of the reaction cell in Figure 3.2. When a reaction is studied, all the reactants and reaction products are pumped into the reaction cell where they are photoionised. The photoelectrons produced propagate in all directions within the reaction cell. The cell contains two sets of adjustable focussing slits which allows only

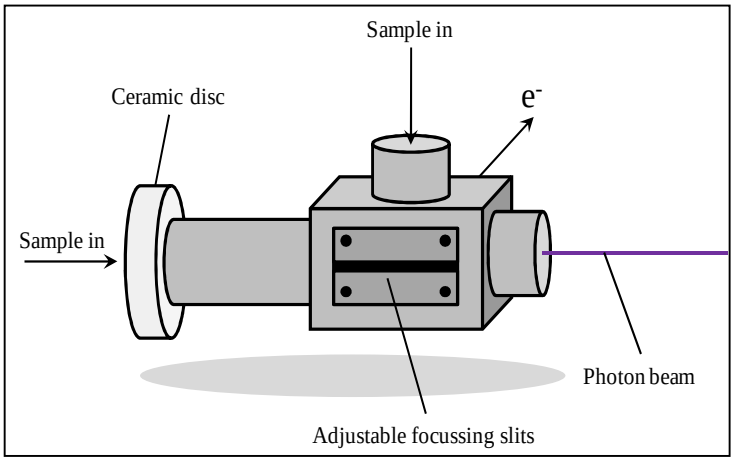

Figure 3.2: *Diagram of the reaction cell used in this work on both small and big spectrometers.*

photoelectrons emitted at 90° with respect to the photon source to enter the analyser region and be detected. However, before being detected, the emitted photoelectrons must pass through two further sets of adjustable focussing slits, entrance and exit slits, after leaving the reaction cell and these are shown as S_1 and S_2 respectively in Figure 3.1. In practice the spectrometer slit widths are adjusted to optimise the resolution and signal intensity. The signal-to-noise ratio and spectral resolution are also directly affected by contamination of any of the following components, the reaction cell, the entrance and exit slits, the ionisation chamber and the analyser chamber. Contamination can result in a build up of surface charge which can perturb the trajectories of the emitted photoelectrons resulting in a loss of resolution, intensity and a decrease in the signal-to-noise ratio. In order to reduce these effects all the components which are located within the ionisation region and the hemispheres in the analyser region are coated with a fine layer of colloidal graphite (DAG). This provides a conductive film which allows any build up of surface charge from contamination to be easily dissipated, helping maintain spectral resolution during an experiment. To avoid inelastic scattering of ejected photoelectrons, the ionisation and analyser chambers are each positioned directly above a diffusion pump (see Figure 3.1). This provides background operating pressures of 10^{-6} torr. Pressures typically do not exceed 10^{-5} torr in the ionisation chamber during an experiment when samples are admitted.

3.1.3 The Analyser Chamber

A 150° electrostatic hemispherical analyser is used on both the small and the big spectrometers throughout this work. The analyser chamber and the ionisation chamber are each pumped by diffusion pumps as seen in Figure 3.1. The pressure in the analyser region is typically 10^{-6} torr. The analyser consists of two hemispheres, an inner and an

outer sphere of radius R_1 and R_2 respectively to which equal and opposite voltages are applied, a positive voltage to the inner sphere and a negative voltage to the outer sphere. This is shown in Figure 3.3. Applying equal and opposite potentials to the hemispheres creates an electrostatic field between each sphere in the photoelectron trajectory region of which only photoelectrons of kinetic energy equal to [10],

$$KE = \frac{1}{2}V\left[\frac{(R_2 + R_1)}{(R_2 - R_1)}\right] \tag{3.4}$$

can reach the detector, where V is the potential applied to the hemispheres. Sweeping this field by changing the applied potentials allows photoelectrons of different kinetic energies to be selected and transmitted through the analyser onto the detector. A ramp generator is used to sweep the voltages linearly applied to each sphere in order to obtain a photoelectron signal over a large electron kinetic energy range.

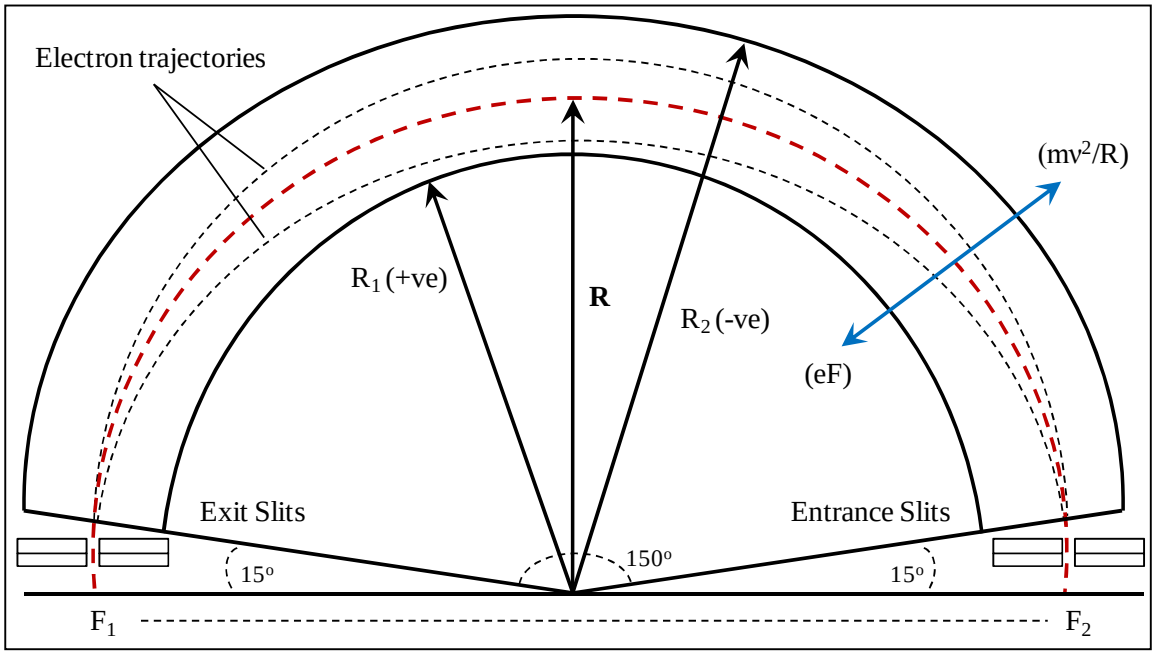

Figure 3.3: *Schematic diagram of the 150° electron energy analyser. The central orbital radius, shown in red, is 10 cm for the small spectrometer and 20 cm for the big spectrometer.*

This type of analyser has a double focussing property. This means that photoelectrons can travel from the entrance to exit slits with numerous trajectories. This results in more electrons being detected and an improved signal-to-noise ratio i.e. enhanced sensitivity. This feature is invaluable for detecting electrons of low kinetic energies (< 8 eV). For an electron to orbit between both hemispheres, the stability of that orbit is dependent on

the electrical force, (eF), acting on the electron being equal to the centripetal force, $\left(\frac{mv^2}{R}\right)$, where, *e* is the electron charge, *m* is the mass, *F* is the electrical field, v is the electron velocity and *R* is the mean radius of the electron orbit. This is shown in red in Figure 3.3. The kinetic energy of an electron is given by equation 3.5.

$$KE = \frac{1}{2}mv^2 = E \tag{3.5}$$

Therefore for a stable orbit,

$$E = \frac{1}{2}eFR \tag{3.6}$$

Because of the finite entrance and exit slit widths shown as S_1 and S_2 respectively in Figure 3.1, variations in the electron orbital radius must be taken into consideration and equation 3.6 can be used to give,

$$\Delta E = \frac{1}{2}eF\Delta R \tag{3.7}$$

where *ΔE* is the electron energy spread for a change in radius *ΔR*. The change in *R*, *ΔR*, due to finite slit widths, can be written as,

$$\Delta R = \frac{total\ slit\ width}{2} = \frac{S}{2} \tag{3.8}$$

where *S* is the total slit width. Thus the spread in energy of the electrons (ΔE) at a given energy (E) depends on the geometry of the electron energy analyser. Equations 3.7 and 3.8 can be used to give [11],

$$\frac{\Delta E}{E} = \frac{S}{2R} \tag{3.9}$$

Therefore reducing the total slit width will reduce the energy spread of electrons, increasing the resolution whilst lowering the band intensity. Conversely, increasing the electron mean radial orbit, *R*, at a given, *S*, will increase the spectrometer's resolution. In equation 3.7 and 3.9, *ΔE*, is the base width of a band.

For typical band shapes obtained with a hemispherical analyser, it has been shown that the half-width and the base-width are related via [11],

$$\Delta E_{Base} = 2.3\ \Delta E_{1/2} \tag{3.10}$$

Therefore, combing equations 3.9 and 3.10 gives,

$$\frac{\Delta E_{1/2}}{E} = \frac{S}{2R} \cdot \frac{1}{2.3} \tag{3.11}$$

This equation therefore gives the instrumental contribution to the experimental resolution arising from the geometric parameters of the analyser and the slits. Contributions to the resolution of the spectrometer other than those determined by these instrumental factors, which are smaller, are from line broadening in the photon source, Doppler broadening and self-reversal [12, 13].

Doppler broadening is the broadening of spectral lines caused by the thermal motions of the target atoms or molecules. It can be reduced by operating at reduced sample temperatures. Self-reversal refers to unexcited helium in the path of the photon flux. The core of the flux is more highly absorbed relative to the outer helium flux because the emission is from “hot” helium and absorption is by “cold” helium. This can cause a build up in intensity along the width of the photon beam increasing the line width. Local contact potentials also contribute to line broadening and so surfaces are coated with a layer of DAG to reduce this effect. Taking these factors, along with instrumental contributions, into consideration, the typical operating resolution of both the small and the big PE spectrometers used in this work is 20-30 meV as measured for the $(3p)^{-1}$ ionisation of argon with a count rate of ~$3x10^4$ counts sec^{-1}.

3.1.4 Detector and Electronics

The photoelectrons which pass through the exit slits are detected by a channel electron multiplier, also called a channeltron. This is a spirally shaped glass tube coated in a semi conductive film. The front of the channeltron is earthed and a +2.5 kV potential is applied to the other end. By applying a large positive potential to the multiplier, the photoelectrons are accelerated through the tube structure. When a photoelectron is incident on the semi conductive material of the channeltron, a secondary emission process takes place.

The induced emission causes a cascade effect, where for each electron incident on the material between one and three electrons are produced as secondary emitters [14].

These secondary emitted electrons are then accelerated along the tube and when incident on the surface they produce another series of secondary emitters and so on. This process is shown in Figure 3.4. The signal from the channeltron is first sent to a pre-amplifier and then it is further amplified before being sent to a ratemeter. The output signal from the ratemeter is recorded using a chart recorder or the output from the amplifier is recorded on a computer using software coded in C.

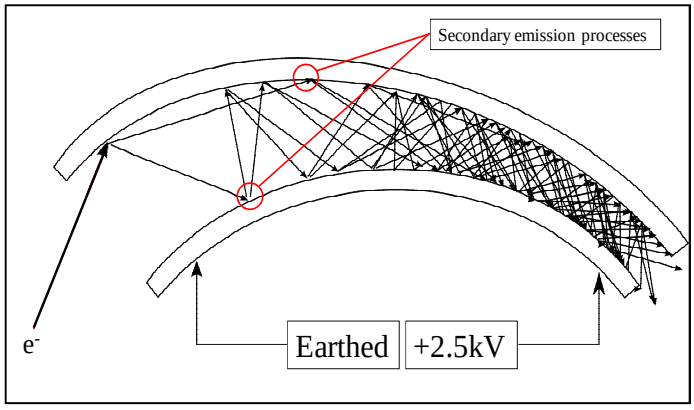

Figure 3.4: *Schematic diagram of the electron cascade process which occurs in the channeltron when an electron is incident on its surface [14].*

3.2 Inlet Systems

3.2.1 A Simple Glass Inlet System

All reactions investigated with simple inlet systems, similar in design to those shown in Figure 3.5 and 3.6, were studied using the small PE spectrometer. Glass inlet systems (made from borosilicate glass) can be added to the ionisation chamber of a PE spectrometer in order to study gas-phase reactions as a function of mixing distance or temperature as they are relatively unreactive and can be heated under vacuum, to working temperatures (strain point) of around 510 °C [15]. The ozonolysis of the selected alkene molecules was performed using three different inlet systems designed specifically for each alkene under investigation. The basic inlet system, used for O_3 + 2-methylpropene (2MP) and O_3 + 2, 3 dimethyl-2-butene (DMB), consists of two concentric glass tubes, where the inner tube is movable with

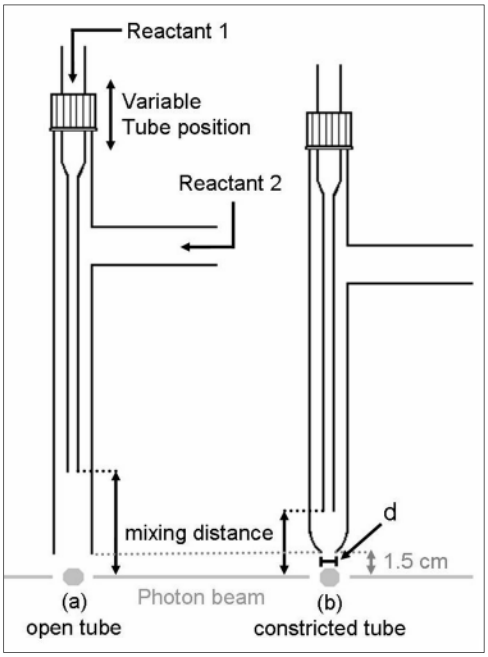

Figure 3.5: *Schematic diagram of two different glass inlet systems.*

respect to the outer tube. This is shown in Figure 3.5. The alkene was introduced via the top of the tube whilst the ozone was introduced via the side arm. 50 cm long glass inlet tubes were used to study 2MP and DMB with constricted ends of inner diameters of 0.5 mm and 1.5 mm respectively. Each inlet tube had inner and outer diameters of 10 and 12 mm respectively. For 2MP and DMB, spectra were recorded every 5 cm from 50 cm to 0 cm. The input flow rates of each reagent were controlled using needle valves. The inner tube was moveable and that meant that reactions could be studied as function of reaction mixing distance. For 2MP and DMB, two baratron pressure transducers, located at 10 cm and 48 cm from the bottom of each inlet, were used to monitor the pressures changes as a function of reaction mixing distance. By taking pressure differential measurements at these two points on the inlet tube during a reaction at known partial pressures, flow rates *(F)* and hence linear flow velocities could be calculated at each reaction mixing distance using the Poiseuille equation [16-18],

$$F = \left(\frac{P_1^2 - P_2^2}{P_0}\right) \times \frac{\pi r^4}{16 L \eta} \qquad (3.12)$$

where, P_1 and P_2 are the first and second pressure measurements, P_0 is the atmospheric pressure, L is the length of the flow-tube or inlet system between the points of pressure measurement for P_1 and P_2, and η is the total gas viscosity. Knowing the linear flow velocities of the gases in the inlet system at known reaction mixing distance meant that a reaction time for a given distance could be determined. Using this information reaction distances can be converted to reaction times (see Chapters 7 and 8).

For the reaction ethene plus ozone, a 30 m long open ended inlet system with inner and outer diameters of 10 and 12 mm respectively, was used. Of the three alkenes studied ethene undergoes the slowest reaction with ozone, having an estimated room temperature rate coefficient of 1.72×10^{-18} cm^3 molecules^{-1} s^{-1} compared to that of 2MP and DMB with room temperature rate coefficients of 1.13×10^{-17} and 1.13×10^{-15} cm^3 molecules^{-1} s^{-1} respectively [19]. Hence, in the ethene case the inlet system used had to be long enough to ensure that ethene underwent complete reaction with ozone by the time it reached the photon beam [20]. A diagram of this inlet system is shown in Figure 3.6.

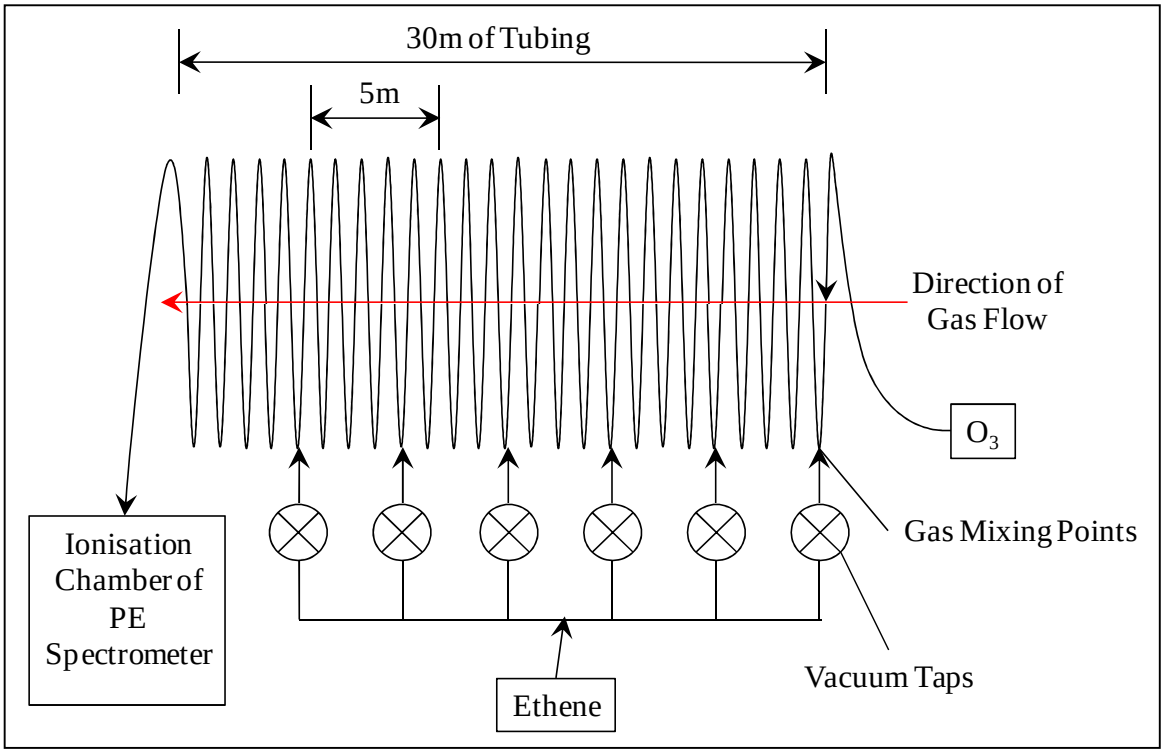

Figure 3.6: *Schematic diagram of the 30 m long inlet system used to study ethene plus ozone at mixing distances every 5 m.*

The inlet system was constructed from 30 m of plastic tubing reinforced with 4 cm long glass tubes, with a 10 mm inner diameter, running throughout the inside length of the plastic tubing with gas mixing points positioned every 5 m. Due to the potentially explosive nature of this reaction, an open ended tube was used to couple the inlet to the ionisation chamber [20]. Pressure measurements were recorded using baratron pressure transducers attached to the vacuum taps every 5 m from the point of ionisation. Spectra were obtained at mixing distances every 5 m from 30 m to 0m, for the ethene plus ozone reaction. The operation of the inlet systems used is discussed further in Chapter 7.

To generate F atoms needed for reaction (3.2a) for the SF_2 work, a microwave discharge (2.45 GHz) of flowing 5% F_2 in helium was used. An inlet system, similar to that shown in Figure 3.5, 20 cm long with inner and outer diameters of 10 mm and 12 mm respectively, was coated in teflon to prevent the fluorine atoms attacking the glass (the moveable inner tube was also teflon coated). The microwave cavity was attached to an alumina tube fitted to the side arm, which was attached to the main body of the outer tube via a 90° bend to prevent low energy electrons produced from the discharge reaching the ionisation region. The reason for using an alumina section of the inlet system for the microwave cavity is to avoid the flowing discharge attacking the glass

and to prevent the teflon melting from the heat which is produced. For the F + OCS reaction, F_2/He was admitted via the side arm and passed through the discharge to yield F atoms. OCS was admitted via the top central inlet.

For the HOCl and Cl_2O work, an open ended straight glass inlet tube, 35 cm long with inner and outer diameters of 10 and 12 mm respectively was used. A glass frit of porosity grade 0 was placed 15 cm from the bottom of the inlet to prevent any solid materials, i.e. HgO powder and glass wool, from entering the ionisation chamber. A B20 cone joint was used at the top in order to provide an entrance wide enough to facilitate easy sample introduction and to aid in the removal of used materials during cleaning.

Simple glass inlet systems are very useful in studying gas-phase reactions qualitatively. Studying reactions and sampled molecules quantitatively can be achieved by interfacing a differentially pumped flow-tube to a PE spectrometer. This application also has the advantage in that rate coefficients as well as number densities and flow velocities can be obtained.

3.2.2 A Differentially Pumped Flow-Tube

In general, flow-tubes are very versatile in that they can be used to study reactions over a range of pressures and temperatures, e.g. $\leq$ 400 torr [21, 22] and 200-600 K respectively under specific flow conditions (laminar or turbulent flow) [23, 24]. Flow-tubes are widely used and preferred over techniques such as flash photolysis, for reaction kinetics studies near 300 K [24]. The instrument used in this work is operated at ambient temperature and at low pressures (1-10 torr) under laminar flow conditions. It is shown in Figure 3.7. In order to interface the high pressure of the flow-tube (1-10 torr) with the low pressure of the ionisation chamber of the spectrometer, (10^{-6} torr), the flow-tube is operated with two stages of differential pumping [25]. This is a technique applied when an interface exists between two systems which have large pressure differences [16-18, 25]. Three pumps are required in order to obtain the desired pressures within the flow-tube used in this work, two Leybold D25B rotary pumps and a larger Edwards SV-200 rotary pump which also maintains the desired flow rate in the flow-tube. The differentially pumped flow-tube coupled to the large spectrometer was used in determining the photoionisation cross-sections (PI-CSs) of the reactants and

stable reaction products observed from the alkene ozonolysis experiments performed using the glass inlet system, described previously in section 3.2.1, on the small spectrometer. These measurements are summarised in Tables 7.1 and 8.1 of Chapters 7 and 8.

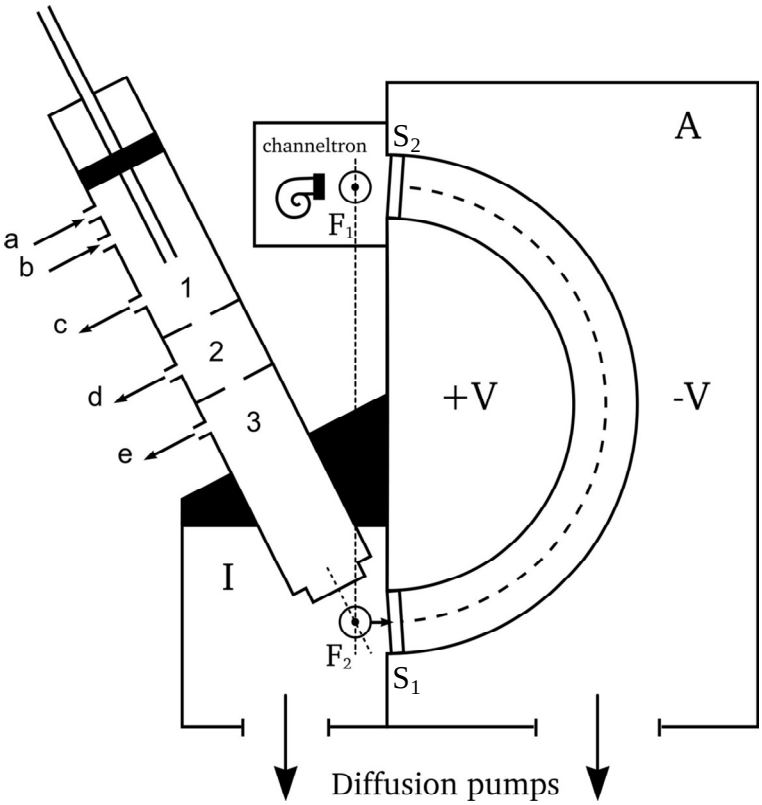

Figure 3.7: *Schematic diagram of a differentially pumped flow-tube coupled to a photoelectron spectrometer [23].*

Chamber 1 is operated at a total pressure of ~3 torr which is controlled by the SV-200 pump, connected to port *c*. Port *a*, provides the carrier gas (typically helium) with linear flow velocities of 3 ms^{-1} to 40 ms^{-1}[20]. Chambers 2 and 3 are pumped by two D25B rotary pumps, connected to *d* and *e* in Figure 3.7, and have total pressures of ~10^{-1} and ≤ 10^{-2} torr respectively [23]. Each chamber is separated by a thin teflon disc. The teflon discs each have a hole of a specific diameter located through their centre. This hole permits sample transfer to occur from one end of the flow-tube to the ionisation region of the spectrometer. Depending on the rate coefficients for a given reaction, the holes in the teflon discs separating each chamber can be altered accordingly to allow more sample throughput by using a wider hole for fast reactions or restrict sample throughput using a smaller hole for slower reactions.

The differentially pumped flow-tube, like the simple inlet systems, is connected to the ionisation chamber of the spectrometer at 15° to the vertical [23]. It is coated internally with teflon to reduce interactions between gases and the surface of the walls of the inner tube. The reactant gas is added via a movable injector located at the top of the flow-tube. The carrier gas, *a*, and sample gas, *b*, are added from the side of the flow-tube, as can be seen from Figure 3.7. The character of the flow in the flow-tube when conducting an experiment should be laminar, yielding a parabolic radial velocity profile of the gas as it flows through the length of the tube, providing a maximum velocity of the gas at the centre of the flow-tube [16-18]. This can be checked by calculating the dimensionless Reynolds number, R_e [26], given by,

$$R_e = \frac{\rho \bar{v} L}{\eta} \tag{3.13}$$

where, ρ is the gas density, $\bar{v}$ is the average linear flow velocity, L is the length of the tube and η is the absolute viscosity for the binary gas mixture. If R_e is less than 2300 the flow is laminar and if it is above 4000 the flow is turbulent. In between 2300 and 4000, both laminar and turbulent flow exists; this is known as *transition flow* [27]. For kinetics experiments, it is important to ensure that R_e < 2300 i.e. the flow-tube is operated under conditions of laminar flow (or plug flow). Operating under laminar flow and pseudo-first order conditions, it is assumed that the concentration of the monitored reagent depends only upon the axial position and that the reactant transport in the axial direction is exclusively due to convection (i.e. axial diffusion is negligible). The laminar flow (or plug flow) approximation is only accurate when axial diffusion and radial concentration gradients are negligible [28].

By changing the reactant mixing distance from the hole in the teflon separating-disc located between chambers 1 and 2, using the moveable injector, reaction rate coefficient measurements can be carried out at a fixed reagent partial pressure by recording PE spectra as a function of reaction mixing distance. It is assumed that when the reagents and products pass through the hole between chamber 1 and 2 the reaction is effectively frozen [23]. For the reaction $A + B \rightarrow Products$, the reaction rate can be written as,

$$Rate = k[A][B] \tag{3.14}$$

where *k* is the reaction rate coefficient and [A] and [B] are reactant concentrations. Rate coefficient measurements are made by measuring the product or reactant concentrations with the moveable injector at different reaction times while the reactant flow rate is held constant [23]. First-order reaction rates depend solely on one reactant and so the rate coefficient can be easily determined. However, measuring second-order reaction rates for two reactants can be difficult as both the reactants have to be monitored simultaneously. The rate of the second-order reaction $A + B \rightarrow Products$ can be written as [29, 30].

$$-\frac{d[A]}{dt} = -\frac{d[B]}{dt} = k_2[A][B] \tag{3.15}$$

This integrates to give,

$$\log_e\left(\frac{{}^{[B_t]}/_{[B_0]}}{{}^{[A_t]}/_{[A_0]}}\right) = ([B_0] - [A_0])k_2 t \tag{3.16}$$

where k_2 is the second-order rate coefficient, and $[A_0]$ and $[B_0]$ are the concentrations of [A] and [B] at zero time.

If the concentration of [B] is much greater than that of [A], then the concentration of [B] is effectively constant i.e. $[B] \gg [A]$, then using,

$$\frac{-dA}{dt} = k_2[A][B] \tag{3.17}$$

This will become, when $[B] \gg [A]$,

$$\frac{-dA}{dt} = k'[A] \tag{3.18}$$

where, $k' = k_2[B]$. Then equation 3.18 gives,

$$\int \frac{-dA}{(A)} = \int k'dt \tag{3.19}$$

Then on integrating and assuming when $t = 0$, $A = A_0$ gives,

$$\log_e\left(\frac{A_0}{A}\right) = k't \tag{3.20}$$

As a result, the pseudo first-order rate coefficient, k' at known concentration of [B] is given by the gradient of the line when plotting $\log_e\left(\frac{A_0}{A}\right)$ against time, *t*. k' and k are related via,

$$k' = k[B] \tag{3.21}$$

If k' is determined at different known concentrations of [B], then k' plotted against [B] would give k_2, which is the second-order rate coefficient [29, 30]. The only previous use of PES in a kinetics study is the work of Wang *et al.*, who studied the first-order rearrangement of a number of compounds as a function of time and derived first-order rate coefficients. Examples of the reactions studied were the isomerisation of CH_3NC to CH_3CN and isomerisation of SSF_2 to FSSF [31-33].

For a reaction $[A] \rightarrow [B]$, the first-order rate coefficient, k_1, is given by,

$$Rate = k_1[A] \tag{3.22}$$

The first-order rate coefficient is therefore determined by the loss of [A] as a function of time; $(\log_e[A])$ is plotted against time to yield a slope of -*k*. Wang *et al.* reported the first-order rate coefficients of selected compounds by plotting $\log_e$[A]/[B] versus time. This resulted in the rate coefficients obtained being in error.

Since the work of Wang, PES has been used to measure the rate coefficient of a second-order reaction. This was done by Dyke *et al.* of the Southampton PES Group, where the rate coefficient for the atmospherically important reaction between molecular chlorine and dimethyl sulphide (DMS) was determined [23],

$$Cl_2 + CH_3SCH_3 \rightarrow \text{Products} \tag{3.23}$$

using the differentially pumped flow-tube described. Measured under pseudo first-order conditions with $[Cl_2] \gg [DMS]$, the rate coefficient was determined by measuring the relative concentration of DMS using the intensity of its first PE band and changing the reaction times using the moveable injector on the flow-tube at a fixed chlorine partial pressure. This was then repeated at different partial pressures of chlorine. Plotting $\log_e\left(\frac{[DMS]_0}{[DMS]_t}\right)$ against reaction time at a known concentration of chlorine gave a gradient which was equal to the pseudo first-order rate coefficient, k'. The second-order rate coefficient was then determined from the slope of the plot k' versus [Cl_2] concentration.

During the course of this project the differentially pumped flow-tube was only used for the photoionisation cross-section (PI-CS) measurements to allow reaction branching ratios to be determined for alkene plus ozone reactions. See Chapters 7 and 8 for details describing the determination of branching ratios.

3.3 High Temperature PES

Solids and liquids of low vapour pressure have been studied using PES in the Southampton group, by gradually heating the sample to increase the vapour pressure, using a radio-frequency (RF) induction heating system, in order to obtain a PE spectrum [34, 35].

In this work an RF induction heating system has been used to study the thermal decomposition of two hydrofluorocarbon (HFC) fire suppressants, pentafluoroethane (HFC-125) and 2-H heptafluoropropane (FM-200). Induction heating has many advantages for investigating the thermal decomposition pathways of molecules and was chosen for the following reasons,

1. High temperatures can be achieved (> 2500 K) and RF interference in the detection circuitry can be eliminated using pulsed gating techniques.
2. The furnace itself is not in direct contact with the induction coils and so heat loss via thermal conduction is eliminated.
3. The high temperatures are localised within the furnace and so radiative heat losses are also minimised.
4. The heating method does not generate any thermal noise and can be used comfortably at temperatures up to 2500 K [34, 35].

The radio frequency induction heating method can be described as follows; when an alternating electrical current is applied to the primary of a transformer, an alternating magnetic field is created. If the secondary of the transformer is located within the magnetic field produced, an electric current will be induced. These currents are known as eddy currents. In induction heating the same principle applies. In the heating system used in this work, the RF power supply sends an alternating current through a water cooled, highly conductive copper tube, 3 mm in diameter, wound in a helix formation of ~6 turns. The coil serves as the transformer primary and the part to be heated, the

susceptor, becomes the secondary. When a conducting material, the susceptor, (e.g. a graphite furnace) is placed within the induction coil and enters the magnetic field, circulating eddy currents are induced within the material. Eddy currents flow along the surface of the susceptor, giving rise to heating without any direct contact between the material and the coil [36, 37]. This is shown in Figure 3.8.

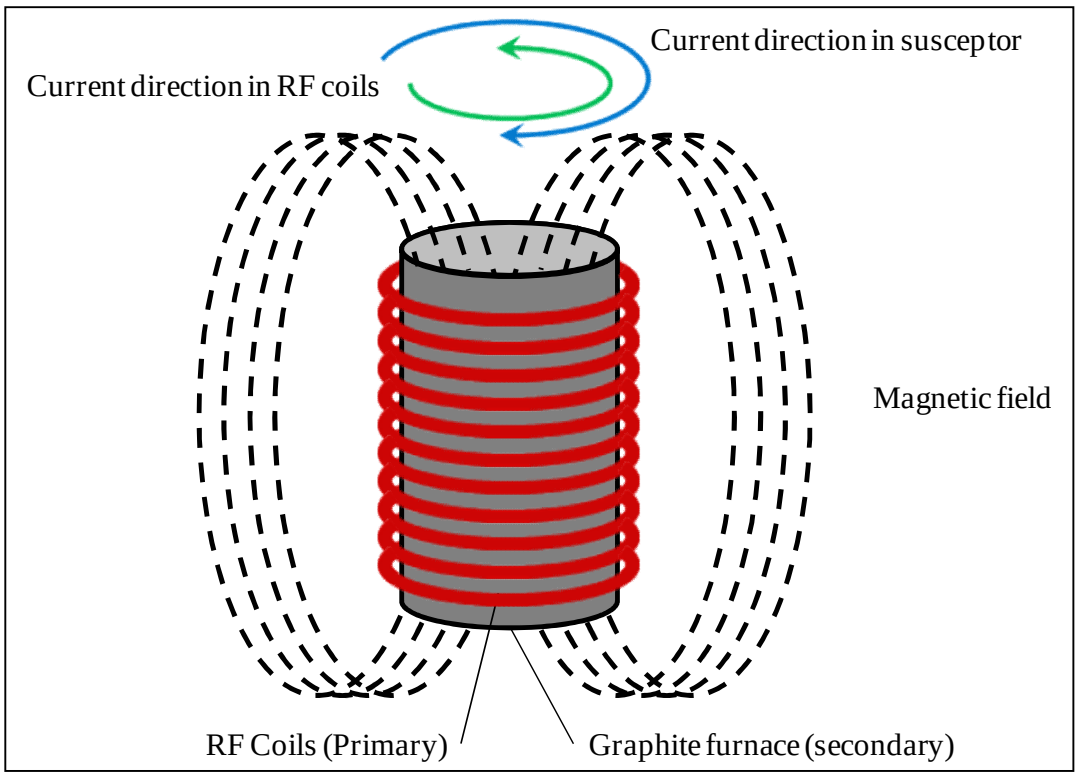

Figure 3.8: *Schematic diagram depicting the movement of currents induced from the RF in the coils and susceptor.*

The induced heat generated by the current flowing in the susceptor is given by,

$$Induced\ heat \propto I^2R \tag{3.24}$$

where I is the induced current and R is the resistance of the susceptor material. The resistance (R_T) of a conductor can be expressed in terms of its resistivity at a given temperature, $\rho(T)$, its length, l, and its cross-sectional area, A, as,

$$R_T = \rho(T)\frac{A}{l} \tag{3.25}$$

It can be seen from equations 3.24 and 3.25 that the heating effect is greatest for large induced currents and highly resistive materials. Since the current is directly proportional to the rate of change of the inducing magnetic field, high frequencies (radio-

frequencies) are used to obtain high temperatures. Radio-frequencies of 1 MHz are used in this work.

When a potential is applied to a conducting material, e.g. a graphite susceptor, with a *direct* current, the direct current flows uniformly throughout the entire cross-sectional area of the susceptor. If, however, an *alternating* current, of any frequency (RF in this work), is applied to the same susceptor, the current is forced away from the centre of the susceptor and flows on its outer surface. This is due to the acceleration of an electric charge in an alternating current [37]. This accelerated charge produces electromagnetic waves that directly cancel out the propagation of the flowing potential toward the centre of the susceptor. This is known as the *skin effect*.

The skin effect causes the effective resistance of the conductor to increase with the frequency of the current. At high frequencies the skin depth becomes smaller. At very high frequencies (~1 MHz), the current no longer flows within the susceptor, but effectively flows on its surface. The depth to which currents will penetrate a given conducting material is given by,

$$Skin\ depth = \sqrt{\frac{2 \times \rho(T)}{\mu_0 \times \mu_r(T) \times \omega}} \tag{3.26}$$

where $\rho(T)$ is the resistivity in ohms per metre at temperature, $T(K)$, μ_0 is the magnetic permeability of free space, $\mu_r(T)$ is the relative permeability at a given temperature and ω is the angular frequency of the RF current. Since $\mu_0 = 4\pi \times 10^{-7}$ $kgms^{-2}A^{-1}$, where A, is in amperes, equation 3.26 can be expressed as,

$$Skin\ depth = \frac{1}{2\pi}\sqrt{\frac{\rho(T) \times 10^{-7}}{\mu_r(T) \times f}} \tag{3.27}$$

where f is the RF frequency. As a result of this, the susceptor is machined as closely as possible to the theoretical skin depth without compromising its structural integrity. The susceptor (furnace) used in this work was a graphite tube, 5 cm x 1 cm, with a wall thickness of *ca.* 1-2 mm. The thickness of the furnace was restricted by the machining techniques used in its manufacture and also its durability when being handled. The base

of the graphite furnace was drilled and tapped to allow a graphite end-cap to be screwed on.

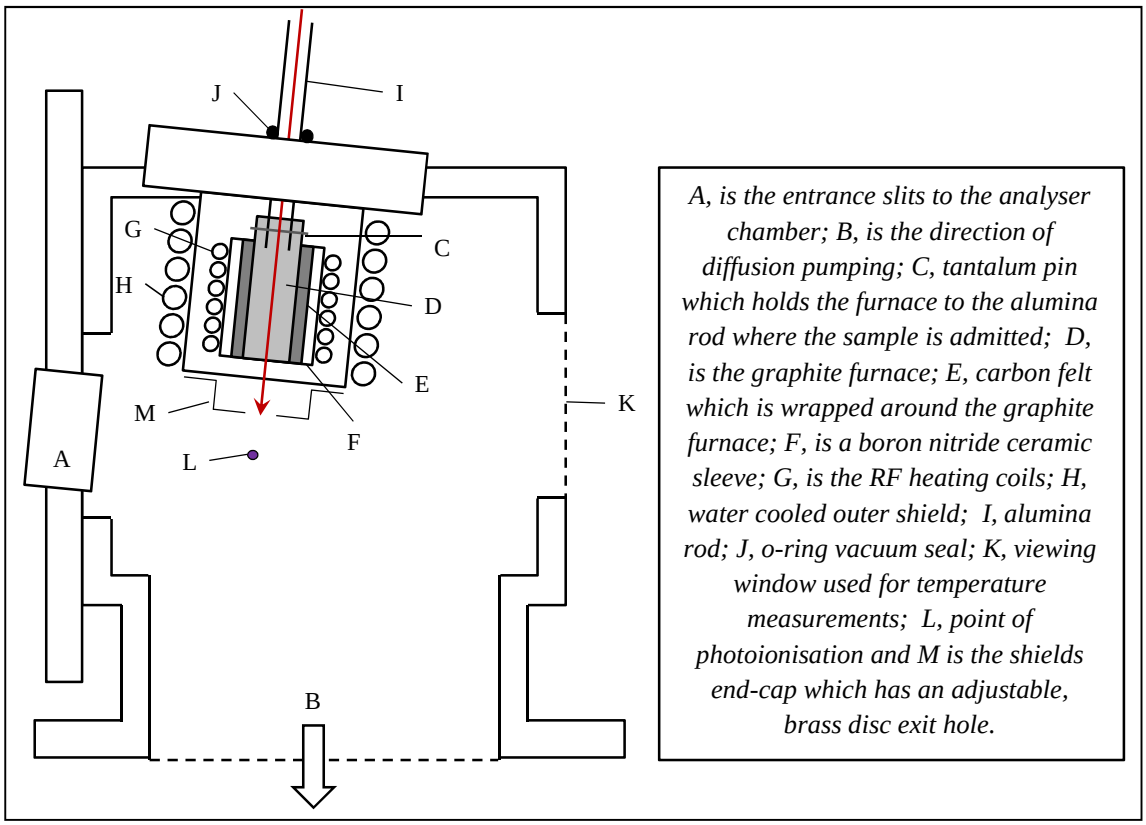

Figure 3.9: *Schematic diagram of the furnace assembly used to study the thermal decomposition of HFC-125 and FM-200.*

The end cap had a 2 mm hole drilled through its centre. The cap was used to increase the residence time of the gas under study within the furnace. A schematic diagram of the ionisation chamber and furnace assembly used is shown in Figure 3.9. The graphite furnace, *D*, was connected to a 20 cm long alumina rod, *I*, using a tantalum pin, *C*. Carbon felt, *E*, was wrapped around the graphite furnace to reduce any radiative heat losses. The furnace and carbon felt were inserted inside an electrically insulating boron nitride ceramic tube which prevented the circuit shorting by segregating the RF coils, *F*, from the furnace. A boron nitride ceramic tube was used due to its high melting point and stability when in contact with carbon felt at temperatures over 2000 K. A water cooled shield, *H*, is used to cover the entire furnace set-up, including the water cooled RF coils, *G*. The water cooled shield is attached to the outer flange of the RF inlet system and therefore earthed. The shield is necessary to prevent excessive thermal electron emission in the ionisation region which can increase background count rates and give poor signal-to-noise when recording PE spectra. It is also used to reduce any

radiative thermal emissions and to help collimate the sample reducing chemical contamination on the slits. The sample is introduced via the alumina rod and its path to the point of photoionisation, *L*, is represented by the red arrow in Figure 3.9. The sample path is further collimated towards the reaction cell by capping the water cooled shield with a brass disc which is inserted into a screw-cap fitting attached to the base of the shield, *M*. The brass disc cap is similar to that used on the graphite furnace having a hole through its centre of *ca.* 2 mm. Various end caps, for both the graphite furnace and the water cooled shield, machined with different hole diameters, were used in order to increase or decrease the residence time of the sample in the furnace and to direct the flow to the photoionisation region while minimising any sample loss. To avoid interference caused by the RF signal when detecting photoelectrons, the RF supply is gated at mains frequency of 50 Hz. Photoelectrons detected are then recorded during each gated pulse. This is shown in Figure 3.10. The internal furnace temperature was measured using a K-type (Ni-Cr/Ni-Al) thermocouple in contact with the internal wall of the susceptor. This procedure could be used to measure internal furnace wall temperatures up to 1300 °C. Above 1300 °C, in the range 1300-2000 °C, an optical pyrometer was used to determine the external furnace wall temperature, by viewing the outside of the furnace through a window on the ionisation chamber. By separately plotting the measured temperatures from both the thermocouple and optical pyrometer as a function of the applied heater voltage, the thermocouple temperatures could be extrapolated to higher values

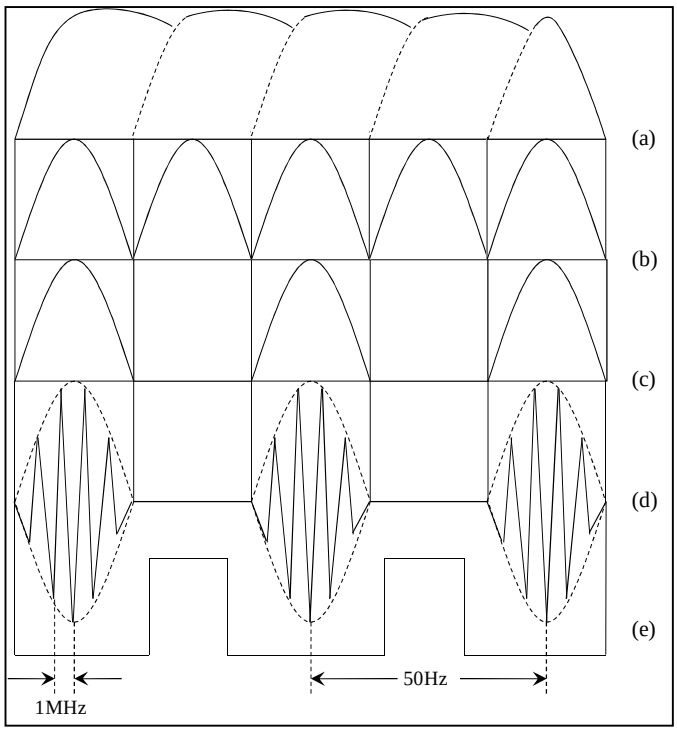

Figure 3.10: *Representation of the gating sequence used for the RF signal during pyrolysis; (a), represents the applied voltage; (b), shows the voltage applied with the smoothing capacitor removed from the RF supply; (c), shows the applied voltage with the rectifier valve removed; (d), shows the RF signal produced in the induction coil and (e), shows the points, out of step with the RF signal, at which data is recorded [33].*

(than 1300 °C) and the optical pyrometer values could be extrapolated to lower values. The experimental temperatures quoted in this work (see Chapters 5 and 6) were the thermocouple measurements up to 1300 °C and the extrapolated thermocouple values up to 2000 °C (i.e. the internal wall temperatures of the furnace, which were compared with the temperatures measured with the pyrometer above 1300 °C to check that the values were reasonable; at each heater voltage the pyrometer temperature (outer wall temperature) was always slightly lower than the thermocouple temperature over the temperature range that both measurements could be made, *ca.* 750-1800 °C).

The results obtained for thermal decomposition of pentafluoroethane (HFC-125) and 2H-heptafluoropropane (FM-200) with the RF induction heating system described in this chapter are presented in Chapter 5 and 6 respectively.

3.4 Synchrotron Radiation PES Studies

A synchrotron radiation source is a continuous, polarised source of radiation. The radiation is emitted by electrons which are circulated in curved trajectories at velocities close to the speed of light [38]. The radiation emitted by these electrons can be selected and tuned continuously from the far-infrared region (50-1000 μm) to the hard X-ray region (0.1-0.01 nm) using a monochromator [38]. Synchrotron radiation was used in this work to record the first bands in the threshold photoelectron (TPE) spectrum of the triatomic molecules HO_2 and SF_2. The detection of threshold electrons is achieved by using a three element lens system which focuses low energy electrons towards the analyser of the spectrometer. A TPE spectrum is then obtained by sweeping the photon energy. This results in a significant improvement in spectral resolution to approximately 5 meV compared to conventional PES which has an operating spectral resolution of typically 20-30 meV. TPE spectra provide complementary information to conventional PE spectra [39].

3.4.1 The ELETTRA Synchrotron Radiation Source

The results obtained for the work carried out on the triatomic molecule SF_2, discussed in Chapter 9, were obtained at the Elettra synchrotron radiation facility, on the circular polarised beamline, BL 4.2. Elettra is a third generation synchrotron radiation laboratory located in Basovizza, Trieste, Italy. The synchrotron is composed of a linear

accelerator (LINAC), a transfer line and a storage ring. The electrons are first generated in a LINAC and then injected into the ring using an electron gun via the transfer line. The electron gun contains ceramic discs which are heated to very high temperatures in order to produce electrons for the storage ring. The LINAC operates at 3 GHz and generates a pulse of electrons every 2 ns that are accelerated up to energies of 1.2 GeV. The electrons are then drawn out of the electron gun by a high electric field of ~100 kV and accelerated through various RF structures. The LINAC itself is 66 m long, and includes the electron gun, a low energy section and seven high energy sections, each 6 m long. The electrons are then transported to the ring by a transfer line, which consists of a series of deflection and focusing magnets. Both the LINAC and the transfer line are located below ground so that they do not interfere with the beamlines. Pulses of electrons are gradually fed into the ring until the desired current is achieved. The storage ring operates at 2.0 or 2.4 GeV and feeds over 24 beamlines offering photon energies from 0.002 eV to 20 keV with a spectral brightness of up to 10^{19} photons/s/mm^2/mrad^2/0.1% bandwidth [40]. Left alone, electrons would travel along straight trajectories [40]. In order to manipulate the path of the electrons as they travel around the storage ring they must be deflected accordingly. Due to the high energies reached by the fast moving electrons in the storage ring, high strength magnets are required to control their trajectories. The effect of magnetic deflection on an electron is governed by the Lorentz force, which is the force exerted by an electromagnetic field (magnet) on an electron as it circumnavigates the storage ring. It is given by,

$$Force = Q\left[E_{field} + \left(\mathrm{v} \times M_{field}\right)\right] \tag{3.28}$$

where, *Force* is in Newton's, Q is the electric charge of the particle in coulombs, E_{field} is the electric field in volts per metre, v is the velocity of the particle in metres per second and M_{field} is the magnetic field in teslas. The storage ring is made up of four types of magnets which are used to provide the magnetic fields required to ensure the stability of the path taken by the electrons as they travel around the ring. The four types of magnets are,

1. Bending magnets. These deflect the circulating beam into a closed circular path.
2. Quadrupole magnets. These are used to focus the beam.
3. Sextupole magnet. These compensate for any chromatic and non-linear effects.
4. Steerer magnets. These perform small adjustments to the circular trajectories.

The ring has a circumference of 260 m and is made up of twelve identical groups of magnets. Two parameters are important in describing the beam, its brightness and its emittance. The brightness of the beam is proportional to the transverse size and divergence of the beam, while the emittance is the area occupied by the beam in phase space. The smaller the emittance is, the better the quality of the beam and the longer its lifetime. To obtain a small emittance, the beam is strongly focused by ring quadrupole and bending magnets. Four single RF cell cavities, operating at 500 MHz, are used to compensate for the energy lost by the electrons when emitting synchrotron radiation within the storage ring [41]. The LINAC, the transfer line and the storage ring all operate under ultra high vacuum to minimise collisions of electrons with residual molecules. This avoids the loss of electrons and increases the lifetime of the beam.

3.4.1.1 The Circular Polarised Beamline, BL 4.2

The BL 4.2, also called the circular polarised beamline, provides radiation in the photon energy range from 5 to 1000 eV. The radiation is produced by a series of electromagnetic elliptical wigglers (EEWs) and undulators, which force the electrons to follow a helical orbit around the EEW axis. These are made from an array of electromagnets. These provide vertical and horizontal magnetic fields which are applied to the electrons as they travel through the storage ring. This is shown in Figure 3.11. The intensity of the vertical magnetic field can be changed by moving the permanent magnets, modifying the vertical displacement of the electrons. The horizontal displacement of the electrons is changed by varying the intensity of the current which passes through the magnets. An important characteristic of synchrotron radiation is the fact that it is polarised. An electromagnetic wave is a propagating perturbation of the electromagnetic field. The electromagnetic field includes an electric field vector and a magnetic field vector. The electric field and the magnetic field perturbations of a wave occur

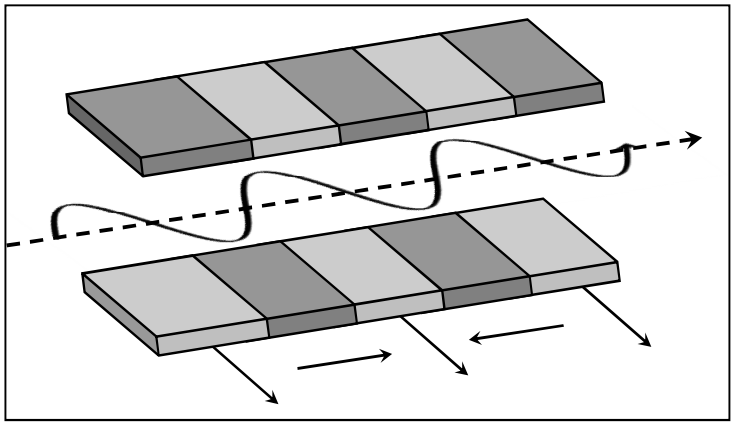

Figure 3.11: *Schematic diagram showing the electron path as it traverses a periodic array of horizontally arranged magnets.*

perpendicular to one another and also perpendicular to the wave motion. If these fields rotate as a function of time then the wave is circularly polarised. As the emission of EEWs and undulators is linearly polarised with respect to the undulation plane, fixing the vertical field of the permanent magnets on the undulator fixes the electric field (and therefore the magnetic field) perturbation of the wave. When the directions of these fields are fixed along the axis of the propagating wave then the corresponding wave is linearly polarised. In order to obtain a smooth spectral distribution when recording PE spectra, the alignment of each array of undulator magnets is of fundamental importance. This requires generating constructive interference from the electromagnetic field produced by the electron as it traverses the undulator. This is done by monitoring a signal at a given harmonic of the radiation at fixed photon energy and moving the permanent magnets accordingly as to compensate for the spectral shift of the signal being monitored. Linear polarisation was used throughout the work carried out on the synchrotron. Polarising the radiation linearly allows for the determination of angular distribution information of molecules and is discussed in sections 2.2 of Chapter 2 and 3.4.2.5 in this chapter. To cover the broad photon energy range efficiently, two independent monochromators are used, one working at normal incidence, giving radiation from 5 to 35 eV, and one working at grazing incidence, giving radiation from 30 to 1200 eV. During this work, only the monochromator operating at normal incidence was used [42]. A schematic layout of the normal incidence monochromator (NIM) configuration is shown in Figure 3.12.

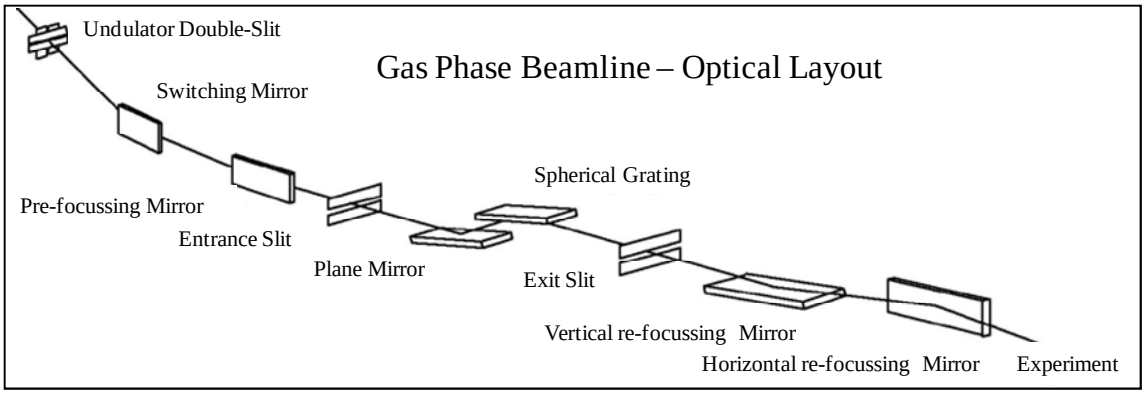

Figure 3.12: *Schematic layout of the BL 4.2 in Normal Incidence Configuration [39].*

In Figure 3.12, the switching mirror is vertical and diverts the radiation horizontally. It protects the later optical components from radiation from the "hard" portion of the spectrum. The second mirror is a pre-focusing mirror and has a toroidal shape. This focuses the radiation onto the entrance slit of the monochromator. The monochromator

is composed of a mirror, positioned horizontally, that deflects the radiation vertically and a set of spherical gratings, (gold or aluminium) that diffract the radiation and focus it onto the exit slit. The radiation is then re-focused by a vertical toroidal mirror which diverts the radiation in the horizontal plane. The position of these mirrors can be manually adjusted to optimise the photon flux, which is measured at the back of the spectrometer using a photodiode sensor. A set of valves are present along the beamline to protect the vacuum contained within the beamline and storage ring. They shut automatically if the pressure rises above preset limits. The last valve is a window valve, transparent to visible radiation, which allows for the alignment of the spectrometer with the photon beam.

3.4.2 The Synchrotron Photoelectron Spectrometer

The main components of the synchrotron PE spectrometer are similar to the small and big PE spectrometers, previously described. It consists of a suitable radiation source, an ionisation region, an analyser region, a detector and a recorder to acquire data. Figure 3.13 shows a schematic diagram of the spectrometer in the plane perpendicular to the photon beam. The spectrometer is evacuated to a sufficiently low pressure to allow electrons to be cleanly transmitted from the point of photoionisation to the detector. In order to prevent contamination of the monochromator optics on the beamline, a high degree of sample differential pumping was employed by using separate turbomolecular pumps to evacuate each chamber individually. The sample gases are introduced via an inlet system (described in section 3.2.1) into the ionisation region where they interact with the photon beam.

To improve the pumping efficiency, the interaction region is enclosed by two metallic boxes, shown in Figure 3.13, that are differentially pumped. Figure 3.14 shows how the differential pumping is applied within the ionisation region as a result of these boxes. Both boxes are coated with DAG in order to reduce any local electric fields that would affect the trajectory of the emitted photoelectrons. The first box (inner box) is earthed. The ejected photoelectrons travel from the interaction region and through the electron lens system before reaching the analyser region. This lens system allows the spectrometer to be used in a fixed or constant pass energy mode in order to obtain PE and TPE spectra. The analyser consists of two concentric 180° hemispheres with a mean

radius of 10 cm. The electrons are detected by a channeltron (previously described in section 3.1.4).

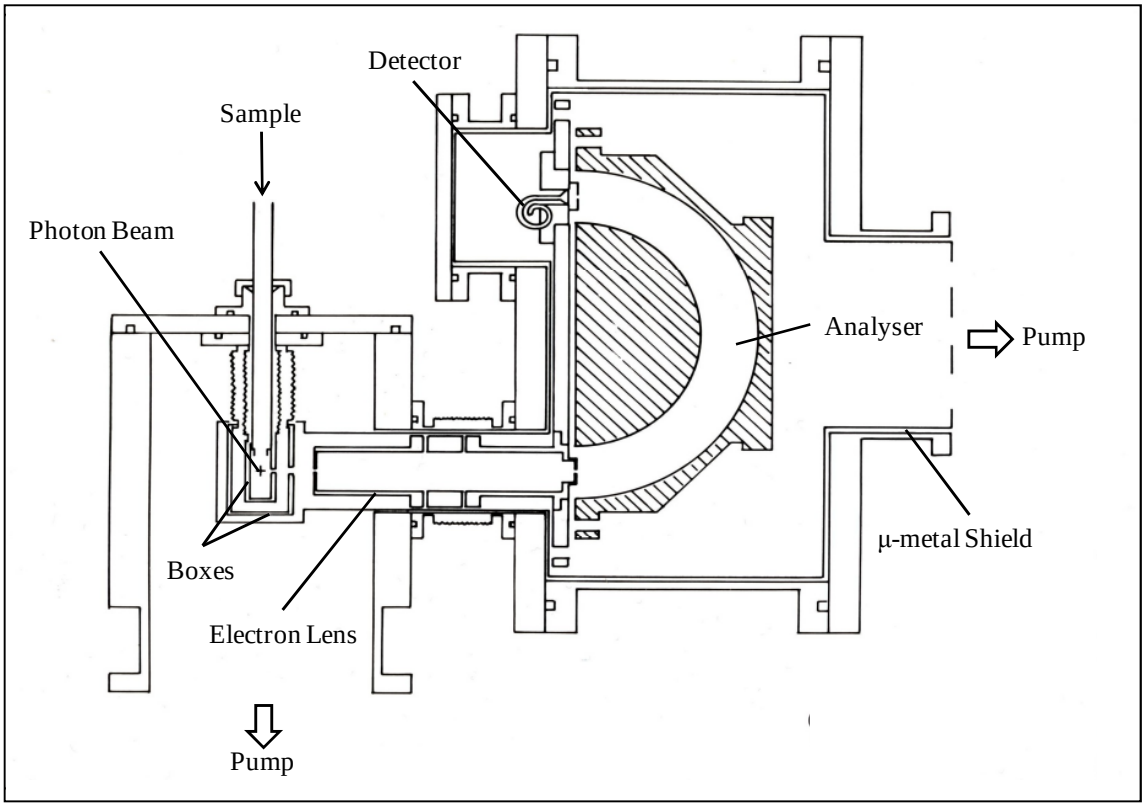

Figure 3.13: *Schematic diagram of the synchrotron photoelectron spectrometer positioned perpendicular to the photon beam.*

The spectrometer is made entirely of non-magnetic materials to avoid any local electric and magnetic fields perturbing the trajectories of the emitted photoelectrons. Helmholtz coils are used to counteract any local magnetic fields, including the earth's magnetic field, on the small and big PE spectrometers discussed in section 3.1. However, due to their size, they are impractical for use at a synchrotron. As the synchrotron spectrometer was regularly transported from the PES laboratory in Southampton to the synchrotron radiation facility in Trieste, Italy, an alternative solution to using Helmholtz coils was necessary. This involved the use of μ-metal shielding. The ionisation region, lenses, analyser and detector were shielded from external interfering electrostatic fields by covering each component internally with μ-metal on the inner vacuum chamber walls. μ-metal is an alloy which has a high magnetic permeability that constrains stray magnetic fields to pass within it rather than through it. Therefore the photoelectrons will not be affected by any local magnetic fields.

The spectrometer was designed so that its height and lateral position could be manually adjusted to align the ionisation region with the focal point of the photon beam before connecting it directly to the beamline. The frame of the spectrometer was attached to a plate which allowed the system to be rotated around the horizontal axis for fine adjustments to the final alignment.

3.4.2.1 The Three Element Lens System

A three element lens system was used to transmit electrons from the point of ionisation to the analyser region, allowing the spectrometer to be operated at fixed pass energy. This enables spectra to be recorded with constant resolution and transmission. The lens system is shown in Figure 3.13 and 3.16. The lenses are made from three cylindrical aluminium elements, coaxially aligned and electrically insulated from each other.

The first lens element is electrically connected to the outer box to which an extraction voltage can be applied (an extraction voltage is only applied when recording TPE spectra, see section 3.4.3 for details) otherwise the first lens element is earthed. The voltage applied to the second lens element, V_2, is used to focus the electrons onto the entrance slit of the analyser. It acts as a focusing element so that the exit slit of the lens system becomes the optical mirror image of the entrance slit. V_2 can be determined experimentally by optimising the voltage applied to it for a particular photoelectron signal at different kinetic energies, at fixed pass energy. The optimum voltage values that give the most intense and well resolved PE band are recorded, and a curve is generated by plotting $(E_i + V_2)/E_i$ versus E_{pass}/E_i [43]. This focus curve is fitted with a fourth order polynomial trendline of which the coefficients obtained are used as input in the controlling software (LABVIEW) to automatically adjust the voltages applied to the second lens to give the optimum focusing voltage at a specific electron kinetic energy. The third lens element accelerates (or decelerates) the electrons so that they enter the analyser with the appropriate kinetic energy. The voltage of this lens is determined from equation 3.29,

$$V_3 = E_{pass} - E_i \tag{3.29}$$

where E_{pass} is the pass energy and E_i is the initial kinetic energy of the ejected photoelectrons. When recording PE spectra, the incident photon energy is fixed and the

voltage applied to the third element in the lens system, V_3, is swept while the analyser is operated at fixed pass energy.

3.4.2.2 The Vacuum System

The spectrometer needs to be kept at low pressure, < 10^{-6} torr, to ensure that the photoelectrons do not undergo inelastic collisions with the background gas between photoionisation and detection. Low pressure is also necessary to avoid absorption of the photons and contamination of the beamline optics. Figure 3.14 shows the differential pumping system [44, 45] used on the spectrometer.

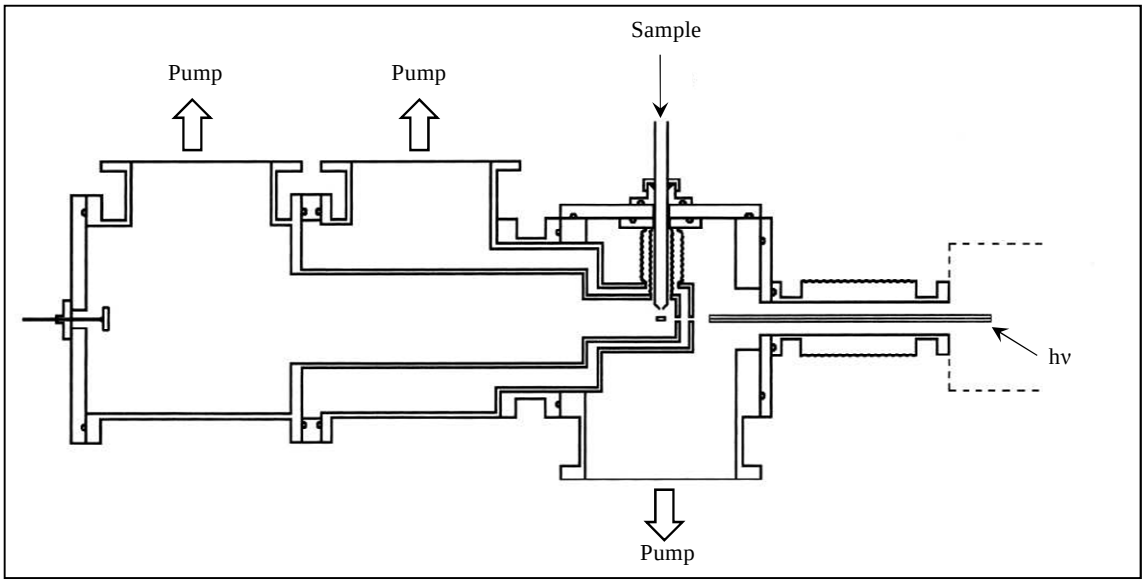

Figure 3.14: *Cross section of the pumping system of the spectrometer surrounding the photoionisation region.*

There are four turbomolecular pumps on the spectrometer, each one backed by a rotary pump. The positions of three turbomolecular pumps are shown in Figure 3.15 and the position of the fourth pump is shown in Figure 3.13 on the rear of the analyser chamber. Figure 3.14 also shows the differential pumping employed on the boxes surrounding the interaction region. The base pressure of the spectrometer is about 10^{-8} torr, as measured outside the boxes, on the walls of the ionisation chamber, by an ionisation gauge. However, as long as the spectrometer pressure does not exceed 10^{-6} torr, there is no significant change of pressure on the beamline pressure gauges

3.4.2.3 The Hemispherical Electron Analyser

The electron energy analyser consists of two concentric 180° hemispheres (inner and outer sectors) made of an aluminium alloy. The two hemispheres are held at different voltages, V_i and V_o, and have different radii, R_i and R_o respectively. To select the mean pass energy, E_{pass}, of the electrons, the voltages applied to the hemispherical electrodes need to be selected. On this spectrometer, R_i = 8 cm and R_o = 12 cm and the inner separation is 4 cm. In order to obtain the required pass energy, E_{pass}, the hemispheres must be at voltages given by [9, 46],

$$V_i = E_{pass}\frac{R_o}{R_i} \tag{3.30}$$

and,

$$V_o = E_{pass}\frac{R_i}{R_o} \tag{3.31}$$

The analyser is usually operated in constant or fixed pass energy mode (usually 5 eV). This means that the voltages applied to the hemispheres are kept constant when recording PE spectra. When PE spectra are recorded, the electron intensity on the detector is recorded as a function of the voltage on the third lens element.

For PES the total width of the entrance and exit slits of the analyser, ΔS, contributes to the base width, ΔE_b, of a recorded photoelectron band, along with the radii of the hemispheres. ΔE_b is related to the pass energy, E_{pass}, via, [9, 11, 46]:

$$\Delta E_b = \frac{\Delta S}{R_i + R_o}E_{pass} \tag{3.32}$$

where,

$$\Delta S = \Delta S_{entrance} + \Delta S_{exit} \tag{3.33}$$

where $\Delta S_{entrance}$ and ΔS_{exit} are the entrance and exit slit widths respectively. The full width half maximum, $\Delta E_{1/2}$ is then related to the base width, ΔE_b by [5, 11],

$$\frac{\Delta E_b}{\Delta E_{1/2}} = 2.3 \tag{3.34}$$

In this work, the slits have a separation of 1mm which gives a $\Delta E_{1/2}$ of 18 meV for pass energy of 5 eV. This resolution can be improved by decreasing the slit size or the pass energy but this is accompanied by a loss of intensity.

3.4.2.4 The Detector and Electronics

The photoelectrons that pass through the lens system and hemispherical analyser are detected by a single channel electron multiplier, also called a channeltron, as described in section 3.1.4. The signal from the channeltron is pre-amplified and amplified before being passed to a General Purpose I/O National Instrument card, connected to a computer. LABVIEW software, specifically written for this spectrometer, records spectra and is used to control the movement of the monochromator attached to the beamline, allowing the photon energy supplied to the ionisation chamber to be swept. The voltages applied to the lenses, hemispheres and outer box are controlled by this software.

3.4.2.5 The Rotation Mechanism

With this spectrometer, angular distribution PE measurements can be performed by measuring PE spectra at two different angles with respect to the direction of the linearly polarised beam [47, 48]. As shown in Figure 3.15, the apparatus was built with a horizontal arm attached to the pump directly underneath the ionisation chamber (P3) and a vertical arm attached to the pump used to evacuate the analyser region (P4), that are both moved with a mechanical screw-drive mechanism. This mechanism allows the whole spectrometer to rotate with respect to the photon beam. In principle angular distribution measurements could be determined by using a magnetic angle changer in the ionisation region [49] or rotating the polarisation of the photon source (in laser experiments) [50]. However, as the plane of polarisation of the linearly polarised synchrotron photon beam cannot be rotated and a magnetic angle changer was not available, the spectrometer was designed to overcome this by rotating the spectrometer around the horizontal plane of polarisation of the radiation.

Figure 3.15 shows the two extreme rotation positions, with angles θ = 0° and θ = 75° between the horizontal direction of polarisation of the photon beam and the detector. To measure the angular distribution parameter or asymmetry parameter, β, of a molecule using this apparatus, spectra are recorded at two different angles (θ = 0° and θ = 54°44' or 54.736°) with respect to the polarisation of the photon source. When spectra are recorded of a molecule at the angle θ = 54°44', better known as the *magic angle*, the intensities of the measured PE bands are independent of the angular distribution parameter, β, and directly proportional to the absolute partial photoionisation cross-section at a given photon energy.

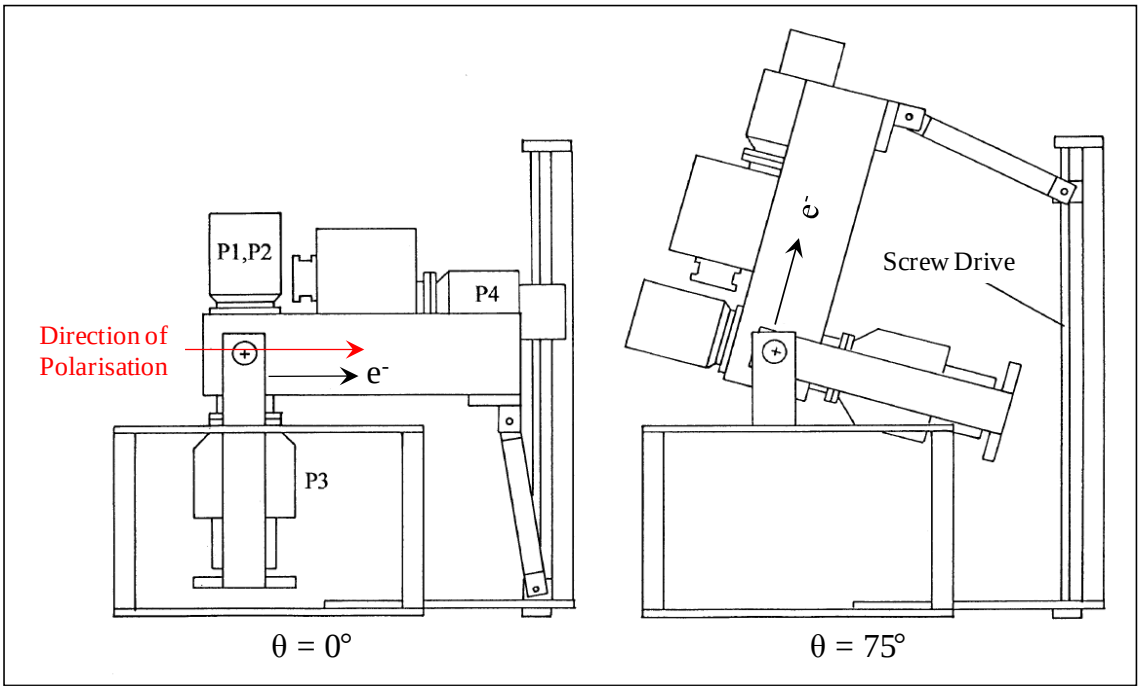

Figure 3.15: *The rotation mechanism used on the synchrotron PE spectrometer when measuring angular distribution parameters.*

The angular distribution parameter can be calculated from a molecule using the method outlined in section 2.2 of Chapter 2 from equation 2.28 by measuring the PE band intensities at two known angles (θ = 0° and θ = 54°44') [49, 48, 51].

When rotating the spectrometer, it is important to make sure that the detection efficiency of the spectrometer stays the same. The main changes in the detection efficiency arise from small misalignments between the axis of rotation and the direction of the photon beam. To account for this, the PE spectrum of helium $(1s)^{-1}$ is recorded at both angles and the angular distribution parameter, β, for photoionisation of helium (which is well established as β = 2 at θ = 0) is evaluated at 28 eV. A comparison

between the measured β parameter and the known β parameter of helium allows the determination of a correction factor that can be applied to each spectrum recorded while carrying out angular distribution measurements (see Chapter 2 for a more detailed explanation).

3.4.3 Threshold Photoelectron Spectra

When recording threshold photoelectron (TPE) spectra, the photon energy is swept while the lenses are maintained at pre-set voltages, operating the analyser at fixed pass energy. The typical voltages applied to the elements of the lens system used for recording TPE spectra are shown in Figure 3.16.

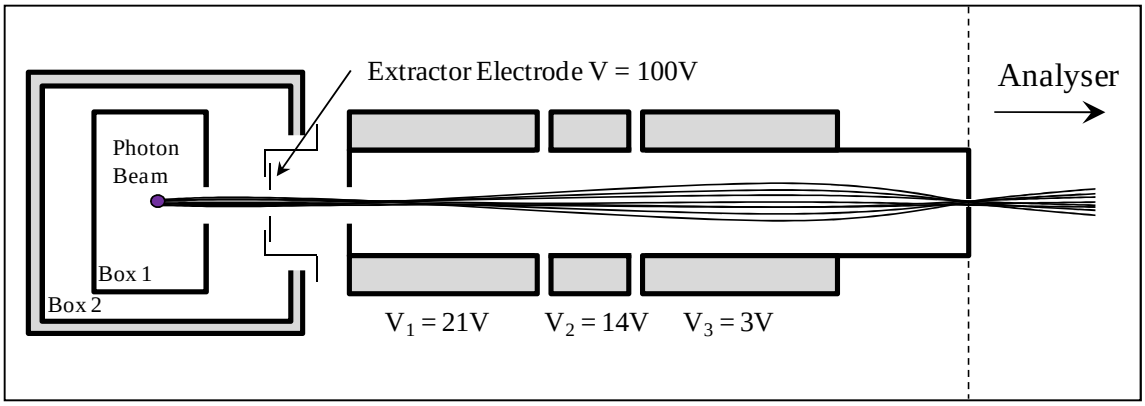

Figure 3.16: *Schematic diagram of the ionisation region and the three element lens system,*

These voltages were obtained by simulating 1 meV electron trajectories using a 100 V extraction voltage applied to the electrode shown in Figure 3.16 using SIMION software [52]. A potential is applied to the extraction electrode generating a penetrating electrostatic field. The field produces a saddle point in the potential distribution which focuses the low energy ($\leq$ 10 meV) threshold electrons towards the three element lens system [39, 53]. The sensitivity is increased (~5 meV) as low energy photoelectrons are collected over a solid angle of 4π, however a loss in angular information is incurred as a direct consequence of this.

Photoelectrons of higher energies, which have initial trajectories along the axis of the lens system, are largely unaffected by the extraction voltage. These high energy photoelectrons create high energy tails on recorded PE bands when detected and are mostly discriminated against by the analyser being operated at fixed pass energy. The entrance slits to the analyser will also help to discriminate against the higher energy

electrons from being detected. To reduce the tailing effect seen on PE bands, occurring from low lying Rydberg states above a threshold, and improve the spectral resolution, the lens voltages are optimised by recording PE spectra of the $(3p)^{-1}$ ionisation of argon. The photon energy was fixed on the $Ar^{+}(^{2}P_{3/2}) \leftarrow Ar(^{1}S_{0})(3p)^{-1}$ ionic state of argon at 15.7596 eV and the voltages applied to the extraction electrode, each of the three lenses and the hemispheres were individually adjusted while observing the signal intensity. Once the voltages on the lenses gave the most intense signal, an argon spectrum was recorded to observe the relative intensities (6:1) and symmetry of the $Ar^{+}(^{2}P_{3/2}, {}^{2}P_{1/2})$ PE bands. If tailing was observed on a PE band then this optimising process was repeated (usually compromising some intensity for resolution) in order to minimise this effect. After tuning the lenses and hence spheres, which operate at the same voltage as the third lens (typically 3 V), TPE spectra could be recorded over a designated photon energy range, acquiring data over long periods of time. The signal intensity and spectral resolution can change during the time when TPE spectra are being recorded. To account for any change and ensure the repeatability of experimental results, the intensity and resolution were checked and optimised after each run in this way using the argon $(3p)^{-1}$ signal.

3.5 Summary

In this chapter the three spectrometers used during this project have been described in detail as well as the photon sources and the various inlet systems used for each experiment in this chapter. The sample preparation methods and experimental procedures for each reaction/molecule investigated during this project have been omitted from this chapter. These will be described in detail in their respective chapters. The spectrometers and experimental techniques described in this chapter are used in the experimental studies outlined in Chapters 5-9.

References

[1] J.M. Dyke, N. Jonathan and A. Morris, Electron Spectroscopy Theory, Techniques and Applications, *Academic Press, London*, 3, 1979, 189.

[2] N. Jonathan, D. J. Smith and K. J. Ross, *Chem. Phys. Lett.*, 9, 1971, 217.

[3] J. M. Dyke, A. R. Ellis, N. Jonathan and A. Morris, *J. C. S. Faraday. Trans II.*, 81, 1985, 1573.

[4] J. M. Dyke, A. Morris and N. Jonathan, *Int. Rev. Phys. Chem.*, 2, 1982, 3.

[5] A. Morris, N. Jonathan, J. M. Dyke, P. D. Francis, N. Keddar and J. D. Mills, *Rev. Sci. Inst.*, 55, 1984, 172.

[6] D. C. Frost, S. T. Lee, C. A. McDowell and N. P. C. Westwood, *J. Elec. Spec. Rel. Phen.*, 12, 1977, 95.

[7] A. Morris, Lecture Notes on Experimental Photoelectron Spectroscopy, *University of Southampton*, 1996.

[8] D. W. Turner, C. Baker, A. D. Baker and C. Brundle, Molecular Photoelectron Spectroscopy. *Wiley Interscience, London*, 1970.

[9] J.H.D. Eland, Photoelectron Spectroscopy, *Butterworths, London*, 1974.

[10] H. Siebahn and L. Karlsson, Photoelectron Spectroscopy, *Springer-Verlag Berlin Heidelberg, New York,* 1982.

[11] A. Pauline and D. Roy, *J. Phys. E. Sci. Instrum.*, 11, 1978, 35.

[12] J. A. R. Samson, *The Review of Scientific Instruments.*, 40, 1969, 1174.

[13] P. W. Atkins, Physical Chemistry, *Oxford University Press, Oxford*, 1986.

[14] A. James, *Phys. Rev.*, 55, 1939, 966.

[15] M. Hart, Manual of Scientific Glassblowing, *British Society of Glassblowers, Lancashire, UK*, 1992.

[16] C.J. Howard, *J. Phys. Chem.*, 3, 1979, 83.

[17] L.F. Keyser, *J. Phys. Chem.*, 88, 1984, 4750.

[18] F, Kaufman, *J. Phys. Chem.*, 88, 1984, 4909.

[19] J. G. Calvert, R. Atkinson, J. A. Kerr, S. Madronich, G. K. Moortgat, T. J. Wallington, and G. Yarwood, The Mechanisms of Atmospheric Oxidation of the Alkenes, *Oxford University Press, Oxford*, 2000.

[20] M. V. Ghosh, J. M. Dyke and D. E. Shallcross, Unpublished work, 2005.

[21] R. V. Poirier and R. W. Carr, *J. Phys. Chem.*, 75, 1971, 1593.

[22] J. P. D. Abbatt, K. L. Demerjian and J. G. Anderson, *J. Phys. Chem.*, 94, 1990, 4566.

[23] J.M. Dyke, M.V. Ghosh, M. Goubet, D.J. Kinnison, G. Levita, A. Morris and D.E. Shallcross, *Phys. Chem. Chem. Phys.*, 7, 2005, 866.

[24] J. V. Seeley, J. T. Jayne and M. J. Molina, *Int. J. Chem. Kinetics.*, 25, 1993, 571.

[25] D. J. Hucknall and A. Morris, Vacuum Technology, Calculations in Chemistry, *Royal Society of Chemistry, Cambridge, UK*, 2003.

[26] D. J. Tritton, Physical Fluid Dynamics, *Oxford University Press, Oxford*, 1988.

[27] J. G. Knudsen and D. L. Katz, Fluid Dynamics, *McGraw-Hill, New York*, 1958.

[28] C. J. Percival, D. E. Shallcross, C. E. Canosa-Mas and J. M. Dyke, *J. Photochem. Photobio. A. Chem.*, 176, 2005, 250.

[29] K. J. Laidler, Chemical Kinetics, *McGraw-Hill, New-Delhi*, 1965.

[30] M.J. Pilling and P.W. Seakins, Reaction Kinetics, *Oxford University Press, Oxford*, 1995.

[31] D. Wang and X. Qian, *J. Elec. Spec.*, 83, 1997, 41.

[32] D. Wang, X. Qian and P. Jiang, *Chem. Phys. Lett*., 258, 1996, 149.

[33] X. Cao, X. Qian, C. Qiao and D. Wang, *Chem. Phys. Lett.*, 299, 1999, 322.

[34] D. Bulgin, J. M. Dyke, F. Goodfellow, N. Jonathan, E. P. F. Lee and A. Morris, *J. Elec. Spec. Rel. Phen.*, 12, 1977, 67.

[35] A. Morris, J. M. Dyke, G. D. Josland, M. P. Hastings and P. D. Francis, *High Temperature Science.*, 22, 1986, 95.

[36] R. A. Lewis, Ph.D. Thesis, Southampton University, 1984.

[37] W. H. Hayt, Engineering Electromagnetics, *McGraw-Hill, New York*, 2006.

[38] G. Margaritondo, Elements of Synchrotron Light. *Oxford University Press Inc, New York*, 2002.

[39] S. Cvejanovic and F. H. Read. *J. Phys. B.*, 7, 1974, 1180.

[40] http://www.elettra.trieste.it/beamlines/GAPH/

[41] M. Eypper, Ph.D. Thesis, Southampton University, 2009.

[42] A. Derossi, F. Lama, M. Piacentini, T. Prosperi, and N. Zema. *Rev. Sci. Instrum.*, 66, 1995, 1718.

[43] E. Harting and F. H. Read, Electrostatic lenses, *Elsevier ed, Amsterdam*, 1976.

[44] L. J. Beeching, A. A. Dias, J. M. Dyke, , A. Morris, S. Stranges, J. B. West, N. Zema and L. Zuin, *Mol. Phys.*, 101, 2003, 575.

[45] L. Zuin, F. Innocenti, M. L. Costa, A. A. Dias, A. Morris, A. C. S. Paiva, S. Stranges, J. B. West and J. M. Dyke, *Chem. Phys.*, 298, 2004, 213.

[46] J. W. Rabalais, Principles of Ultrasviolet Photoelectron Spectroscopy, *Wiley and Sons ed, New York*, 1977.

[47] J. A. R. Samson and A. F. Starace, *J. Phys. B. Atom. Molec. Phys.*, 8 1975, 1806.

[48] J. A. R. Samson and J. L. Gardner, *J. Optic. Soc. Am.*, 62, 1972, 856.

[49] D. Cubric, D. B. Thompson, D. R. Cooper, G. C. King, and F. H. Read. *J. Phys. B.*, 30, 1997, L857.

[50] J. Baker, Ph.D. Thesis, Southampton University, 1991.

[51] F. Innocenti, L. Zuin, M. L. Costa, A. A. Dias, A. Morris, A. C. S. Paiv, S. Stranges, J. B. West and J. M. Dyke, *J. Elec. Spec. Rel. Phen.*, 142, 2005, 241.

[52] F. Innocenti, Ph.D. Thesis, Southampton University, 2004.

[53] F. Innocenti, M. Eypper, S. Beccaceci, A. Morris, S. Stranges, J. B. West, G. C. King and J. M. Dyke, *J. Phys. Chem. A.*, 112, 2008, 6939.

Chapter 4

Theoretical Methods

Photoelectron spectroscopy (PES) provides important information on the electronic structure, vibrational frequencies and the bonding character of molecules and positive ions under investigation (described previously in Chapter 2). Supporting information can also be obtained from molecular orbital (MO) or *ab initio* calculations. MO calculations can be used to assist the interpretation of experimental PE spectra by helping to assign PE bands and to provide additional information such as computed AIEs and the VIEs for bands which may be unresolved or overlapped. Other information concerning the heats of formation and vibrational constants of molecules and ions can also be determined and compared with experimentally derived values. The AIEs and VIEs of two fire suppressant agents, HFC-125 and FM-200, and their thermal decomposition products, have been determined using state-of-the-art *ab initio* calculations. These results are discussed in Chapters 5 and 6 respectively. AIEs, VIEs and neutral and ionic vibrational constants were also determined using *ab initio* calculations for the triatomic molecule SF_2 (see Chapter 9). Adiabatic and vertical excitation energies have been calculated along with reaction enthalpies for the atmospherically important molecule monochlorodimethyl sulphide (CH_2SCH_3Cl). These results are discussed in Chapter 10.

The aim of this chapter is to describe the methods which are used in quantum chemistry to perform such electronic structure calculations. This chapter will describe the main levels of theory which can be used in MO calculations, discussing the necessary approximations required in order to complete calculations in a reasonable time and how

effects such as electron reorganisation and electron correlation can be included. An overview on the construction of basis sets and the notation used for basis sets will also be given.

4.1 The Hartree-Fock-Roothaan Method

Hartree-Fock-Roothaan theory, which was first proposed by Hartree [1], then improved by Fock [2] and later extended by Roothaan [3], is a variational method used to provide an approximate solution to the Schrödinger equation [4] for a closed-shell molecule and is the basis of *ab initio* calculations [5].

4.1.1 The Schrödinger Equation

In quantum mechanics the time-independent Schrödinger equation describes how the wavefunction of a physical system (atom or molecule) changes with coordinates. The wavefunction is related to the energy, *E*, of a system by the time-independent Schrödinger equation,

$$H\Psi = E\Psi \tag{4.1}$$

where *H* is the Hamiltonian operator which is expressed as [6],

$$H = \underbrace{-\sum_i \frac{1}{2}\nabla_i^2 - \sum_a \frac{1}{2m_a}\nabla_a^2}_{\text{Kinetic Energy operator terms}} \underbrace{-\sum_i \sum_a \frac{Z_a}{r_{ia}}}_{\text{Electron-Nuclear Attraction term}} + \underbrace{\sum_{i<j} \frac{1}{r_{ij}}}_{\text{Electron-Electron term}} + \underbrace{\sum_{a<b} \frac{Z_a Z_b}{R_{ab}}}_{\text{Nuclear repulsion term}} \tag{4.2}$$

where *i* and *j* are electrons, *a* and *b* are nuclei, *Z* is the charge on a nucleus, *R* is the internuclear distance and ∇_i^2 is the Laplacian operator for the *i*th electron where [7, 8],

$$\nabla_i^2 = \frac{\partial^2}{\partial x_i^2} + \frac{\partial^2}{\partial y_i^2} + \frac{\partial^2}{\partial z_i^2} \tag{4.3}$$

When performing molecular orbital (MO) calculations on atoms or molecules, it is the aim of these calculations to solve the time-independent Schrödinger equation as accurately as possible. However this equation cannot be solved exactly for molecular systems and therefore certain approximations must be introduced in order to obtain approximate solutions [9]. Two main approximations which are used in an MO

calculation are 1) the Born-Oppenheimer approximation and 2) the one-electron approximation, and these will both be described in the following sections of this chapter.

4.1.2 The Born-Oppenheimer Approximation

The first approximation to be introduced is the Born-Oppenheimer approximation [10]. Due to the large size difference between nuclei and electrons (10^3-10^5), the motion of the nuclei is considered to be negligible (or fixed) when compared to that of the motion of the electrons, i.e. as the nuclei are much heavier than the electrons, the motions of the nuclei take place on a much longer time-scale than the electronic motion [10]. The Born-Oppenheimer approximation therefore assumes that nuclear and electronic motions are separable from one another which results in a separation of the total wavefunction into nuclear and electronic parts. This is shown in equation 4.4 below,

$$\Psi_{total}(r,R) = \Psi_{nuc}(R) \times \Psi_{elec}(r,R) \tag{4.4}$$

where *r* and *R* are the electron and nuclear coordinates respectively for a given state of the system (atom or molecule). As the nuclei are deemed fixed on an electronic time-scale, equation 4.1 can be re-written to give,

$$H_{elec}\Psi_{elec} = E_{elec}\Psi_{elec} \tag{4.5}$$

This is referred to as the *electronic* time-independent Schrödinger equation. The electronic Hamiltonian operator, H_{elec}, can now be expressed as,

$$H_{elec} = \underbrace{\left(-\sum_i \frac{1}{2}\nabla_i^2\right)}_{\text{Kinetic Energy operator}} \underbrace{-\sum_i \sum_a \frac{Z_a}{r_{ia}}}_{\text{Electron-Nuclear Attraction term}} + \underbrace{\left(\sum_{i<j} \frac{1}{r_{ij}}\right)}_{\text{Electron-Electron Interaction term}} = \sum_i h_i + \sum_{i<j} g_{ij} \tag{4.6}$$

where the first term, h_i, is the one-electron Hamiltonian, which consists of the kinetic energy operator for the electrons and the electron-nuclear attractive potential. The second term in equation 4.6, g_{ij}, is the two-electron operator for the interaction between electrons *i* and *j*. As the nuclei are considered fixed on an electronic time-scale, the kinetic energy term describing the nuclear motion in the Hamiltonian, (the second term

shown in equation 4.2), is neglected and the fifth term in equation 4.2, which describes the nuclear-nuclear repulsion, is considered to be constant (as the nuclei are assumed to be fixed) and is therefore omitted from equation 4.6. Nuclear-nuclear repulsion is, however, included in the total energy calculation. Therefore the total electronic energy, E_{elec}, can be calculated for a given electronic state of a molecule by obtaining an approximate solution to equation 4.5 at fixed nuclei positions. By determining the total electronic energy of the molecule at many different nuclear coordinates, a potential energy surface can be computed. This potential energy surface can then be used to obtain information concerning the vibrational energies and vibrational wavefunctions of the molecule in a given state.

4.1.3 The One-Electron Approximation

The second approximation which is made in order to obtain approximate solutions of the electronic time-independent Schrödinger equation for a system containing more than one electron is known as the molecular orbital (MO) or one-electron approximation. It assumes that each electron in the system moves in an average field of all the other electrons and nuclei in the system. With this approximation, the total electronic wavefunction can be taken as a product of one-electron wavefunctions, called spin orbitals, where each electron in the system is represented by a one-electron spin orbital, $\lambda(i)$ [11].

The Pauli Exclusion Principle states that as electrons are fermions, the total electronic wavefunction must be antisymmetric with respect to electron interchange [12]. This condition can be accounted for by writing the total electronic wavefunction in the form of a single Slater determinant, as interchange of any two rows leads to a change of sign of the determinant. The resulting wavefunction is therefore antisymmetric with respect to the exchange of two electrons and can be expressed as [13, 14],

$$\Psi_{elec} = \frac{1}{\sqrt{n!}} \begin{vmatrix} \lambda_1(1) & \lambda_2(1) & \cdots & \lambda_n(1) \\ \lambda_1(2) & \lambda_2(2) & \cdots & \lambda_n(2) \\ \vdots & \vdots & \ddots & \vdots \\ \lambda_1(n) & \lambda_2(n) & \cdots & \lambda_n(n) \end{vmatrix} \tag{4.7}$$

where n is the total number of electrons in the molecule and $\frac{1}{\sqrt{n!}}$ is the normalisation coefficient. Using the expression for the electronic Hamiltonian, in equation 4.6, and

using equation 4.7, which shows the electronic wavefunction expressed as a single Slater determinant, the total energy, expressed in terms of spin orbitals, can be written as,

$$E = \sum_i I_i' + \sum_{i>j} [J_{ij}' - K_{ij}'] \tag{4.8}$$

where I_i' is the one-electron integral, written in terms of the one-electron operator, h_i, which includes the electron kinetic energy operator and the electron-nuclear attraction terms. The two-electron term, g_{ij}, in equation 4.6, gives rise to a Coulomb, J_{ij}, and an exchange, K_{ij}, term in the total energy expression for the system, shown in equation 4.8. The integrals in equation 4.8 are [3],

$$I_i' = \int \lambda_i^*(1) h_i \lambda_i(1) d\tau \tag{4.9}$$

$$J_{ij} = \iint \lambda_i^*(1)\lambda_j^*(2) \frac{1}{r_{ij}} \lambda_i(1)\lambda_j(2)\, d\tau \tag{4.10}$$

$$K_{ij} = \iint \lambda_i^*(1)\lambda_j^*(2) \frac{1}{r_{ij}} \lambda_j(1)\lambda_i(2)\, d\tau \tag{4.11}$$

The Coulomb integral, J_{ij}, represents the interaction of an electron with an average of all other electrons and the exchange integral, K_{ij}, represents the interaction of an electron with electrons of the same spin. A spin orbital, $\lambda(i)$, also describes the electron spatial distribution of electron *i* which is defined by,

$$\lambda(i) = \begin{cases} \phi(r_i)\alpha \\ \phi(r_j)\beta \end{cases} \tag{4.12}$$

where α and β correspond to spins (↑) and (↓) respectively, with values of $s = +½$ and $s = -½$. Two electrons can occupy the same space orbital provided that they have different spin. From a given a set of *K* spatial orbitals, $(\phi_1, \ldots, \phi_K)$, a set of *2K* restricted spin orbitals $(\lambda_1, \ldots, \lambda_{2K})$ can be formed. An unrestricted spin orbital in a closed-shell system, on the other hand, will have different spatial functions for α and β spins (see section 4.1.6 regarding unrestricted Hartree-Fock theory) [15]. Spatial molecular orbitals are assumed to be orthonormal,

$$\int \phi_i^*(r)\phi_j(r)\,dr = \delta_{ij} \tag{4.13}$$

i.e. if $i = j$ then $\delta = 1$ and if $i \neq j$ then $\delta = 0$. For a closed-shell system equation 4.8 can be integrated out over spin, to give [3],

$$E = 2\sum_i I_i + \sum_{ij}\left[2J_{ij} - K_{ij}\right] \tag{4.14}$$

where the integrals, I_i, J_{ij} and K_{ij} are the equivalent of those shown in equations 4.9-11, but expressed in terms of spatial orbitals, ϕ_i. In order to determine the true ground state wavefunction, Ψ_0, for an atom or molecule, the total energy is evaluated using a trial wavefunction, Ψ_{trial}, which is a good approximation of the true ground state wavefunction, Ψ_0, and is given by,

$$E_{trial} = \frac{\int \Psi_{trial}^* H \Psi_{trial} d\tau}{\int \Psi_{trial}^* \Psi_{trial} d\tau} \tag{4.15}$$

where E_{trial} is known as the *expectation value* of the energy. The variation principle states that for any trial wavefunction used to define a system, the expectation value of the energy, E_{trial}, can never be less than the true ground state energy, E_0, i.e. [16],

$$E_{trial} \geq E_0 \tag{4.16}$$

If the trial wavefunction is written as a linear combination of the true solutions of the system Ψ_j,

$$\Psi_{trial} = \sum_j c_j \Psi_j \tag{4.17}$$

then the difference in the energy, determined using a trial wavefunction and the true ground state energy, is given by substituting equation 4.17 into equation 4.15 to give,

$$E_{trial} - E_0 = \frac{\sum_j c_j^* c_j \left(E_j - E_0\right)}{\sum_j c_j^* c_j} \tag{4.18}$$

The best trial wavefunction used to describe a system is one which produces the lowest possible total energy i.e. closest to the true ground state energy of the system [16]. The choice of the initial trial wavefunction is therefore crucial for the success of the method. However, it must be noted that this theorem is valid only for the total energy of the system and not for calculating any other properties. Therefore the best wavefunction used to describe a closed-shell system is found by calculating *E*, from equation 4.14, for a number of trial spatial orbitals, ϕ_i, until a minimum energy is reached.

To derive a set of pseudo-eigenvalue equations, *E* is minimised using the Lagrange method of undetermined multipliers, subject to the overlap integral condition,

$$S_{ij} = \int \phi_i^* \phi_j d\tau = \delta_{ij} \tag{4.19}$$

So for small variations in ϕ_i, equation 4.14 becomes equation 4.20 at an energy minimum,

$$\delta E = 2\sum_i \delta I_i + \sum_{ij} \left[2\delta J_{ij} - \delta K_{ij}\right] = 0 \tag{4.20}$$

with the sum of *i* and *j* running over all occupied space orbitals. Also for small variations in ϕ_i,

$$\delta S_{ij} = 0 \tag{4.21}$$

In order to minimise the energy subject to the overlap condition in equation 4.19, the Lagrange method of undetermined multipliers is used and equation 4.19 is multiplied by a constant, $-2\varepsilon_{ij}$, and added to 4.19 to give the new energy expression,

$$E' = E - 2\sum_{ij} \varepsilon_{ij} S_{ij} \tag{4.22}$$

where ε_{ij} are constants. Equation 4.22 can be expanded to give,

$$\delta E' = 2\sum_i \delta I_i + \sum_{ij} \left[2\delta J_{ij} - \delta K_{ij} - 2\varepsilon_{ij}\delta S_{ij}\right] = 0 \tag{4.23}$$

Use of this equation leads to [17],

$$F(i)\phi_i = \varepsilon_i\phi_i \tag{4.24}$$

where ϕ_i are the molecular orbital wavefunctions and ε_i are the molecular orbital energies. *F* is the one-electron *Fock* operator and is expressed as,

$$F(i) = H_N + \sum_j \left(2J_j - K_j\right) \tag{4.25}$$

The second term in equation 4.25 consists of Coulomb and exchange operators acting on electron *i*. The Fock operator depends on all occupied molecular orbitals, notably the operators J_j and K_j which depend on all the occupied orbitals, i.e. the Fock operator is not known until the equations 4.24 and 4.25 are solved, and to solve these, an iterative "self-consistent" procedure is required.

This is achieved by making an initial estimate of the molecular orbitals to obtain a trial Fock operator from equation 4.25, which is then used in equation 4.24 to solve for a new set of MOs. These new MOs are then compared to the initial MOs. The process is then repeated until there is no change between the initial and final MOs, or if there is no difference in the total electronic energy computed for successive iterations to within a preset tolerance. This is known as the Hartree-Fock Self Consistent Field method (Hartree-Fock SCF method).

Roothaan extended the Hartree-Fock method by expressing the MOs as linear combinations of atomic orbitals (LCAO) as,

$$\phi_i = \sum_q c_{iq}\chi_q \tag{4.26}$$

where χ_q are atomic orbitals, or basis functions, and c_{iq} is an expansion coefficient. This is known as the Hartree-Fock-Roothaan approximation. Substituting equation 4.26 into 4.24, multiplying by χ_q and then integrating gives the LCAO Hartree-Fock-Roothaan equations,

$$\sum_q c_{iq}\left(F_{pq} - S_{pq}\varepsilon_i\right) = 0 \tag{4.27}$$

The LCAO-SCF method requires computation of two kinds of integrals,

$$I_{pq} = \int \chi_p^*(1) H_N(1) \chi_q(1) d\tau(1) \tag{4.28}$$

and,

$$(pq|rs) = \iint \chi_p^*(1) \chi_r(2) \frac{1}{r_{12}} \chi_q^*(1) \chi_s(2)\, d\tau(1) d\tau(2) \tag{4.29}$$

The terms in equation 4.27 are,

$$F_{pq} = \int \chi_p^* \chi_q d\tau = I_{pq} + \sum_j [2(pq|jj) - (pj|jq)] \tag{4.30}$$

and,

$$S_{pq} = \int \chi_p^* \chi_q d\tau \tag{4.31}$$

where S_{pq} is the overlap integral between basis functions χ_p and χ_q. The Hartree-Fock-Roothaan secular equations shown in equation 4.27 also have to be solved by minimising the energy in an iterative way. This is done by computing S_{pq} and making an initial estimate of the expansion coefficients, c_{iq}, in order to compute values for F_{pq}. Once F_{pq} and S_{pq} are known then ε_i can be obtained from,

$$\left| F_{pq} - S_{pq} \varepsilon_i \right| = 0 \tag{4.32}$$

Using the ε_i value obtained from equation 4.32, a new set of expansion coefficients can be determined from equation 4.27. This process is repeated until the total energy reaches a minimum, within a pre-determined tolerance. If a larger number of basis functions are used, a better description of the one electron MOs is obtained. The Hartree-Fock limit is reached when increasing number of basis functions gives rise to no change in the total converged SCF energy.

However performing calculations at the Hartree-Fock limit is usually not possible as it takes a considerable amount of computer time. In practice, a smaller number of basis functions are chosen order to make the calculation possible.

4.1.4 Koopmans' Theorem

As ionisation energies are one of the main quantities obtained from experimental PE spectra, it is important to be able to calculate such energies in order to compare calculated values with those obtained experimentally. This will assist in PE band assignment. The ionisation energy for a closed shell molecule can be calculated using Koopmans' theorem from a Hartree-Fock calculation on the neutral molecule. Koopmans' theorem states that in a closed-shell molecule, the vertical ionisation energy, IE_j, (referred to as VIE) of an emitted electron is equal in magnitude to the negative of the orbital energy, $-\varepsilon_j$, from which the electron originated, where the orbital energy is obtained from an *ab initio* calculation performed at the Hartree-Fock limit. This relationship is shown in equation 4.33 [18],

$$IE_j = -\varepsilon_j \tag{4.33}$$

However, Koopmans' theorem is only an approximation, as it does not take into consideration the effects of electron reorganisation (the orbital relaxation when passing from the neutral to the ion) and the electron correlation energy change on ionisation (the difference in correlation energy between the molecule and the ion which is discussed in section 4.1.5 of this chapter). As a result, vertical ionisation energies obtained are often too high. To improve the estimation of vertical ionisation energies, the reorganisation energy, R, and the electron correlation energy change, C, need to be included in equation 4.33. Koopmans' vertical ionisation energies are related to the experimental vertical ionisation energies by,

$$IE_{vertical} = IE_{Koopmans'} - R + C \tag{4.34}$$

Koopmans' theorem usually gives a good approximation of experimental vertical ionisation energies as reorganisation energies and electron correlation energy corrections are often of the same magnitude and tend to cancel each other. However, this is not guaranteed as the computed vertical ionisation energies obtained from Koopmans' theorem are often too high, as mentioned, which implies that $R \geq C$. It is possible to allow for the reorganisation effect by performing separate Hartree-Fock calculations on the neutral molecule and the ionic species. The vertical ionisation energy is then obtained from the difference between the total energy of the neutral

molecule and that of the ion. This is called the ΔSCF method [19]. ΔSCF values are often too low as electron correlation effects are neglected in the calculations.

4.1.5 Electron Correlation

In Hartree-Fock theory, electrons are assumed to be moving in an average potential of all the other electrons which is not a true representation of the instantaneous electron-electron interactions which occur in molecules. This instantaneous electron-electron interaction is not accounted for in the Hartree-Fock method, as it is treated in an average way, and this gives rise to an electron correlation error. The electron correlation energy of a molecule in a given state, E_{corr}, is defined as the difference between the Hartree-Fock energy, E_{HF}, obtained using a very large basis set, i.e. at the Hartree-Fock limit, and the exact non-relativistic energy, E_{Exact}, i.e.,

$$E_{corr} = E_{Exact} - E_{HF} \tag{4.35}$$

Correlation effects can be separated out into dynamical and non dynamical effects [20]. Dynamical electron correlation is largely structure dependent and arises from an overestimation of short range electron interaction in Hartree-Fock wavefunctions. However, non-dynamical electron correlation energy effects occur when the state of a molecule investigated is close in energy to another state and interaction occurs, i.e. non-dynamical electron correlation arises from the degeneracy or near-degeneracy of configurations involving valence orbitals [21].

Several methods, known as post-Hartree-Fock methods, have been developed to include these correlation effects. They include configuration interaction (CI) which is one of the most important methods used to account for the missing electron correlation, and Møller-Plesset perturbation theory (MP-PT) which improves on the Hartree-Fock method by including the effects of electron correlation using Rayleigh–Schrödinger perturbation theory (RS-PT), usually to second (MP2), third (MP3) or fourth (MP4) order [22].

In this work, these methods have been used to account for electron correlation effects in *ab initio* calculations and the results are presented in Chapters 5, 6 and 10.

4.1.6 Restricted and Unrestricted Hartree-Fock Methods

It must be noted, the Hartree-Fock LCAO-SCF method described above, is only applicable when performing calculations on closed-shell molecules and is referred to as a *spin restricted* calculation as it uses the same spatial function for both α and β electrons when paired in the same molecular orbital. This is known as the restricted Hartree-Fock method (RHF). When the restricted Hartree-Fock method is applied to an open-shell system, α and β electrons in filled molecular orbitals share the same space orbitals, but α and β electrons which are unpaired have separate space orbitals. Therefore, occupied and unoccupied molecular orbitals require different sets of energy expressions.

Another method which can be used for calculations on open-shell systems is known as the *unrestricted* Hartree-Fock (UHF) method. In the unrestricted Hartree-Fock method different spatial orbitals are used for α and β electrons. As a consequence, the two sets of electrons do not experience the same Coulomb and exchange potentials and therefore they will have different associated energies and spatial distributions as there is no *restriction* on the spatial orbitals [23]. UHF calculations have the advantage of providing lower total energies than RHF calculations. However, one disadvantage of UHF calculations is that a UHF wavefunction with an unpaired electron may not yield a pure doublet state and may be "contaminated" with quartet states. The amount of contamination is evaluated by comparing the expectation value of the S^2 operator, which is checked at the end of the calculation, with the expected value for the pure spin state. Time and cost are important aspects when running calculations and these are dependent on two factors, the level of theory used, e.g. Hartree-Fock or Møller-Plesset, in the calculation (more detail on different levels of theory used in MO calculations is discussed in section 4.3.1-3) and the size of the basis set, i.e. the number of basis functions used when performing a calculation and this is described in the next section.

4.2 Basis Sets

As already described, molecular orbitals can be expressed as linear combinations of basis functions. The set of basis functions used in a calculation is termed the *basis set*. The larger the basis set, the lower the total energy, and the accuracy of the calculation increases. However the computational time required in order to perform a Hartree-Fock

calculation scales by n^4 (where n is the number of basis functions used). Therefore the choice of basis set used for a molecular orbital calculation must take into account the time of the calculation and hence the overall cost to run the calculation.

Two main types of basis functions are commonly used to describe atomic orbitals; Slater Type Orbitals (STOs) and Gaussian Type Orbitals (GTOs). Slater type orbitals have the functional form [13, 14],

$$\chi(r,\theta,\varphi) = NY_{l,m}(\theta,\varphi)r^{n-1}e^{-\zeta r} \tag{4.36}$$

where N is a normalisation constant, n, l and m are the principal, angular momentum and magnetic quantum numbers respectively, $Y_{l,m}(\theta, \varphi)$ is a spherical harmonic function and ζ is an orbital exponent. STOs reproduce atomic electronic distributions reasonably well. However two-electron integrals expressed in terms of STOs cannot be evaluated analytically and can only be evaluated numerically, with considerable computational effort. However, two-electron integrals expressed in GTOs can be evaluated analytically. Gaussian type orbitals have the form [24, 25],

$$\chi(x,y,z) = Nx^a y^b z^c e^{-\zeta r^2} \tag{4.37}$$

where a, b and c are integers whose sum is equal to the angular momentum quantum number l. It is seen from equation 4.37 that there is no dependence on the principal quantum number, n. GTOs, in contrast to STOs, do not satisfactorily reproduce the proper electronic distribution at short or long distances from the nuclei. This can be corrected by using more GTOs to represent an AO.

Basis sets which use the same number of GTOs (or STOs) as there are core and valence AOs to represent a molecule are called *minimal* basis sets. When two basis functions are used to describe each AO, the basis set is called a double zeta basis set (DZ) and when three basis functions are used the basis set is termed a triple-zeta basis set (TZ), and so on.

To account for anisotropic charge distribution effects which occur on bonding, as the charge distribution of an atom in a molecule differs from that of an isolated atom, polarisation functions are used. The effect of polarisation can be included in a basis set by incorporating a *p*-type basis function for a *1s* orbital and a *d*-type basis function for

p-orbitals. Certain notation is used when constructing a basis set. A single (*) indicates the use of a *d*-type polarisation function on the heavy, non-hydrogen, atoms, whereas a second (*) indicates the use of a *p*-type polarisation function for hydrogen atoms [26]. In order to provide a better description at longer distances from the nuclei, a diffuse function can be added to the basis set. Diffuse functions are indicated by a (+). Similar to polarisation functions a single (+) sign indicates the use of a diffuse function only on each heavy, non-hydrogen, atom in the molecule and a basis set which includes (++) indicates that the diffuse functions are included for both the heavier atoms and the hydrogen atoms.

A basis set must first correctly describe the core and valence electronic distributions of a molecule. A common type of basis set used is called a *split-valence K-LM G* basis set, which uses a minimal set of *K* basis functions to describe the core electrons and a basis set of higher quality (*L* and *M* functions) to describe the valence electrons [27, 28]. This method provides a good compromise between time (cost) and accuracy, and is generally used for geometry optimisation [29-31]. Another type of basis set used has the notation *aug-cc-pVQZ*. These types of basis sets are designed for calculations which include electron correlation and have several built-in *p* and *d*-type polarisation functions. Expanding the size of this type of basis set allows the results obtained to be extrapolated to the complete basis set (CBS) limit.

Ab initio calculations have been performed in this work to determine the AIE and VIE of the first PE bands and the VIEs of all subsequent PE bands of the fire suppressants HFC-125 and FM-200 using the *split-valence K-LM G* and *aug-cc-pVQZ* type basis sets at various levels of theory. The values obtained compare well with those determined experimentally. VIEs are determined, using the ΔSCF method, by performing separate SCF energy calculations for the neutral molecule and the ion (using the equilibrium geometry from the neutral molecule for the ion) and taking the difference in the total energies obtained. The AIEs are determined using the same SCF procedure using the respective equilibrium geometries for the neutral molecule and the ion. The results of the calculations performed for HFC-125 and FM-200 are reported in Chapters 5 and 6 respectively. Various theoretical methods have been used, along with different types and sizes of basis sets, to compute ionisation energies which involve a geometry optimisation and a single point calculation at a higher level. An example, taken from

Table 5.2 of Chapter 5 used to compute AIEs and VIEs, which describes the parameters and level of calculations, highlighting the use of both the *split-valence K-LM G* and *aug-cc-pVQZ* type basis sets, is shown below.

$$\overbrace{\underbrace{RCCSD(T)}_{1}/\underbrace{aug-cc-pVQZ}_{2}}^{\text{Single Point Calculation}}//\overbrace{\underbrace{MP2}_{3}/\underbrace{6-31++G^{**}}_{4}}^{\text{Geometry Optimisation}} \quad (4.38)$$

This notation indicates that first a geometry optimisation is performed at the MP2 level using a split-valence type basis set (sections 3 and 4) and then a single point calculation is performed at a higher level, RCCSD(T), using an aug-cc-pVQZ type basis set (sections 1 and 2) using the MP2 optimised geometry.

Section 1 represents the method, i.e. the level of theory, used in the single point calculation. In this case RCCSD(T) stands for Restricted Coupled Cluster theory with Single and Double excitations plus a perturbative Triple excitation (the coupled cluster method is explained in section 4.3.2). Section 2 represents the basis set used at the RCCSD(T) level of theory. The basis set used is the aug-cc-pVQZ type basis set which stands for Augmented (meaning there are diffuse functions)-Correlation Consistent-Polarised Valence Quadruple Zeta. This type of basis set was introduced by Dunning *et al.* for calculations which included calculation of electron correlation [32]. Section 3 represents the level of theory used (MP2 is Møller-Plesset perturbation theory at second order) and is discussed in section 4.3.3. Section 4 represents a split-valence type basis set used at the Møller-Plesset level of theory and is written in *Pople* notation. Pople pioneered the development of *ab initio* quantum chemistry calculations and played a key role in the development of the Gaussian suite of programs (the Gaussian03/09 suite of programs was used during this work) [33]. The split-valence type basis set shown can be described as follows; *6*-31++G** indicates that six Gaussian functions are used to describe each core atomic orbital basis function. 6-*31*++G** indicates that three Gaussians and one Gaussian are used for the valence orbitals to describe each valence atomic orbital basis function [34]. In this basis set, it is seen that two (++) and two (**) are used. This shows that polarisation and diffuse functions are included in the calculation for all hydrogen and non-hydrogen atoms. How a calculation is actually

performed, regardless of the size and type of the basis set used, depends on the theoretical method chosen to perform the calculation.

4.3 Levels of Theory

4.3.1 Configuration Interaction (CI)

In the configuration interaction (CI) method a wavefunction is expanded as a linear combination of several Slater determinants, unlike the Hartree-Fock method which uses a single Slater determinant to represent a wavefunction [35]. When a CI calculation is performed on a closed-shell molecule the initial calculation solves the Hartree-Fock equations using a given basis set for a single determinantal wavefunction. This is known as the reference determinant, Ψ_{ref}. The MOs of interest within the system can be separated out into occupied and virtual (or empty orbitals) MOs. Excitation of one or more electrons from occupied orbitals to virtual orbitals leads to the excited configurations, Ψ_1, Ψ_2…etc where Ψ_n is a configuration state function. A trial wavefunction can then be expressed as the sum of all substituted determinants as,

$$\Psi_{trial} = c_0\Psi_{ref} + c_1\Psi_1 + c_2\Psi_2 + \ldots\ldots \tag{4.39}$$

where Ψ_{ref} is the single determinantal (reference) wavefunction obtained using Hartree-Fock theory and Ψ_n (where n is an integer) are determinants that represent configurations obtained by excitation from occupied spin orbitals in the reference determinant to unoccupied (virtual) spin orbitals. The coefficients, c_n, reflect the weight of each determinant and are determined from the requirement to minimise the total energy of the electronic state.

Only configuration functions of the same symmetry as the state of interest are included in equation 4.39. Applying the variational method to the trial wavefunction yields a set of secular equations,

$$\sum_s c_{si}(H_{st} - E_i\delta_{st}) = 0 \tag{4.40}$$

where E_i is the energy, δ_{st} is the Kronecker delta and H_{st} is a configurational integral,

$$H_{st} = \int_{\dots}\int \Psi_s H \Psi_t d\tau_1 d\tau_2 \dots d\tau_n \tag{4.41}$$

where n is the number of electrons. For most systems, the Hartree-Fock determinant is the main term in the linear combination, i.e. c_0 is usually close to 1.

The exact solution of the non-relativistic Schrödinger equation could be obtained if the full CI method was used with a complete basis set (CBS) [36]. However, it is not practical to consider all excited configurations as the total number of permutations of electrons and orbitals can become extremely large. To reduce the number of determinants in the CI expansion only a few levels of excitation are considered.

The best way to restrict the size of the CI expansion is only to consider configuration functions which provide the most significant contributions to the wavefunction of the state of interest [37]. For example, in the configuration interaction singles (CIS) method, considering only single excitations, or configuration interaction doubles (CID) method, which considers only double excitations, only wavefunctions that differ from the Hartree-Fock wavefunction by a single or double excitations are considered. Even at the CISD (which involves single and double excitations) level, the number of excited configurations generated can still be very large. Quadruple excitations will also contribute to the total energy and need to be taken into account. To avoid performing a calculation that includes single, double, triple and quadruple excitations (CISDTQ), a formula known as the Davidson correction can be used to estimate the contribution of quadruple excited determinants, ΔE_Q, to the correlation energy from [38],

$$\Delta E_Q = (1 - c_0^2)(E_{CISD} - E_{SCF}) \tag{4.42}$$

where E_{CISD} is the ground state energy in a CISD calculation, E_{SCF} is the ground state energy associated with Ψ_{ref} obtained in a Hartree-Fock-SCF calculation and c_0 is the coefficient of the reference determinant in a CISD calculation. An extension of the CI method is called the coupled cluster method [39].

4.3.2 Coupled Cluster (CC) Method

In the Coupled Cluster (CC) method, the full CI wavefunction is given in the exponential form,

$$\Psi_{cc} = e^{T}\Psi_0 \tag{4.43}$$

where *T* is the cluster operator defined as,

$$T = T_1 + T_2 + T_3 + \ldots\ldots T_n \tag{4.44}$$

where *n* is the total number of electrons and the T_i operators generate all *i*th excited Slater determinants,

$$T_i = \sum_{i}^{occ}\sum_{a}^{vir} t_i^a \Psi_i^a \tag{4.45}$$

where *t* are amplitudes, *i* are the occupied orbitals and *a* are the unoccupied (virtual) orbitals. If all levels of excitations are included, a wavefunction computed at the CC level would be exact. However, this is possible only with small systems. In practice, the cluster operator must be truncated at some excitation level. For example, CCSD denotes a CC method with only single and double excitations. It uses $T = T_1 + T_2$. CCSD involves computational effort which is proportional to n^6 while the next level of computation, which involves triple excitations (CCSDT), is much more costly, scaling by n^8 [40, 41]. Alternatively, the triple excitation contributions can be evaluated by means of another method, perturbation theory, and added to the CCSD amplitudes. This is less computationally demanding. This hybrid method is referred to as CCSD(T) and is commonly used as it is a very robust method.

The CI method has the disadvantage in that it is not size consistent, i.e. the wavefunction and energy calculated for the atoms in a molecule at infinite separation are not identical to those calculated for the isolated atoms, though the method does have the advantage of being variational (unlike the CC method which is not variational). An alternative to CI is Møller-Plesset Perturbation Theory. These calculations are size consistent. However like CC methods they are also not variational.

4.3.3 Møller-Plesset Perturbation Theory

Perturbation methods are size consistent as the energy from two equal fragments at infinite distance is equal to twice the energy of the single fragment, and the equations for two or more fragments are separable [21]. Møller-Plesset perturbation theory is one

of the most commonly used MO *ab initio* methods. It starts by assuming the sum of all the one-electron Fock operators for each electron within a molecular system as the unperturbed Hamiltonian (zero-order), H_0.

$$H_0 = \sum_i F_i \tag{4.46}$$

When a perturbation, H_1, is then applied, the electronic Hamiltonian, H, can be expressed as,

$$H = \sum_i F_i + H_1 \tag{4.47}$$

From perturbation theory the exact wavefunction can be formulated as,

$$\Psi_\lambda = \Psi_0 + \lambda_1\Psi_1 + \lambda_2\Psi_2 + \lambda_3\Psi_3 \ldots \tag{4.48}$$

In which Ψ_i is the ith order contribution to the ground state Hartree-Fock wavefunction, Ψ_0. In the same way the total energy can be expanded to give,

$$\mathrm{E}_\lambda = \mathrm{E}_0 + \lambda_1\mathrm{E}_1 + \lambda_2\mathrm{E}_2 + \lambda_3\mathrm{E}_3 \ldots \tag{4.49}$$

The parameter, λ, is then set to one and the series is truncated at the chosen order, n. The method is then denoted MPn. It can be shown that the Hartree-Fock energy, E_{HF}, for the ground state wavefunction, Ψ_0, is,

$$E_{HF} = \iint \Psi_0(H_0 + H_1)\Psi_0 d\tau_1 d\tau_2 \tag{4.50}$$

The energy values for a given perturbation level can then be expressed as,

$$E_0 = \iint \Psi_0 H_0 \Psi_0 d\tau_1 d\tau_2 \tag{4.51}$$

$$E_1 = \iint \Psi_0 H_1 \Psi_0 d\tau_1 d\tau_2 \tag{4.52}$$

$$E_2 = \iint \Psi_0 H_2 \Psi_1 d\tau_1 d\tau_2 \tag{4.53}$$

$$E_3 = \iint \Psi_0 H_3 \Psi_2 d\tau_1 d\tau_2 \tag{4.54}$$

It can be seen from equations 4.50-4.52 that the Hartree-Fock energy is the sum of E_0 + E_1. The first correction to the ground state energy is given by a second-order perturbation energy as,

$$E_2 = \sum_{j \neq 0} \frac{\iint \Psi_j H_1 \Psi_0 d\tau_1 d\tau_2 \iint \Psi_0 H_1 \Psi_j d\tau_1 d\tau_2}{E_j - E_0} \tag{4.55}$$

Only doubly excited determinants, Ψ_i, have non-zero H_0 matrix elements with Ψ_0 and so only double excitations contribute to E_2. When this second-order correction is incorporated, the method is called MP2. MP2 is one of the most successful methods in quantum chemistry as it accounts for 50-80% of electron correlation using a relatively small amount of computational time. Also no major assumptions need to be made other than determining the initial reference wavefunction.

The energy expression can be corrected for third and fourth-order perturbations i.e. yielding a perturbative series of MP1, MP2, MP3, MP4 etc, where MP1 has been shown to be equivalent to the Hartree-Fock energy from equation 4.50. In the Møller-Plesset method the first and second derivatives of the energy can be determined analytically which has the advantage for locating stationary points and calculating harmonic vibrational frequencies efficiently. This was the method used in this work to determine the optimised geometries and vibrational frequencies of the molecules studied (see Chapters 5 and 6).

4.4 Summary

This chapter has described the theoretical methods which have been used to perform *ab initio* calculations in support of the experimental work of this project and how these calculations can be used to determine various relevant quantities for a molecule, e.g. the determination of AIEs and VIEs for both open and closed-shell molecules. These methods have been used by Dr E. P. F. Lee of the Southampton PES group to determine the AIEs, VIEs and reaction enthalpies associated with the fire suppressant agents HFC-125 and FM-200 and the atmospherically important molecule monochlorodimethyl sulphide (CH_3SCH_2Cl). These results are discussed in Chapters 5, 6 and 10 respectively.

References

[1] D. R. Hartree, *Proc. Camb. Phil. Soc.*, 24, 1928, 89.

[2] V. Fock, *Z. Phys.*, 61, 1930, 126.

[3] C. C. J. Roothaan, *Rev. Mod. Phys.*, 23, 1951, 69.

[4] E. Schrödinger, *Ann. Phys.*, 79, 1926, 361.

[5] D. R. Hartree, W. Hartree and B. Swirles, *Phil. Trans. Roy. Soc. A.*, 238, 1939, 229.

[6] C. J. Cramer, Essentials Computational Chemistry, 2nd Edition, *John Wiley and Sons*, *Chichester*, 2007.

[7] F. Jensen, Introduction to Computational Chemistry, *John Wiley and Sons*, *Chichester*, 1999.

[8] P. Atkins and R. Friedman, Molecular Quantum Mechanics, 4th Edition, *Oxford University Press*, 2005.

[9] S. C. Wang, *Phys. Rev.*, 31, 1928, 579.

[10] M. Born and R. Oppenheimer, *Ann. Phys.*, 84, 1927, 457.

[11] A. Szabo and N. S. Ostlund, Modern Quantum Chemistry: Introduction to Advanced Electronic Structure Theory, *Dover Publications, New York*, 1989.

[12] C. C. J. Roothaan, *Rev. Mod. Phys.*, 32, 1960, 179.

[13] W. Pauli, *Z. Phys. A-Hadron. Nucl.*, 31, 1925, 765.

[14] J. C. Slater, *Phys. Rev.*, 34, 1929, 1293.

[15] J. C. Slater, *Phys. Rev.*, 36, 1930, 57.

[16] J. K. L. MacDonald, *Phys. Rev.*, 43, 1933, 830.

[17] R. G. Parr, Quantum Theory of Molecular Electronic Structure, *W. A. Benjamin*, *New York*, 1963.

[18] T. Koopmans, *Physica.*, 1, 1934, 104.

[19] M. F. Guest and V. R. Saunders, *Mol. Phys.*, 29, 1975, 873.

[20] O. Sinanoglu and D. F. Tuan, *J. Chem. Phys.*, 38, 1963, 1740.

[21] D. K. W. Mok, R. Neumann and N. C. Handy, *J. Phys. Chem.*, 100, 1996, 6225.

[22] C. Møller and M. S. Plesset, *Phys. Rev.*, 46, 1934, 618.

[23] J. A. Pople and R. K. Nesbet, *J. Chem. Phys.*, 22, 1954, 571.

[24] S. F. Boys, *Proc. Roy. Soc. Lond. A Math.*, 200, 1950, 542.

[25] F. E. Harris, *Rev. Mod. Phys.*, 35, 1963, 558.

[26] E. Clementi and D. R. Davis, *J. Comput. Phys.*, 1, 1966, 223.

[27] J. S. Binkley, J. A. Pople and W. J. Hehre, *J. Am. Chem. Soc.*, 102, 1980, 939.

[28] M. J. Frisch, J. A. Pople and J. S. Binkley, *J. Chem. Phys.*, 80, 1984, 3265.

[29] P. J. Hay and W. R. Wadt, *J. Chem. Phys.*, 82, 1985, 270.

[30] W. R. Wadt and P. J. Hay, *J. Chem. Phys.*, 82, 1985, 284.

[31] P. J. Hay and W. R. Wadt, *J. Chem. Phys.*, 82, 1985, 299.

[32] T. H. Dunning, *J. Chem. Phys.*, 90, 1989, 1007.

[33] M. J. Frisch, G. W. Trucks, H. B. Schlegel, G. E. Scuseria, M. A. Robb, J. R. Cheeseman, J. A. Montgomery Jr., T. Vreven, K. N. Kudin, J. C. Burant, J. M. Millam, S. S. Iyengar, J. Tomasi, V. Barone, B. Mennucci, M. Cossi, G. Scalmani, N. Rega, G. A. Petersson, H. Nakatsuji, M. Hada, M. Ehara, K. Toyota, R. Fukuda, J. Hasegawa, M. Ishida, T. Nakajima, Y. Honda, O. Kitao, H. Nakai, M. Klene, X. Li, J. E. Knox, H. P. Hratchian, J. B. Cross, V. Bakken, C. Adamo, J. Jaramillo, R. Gomperts, K. Raghavachari, J. B. Foresman, J. V. Ortiz, Q. Cui, A. G. Baboul, S. Clifford, J. Cioslowski, B. B. Stefanov, G. Liu, A. Liashenko, P. Piskorz, I. Komaromi, R. L. Martin, D. J. Fox, T. Keith, M. A. Al-Laham, C. Y Peng, A. Nanayakkara, M. Challacombe, P. M. W. Gill, B. Johnson, W. Chen, M. W. Wong, C. Gonzalez and J. A. Pople, *Gaussian 03, Revision E.01, Gaussian, Inc., Wallingford CT*, 2004.

[34] W. J. Hehre, R. Ditchfield, and J. A. Pople, *J. Chem. Phys.*, 56, 1972, 2257.

[35] A. E. Leach, Molecular Modelling, Principles and Applications, 2nd Edition, *Henry Ling Ltd, Dorchester*, 2001.

[36] V. R. Saunders and J. H. Van. Lenthe, *Mol. Phys.*, 48, 1983, 932.

[37] P. O. Löwdin, *Adv. Chem. Phys.*, 2, 1959, 207.

[38] L. Brillouin, *J. Phys. Radium.*, 3, 1932, 373.

[39] S. R. Langhoff and E. R. Davidson, *Int. J. Quantum. Chem.*, 8, 1974, 61.

[40] W. J. Hehre, L. Radom, P. V. R. Schleyer, and J. A. Pople, Ab Initio Molecular Orbital Theory, *Wiley Interscience, New York*, 1986.

[41] R. J. Bartlett, *J. Chem. Phys.*, 93, 1989, 1697.

Chapter 5

A Study of Pentafluoroethane and its Thermal Decomposition using PES and *ab initio* Molecular Orbital Calculations

New fire extinguishants are currently being sought with low ozone depletion potentials (ODPs) and low global warming potentials (GWPs). Halogenated hydrocarbons (halons) have been found to exhibit good fire suppression properties. However, bromine and chlorine containing hydrocarbons and fluorocarbons (e.g. CH_3Cl, CF_3Br, CF_2Cl_2 and CF_2Br_2), whilst exhibiting good fire suppression properties, give rise to environmental problems in that they have significant ODP and GWP values [1]. As a result, hydrofluorocarbons (HFCs) are being considered as alternative fire extinguishants. Also, HFCs are replacing chlorofluorocarbons (CFCs) in industrial applications, such as refrigeration and foam blowing because of their less harmful effects on stratospheric ozone [2]. The use of HFCs in these areas has prompted a number of studies of their chemical and physical properties related to these applications [3-9].

Pentafluoroethane (CF_3CHF_2), also referred to as HFC-125 or R-125, is one of the simplest HFCs. It has been studied in some detail in the gas-phase by microwave, infrared, Raman and far-infrared spectroscopy [10-12]. However, its thermal decomposition had not been investigated experimentally. To establish how CF_3CHF_2 suppresses and extinguishes flames, its thermal decomposition was studied in a flow system using PES. Although CF_3CHF_2 has not been studied previously using PES, the

threshold photoelectron (TPE) spectrum and ion yield curves of the observed ionic fragments obtained after photoionisation have been recorded in the photon energy range 12.0-25.0 eV using synchrotron radiation as the photon source [13]. Also, the fragmentation of the valence electronic states of $CF_3CHF_2^+$ has been studied using the threshold photoelectron-photoion coincidence (TPEPICO) technique [13]. In the TPE spectrum the first band was broad and vibrationally unresolved which is consistent with a significant geometry change on ionisation. The band onset was measured as (12.70 ± 0.05) eV and the band maximum (the VIE) was measured as (13.76 ± 0.05) eV [13]. A vacuum ultraviolet (v.u.v) photoionisation study [14], determined the experimental first adiabatic ionisation energy (AIE) as (12.25 ± 0.10) eV, which is consistent with AIE values of 12.25 and 12.26 eV computed using the G2 and G3 methods [13, 14]. The discrepancy of ~0.5 eV between the experimental onset of (12.70 ± 0.05) eV from the TPE study and the computed AIEs at the G2 and G3 levels was attributed in the TPEPICO study [13] to the inability of the TPE method to obtain a measurable signal at the ionisation threshold for a molecule that has small Franck-Condon factors for direct ionisation near threshold. It is, however, notable in the photoionisation work of reference [14], that the parent ion ($CF_3CHF_2^+$) was not observed at any of the photon energies used (in the region 12.0-22.5 eV) and the value for the first AIE, quoted as (12.25 ± 0.10) eV, appears to have been derived from analysis of v.u.v absorption spectra (although no details of this are given).

In this work, PE spectra of CF_3CHF_2 and its pyrolysis products were recorded as a function of temperature in a flow system (described in section 3.3 of Chapter 3). In addition, state-of-the-art *ab initio* calculations have been performed on CF_3CHF_2 and $CF_3CHF_2^+$, and the fragments obtained from CF_3CHF_2 and $CF_3CHF_2^+$. These were carried out to obtain reliable AIE and VIE values in order to assist interpretation of the experimental PE spectra and also to obtain a reliable enthalpy of formation ($\Delta H_{f,298K}^{Ø}$) for CF_3CHF_2 and its cation in their ground electronic states. All calculations were performed by Dr E. P. F. Lee of the Southampton PES group and are included in this chapter for completeness.

5.1 Experimental

The PE spectrum of CF_3CHF_2 was recorded using the big spectrometer (described in section 3.1 of Chapter 3) with a high temperature RF heating system coupled to the ionisation region (as described in section 3.3 of Chapter 3) [15, 16]. Typical operating resolution of the spectrometer throughout this work was 20-25 meV, as measured for the $(3p)^{-1}$ ionisation of argon. PE spectra of CF_3CHF_2 (Ineos Fluor, 99.7%) and CF_3H (Aldrich, 98%), a product observed during pyrolysis, were recorded and calibrated by admitting the sample into the spectrometer at the same time as argon and methyl iodide (CH_3I). Argon and methyl iodide are used as calibrants when recording PE spectra as they have sharp, intense He(I) PE bands of well known ionisation energies covering a spectral range of 6 eV [17-20]. All recorded PE spectra presented in this thesis have been calibrated using this method unless described otherwise.

Spectra were recorded at different furnace temperatures, obtained by increasing the heater voltage of the induction heating system. The internal furnace temperature was measured using a K-type (Ni-Cr/Ni-Al) thermocouple in contact with the internal wall of the susceptor. This procedure could be used to measure internal furnace wall temperatures up to 1300 °C. Above 1300 °C, in the range 1300-2000 °C, an optical pyrometer was used to determine the external furnace wall temperature, by viewing the outside of the furnace through a window on the ionisation chamber (shown as *K* in Figure 3.9 in section 3.3 of Chapter 3). Measured temperatures values, using the thermocouple and pyrometer, are given in Table 5.1 with extrapolated values above 1300 °C indicated with a *.

Anode Voltage (mV)	Thermo Voltage (mV)	ThermocoupleTemp (˚C)	Pyrometer Temp (˚C)
1.4	19.0	750	700
1.6	21.7	835	760
1.8	24.9	958	870
2.0	31.3	1121	990
2.4	34.6	1197	1060
2.4	38.8	1304	1130
2.6	-	1424*	1250
2.8	-	1481*	1300
3.0	-	1550*	1360

Table 5.1: *Conversion of anode voltages from the induction heating system to temperatures made using thermo-voltage values calibrated for a K-type (Ni-Cr/Ni-Al) thermocouple.*

By separately plotting the measured temperatures from both the thermocouple and optical pyrometer as a function of the applied heater voltage, the thermocouple

temperatures could be extrapolated to higher values (i.e. > 1300 °C) and the optical pyrometer values could be extrapolated to lower values (i.e. < 700 °C). The experimental temperatures quoted in this work were the thermocouple measurements up to 1300 °C and the extrapolated thermocouple values up to 2000 °C (i.e. the internal wall temperatures of the furnace, which were compared with the temperatures measured with the pyrometer above 1300°C to check that the values were reasonable; at each heater voltage the pyrometer temperature (outer wall temperature) was always lower than the thermocouple temperature (inner wall temperature) over the temperature range that both measurements could be made, approximately 750-1300 °C).

5.2 Computational Details

Geometry optimisation and harmonic frequency calculations were carried out for CF_3CHF_2 and $CF_3CHF_2^+$ using the Gaussian03 suite of programs [21], employing the density functional theory (DFT) method with the B3LYP functional and the MP2 method. Single energy calculations for improved relative electronic energies were performed at the RCCSD(T) level using the MOLPRO programs [22]. Various standard basis sets were used, and extrapolation of the computed first adiabatic and vertical ionisation energies to the complete basis set (CBS) limit was carried out using the $1/X^3$ formula [22]. In addition, higher vertical ionisation energies have been computed at the Hartree-Fock, negatives of computed orbital energies of the neutral molecule; Koopmans' Theorem values, (see section 4.1.4 of Chapter 4) time-dependent density functional theory (computed TD-DFT excitation energies of the cation using the B3LYP functional plus the first VIE) and equations-of-motion coupled-cluster single and double excitations (IP-EOM-CCSD employing the ACES2 programs [23]) levels, using different standard basis sets. Zero-point energy (ZPE) corrections were made to computed AIE values (to give AIE_0 values) employing unscaled computed MP2 harmonic vibrational frequencies. The enthalpy of formation ($\Delta H_{f,298K}^{Ø}$) of CF_3CHF_2 was computed by considering three different reactions:

$$CF_3CHF_2 + CH_4 + CHF_3 \rightarrow C_2H_6 + 2CF_4 \quad (5.1)$$

$$CF_3CHF_2 + 5H_2 \rightarrow C_2H_6 + 5HF \quad (5.2)$$

$$CF_3CHF_2 + 6H_2 \rightarrow 2CH_4 + 5HF \quad (5.3)$$

Reaction (5.1) is isodesmic, and hence it should be the least demanding in terms of theory and yield the most reliable results. However, reactions (5.2) and (5.3) were also considered in order to give some estimates of the computational uncertainties associated with the level of calculation employed. The enthalpy changes of these reactions were computed at the RCCSD(T)/cc-pVTZ//MP2/6-31++G** and RCCSD(T)/cc-pVQZ//MP2/6-31++G** levels (described in section 4.2 of Chapter 4; see also equation 4.38 of Chapter 4 for a description of the notation used when describing basis sets) and extrapolated to the CBS limit using the $1/X^3$ formula. $\Delta H_{f,298K}^{Ø}(CF_3CHF_2)$ was then evaluated using best $\Delta H_{f,298K}^{Ø}$ values (i.e. the most reliable values and/or the values with the smallest uncertainties) available for other species involved in each of these reactions. The $\Delta H_{f,298K}^{Ø}$ values of H_2, HF, CH_4, CHF_3, CF_4 and C_2H_6 used are 0.0, -(65.32 ± 0.17) [24], (-17.56 ± 0.10) [25], (-166.18 ± 0.05) [26], (-223.0 ± 0.3) [25]) and (-20.03 ± 0.05) [26] kcal.mol^{-1}, respectively. $\Delta H_{f,298K}^{Ø}(CF_3CHF)$ was also computed by considering the following reaction,

$$CF_3CHF + CH_4 + CHF_3 \rightarrow C_2H_6 + CF_4 + CF_3 \qquad (5.4)$$

To evaluate $\Delta H_{f,298K}^{Ø}(CF_3CHF)$ from this reaction, $\Delta H_{f,298K}^{Ø}$ value of (-111.7 ± 0.5) kcal.mol^{-1} [26] was used for CF_3 as well as the appropriate values listed above.

5.3 Results and Discussion

5.3.1 The Photoelectron Spectrum of CF_3CHF_2

The PE spectrum of CF_3CHF_2, shown in Figure 5.1, shows six PE bands. The VIEs of these bands, as well as the measured onset of the first band, the AIE, were averaged over ten expanded spectra. The VIEs measured for each band observed in the PE spectrum are marked in Figure 5.1 as *A* - *F*.

Comparison between the PE and the TPE spectra (red) [13], seen in Figure 5.2, shows that the band onset and VIE for the first band measured by the two techniques are essentially the same (PE values; onset (12.71 ± 0.05) eV, VIE (13.76 ± 0.02) eV; TPE values (12.70 ± 0.05) eV; VIE (13.76 ± 0.05) eV). However, major differences are observed at higher ionisation energies. The TPE spectrum appears less well resolved than the PE spectrum particularly above 15.0 eV.

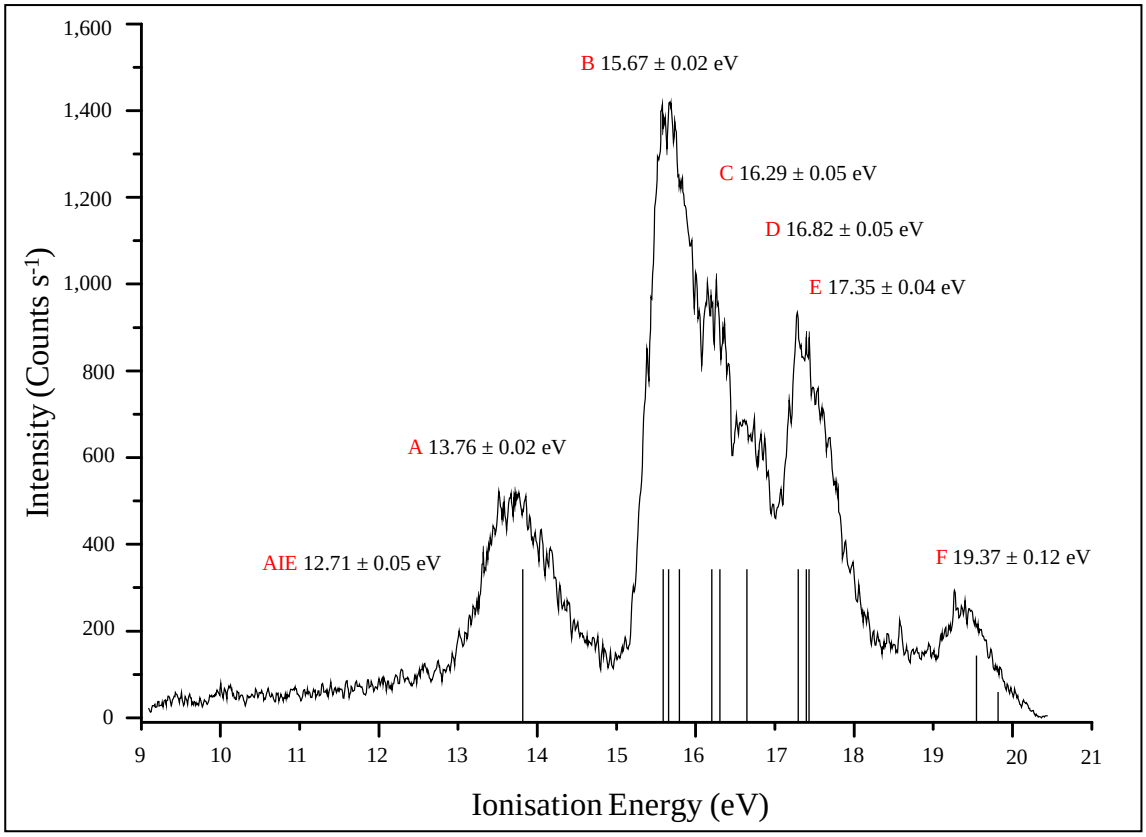

Figure 5.1: *Photoelectron spectrum of CF_3CHF_2 recorded with HeI (21.22 eV) radiation. The gas sample was admitted from a lecture bottle at room temperature. The vertical lines on this diagram are vertical ionisation energies computed with EOM-CCSD/cc-pVTZ calculations.*

In the PE spectrum, the first band is quite well separated from the second band but in the TPE spectrum the high energy side of the first band is more intense and has a larger band overlap with the second band. Also, in the PE spectrum the second band maximum is measured as (15.67 ± 0.02) eV whereas in the TPE spectrum it is measured as (16.37 ± 0.05) eV. It appears that the second band maximum in the TPE spectrum, at (16.37 ± 0.05) eV, correlates best with the third band in the PE spectrum at (16.29 ± 0.05) eV, and the third band in the TPE spectrum, at (17.53 ± 0.05) eV, correlates best with the fifth band in the PE spectrum at (17.35 ± 0.04) eV. The band envelopes seen in the PE spectra are determined by the Franck-Condon factors for direct ionisation between the neutral ground state and the relevant cationic states. In comparison, the TPE band envelopes have contributions both from direct ionisation, as in the PE spectra, and indirect ionisation (autoionisation) from highly excited neutral states which lie above an ionisation threshold.

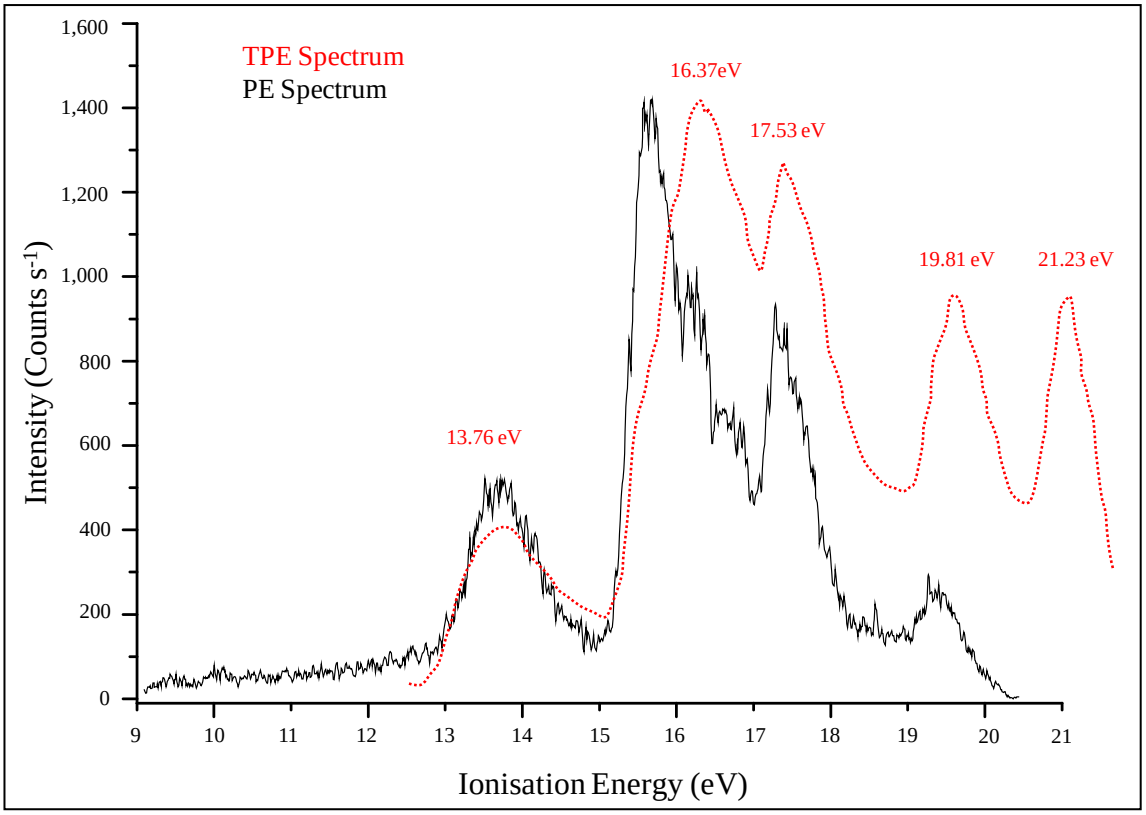

Figure 5.2: *Comparison of the PE spectrum obtained in this work with the TPE spectrum taken from reference [13].*

These excited states are Rydberg states which are members of a series which converge to higher ionisation thresholds, (briefly described in section 2.1 of Chapter 2). The different band envelopes observed in the two types of spectra, notably on the high ionisation energy side of the first band and for bands above 15.0 eV in the TPE spectrum, the TPE spectrum appears to be less well resolved than the PE spectrum as can be seen in Figure 5.2. Relative band intensities will also be different between TPE spectra, which will depend on photoionisation cross-sections close to threshold, and the PE spectra, which depend on photoionisation cross-sections typically 4-5 eV above threshold.

5.3.2 Results of Electronic Structure Calculations

Geometry optimisation calculations carried out at the B3LYP/6-31++G**, MP2/6-31++G** and MP2/6-311++G(2d,2p) levels gave C_S structures for both the $\tilde{X}^1A'$ state of the neutral CF_3CHF_2 molecule and the $\tilde{X}^2A'$ state for the cation which are in agreement with results of previous studies [13]. The computed geometry change upon ionisation is mainly in the C-C bond length, which increases from 1.5415, 1.5291 and

1.5250 Å in the neutral to 2.1085, 2.0103 and 2.0167 Å in the cation at the three levels of calculation, respectively. These bond lengths compare favourably with values obtained for the neutral and cation of 1.5187 and 1.9756 Å at the MP2(full)/6-31G(d) level in reference [13]. The first adiabatic (AIE) and vertical (VIE) ionisation energies have been computed at different levels of calculations and are given in Table 5.2.

Extrapolation to the CBS limit has been carried out using four different sets of computed data (E_{CBS1} to E_{CBS4} values in Table 5.2), and the best estimated values were obtained via four different routes (E_{best1} to E_{best4} values). The final, best, computed AIE and VIE values were estimated by taking the average of the four sets of E_{best} values. Including corrections for zero-point energies (ΔZPE, using unscaled computed harmonic vibrational frequencies obtained at the MP2/6-31++G** level of calculation) of the two states involved, the best computed AIE_0 value is (12.26 ± 0.02) eV. This value is in good agreement with computed G2 and G3 values of 12.25 and 12.26 eV [13, 14], but lower than the band onset of (12.71 ± 0.05) eV measured in the PE spectrum. Also, the best estimated VIE value of (14.051 ± 0.059) eV is larger than the experimental band maximum of the first band in the PE and threshold PE spectra of (13.76 ± 0.02) and (13.76 ± 0.05) eV [13] by 0.29 eV. In references [13] and [14], the MP2(full)/6-31G(d) structures for the neutral and cation were employed for energy calculations using the G2 and G3 multilevel methods [27, 28]. MP2/6-31++G** structures were used for the neutral and cation in RCCSD(T) calculations using a number of increasingly large basis sets. The computed AIE and VIE values were then extrapolated to the CBS limit, as seen in Table 5.2.

The highest level of correlation method used in the G2 and G3 methods is the QCISD(T) method (with the 6-31G* basis set), and the largest basis set used (at the MP2 level) is of the 6-311G(2df,2p) quality (denoted as the G3 large basis set). The aim of G2 and G3 is to achieve the accuracy of the QCISD(T)/6-311++G(2df,2p) level [27, 28]. It has been noted in a recent paper on the G4 method that, an alternate and more accurate approach to the G1, G2 and G3 methods for the calculation of thermochemical data is based on CCSD(T) calculations using very large correlation consistent basis sets extrapolated to the complete basis set limit [29]. This approach is employed in the present study. In this connection, the CBS results based on RCCSD(T) calculations given in Table 5.2 should be the most reliable.

Methods	AIE	VIE	Nbasis[a]
B3LYP/6-31++G**	12.091	13.303	139
MP2/6-31++G**	12.324	13.594	139
MP2/6-311++G(2d,2p)	12.187	13.533	199
RCCSD/cc-pVTZ//MP2/6-31++G**	12.118	14.002	224
RCCSD/aug-cc-pVTZ//MP2/6-31++G**	12.283	14.145	345
RCCSD/cc-pVQZ//MP2/6-31++G**	12.267	14.179	415
RCCSD/aug-cc-pVQZ//MP2/6-31++G**	12.322	14.226	606
RCCSD(T)/cc-pVTZ//MP2/6-31++G**	12.033	13.720	224
RCCSD(T)/aug-cc-pVTZ//MP2/6-31++G**	12.226	13.881	345
RCCSD(T)/cc-pVQZ//MP2/6-31++G**	12.201	13.905	415
RCCSD(T)/aug-cc-pVQZ//MP2/6-31++G**	12.266	14.013	606
$E_{best1} = E_{CBS1}\{1/X^3$:RCCSD(T)/cc-pVQZ; cc-pVTZ$\}$	12.324	14.040	
$E_{CBS2}\{1/X^3$:RCCSD/cc-pVQZ; cc-pVTZ$\}$	12.375	14.309	
$\Delta E_{(T)}$ {RCCSD(T); RCCSD/cc-pVQZ}	-0.066	-0.275	
$E_{best2} = E_{CBS2} + \Delta E_{(T)}$	12.309	14.034	
$E_{CBS3}\{1/X^3$:RCCSD/aug-ccpVQZ; aug-ccpVTZ$\}$	12.349	14.284	
$\Delta E_{(T)}$ {RCCSD(T); RCCSD/aug-cc-pVTZ}	-0.058	-0.264	
$E_{best3} = E_{CBS3} + \Delta E_{(T)}$	12.292	14.021	
$E_{best4}=E_{CBS}\{1/X^3$:RCCSD(T)/aug-cc-pVQZ; aug-cc-pVTZ$\}$	12.295	14.11	
Best estimate AIE_e, VIE (E_{best} average)	12.305 ± 0.019	14.051 ± 0.059	
Δ(ZPE): MP2/6-311++G(2d, 2p) frequencies	-0.0452		
Best estimated AIE_0 (included ZPE correction)	12.26 ± 0.02		
G2 [13]	12.25	13.79	
G3 [14]	12.26		
TPES [13]	12.70 ± 0.05	13.76 ± 0.05	
VUV Absorption spectrum [14][b]	12.25 ± 0.10		
Photoelectron spectrum, this work	12.71 ± 0.05	13.76 ± 0.02	

Table 5.2: *Computed AIEs and VIEs (eV) of the first ionisation of CF_3CHF_2 obtained at different levels of calculations.*

[a] Total number of contracted functions used in the calculation.

[b] The photoionisation mass-spectrometry study [14] did not detect any $CF_3CHF_2^+$ and hence no photoionisation efficiency (PIE) curve for CF_3CHF_2 was reported. The IE reported was derived from analysis of vacuum ultraviolet absorption spectrum. See original work [14].

It is clear therefore that the recommended first adiabatic ionisation energy of CF_3CHF_2 is ~0.5 eV below the measured band onset in both the PE and TPE spectra. This must arise from lack of intensity in the low energy region of the first band of this molecule because of a large geometry change on ionisation (~0.5 Å increase in the C-C bond length) and consequent poor Franck-Condon factors in the threshold region. This is supported by Franck-Condon factor calculations performed for the first photoelectron band CF_3CHF_2, by treating CF_3–CHF_2 as diatomic, using the vibrational frequencies for the C-C stretching mode in the neutral of 1484 cm^{-1} and in the cation of 1128 cm^{-1}

computed at the MP2/6-31++G(2d,2p) level and the computed C-C bond length change on ionisation. In order to understand the discrepancy between theory and experiment in the VIE position of the first PE band of CF_3CHF_2 mentioned above, notably the apparent loss of intensity in the experimental PE band at the computed VIE region of *ca.* 14.05 eV, the enthalpies of ten dissociation channels of the $CF_3CHF_2^+$ were considered to see whether any of these dissociation channels could affect the shape of the first PE band. To do this, some calculations were carried out to obtain the $\Delta H_{f,298K}^{Ø}$ and/or AIE_0 values of CF_3CHF_2, CF_3CHF and CHF_2 and/or their cations, because some of these values are either not available or cannot be considered as very reliable. The results of the relevant *ab initio* calculations are summarised in Tables 5.3 and 5.4.

$\Delta H_{f,298K}^{Ø}$	CF_3CHF_2	$CF_3CHF_2^+$	CF_3CHF	CF_3CHF^+
RCCSD(T)/cc-pVTZ//MP2/6-31++G**	-264.5		-201	
RCCSD(T)/cc-pVQZ//MP2/6-31++G**	-265.5		-201.2	
CBS(1/X^3:cc-pVTZ;cc-pVQZ)	-266.3 (20)		-201.3 (17)	
Best $\Delta H_{f,298K}^{Ø}$ [b]		**16.4 (22)**		**19.4 (18)**
AIE				
RCCSD(T)/cc-pVTZ//MP2/6-31++G**	12.033			
RCCSD(T)/cc-pVQZ//MP2/6-31++G**	12.201			
CBS{1/X^3:RCCSD(T)/cc-pVTZ;cc-pVQZ}	12.324			
Best AIE_0 [c]	**12.26 (1)**			
RCCSD(T)/aug-cc-pVDZ//MP2/6-31++G**			9.580[d]	
RCCSD(T)/aug-cc-pVTZ//MP2/6-31++G**			9.571[d]	
CBS{1/X^3:RCCSD(T)/aug-cc-pVDZ;aug-cc-pVTZ}			9.568[d]	
Best AIE_0			**9.571 (4)[d]**	

Table 5.3: *Computed enthalpies of formation ($\Delta H_{f,298K}^{Ø}$ in kcal.mol^{-1}) of CF_3CHF_2 and CF_3CHF, and their cations, and their computed AIE_0 (eV) obtained at different levels of calculation.*

[a] The $\Delta H_{f,298K}^{Ø}$ of CF_3CHF_2 and CF_3CHF were evaluated by considering the isodesmic reactions (5.1) and (5.4), respectively. The $\Delta H_{f,298K}^{Ø}$ of their cations were evaluated by $\Delta H_{f,298K}^{Ø}$(neutral) + AIE_0 (see footnote b).

[b] The CBS value of $\Delta H_{f,298K}^{Ø}$ of the neutral plus the best AIE_0 value.

[c] For CF_3CHF_2, see Table 5.2 for the evaluation of the best AIE_0 value, which is the average of four best estimated values; see text.

[d] E. P. F. Lee private communication; unpublished results.

The best computed $\Delta H_{f,298K}^{Ø}$ values of CF_3CHF_2 and CF_3CFH are (-266.3 ± 2.0) and –(201.3 ± 1.7) kcal.mol^{-1} (by considering reactions (5.1) and (5.4), both isodesmic reactions; see Table 5.3), respectively. It should be noted that the quoted uncertainties are the maximum uncertainties (considering values used in the evaluation, which give the largest uncertainties, and/or the largest uncertainties of the values used), and they are mainly from uncertainties in available $\Delta H_{f,298K}^{Ø}$ values of other species involved in the reactions considered. The computed uncertainties in the reaction enthalpies are only

(± 0.78) and (± 0.17) kcal.mol^{-1} (the difference between the CBS and RCCSD(T)/cc-pVQZ values), respectively. Employing these $\Delta H_{f,298K}^{Ø}$ values, and the best computed AIE_0 values of (12.26 ± 0.02) and (9.571 ± 0.004) eV, for CF_3CHF_2 and CF_3CHF (Table 5.3), the best computed $\Delta H_{f,298K}^{Ø}$ values of their cations are estimated to be (16.4 ± 2.2) and (19.4 ± 1.8) kcal.mol^{-1}, respectively. Also, for CHF_2 employing the best computed AIE_0 of (8.70 ± 0.01) eV obtained here, shown in Table 5.4 below, and the best available computed $\Delta H_{f,298K}^{Ø}$ value of -57.9 kcal.mol^{-1} from reference [30], $\Delta H_{f,298K}^{Ø}(CHF_2^+)$ is estimated to be (142.7 ± 0.2) kcal.mol^{-1}.

Method	AIE	VIE	Nbasis[a]
B3LYP/6-31++G**	8.96		
MP2/6-31++G**	8.6		
RCCSD/aug-cc-pVQZ//MP2/6-31++G**	8.661	10.391	286
RCCSD/aug-cc-pV5Z//MP2/6-31++G**	8.667	10.448	461
RCCSD(T)/aug-cc-pVQZ//MP2/6-31++G**	8.637	10.251	286
RCCSD(T)/aug-cc-pV5Z//MP2/6-31++G**	8.644	10.267	461
CBS{1/X^3:RCCSD(T)/aug-cc-pVQZ;aug-cc-pV5Z}	8.65 ± 0.01	10.28 ± 0.01	
ΔZPE (MP2)	0.053		
Best AIE_0	8.70 ± 0.02		
UMP2/6-31G** (AIE_0) ref.[46]	8.4		
REMPI (AIE_0) ref.[46]	~8.5		

Table 5.4: *Computed first AIEs and VIEs (eV) of the CHF_2^+ $\tilde{X}^1A_1$ + e ← CHF_2 $\tilde{X}^2A'$ ionisation obtained at different levels of calculations.*

[a] Total number of contracted functions used in the calculation.

The quoted uncertainty of (± 0.2) kcal.mol^{-1} is based on the uncertainty in the best computed AIE_0 value (the difference between the CBS and RCCSD(T)/aug-cc-pV5Z value). However, comparing the best $\Delta H_{f,298K}^{Ø}(CHF_2^+)$ value obtained in this work with previously available recommended values, a more realistic maximum uncertainty is estimated to be 1.5 kcal.mol^{-1}. Available $\Delta H_{f,298K}^{Ø}$ values of the species involved in the ten dissociation channels of the $CF_3CHF_2^+$ cation considered are compiled in Table 5.5.

The most reliable $\Delta H_{f,298K}^{Ø}$ values available for these species were used to evaluate the enthalpies of reaction for the ten dissociation reactions of $CF_3CHF_2^+$ considered, which are tabulated in Table 5.6. It can be seen from Table 5.6 that, only the $CF_3CHF_2^+ \rightarrow CF_2CF_2^+ + HF$ dissociation channel (labelled as reaction 7) is exothermic. However, the barrier to the transition state on the reaction coordinate for this channel is expected to be

high, because this reaction is expected to proceed via breaking of both CF and CH bonds and involves a large geometry change.

Species	$\Delta H_{f,298K}^{Ø}$	Method	Reference	IE
CF_3CHF_2	-266.3(20)	CBS reaction 5.1[a] (isodesmic)	Present work	
$CF_3CHF_2^+$	16.4(22)	Calc Present Work AIE_0(CBS)	Best $\Delta H_{f,298K}^{Ø}(CF_3CHF_2)$ + IE	12.26(1) eV
CF_3	-111.7(5)	Thermodynamic Network	Ref.[26]	
CF_3^+	97.6(22)	Average of recent publ. values	Refs.[26,41,42,47,49,50]	
CHF_2	-57.884	Calc CBS+CV+rel+SO	Ref.[30]	
CHF_2^+	142.7(2)	Calc Present Work[b] AIE_0(CBS)	Best $\Delta H_{f,298K}^{Ø}(CHF_2)$ + IE	8.70(1) eV
CHF_3	-166.18(50)	Thermodynamic Network	Ref.[26]	
CHF_3^+	153.2(12)	Average of recent publ. values	Refs.[37,38,51,52]	
CF_2	-45.7(3)	Thermodynamic Network	Ref.[26]	
CF_2^+	216.3(8)	AIE from TPES; ref.[35]	Best $\Delta H_{f,298K}^{Ø}(CF_2)$ + IE	11.362(5) eV
CF_4	-223.1(1)	Thermodynamic Network	Ref.[226]	
CF_4^+	116.4(20)	G3 MP2	Ref.[30]	
CHF	36.3(6)	Average of recent values	Refs.[30,53]	
CHF^+	268.3(18)	IE (REMPI) ref.[47]	Ave. $\Delta H_{f,298K}^{Ø}(CHF)$ + IE	10.06(5) eV
CF_2CF_2	-160.6(8)	Average of recent values	Refs.[26,30,49]	
$CF_2CF_2^+$	73.2(13)	AIE from PES; ref.[32]	Ave. $\Delta H_{f,298K}^{Ø}(CF_2CF_2)$ + IE	
HF	-65.2(2)	Average of recent values	Refs.[24,54]	
HF^+	304.8(2)	IE from PES; refs.[31,48]	Ave. $\Delta H_{f,298K}^{Ø}(HF)$ + IE	16.044(3) eV
F	18.970(72)	Review 1984	Ref.[24]	
F^+	420.75	IE from ref.[38]	$\Delta H_{f,298K}^{Ø}(\Phi)$ + IE	17.42282 eV
CF_3CHF	-201.3(17)	Calc CBS reaction 5.4[c]	Present work	
CF_3CHF^+	19.4(18)	Calc AIE_0(CBS)[d]	$\Delta H_{f,298K}^{Ø}(X\Phi_3XH\Phi)$ + IE	9.571(4) eV

Table 5.5: *Enthalpies of formation, $\Delta H_{f,298K}^{Ø}$ (kcal.mol^{-1}) and ionisation energy (IE in eV) of species used in this work, related to the dissociation of CF_3CHF_2 and $CF_3CHF_2^+$.*

[a] The value given is with reaction (5.1). With reactions (5.2) and (5.3), the corresponding values obtained are -264.0 and -264.5 kcal.mol^{-1} respectively; the electron convention we are using is the zero electron energy convention.

[b] See Table 5.4.

[c] See Table 5.3.

[d] See footnote d of Table 5.3.

In addition, the fact that no $CF_2CF_2^+$ was detected in the TPEPICO study of CF_3CHF_2 [13] also suggests a fairly high reaction barrier for this dissociation channel. This is also in reasonably good agreement with the experimental results obtained from the TPEPICO [13] study, which show that in the region of the ground electronic state of $CF_3CHF_2^+$, the first fragment ion observed is CHF_2^+ with an appearance energy of (12.75 ± 0.05) eV. Because the neutral molecule has a significantly shorter computed C-

C equilibrium bond length than the cation as mentioned above, vertical ionisation at the computed VIE of 14.03 eV, will access a region of the repulsive wall of the cation, which is *ca.* 1.1 eV above the CF_3 + CHF_2^+ dissociation limit (at a computed IE of (12.89 ± 0.20) eV). Consequently, there is a loss of intensity in the PE band at the computed VIE region of *ca.* 14.0 eV due to this dissociation channel. The above considerations provide a plausible explanation for the discrepancy between theory and experiment in the VIE position (or band maximum) of the first band in the PE spectrum of CF_3CHF_2, involving loss of intensity in the high IE region of this PE band. Another dissociation channel of $CF_3CHF_2^+$, to give CF_3^+ + CHF_2 (reaction 1 in Table 5.6), was observed in reference [13] at an appearance energy of (13.29 ± 0.06) eV i.e. (0.54 ± 0.11) eV above CHF_2^+ + CF_3. This is consistent with the observed difference in computed reaction enthalpies for these two reactions of 0.38 eV shown in Table 5.6 below.

Reaction	Dissociation products	ΔH_{298K}^{RX} (kcal.mol^{-1})	ΔH_{298K}^{RX} (eV)
1	CF_3^+ + CHF_2	23.3 (59)	1.01 (26)
2	CF_3 + CHF_2^+	14.6 (42)	0.63 (18)
3	CHF_3^+ + CF_2	90.9 (37)	3.94 (16)
4	CHF_3 + CF_2^+	33.7 (35)	1.46 (15)
5	CF_4^+ + CHF	136.3 (48)	5.91 (21)
6	CF_4 + CHF^+	28.6 (41)	1.24 (18)
7	$CF_2CF_2^+$ + HF	-8.4 (37)	-0.36 (16)
8	CF_2CF_2 + HF^+	127.8 (32)	5.54 (14)
9	CF_3CHF + F^+	203.1 (40)	8.81 (17)
10	CF_3CHF^+ + F	22.0 (41)	0.95 (18)

Table 5.6: *Computed reaction enthalpies of various dissociation channels of $CF_3CHF_2^+$ obtained by using the most reliable $\Delta H_{f,298}^{\emptyset}$ values available for the species involved (see Table 5.5).*

Computed VIE values to low-lying cationic states of CF_3CHF_2 obtained at different levels of theory are given in Table 5.7. It is clear that the computed VIE values obtained at the Hartree-Fock (HF) level via Koopmans' Theorem are too high. Computed VIE values obtained at the B3LYP level (computed time-dependent (TD-B3LYP) excitation energies of the cation plus computed or experimental first VIE value) and at the IP-EOM-CCSD level employing different basis sets are compared in Figure 5.3. It can be seen that basis set effects on the EOM-CCSD VIE values are small, at least with the three basis sets used. Also, the B3LYP VIE values are quite close to the EOM-CCSD values, though the former values are more spread out, and comparison of Figures 5.1 and 5.3 shows that their agreement with experiment is not as good as the EOM-CCSD

VIE values. The computed EOM-CCSD/cc-pVTZ VIEs have been plotted on Figure 5.1. It can be seen from Figure 5.1 that the agreement between the EOM-CCSD VIE values and the experimental PE spectrum is very good. Particularly, the groupings of computed VIEs agree very well with the experimental band groupings and relative intensities.

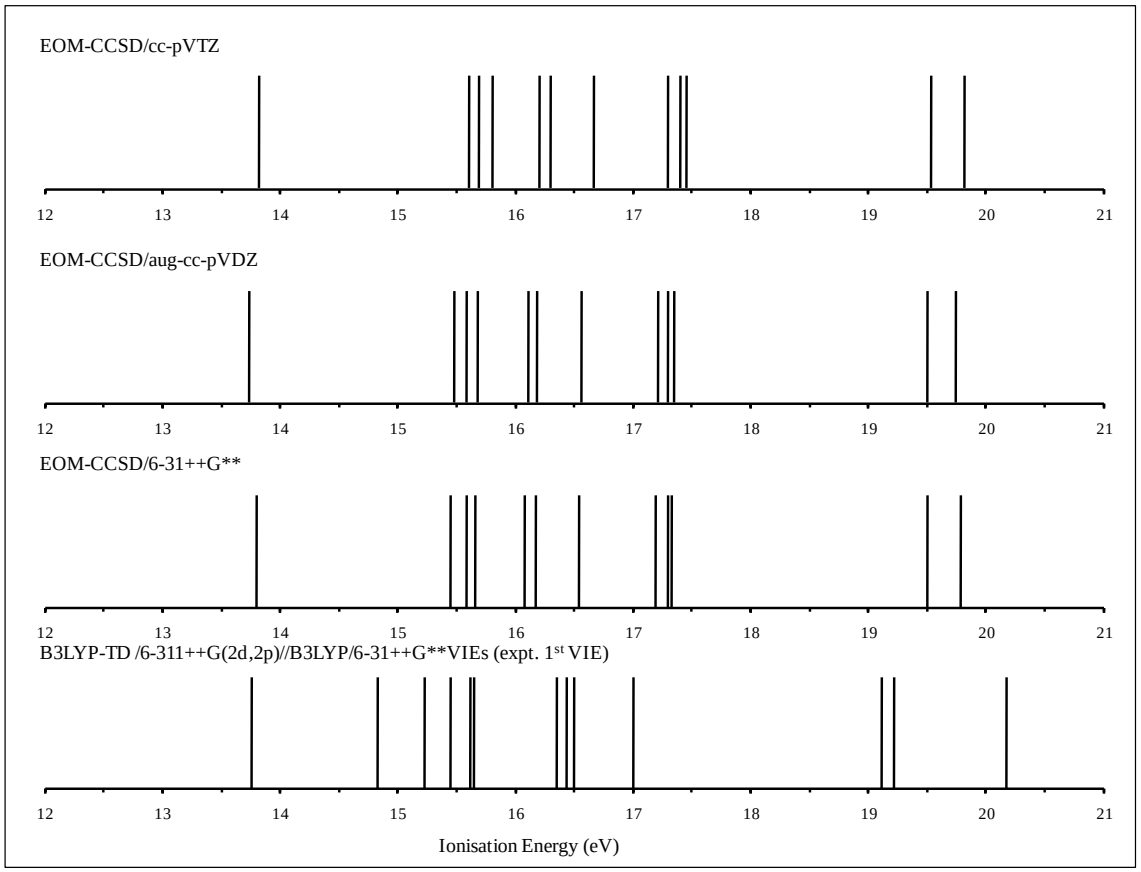

Figure 5.3: *Comparison of computed VIEs of CF_3CHF_2 obtained with the IP-EOM-CCSD method using different basis sets and with B3LYP calculations (lowest panel).*

The comparison shown in Figure 5.1 of the experimental bands and computed VIEs, obtained at the IP-EOM-CCSD/cc-pVTZ level (see Table 5.7, column 9) allows the ionic states associated with each band to be established. The first band corresponds to ionisation to the $\tilde{X}^2A'$ ionic state obtained from the $(18a')^{-1}$ ionisation, the second band corresponds to ionisation to the $^2A'$, $^2A''$ and $^2A''$ ionic states obtained from the $(17a')^{-1}$,$(11a'')^{-1}$ and $(10a'')^{-1}$ ionisations, and the third band corresponds to ionisation to the $^2A''$ and $^2A'$ ionic states obtained from the $(9a'')^{-1}$ and $(16a')^{-1}$ ionisations. The electronic structure and high-lying occupied molecular orbitals of CF_3CHF_2 have been presented and discussed in reference [13], and hence this will not be repeated here.

	HF-KT		B3LYP-TD		IP-EOM-CCSD[c]			
$(m.o.)^{-1}$	VIE	E_{ex}	VIE	VIE	$(m.o.)^{-1}$	6-31++G**	aug-cc-VDZ	VTZ
18a′	15.536	0	14.051[a]	13.76[b]	18a′	13.79	13.73	13.83
17a′	17.591	1.688	15.739	15.448	11a″	15.45	15.48	15.6
11a″	18.144	1.081	15.132	14.84	17a′	15.58	15.58	15.67
10a″	18.408	1.46	15.511	15.22	10a″	15.64	15.67	15.8
9a″	18.775	2.591	16.642	16.351	9a″	16.07	16.1	16.2
16a′	18.806	1.848	15.899	15.607	16a′	16.17	16.19	16.3
8a″	19.256	1.88	15.931	15.64	8a″	16.53	16.56	16.65
15a′	19.933	2.673	16.724	16.433	15a′	17.19	17.2	17.29
7a″	19.976	2.743	16.794	16.503	7a″	17.29	17.31	17.39
14a′	20.026	3.238	17.289	16.997	14a′	17.33	17.36	17.44
6a″	21.656	5.356	19.407	19.116	6a″	19.51	19.51	19.54
13a′	22.109	5.459	19.51	19.219	13a′	19.78	19.76	19.8
5a″	23.396	6.405	20.45	20.165	12a′	21.02	21.01	21.03
					5a″	21.07	21.06	21.08

Table 5.7: *Computed VIEs (eV) to low-lying cationic states of $CF_3CHF_2^+$, obtained from Hartree-Fock (by Koopmans' Theorem; HF-KT) and time-dependent density functional theory (B3LYP-TD; computed excitation energies (E_{ex}) of low-lying cationic states plus the first VIE) calculations employing the 6-311++G(2d,2p) basis set, and obtained from IP-EOM-CCSD calculations using different basis sets.*

[a] Computed best First VIE from Table 5.2.

[b] Experimental first VIE from the He(I) photoelectron spectrum.

[c] AVDZ and VTZ are the aug-cc-pVDZ and cc-pVTZ basis sets. The total numbers of contracted basis functions of the three basis sets used in the IP-EOM-CCSD calculations are 139, 170 and 244, respectively.

5.3.3 Thermal Decomposition Studies of CF_3CHF_2

Spectra were recorded as a function of furnace temperature up to 1600 °C where almost complete decomposition of CF_3CHF_2 occurred. Two typical spectra, recorded at furnace temperatures of 1000 and 1200 °C, are shown in Figure 5.4, denoted as A and B respectively. For each pyrolysis spectrum recorded, the intensity of the first PE band of CF_3CHF_2 was normalised to the intensity of the corresponding first band observed in the pyrolysed spectrum and its overall contribution was then subtracted. Subtracting off the spectral contribution of CF_3CHF_2 from the pyrolysed spectra allowed the first band of CF_3H to be observed more clearly. Then, the calibrated spectrum of CF_3H, recorded in a separate experiment, was used to remove its contribution to the pyrolysed spectrum by matching the intensity of the first PE band to the corresponding band seen in the pyrolysed spectrum. Monitoring the observed PE band intensities at different furnace temperatures allowed a plot to be made of the normalised band intensities as a function of temperature. This is shown in Figure 5.5.

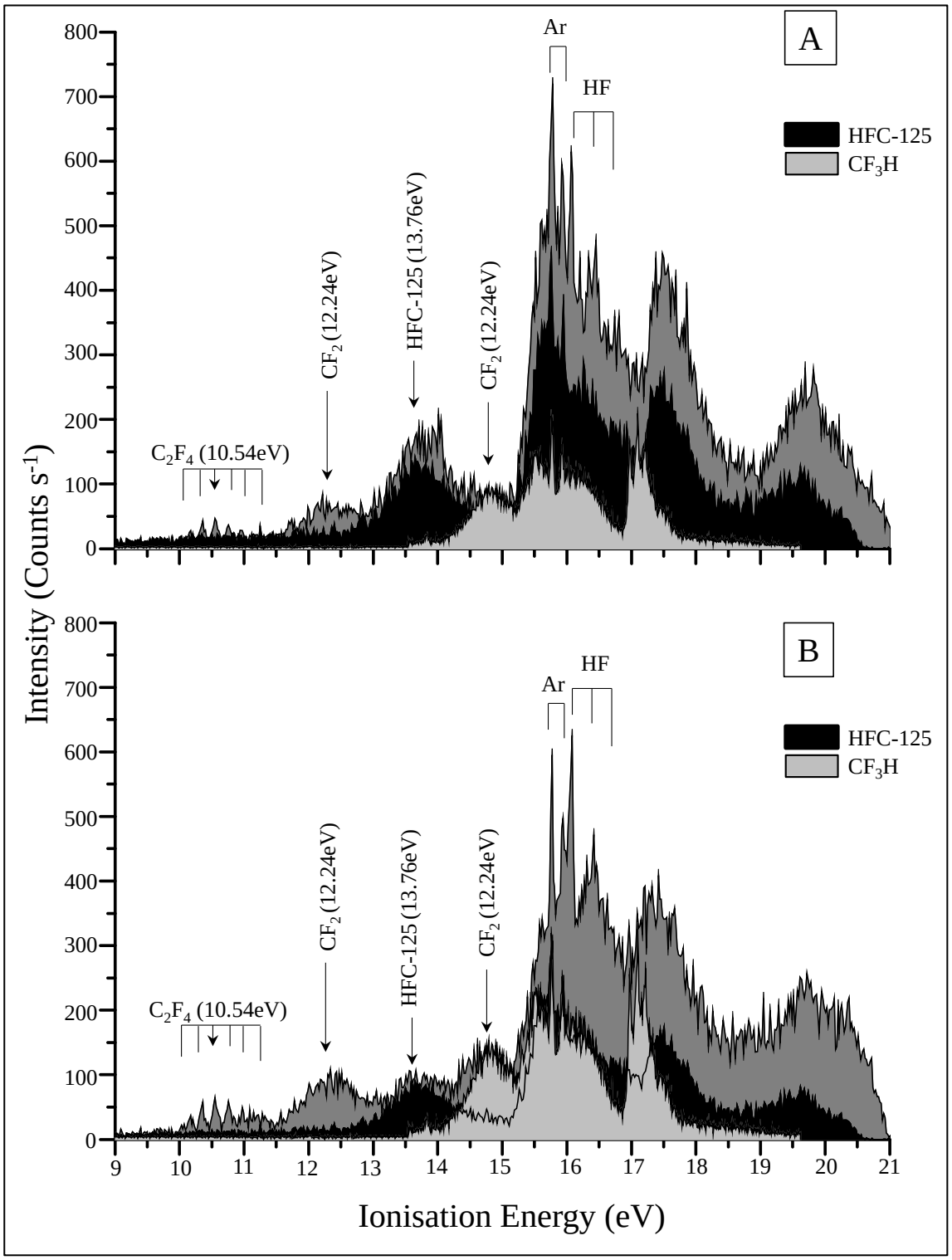

Figure 5.4: *PE spectra recorded from the thermal decomposition of CF_3CHF_2 at furnace temperatures of A. 1000 ℃ and B. 1200 ℃ respectively.*

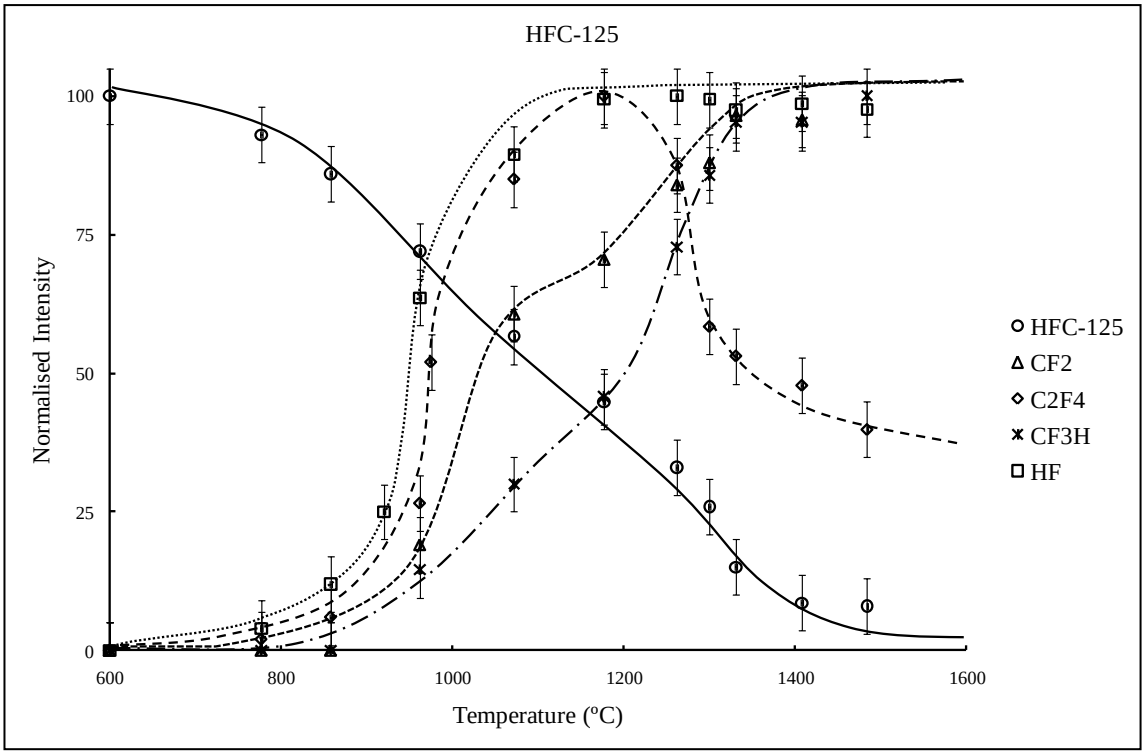

Figure 5.5: *Normalised experimental band intensities of CF_3CHF_2 and observed thermal decomposition products plotted as a function of temperature. These plots were obtained, for each molecule considered, by taking the most intense first band observed during the pyrolysis and normalising all of the other first band intensities for that molecule, measured at different stages of the pyrolysis, to that value.*

The molecules observed on pyrolysis of CF_3CHF_2, diluted in argon, are HF, C_2F_4, CF_2 and CF_3H. The first three of these molecules were the most straightforward to identify in spectra recorded on pyrolysis as the first band of HF is sharp at 16.04 eV VIE [31], C_2F_4 shows a broad structured first band between 10.0 and 11.5 eV (AIE 10.12 eV, VIE 10.54 eV [32-34]) and the first band of CF_2 is broad and is centred at 12.24 VIE [35-36]. Both the C_2F_4 and CF_2 first bands are not overlapped with the spectrum of CF_3CHF_2 or any bands produced on pyrolysis, and although the first band of HF overlaps with the second band of CF_3CHF_2, it is sharp and easy to identify. The first band of CF_3H occurs between the first and second bands of CF_3CHF_2. Separate spectra were recorded for CF_3H. The first VIE was calibrated as (14.78 ± 0.01) eV which compares well with previous VIE values of 14.77 and 14.80 eV [37-39].

It appears that at the lowest temperatures at which decomposition occurs, 700-1000 °C, HF + C_2F_4 are produced followed by decomposition of C_2F_4 to CF_2, i.e. reaction (5.5), ($\Delta H_{f,298K}^{Ø}$ = (40.5 ± 3.0) kcal.mol^{-1}), occurs followed by reaction (5.6), ($\Delta H_{f,298K}^{Ø}$ = (69.2 ± 1.4) kcal.mol^{-1}).

$$CF_3CHF_2 \rightarrow C_2F_4 + HF \quad (5.5)$$

$$C_2F_4 \rightarrow 2CF_2 \quad (5.6)$$

At higher temperatures, above 1000 °C, it appears that reaction (5.7), ($\Delta H_{f,298K}^{Ø}$ = (54.4 ± 2.8) kcal.mol^{-1}), begins to become significant, and at approximately 1200 °C C_2F_4 maximises and drops in intensity at higher temperatures whilst CF_3H continues to increase. In this region CF_2 also increases as it is produced from reaction (5.7) and from C_2F_4 decomposition (reaction (5.6)).

$$CF_3CHF_2 \rightarrow CF_2 + CF_3H \quad (5.7)$$

Use of the most reliable $\Delta H_{f,298K}^{Ø}$ values for the reactants and products in reactions (5.5-5.7), shown in Table 5.5, leads to the reaction enthalpies for reaction (5.5), (5.6) and (5.7) shown above. Reaction (5.5), involving HF elimination, is the least endothermic and is observed first at the lowest temperatures. Once C_2F_4 is produced, it appears that it can decompose via reaction (5.6). Reaction (5.7) is more endothermic than reaction (5.5) and is observed at higher temperatures. Although reaction enthalpies have been computed for reaction (5.5), (5.6) and (5.7), it should be noted that no activation energies have been calculated. These studies monitor the gas-phase products as a function of temperature in a flow system and are therefore valuable in providing information of how CF_3CHF_2 decomposes on heating (e.g. in a combustion environment). However, they provide no information on the mechanism of the decomposition reactions. For example, some decomposition of CF_3CHF_2 on the heated furnace surface or decomposition via a free radical mechanism cannot be ruled out although no evidence of free radicals such as F or CF_3 was seen in the spectra; for example the first band of F atoms is expected at 17.42 eV [40] and the first band of CF_3 is expected to be broad with an AIE of (9.05 ± 0.01) eV and a VIE of (10.86 ± 0.01) eV [41-45].

5.4 Conclusion

The pyrolysis products of flowing CF_3CHF_2 diluted with argon have been studied as a function of temperature. The results obtained have been interpreted in terms of two decomposition reactions of CF_3CHF_2, reactions (5.5) and (5.7), as well as the reaction, $C_2F_4 \rightarrow 2CF_2$.

The PE spectrum of CF_3CHF_2 has been interpreted and assigned using state-of-the-art *ab initio* calculations. Comparison with the published TPE spectrum show good agreement for the first band but the higher energy bands appear less well resolved in the TPE spectrum. This arises because autoionisation from high-lying Rydberg states, which are parts of series converging to higher ionisation thresholds, contribute to the intensity in the higher ionisation region (above 14.0 eV). The experimental first VIE is lower than the computed first VIE (by ~0.3 eV). This is rationalised in terms of dissociation of $CF_3CHF_2^+$ in the vertical transition region from the neutral. Dissociation energies of the ground state of $CF_3CHF_2^+$ to CHF_2^+ + CF_3 and to CF_3^+ + CHF_2 are calculated and the values obtained support this. The recommended first adiabatic ionisation energy of CF_3CHF_2 is ~ 0.5 eV below the measured band onset in both the PE and TPE spectra. This arises from lack of intensity in the low energy region of the first band of this molecule because of a large geometry change on ionisation and consequent poor Franck-Condon factors in the threshold region. Reliable experimental determination of this AIE will probably only be achieved by recording a high-resolution zero-electron kinetic energy (ZEKE-PFI) spectrum of this molecule, possibly by a two-colour process involving initial excitation to an excited state with an equilibrium geometry closer to that of the ion than that of the neutral ground state.

The thermal decomposition of a second, larger, HFC fire suppressant, 2-H heptafluoropropane (CF_3CHFCF_3), at low pressure, heavily diluted in argon, has also been carried out in this project and has been studied, using PES, over the temperature range 600-2000 °C using the same RF heating system as used in this study. This investigation is discussed in the following chapter.

References

[1] W.K. Chow, E.P.F. Lee, F. T. Chau and J. M. Dyke, *Architectural Science Review*, 47, 2004, 223.

[2] T. J. Wallington and O. J. Nielson, Progress in Atmospheric Chemistry, *World Scientific, Singapore*, 1995, Chapter 15.

[3] C. S. Jwo, C. C. Ting and W. R. Wang, *Measurement*, 42, 2009, 697.

[4] C. Scheutz, Y. Dote, A. M. Fredensland, H. Mosbaek and P. Kjeldsen, *Environmental Science and Technology*, 41, 2007, 713.

[5] D. O. Schafer, D. Godwin, and J. Harnisch, *Energy Journal Special Issue*, 3, 2006, 63.

[6] G. J. M Velders, D. W. Fahey, J. S. Daniel, M. McFarland and S. O. Anderson, *Proc. National Academy Sciences*, USA, 106, 2009, 10949.

[7] http://www.gulfwidesafety.com/gws/halon_news.asp
http://www.arap.org/docs/fire.html

[8] S. Papasawa, S. Tai, A. Esslinger, K. H. Illinger and J. E. Kenny, *J. Phys Chem.*, 99, 1995, 3438.

[9] Y. Chen, S. J. Paddison, and E. Tschuikow-Roux, *J. Phys. Chem.*, 98, 1994, 1100.

[10] M. Onda, K. Tsuda and T. Kimura, *J. Mol. Struct.*, 733, 2005, 1.

[11] D. C. Thompson, E. G. Robertson, I. Aleksic and D. McNaughton, *J. Mol. Spectrosc.*, 230, 2005, 133.

[12] E. Eltayeb, G. A. Guirgis, A. R. Fanning and J. R. Durig, *J. Raman Spectroscopy*, 27, 1996, 111.

[13] W. Zhou, D. P. Seccombe, R. P. Tuckett and M. K. Thomas, *Chemical Physics*, 283, 2002, 419.

[14] B. Yang, C. Q. Huang, R. Yang, L.X. Wei, J. Wang, S. S. Wang, X. B. Shan, F. Qi, Y. W. Zhang, L. S. Sheng, Z. Y. Wang, L. Q. Hao and S. K. Zhou, *Acta Physico-Chimica Sinica*, 21, 2005, 539.

[15] A. Morris, J. M. Dyke, G. D. Josland, M. P. Hastings, and P. D. Francis, *High Temp. Science*, 22, 1986, 95.

[16] D. Bulgin, J. M. Dyke, F. Goodfellow, N. Jonathan, E. P. F. Lee and A. Morris, *J. Elect. Spectrosc. Rel. Phenom.*, 12, 1977, 67.

[17] K. Kimura, S. Katsumata, Y. Achiba, T. Yamasaki and S. Iwata, Handbook of HeI Photoelectron Spectra, *Japan Scientific Press*, *Tokyo*, 1981.

[18] D. W. Turner, C. Baker, A. D. Baker and C. R. Brundle, Molecular Photoelectron Spectroscopy, *Wiley Interscience*, *London*, 1970.

[19] D. R. Lloyd, *J. Phys. E*., 3, 1970, 269.

[20] M. J. Frisch, G. W. Trucks, H. B. Schlegel, G. E. Scuseria, M. A. Robb, J. R. Cheeseman, J. A. Montgomery Jr., T. Vreven, K. N. Kudin, J. C. Burant, J. M. Millam, S. S. Iyengar, J. Tomasi, V. Barone, B. Mennucci, M. Cossi, G. Scalmani, N. Rega, G. A. Petersson, H. Nakatsuji, M. Hada, M. Ehara, K. Toyota, R. Fukuda, J. Hasegawa, M. Ishida, T. Nakajima, Y. Honda, O. Kitao, H. Nakai, M. Klene, X. Li, J. E. Knox, H. P. Hratchian, J. B. Cross, V. Bakken, C. Adamo, J. Jaramillo, R. Gomperts, K. Raghavachari, J. B. Foresman, J. V. Ortiz, Q. Cui, A. G. Baboul, S. Clifford, J. Cioslowski, B. B. Stefanov, G. Liu, A. Liashenko, P. Piskorz, I. Komaromi, R. L. Martin, D. J. Fox, T. Keith, M. A. Al-Laham, C. Y Peng, A. Nanayakkara, M. Challacombe, P. M. W. Gill, B. Johnson, W. Chen, M. W. Wong, C. Gonzalez and J. A. Pople, *Gaussian 03, Revision E.01*, *Gaussian, Inc., Wallingford CT*, 2004.

[21] H. J. Werner, P. J. Knowles, R. Lindh, F. R. Manby, M. Schütz, P. Celani, T. Korona, G. Rauhut, R. D. Amos, A. Bernhardsson, A. Berning, D. L. Cooper, M. J. O. Deegan, A. J. Dobbyn, F. Eckert, C. Hampel, G. Hetzer, A. W. Lloyd, S. J. McNicholas, W. Meyer, M. E. Mura, A. Nicklass, P. Palmieri, R. Pitzer, U. Schumann, H. Stoll, A. J. Stone, R. Tarroni and T. Thorsteinsson, *MOLPRO*, a package of *ab initio* programs, 2008.

[22] A. Halkier, T. Helgaker, W. Klopper, P. Jorgensen and A. G. Csaszar, *Chem. Phys. Letts.*, 310, 1999, 385.

[23] J. F. Stanton, J. Gauss, J. D. Watts, M. Nooijen, N. Oliphant, S. A. Perera, P. G. Szalay, W. J. Lauderdale, S. A. Kucharski, S. R. Gwaltney, S. Beck, A. Balková, D. E. Bernholdt, K. K. Baeck, P. Rozyczko, H. Sekino, C. Hober and R. J. Bartlett, Integral packages included are VMOL (J. Almlöf and P. R. Taylor); VPROPS; (P. Taylor) ABACUS; (T. Helgaker, H. J. Aa, P. Jensen, P. Jørgensen, J. Olsen and P. R. Taylor). ACES II (version 2.6.0 release 2, Jan. 2006) is a program product of the Quantum Theory Project, University of Florida.

[24] J. D. Cox, D. D. Wagman, and V. A. Medvedev, CODATA Key Values for Thermodynamics, *Hemisphere Publishing Corp*., *New York*, 1984, 1.

[25] E. P. F. Lee, J. M. Dyke, W. K. Chow, F. T. Chau and D. K. W. Mok, *Chem. Phys. Letts.*, 402, 2005, 32.

[26] A. Burcat and B. Ruscic, "Third Millennium Ideal Gas and Condensed Phase Thermochemical Database for Combustion with updates from Active Thermochemical (AcTc) Tables" ANL-05/20 and TAE 960 Technion-IIT, Aerospace Engineering, and Argonne National Laboratory, Chemistry Division, September 2005 (last update May 2008).

[27] L. A. Curtiss, K. Raghavachari, G. W. Trucks and J. A. Pople, *J. Chem. Phys.*, 94, 1991, 7221.

[28] L. A. Curtiss, K. Raghavachari, P. C. Redfern, V. Rassolov and J. A. Pople, *J. Chem. Phys.*, 109, 1998, 7764.

[29] L. A. Curtiss, P. C. Redfern and K. Raghavachari, *J. Chem. Phys.*, 126, 2007, 084108.

[30] C. W. Bauschlicher Jr and A. Ricca, *J. Phys. Chem. A.*, 104, 2000, 4581.

[31] J. Berkowitz, *Chem. Phys. Letts.*, 11, 1971, 21.

[32] S. Eden, P. Limao-Vieira, P. A. Kendall, N. J. Mason, J. Delwiche, M. J. Hubin-Franskin, T. Tanaka, M. Kitajima, H. Tanaka, H. Cho and S. V. Hoffman, *Chemical Physics*, 297, 2004, 257.

[33] R. F. Lake and H. Thompson, *Proc. Roy. Soc. A*, 315, 1970, 323.

[34] G. K. Jarvis, K. J. Boyle, C. A. Mayhew and R. P. Tuckett, *J. Phys. Chem. A*, 102, 1998, 3230.

[35] J. M. Dyke, L. Golob, N. Jonathan, A. Morris and M. Okuda, *J.C.S.Faraday II*, 70, 1974, 1828.

[36] F. Innocenti, M. Eypper, E. P. F. Lee, S. Stranges, D. K. W. Mok, F. T. Chau, G. C. King G.C. and J.M. Dyke, *Chem. Eur. J.*, 14, 2008, 11452.

[37] B. P. Pullen, T. A. Carlson, W. E. Moddeman, G. K. Schweitzer, W. E. Bull and F. A. Grimm, *J.Chem. Phys.*, 53, 1970, 768.

[38] C. R. Brundle, M. B. Robin and H. Basch, *J.Chem. Phys.*, 53, 1970, 2196.

[39] M. A. Parkes, R. Y. L. Chim, C. A. Mayhew, V. A. Mikhailov and R. P. Tuckett, *Mol. Phys.*, 104, 2006, 263.

[40] C. E. Moore, *Natl. Stand. Ref. Data Ser.*, (U.S. Natl. Bur. Stand.), 34, 1970, 1.

[41] R. L. Asher and B. Ruscic, *J. Chem. Phys.*, 106, 1997, 210.

[42] M. Horn, M. Oswald, R. Oswald and P. Botschwina, *Ber. Bunsenges Phys. Chem.*, 99, 1995, 323.

[43] G. A. Garcia, P. M. Guyon and I. Powis, *J. Phys. Chem. A*, 105, 2001, 8296.

[44] J. M. Bowman, X. Huang, L. B. Harding and S. Carter, *Mol. Phys.*, 104, 2006, 33.

[45] G. K. Jarvis and R. P. Tuckett, *Chem. Phys. Letts.*, 295, 1998, 145.

[46] D. V. Dearden, J. W. Hudgens, R. D. Johnson III, B. P. Tsai and S. A. Kafafi, *J. Phys. Chem.*, 96, 1992, 585.

[47] K. K. Irikura, J. W. Hudgens and R. D. Johnson III, *J. Chem. Phys.*, 103, 1995, 1303.

[48] T. E. H. Walker, P. M. Dehmer and J. Berkowitz, *J. Chem. Phys.*, 59, 1973, 4292.

[49] D. A. Dixon, D. Feller and G. Sandrone, *J. Phys. Chem. A.*, 103, 1999, 4744.

[50] A. Ricca, *J. Phys. Chem. A.*, 103, 1999, 1876.

[51] I. Novak, A. W. Potts, F. Quinn, G. V. Marr, B. Dobson, I. H. Hillier and J. B. West, *J. Phys. B.*, 18, 1951, 1581.

[52] S. Stokes and A. B. F. Duncan, *J.A.C.S.*, 80, 1958, 6177.

[53] Y. G. Lazarou, V. C. Papadimitriou, A. V. Prosmitis and P. Papagiannakopoulos, *J. Phys. Chem. A.*, 106, 2002, 11502.

[54] M. W. Chase, NIST-JANAF Thermochemical Tables 4th Edition, *J. Phys. Chem. Ref. Data*, 1998, Monograph 9, 1.

Chapter 6

A Study of 2-H Heptafluoropropane and its Thermal Decomposition using PES and *ab initio* Molecular Orbital Calculations

2-H heptafluoropropane (also referred to as HFP, HFC-227 or FM-200) is widely used as a fire suppressant replacing halogenated compounds such as CF_3Br (Halon 1301) and CF_2ClBr (Halon 1211) whose production has been banned under international agreements such as the Montreal Protocol because of their detrimental effect on the earth's ozone layer. However, the environmental effects of halon alternatives have not been fully established. For example, hydrofluorocarbons (HFCs) such as HFC-227 are expected to have long lifetimes in the atmosphere because of their slow reactions with key free radicals such as OH and they may have significant global warming potentials (GWPs). It is also very important to investigate the thermal behaviour of halon alternatives, particularly investigating what products are formed on pyrolysis, if they are to be used successfully as fire suppressants.

As a first step towards establishing how CF_3CHFCF_3 suppresses and extinguishes a flame, its thermal decomposition was studied in this work using photoelectron spectroscopy (PES). Despite previous experimental [1-5] and theoretical studies [6] of the thermal decomposition of CF_3CHFCF_3, its primary thermal decomposition pathways are still not well established. Some spectroscopic studies of CF_3CHFCF_3 in flames have been made. The infrared spectrum of CF_3CHFCF_3 has been studied in the gas-phase [7],

Fourier-transform infrared (FTIR) spectroscopy and laser-induced breakdown spectroscopy (LIBS) have also been used to monitor CF_3CHFCF_3 and other products in fires inhibited by CF_3CHFCF_3 [8, 9]. Hynes *et al.* [1] carried out a shock tube study of the pyrolysis of CF_3CHFCF_3 over the temperature range 1200-1500 K at pressures between 16 and 18 atm. (which are much higher than the pressures used in this work). Product analysis was performed using gas chromatography (GC-MS) and FTIR spectroscopy with the aim of developing a detailed chemical mechanism to describe the decomposition of CF_3CHFCF_3. The results of the experiments and modelling showed that the major initiation reaction was bond fission (i.e. $CF_3CHFCF_3 \rightarrow CF_3 + CF_3CHF$). The abstraction of the secondary H-atom by F atoms was also predicted to be important whereas the 1, 2 HF elimination process ($CF_3CHFCF_3 \rightarrow CF_3CF{=}CF_2 + HF$) was slower. Yamamoto *et al.* [2] studied the thermal decomposition of CF_3CHFCF_3 heated in a flow-system at atmospheric pressure, diluted 5% v/v in air, and used GC/MS to analyse the products. Under the conditions used, it was found that CF_3CHFCF_3 began to decompose at 500 °C and had fully decomposed by 800 °C. The main decomposition product was found to be perfluoroisobutane.

In a related computational study by Peterson and Francisco [6], *ab initio* and density functional methods have been used to investigate twelve possible primary decomposition pathways of CF_3CHFCF_3. Reaction enthalpies were calculated for all twelve pathways and energy barriers were calculated for the five most thermodynamically favoured (least endothermic) reactions. Two possible decomposition reactions are,

$$CF_3CHFCF_3 \rightarrow CF_3CF{=}CF_2 + HF \qquad (6.1)$$

$$CF_3CHFCF_3 \rightarrow CF_3CHF + CF_3 \qquad (6.2)$$

Reaction enthalpies ($\Delta H_{f,298K}^{\emptyset}$) were calculated for reactions (6.1) and (6.2) as 34.8 and 92.3 kcal.mol^{-1} respectively using QCISD(T)/6-311G(d,p)//UMP2/6-31G(d) methods. Reaction (6.1) is the least endothermic decomposition reaction and reaction (6.2) is the initiation reaction proposed in the shock tube study [1]. *Ab initio* and DFT calculations have been performed previously in the Southampton PES group on CF_3CHFCF_3 and its reactions with fluorine and hydrogen atoms [10-12]. The heat of formation of CF_3CHFCF_3, $\Delta H_{f,298K}^{\emptyset}$ (CF_3CHFCF_3), was computed using DFT, MP2, RCCSD(T) and

model chemistry methods (G2(MP2), G2, G3 and CBS-Q) employing three reaction schemes, and the RCCSD(T)/CBS limit value was derived as (-370.6 ± 2.3) kcal.mol^{-1} [10]. This is believed to be the most reliable value available for $\Delta H_{f,298K}^{Ø}$ (CF_3CHFCF_3). The reaction enthalpy (298 K) and barrier height (0 K) for H-atom abstraction with fluorine atoms ($CF_3CHFCF_3 + F \rightarrow CF_3CFCF_3 + HF$) have also been calculated using high level *ab initio* methods to give the recommended values of (-34.7 ± 1.0) and (-0.9 ± 0.9) kcal.mol^{-1}[11]. Similarly, recommended values for the reaction enthalpy (298 K) and barrier height (0 K) for the H-atom reaction $CF_3CHFCF_3 + H \rightarrow CF_3CFCF_3 + H_2$ are (-0.7 ± 0.7) and (13.3 ± 0.5) kcal.mol^{-1} [12].

In this work, the photoelectron spectra of CF_3CHFCF_3 and its pyrolysis products have been recorded as a function of temperature in a flow system. In addition, state-of-the-art *ab initio* calculations have been performed on CF_3CHFCF_3 and $CF_3CHFCF_3^+$, and fragments obtained from CF_3CHFCF_3 and $CF_3CHFCF_3^+$. These calculations were carried out to obtain reliable adiabatic and vertical ionisation energy (AIE/VIE) values in order to assist interpretation of the experimental PE spectra. This investigation was performed in parallel with a related study on CF_3CHF_2, which is discussed in the previous chapter.

6.1 Experimental

The PE spectrum of CF_3CHFCF_3 was recorded using the big spectrometer (described in section 3.1 of Chapter 3) with a high temperature RF heating system coupled to the ionisation region (as described in section 3.3 of Chapter 3). Typical operating resolution of the spectrometer throughout this work was 20-25 meV, as measured for the $(3p)^{-1}$ ionisation of argon [13, 14]. PE spectra of CF_3CHFCF_3 (Remtec, >99%) were recorded and calibrated by admitting the sample into the spectrometer at the same time as argon and methyl iodide [15-17], as previously described in section 5.1 of Chapter 5. PE spectra of the assigned pyrolysis products, CF_3H (Aldrich, 98%) and hexafluoropropene, C_3F_6 (Fluorochem > 99%), were also recorded and calibrated in the same way. The PE spectrum of C_2F_6 (Fluorochem, 99.9%) was also recorded and calibrated. However C_2F_6 was not observed in the spectra recorded during pyrolysis. The experimental method used to study the thermal decomposition of CF_3CHFCF_3 was the same as that for the thermal decomposition investigation of HFC-125 (CF_3CHF_2)

described in Chapter 5. The apparatus used was also the same and has been previously described in section 3.3 of Chapter 3.

6.2 Computational Details

Calculations were carried out on CF_3CHFCF_3, and the possible pyrolysis products $CF_3CF{=}CF_2$, CF_3CHF, and CF_3CF. For neutral and cationic states, geometry optimisation and harmonic frequency calculations were carried out using the Gaussian03 suite of programs [18], using the density functional theory (DFT) method with the B3LYP functional and the MP2 method. Single energy calculations for improved relative electronic energies were performed at the RCCSD(T) level employing the MOLPRO programs [19]. Various standard basis sets were used, and extrapolation of the computed first adiabatic (AIE) and vertical (VIE) ionisation energies to the complete basis set (CBS) limit was carried out using the $1/X^3$ formula [20]. In addition, higher vertical ionisation energies have been computed at different levels of theory. These include the Koopmans' Theorem (negatives of computed Hartree-Fock orbital energies of the neutral molecule, discussed in section 4.1.4 of Chapter 4), time-dependent density functional theory (computed TD-DFT excitation energies of the cation using the B3LYP functional plus the first VIE) and equations-of-motion coupled-cluster single and double excitation (IP-EOM-CCSD) methods using different standard basis sets. The IP-EOM-CCSD calculations were performed using the ACES2 suite of programs [21]. These calculations were performed by Dr E. P. F. Lee of the Southampton PES group and are included here for completeness.

6.3 Results and Discussion

6.3.1 The photoelectron Spectra of CF_3CHFCF_3 and C_3F_6

The He(I) photoelectron spectrum of CF_3CHFCF_3 shows six bands (Figure 6.1). The VIEs of these bands, as well as the measured onset of the first band were averaged over ten expanded spectra. As can been seen in Figure 6.1, six main bands are observed in this spectrum with VIE values of (14.18 ± 0.01), (15.92 ± 0.01), (16.68 ± 0.01), (17.49 ± 0.01), (18.65 ± 0.01) and (19.54 ± 0.01) eV. The AIE of the first PE band was measured to be (13.11 ± 0.01) eV. This spectrum does not appear to have been recorded before and its assignment is discussed in the next section.

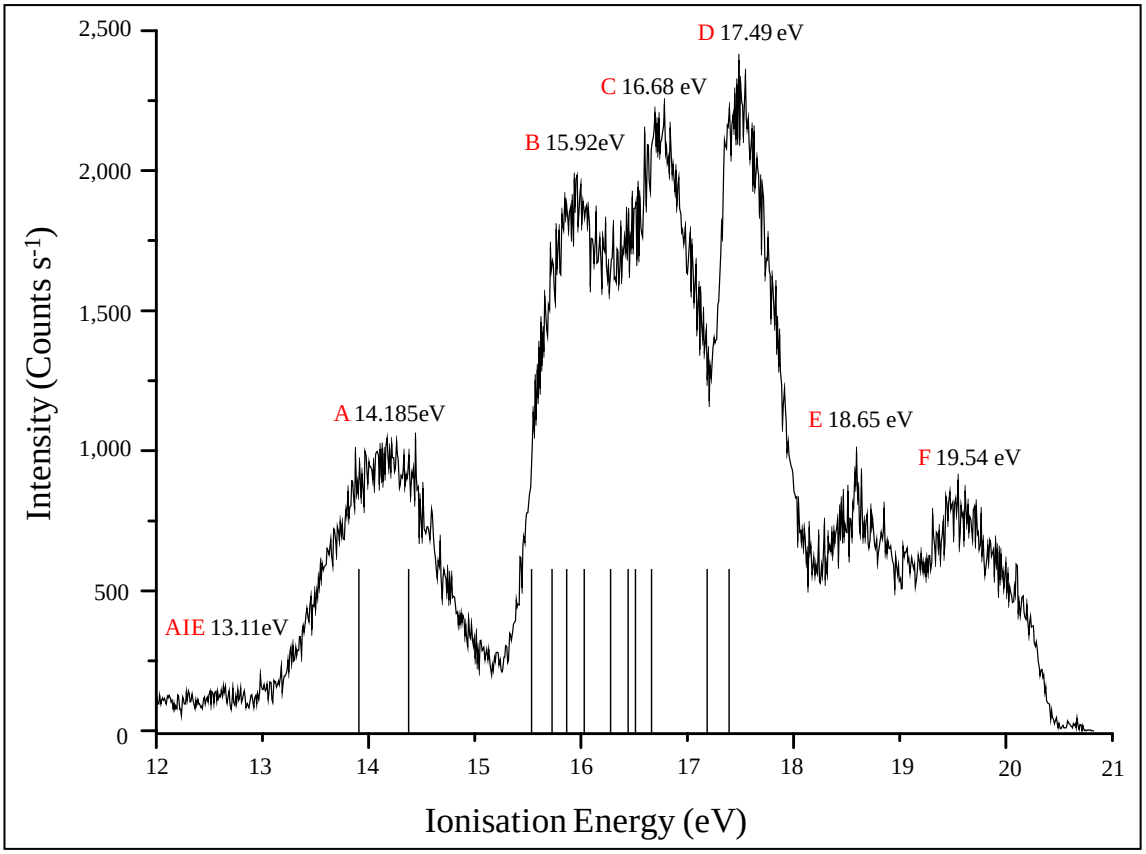

Figure 6.1: *Photoelectron spectrum of CF_3CHFCF_3 recorded with HeI (21.22 eV) radiation. The vertical lines on this diagram are vertical ionisation energies computed with EOM-CCSD/aug-cc-pVDZ calculations.*

A good quality photoelectron spectrum of C_3F_6 has also not been published before. This was needed to analyse the spectra recorded on pyrolysis of CF_3CHFCF_3 on the same spectrometer. The photoelectron spectrum of hexafluoropropene, C_3F_6, one of the main pyrolysis products of CF_3CHFCF_3 is presented in Figure 6.2. As can been seen, four main bands are observed in this spectrum with VIE values of (11.02 ± 0.02), (14.61 ± 0.04), (15.88 ± 0.04) and (16.91 ± 0.05) eV. The first band shows resolved vibrational structure with at least six regularly spaced components. The first vibrational component (AIE position) is measured at (10.63 ± 0.02) eV. As shown by the electronic structure calculations, this band arises from ionisation from the outermost filled molecular orbital which is π-bonding in character, and the vibrational structure arises from excitation of the C-C stretching mode in the ion (the C=C bond in the neutral). Measurement of the component separations and use of an anharmonic oscillator expression (see equations 2.16 to 2.18 in section 2.11 of Chapter 2 for a detailed description) for the vibration excited on ionisation gave ω_e = (1640 ± 30) cm^{-1} and $\omega_e x_e$ = (16 ± 10) cm^{-1} for the

vibration excited in the ion. This value of ω_e compares with 1797 cm^{-1} for the C=C mode in the neutral molecule determined by gas phase infrared spectroscopy [22]. This reduced value of the C=C stretching mode in the ionic state is consistent with ionisation from the outermost C=C π-bonding orbital. Previous studies of this molecule by PES include an early study by Cullen *et al*. [23] in which only the first AIE was quoted at 10.62 eV, and a later study by Freiser and Beauchamp in which a low resolution spectrum was published and the AIE and VIE of the first band were quoted at 10.62 and 11.10 eV respectively [24]. Later a threshold PE spectrum of C_3F_6 was recorded by Tuckett *et al*. [25]. This showed regular vibrational structure in the first band, with an average vibrational spacing measured as 1613 cm^{-1}, consistent with the PE spectrum obtained in this present work. A comparison of the PE spectrum of this work and TPE spectrum of reference [25] is shown in Figure 6.2.

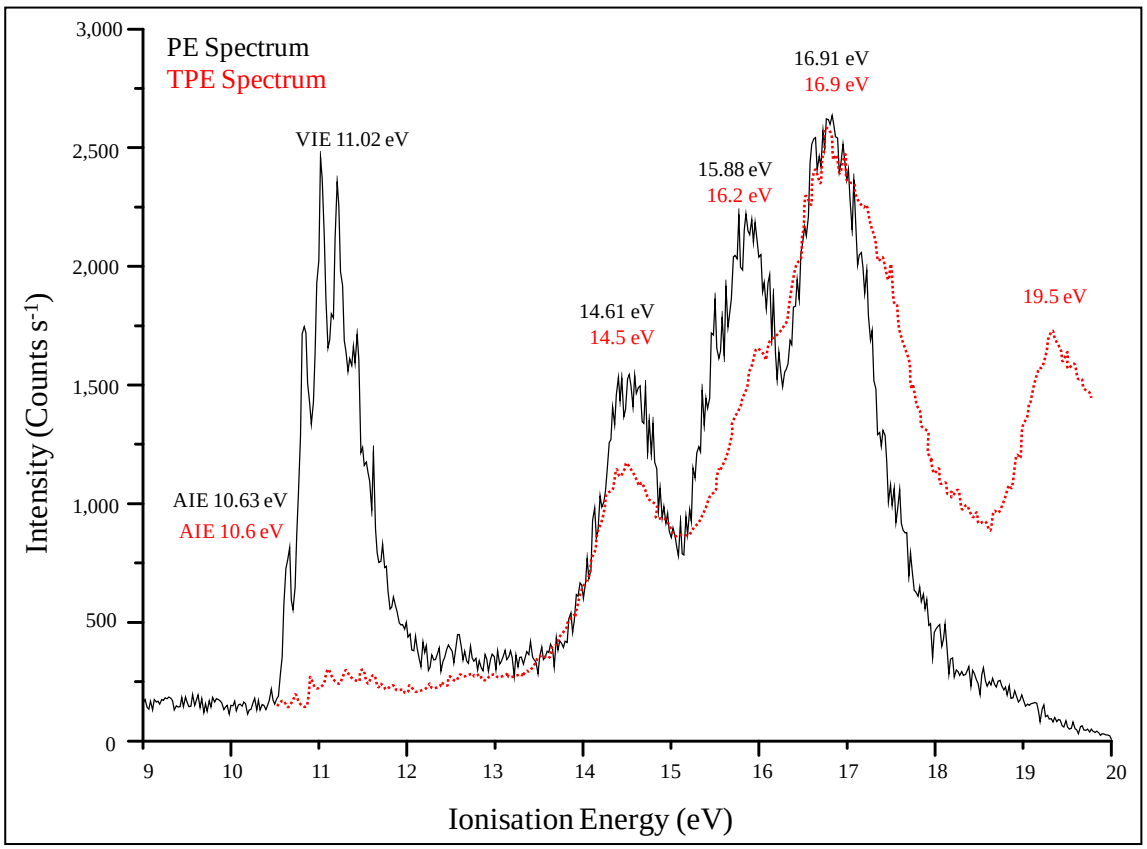

Figure 6.2: *PE spectra of hexafluoropropene: comparison of the PE spectrum obtained in this work with the threshold photoelectron (TPE) spectrum taken from reference [25].*

It can be seen from Figure 6.2, that the first band is much weaker in the TPE spectrum than in the PE spectrum, although the observed AIE and VIE values are essentially the same. Also, the resolution of the bands in the 13.0-18.0 eV region is poorer in the TPE

spectrum and a band maximum (at 16.20 eV) is observed in the TPE spectrum which is not present in the PE spectrum. This effect was also observed on comparing PE and TPE spectra of CF_3CHF_2 (see Figure 5.2 of Chapter 5) and arises because TPE band envelopes have contributions both from direct ionisation, as in PE spectra, and autoionisation from highly excited neutral states which lie above an ionisation threshold. These excited states are Rydberg states which are members of series which converge to higher ionisation thresholds.

6.3.2 Results of Electronic Structure Calculations

6.3.2.1 CF_3CHFCF_3 and its Cation

Geometry optimisation and harmonic vibrational frequency calculations on CF_3CHFCF_3 have been reported previously [6] and hence the discussion of these results will not be repeated here. The ground state of the neutral has a C_s structure [6] with the plane of symmetry through the central carbon atom perpendicular to the CCC skeleton.

For the ground electronic state of the cation, $CF_3CHFCF_3^+$ (resulting from the $(18a'')^{-1}$ ionisation of CF_3CHFCF_3), geometry optimisation under a constraint of C_s symmetry (as with CF_3CHFCF_3) led to a saddle point with an imaginary frequency of 583.3i cm^{-1} at the B3LYP/6-31++G** level of calculation. This vibrational mode is of a″ symmetry and consists of mainly asymmetric stretching of the two CC bonds in the CCC skeleton. However, MP2/6-31++G** geometry optimisation gave a true minimum with all real frequencies (the $^2A''$ state resulting from the $(18a'')^{-1}$ ionisation of the neutral molecule; the two equivalent CC bond lengths are 1.6847Å, 1.5285 Å in the neutral). Further geometry optimisation with an asymmetric CCC skeleton of C_1 symmetry (i.e. two different CC bond lengths) led to a true minimum, with long and short CC bonds, at all levels of calculations: B3LYP/6-31++G** (2.120 and 1.550 Å), MP2/6-31++G** (5D) (2.038; 1.541 Å) and MP2/6-31++G** (2.039; 1.541 Å). The MP2/6-31++ G** C_s true minimum (the $^2A''$ state) mentioned above is 4.20 $kcal.mol^{-1}$ higher in energy (PUMP2 energies) than the C_1 true minimum. At the RCCSD(T)/cc-pVTZ//MP2/6-31++G** level of calculation, the C_1 structure is 6.44 $kcal.mol^{-1}$ lower in energy than the C_s structure. For the C_1 structure, the RCCSD(T)/cc-pVTZ single energy calculation was the largest calculation carried out with the computation resource available (calculations on the lower, C_1 symmetry structure are considerably more demanding than the C_s

structure). For the C_s structure, the RCCSD/cc-pVQZ single energy calculation was the largest calculation possible and it was not possible to complete the calculation of the perturbative triple excitations in the RCCSD(T)/cc-pVQZ calculation with the computational resources available. For calculations of VIEs, the MP2/6-31++G** (5D) geometry of the neutral (a C_s structure from a previous study [10]) was used.

Computed first adiabatic ionisation energies (AIEs) and vertical ionisation energies (VIEs) obtained at different levels of calculation are summarised in Table 6.1.

Method/basis//geometry	AIE (C_1)	AIE (C_S)	VIE	Nb[a]
B3LYP/6-31++G**	12.426		13.365	196
MP2/6-31++G** (5D)	12.726		15.32	186
MP2/6-31++G**	12.71	12.892	15.315	196
MP2/6-311++G(2d,2p)			15.159	280
RCCSD/cc-pVTZ//MP2/6-31++G**(5D)	12.49		14.202	314
RCCSD/cc-pVTZ//MP2/6-31++G**	12.49	12.863		314
RCCSD/cc-pVTZ//B3LYP/6-31++G**	12.483			314
RCCSD/aug-cc-pVTZ//MP2/6-31++G**(5D)			14.35	483
RCCSD/aug-cc-pVTZ//MP2/6-31++G**		13.105		483
RCCSD/cc-pVQZ//MP2/6-31++G**(5D)			14.389	580
RCCSD/cc-pVQZ//MP2/6-31++G**		13.017		580
RCCSD(T)/cc-pVTZ//MP2/6-31++G**(5D)	12.406		13.886	314
RCCSD(T)/cc-pVTZ//MP2/6-31++G**	12.406	12.686		314
RCCSD(T)/cc-pVTZ//B3LYP/6-31++G**	12.408			314
RCCSD(T)/aug-cc-pVTZ//MP2/6-31++G**(5D)			14.045	483
RCCSD(T)/aug-cc-pVTZ//MP2/6-31++G**		12.863		483
$E_{CBS}(1/X^3$:RCCSD/cc-pVTZ; cc-pVQZ)		13.123	14.526	
$\Delta E_{(T)1}$\{RCCSD(T); RCCSD/aug-cc-pVTZ\}		-0.151	-0.305	
$\Delta E_{(T)2}$\{RCCSD(T); RCCSD/cc-pVTZ\}		-0.177	-0.317	
$E_{best}^{max} = (E_{CBS} + \Delta E_{(T)1})$		12.972	14.221	
$E_{best}^{min} = (E_{CBS} + \Delta E_{(T)2})$		12.946	14.209	
Best estimated AIE (E_{best} average)[b]		12.96 ± 0.10	14.22 ± 0.17	
ΔZPE (MP2)	-0.054	-0.047		
Best estimated AIE_0 (included ZPE correction)		12.91 ± 0.10		
Photoelectron spectrum, this work		13.11 ± 0.05	14.18 ± 0.05	

Table 6.1: *Computed first AIEs and VIEs (eV) of the $(18a'')^{-1}$ ionisation of CF_3CHFCF_3 obtained at different levels of calculations.*

[a] Number of contracted basis functions.

[b] The uncertainties are estimated as the differences between the best estimated values and the RCCSD(T)/aug-cc-pVTZ values.

The best estimated AIE to the C_s structure of the cation is (12.96 ± 0.10) eV (see footnote b of Table 6.1 for the estimated uncertainties). This includes contributions from extrapolation to the complete basis set limit (CBS in Table 6.1; employing the

RCCSD/cc-pVTZ and RCCSD/cc-pVQZ values) and triple excitations in the RCCSD(T) calculations, assuming that these contributions are additive. Including correction for zero-point energies of the two states (ΔZPE), the AIE_0 is (12.91 ± 0.10) eV. This value is probably an upper limit, as the C_1 structure of the cation has a lower energy than the C_s structure at different levels of calculation as discussed. The AIE to the lower energy C_1 structure of the cation computed at the RCCSD(T)/cc-pVTZ//MP2/6-31++G** level is 12.406 eV. This value is the computed AIE value to the C_1 structure of the cation at the highest level carried out in the present study, and can be compared to a value of 12.686 eV to the C_s structure obtained at the same level of calculation. If the same magnitudes of the various corrections (CBS and triple excitations; see Table 6.1) to the AIE value to the C_s structure are assumed for the C_1 structure, the best AIE value to the C_1 structure is estimated to be 12.68 eV. Including zero-point energy corrections, the best AIE_0 value to the C_1 structure of the cation is 12.63 eV. Combining this AIE_0 value with the best $\Delta H_{f,298K}^{Ø}(CF_3CHFCF_3)$ value of (-370.6 ± 2.3) kcal.mol^{-1} obtained previously [10], $\Delta H_{f,298K}^{Ø}(CF_3CHFCF_3^+)$ has a value of (-79.3 ± 4.6) kcal.mol^{-1} (assuming an uncertainty of 0.10 eV associated with the AIE_0 value used).

Comparing theory with experiment, the onset of the first band observed in the experimental PE spectrum of CF_3CHFCF_3 has a measured ionisation energy (IE) of (13.11 ± 0.05) eV, which is larger than the best estimated AIE_0 value of 12.63 eV to the C_1 structure of the cation by 0.48 eV. Nevertheless, since the computed geometry change upon ionisation, whether to the C_s or C_1 structure of the cation, is quite large (significant changes in the C-C bond lengths occur), the Franck-Condon factors in the AIE_0 region are expected to be small. Consequently, it is not surprising that the AIE position is not observable in the experimental PE spectrum, and the observed band onset of the first PE band has a higher IE than the true AIE_0. The best estimated VIE value is (14.22 ± 0.17) eV, in good agreement with the observed band maximum of (14.18 ± 0.05) eV. Nevertheless, computed higher VIEs (in Table 6.2) suggest that the first band in the observed photoelectron spectrum consists of two ionisations. Regarding the vibrational structure of the first photoelectron band of CF_3CHFCF_3, the computed geometry change upon ionisation whether to the C_s or C_1 structure of the cation is mainly in the two CC bond lengths. In this connection, vibrational modes of the cation involving CC stretches are expected to be excited upon ionisation. In addition, as

mentioned above, computed VIE values for the second one-electron ionisation suggest that the observed first PE band also includes this ionisation. In view of the above considerations, it is not surprising that the observed first PE band does not exhibit any resolvable vibrational structure because it consists of two overlapping ionisations with their associated vibrational structures.

$(m.o.)^{-1}$	HF-KT[a]	TD-B3LYP[b]		IP-EOM-CCSD[c]			
	VIE	E_{ex}[b]	VIE[d]	6-31G**	6-31++G**	6-311++G**	Aug-cc-pVDZ
18a″	15.83	0	14.22[d]	13.5	13.95	14.08	13.91
23a′	16.229	0.552	14.77	13.99	14.41	14.54	14.38
17a″	18.368	0.983	15.2	15.18	15.54	15.65	15.56
22a′	18.529	1.133	15.35	15.34	15.71	15.81	15.73
16a″	18.615	1.497	15.72	15.49	15.86	15.97	15.88
15a″	18.748	1.54	15.76	15.66	16.02	16.13	16.03
21a′	18.903	1.828	16.05	15.9	16.27	16.37	16.29
20a′	19.018	1.981	16.2	15.04	16.43	16.53	16.44
19a′	19.077	2.501	16.72	16.13	16.52	16.62	16.52
14a″	19.51	2.604	16.82	16.29	16.67	16.78	16.68
13a″	19.92	2.72	16.94	16.81	17.2	17.29	17.2
12a″		2.942	17.16	16.98			
17a′		3.029	17.25	17.12			
18a′		3.142	17.36	17.04	17.42	17.51	17.42
16a′		4.632	18.85	18.42			
15a′		5.635	19.85	19.46			
11a″		5.991	20.21	20.11			
10a″		6.23	20.45				
14a′		6.67	20.89				
13a′		6.803	21.02				
9a″		6.957	21.18				

Table 6.2: *Computed VIEs (eV) to, and excitation energies (E_{ex}) of, low-lying cationic states of $CF_3CHFCF_3^+$ obtained from Hartree-Fock (using the Koopmans' Theorem), time-dependent (TD) density functional theory (using the B3LYP functional) and IP-EOM-CCSD calculations using different basis sets.*

[a] VIEs estimated by the Koopmans' Theorem (KT); negative computed orbital energies from HF/6-311++G(2d,2p) calculation of CF_3CHFCF_3 at its MP2/6-311++G(2d,2p) optimised geometry.

[b] The computed excitation energies (E_{ex}) of low-lying cationic states of $CF_3CHFCF_3^+$ are from time dependent (TD) DFT calculations, using the B3LYP functional and the 6-311++G(2d,2p) basis set, at the MP2/6-311++G(2d,2p) optimised geometry of CF_3CHFCF_3.

[c] Computed VIEs to low-lying cationic states of $CF_3CHFCF_3^+$ obtained from IP-EOM-CCSD calculations using different basis sets (the total numbers of contracted basis functions in these basis sets are 155, 196, 227 and 239, respectively) at the MP2/6-31++G** optimised geometry of the neutral molecule.

[d] VIEs to the excited states of the cation were estimated by employing the best estimated first VIE from Table 6.1 to the ground cationic state and the corresponding computed DFT-TD excitation energies.

The computed higher VIE values obtained at different levels of calculation are summarised in Table 6.2. The highest level of calculation used for the higher VIEs is the IP-EOM-CCSD method. It is clear that the VIE values obtained by Koopmans' Theorem with the computed Hartree-Fock orbital energies (HF-KT) are too high, when compared with corresponding computed IP-EOM-CCSD values and experimental values. The VIE values obtained using computed time-dependent DFT excitation energies of the cation (using the B3LYP functional; TD-B3LYP) and the best estimated first VIE (from Table 6.1), agree with corresponding computed IP-EOM-CCSD/aug-cc-pVDZ values to within 0.4 eV. However, when they are compared in the bar diagrams shown in Figure 6.3, it can be seen that the "patterns" are quite different. Specifically, the computed IP-EOM-CCSD VIEs form distinct "groups", which agree very well with the experimental photoelectron spectrum (see Figure 6.1).

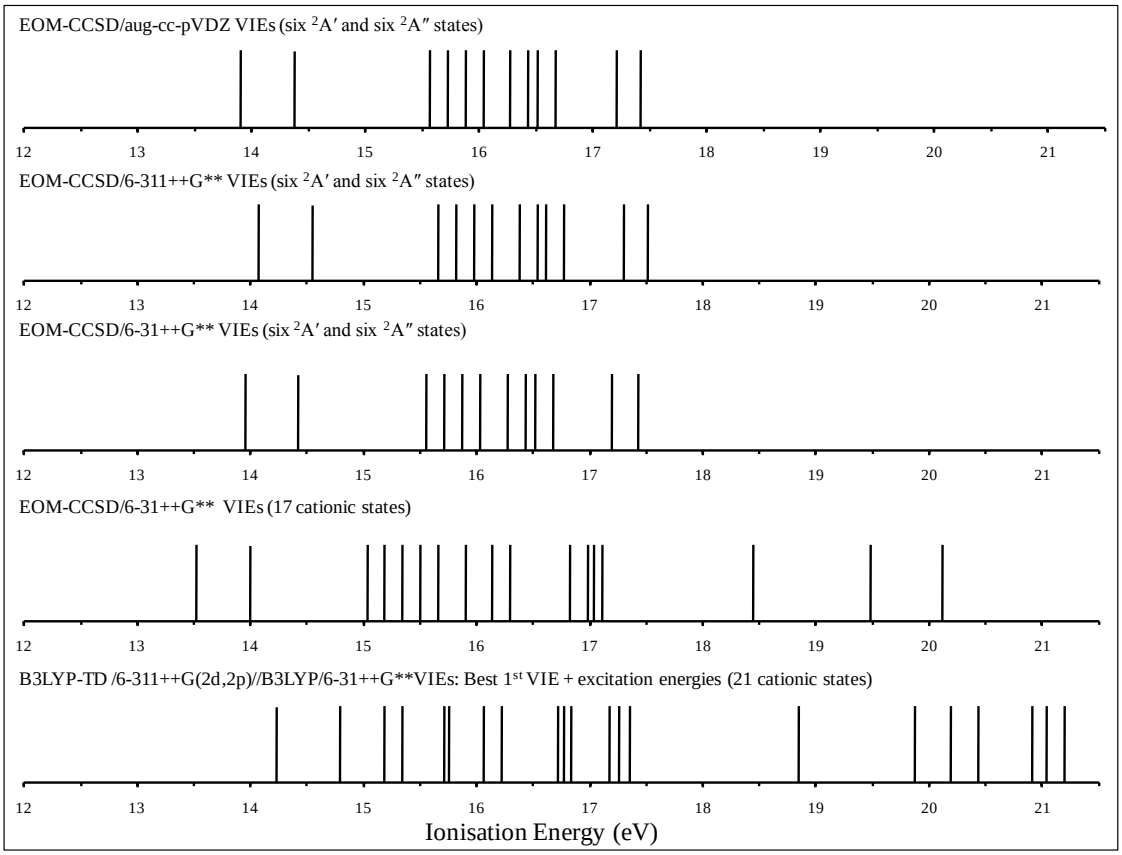

Figure 6.3: *Comparison of computed VIEs of CF_3CHFCF_3 obtained with the IP-EOM-CCSD method using different basis sets and with the B3LYP calculations (lowest panel).*

However, the computed TD-B3LYP VIEs do not form any clear groupings, as they are rather evenly spread out, and do not agree very well with experiment (see Figure 6.3). Regarding the IP-EOM-CCSD(T) values obtained using different basis sets, the 6-31G** values are too low, while those of the other three larger basis sets have similar

values. For the first VIE, the IP-EOM-CCSD values of *ca.* 14.0 eV obtained with the larger basis sets are slightly smaller than the best estimated value of 14.22 eV given above. From the comparison between theory and experiment as shown in Figure 6.1, it can be seen that if the computed IP-EOM-CCSD/aug-cc-pVDZ VIEs are all shifted to slightly higher IEs (by *ca.* 0.3 eV), the agreement between the computed IP-EOM-CCSD VIEs and the experimental PE spectrum will be even better than that shown in Figure 6.1. In any case, the "pattern" of the computed IP-EOM-CCSD VIE values matches very well with the relative intensities of PE bands in the experimental spectrum. In this connection, it is clear that the $(23a')^{-1}$ ionisation with a computed IP-EOM-CCSD VIE of *ca.* 14.5 eV (see Table 6.2) contributes also to the first observed PE band (see Figure 6.1).

6.3.2.2 $CF_3CF=CF_2$ and its Cation

The optimised structures of both $CF_3CF=CF_2$ and its cation in their ground electronic states have C_s symmetry [26, 27]. The computed geometry change upon ionisation of $CF_3CF=CF_2$ to the $\tilde{X}^2A''$ state of the cation lies mainly in the CF-CF_2 bond length, which increases from computed values of 1.337 and 1.334 Å in the neutral molecule to 1.423 and 1.425 Å in the cation at the MP2/6-31++G** and B3LYP/6-31++G** levels of calculation respectively. The ionisation to the $\tilde{X}^2A''$ state of $CF_3CF=CF_2^+$ corresponds to removal of an electron from the 10a'' molecular orbital, which is essentially a π-bonding orbital localised to the C=C double bond in the $CF_3CF=CF_2$ molecule [26]. The computed spin density of the unpaired electron in the ionic state lies mainly on the central C (0.73 and 0.51 at the HF and B3LYP levels respectively, and 0.26 and 0.27 on the terminal C of the CF_2 group). The computed harmonic vibrational frequency of the C=C stretching mode of neutral $CF_3CF=CF_2$ has values of 1851 and 1836 cm^{-1} from MP2 and B3LYP calculations, respectively (which can be compared with 1797 cm^{-1} measured for the C=C stretching mode in the infrared spectrum [22]) while that of the cation has computed values of 1702 and 1631 cm^{-1}. These computed harmonic vibrational frequencies of the cation agree reasonably well with the experimental ω_e value of (1640 ± 30) cm^{-1} measured in the first photoelectron band of $CF_3CF=CF_2$. The computed first AIEs and VIEs obtained at different levels of calculation are summarised in Table 6.3, and the computed VIEs obtained from IP-EOM-CCSD calculations are tabulated in Table 6.4.

Methods	AIE	VIE	Nb[a]
B3LYP/6-31++G**	10.5	11.07	171
MP2/6-31++G**	10.52	11.13	171
IP-EOM-CCSD/aug-cc-pVDZ//MP2/6-31++G**		11.19	207
IP-EOM-CCSD/cc-pVTZ//MP2/6-31++G**		11.28	270
RCCSD/cc-pVTZ//MP2/6-31++G**	10.334	11.123	270
RCCSD/aug-cc-pVTZ//MP2/6-31++G**	10.495	11.266	414
RCCSD/cc-pVQZ//MP2/6-31++G**	10.475	11.282	495
RCCSD(T)/cc-pVTZ//MP2/6-31++G**	10.354	11.085	270
RCCSD(T)/aug-cc-pVTZ//MP2/6-31++G**	10.543	11.251	414
E_{CBS}(RCCSD/cc-pVTZ,cc-pVQZ;1/X^3)	10.578	11.398	
$\Delta E_{(T)1}${RCCSD(T); RCCSD/aug-cc-pVTZ}	0.048	-0.015	
$\Delta E_{(T)2}${RCCSD(T); RCCSD/cc-pVTZ}	0.021	-0.037	
$E_{best}^{max} = (E_{CBS} + \Delta E_{aug1} + \Delta E_{(T)1})$	10.626	11.383	
$E_{best}^{min} = (E_{CBS} + \Delta E_{aug2} + \Delta E_{(T)2})$	10.599	11.361	
Best estimated AIE (E_{best} average)[b]	10.61 ± 0.07	11.37 ± 0.12	
ΔZPE (MP2)	0.02		
Best estimated AIE_0 (included ZPE correction)	10.63 ± 0.07		
He(I) photoelectron spectrum; this work	10.63 ± 0.02	11.02 ± 0.02	

Table 6.3: *Computed first AIEs and VIEs (eV) of the $(10a'')^{-1}$ ionisation of $CF_3CF=CF_2$ obtained at different levels of calculations.*

[a] Number of contracted basis functions.

[b] The uncertainties are estimated as the differences between the best estimated values and the RCCSD(T)/aug-cc-pVTZ values.

$(m.o.)^{-1}$	Aug-cc-pVDZ	cc-pVTZ	Expt.PE spectrum (this work)
10 a''	11.19	11.28	11.02 ± 0.02
26a'	14.60	14.70	14.61 ± 0.04
9a''	15.49	15.62	15.57 ± 0.05
25a'	15.89	16.00	15.88 ± 0.04
8a''	15.97	16.08	
24a'	16.52	16.63	
23a'	16.77	16.86	
7a''	16.93	17.02	
6a''	16.99	17.11	
22a'	17.14	17.24	16.91 ± 0.05
21a'	17.23	17.32	
5a''	17.55	17.63	
4a''	19.23	19.32	
20a'	19.53	19.56	

Table 6.4: *Computed vertical ionisation energies (eV) to low-lying cationic states of $CF_3CF=CF_2$ obtained from IP-EOM-CCSD calculations using two different basis sets.*

As can be seen in Table 6.3, the best estimated AIE_0 was obtained as (10.63 ± 0.07) eV in good agreement with the experimental value of (10.63 ± 0.02) eV measured in this work. Similarly the best computed VIE is (11.37 ± 0.12) eV which compares reasonably well with the experimental value of (11.02 ± 0.02) eV shown in Table 6.3.

6.3.2.3 CF_3CHF and its Cation

As reaction (6.2), to give $CF_3CHF + CF_3$, was expected from the computational work of Peterson and Francisco [6] to be a possible decomposition channel, it was decided to estimate the AIE and VIE of CF_3CHF to aid the analysis of the experimental pyrolysis spectra. Although the photoelectron spectrum of CF_3 has not been recorded, its first band is expected to be broad with an AIE (9.05 ± 0.01) eV and a VIE of (10.86 ± 0.01) eV [28-32] and hence for this radical no *ab initio* calculations of AIE and VIE values were necessary. UHF/6-31G* and MP2/6-31G* calculations have been carried out previously on the CF_3CHF radical [6, 33]. However, to our knowledge, the CF_3CHF^+ cation has not been investigated before by *ab initio* calculations. In addition to the $\tilde{X}^2A$ state of CF_3CHF, the lowest singlet and triplet states of CF_3CHF^+ have been investigated. Geometry optimisation and harmonic frequency calculations at both the MP2/6-31++G** and B3LYP/6-31++G** level gave a C_s structure for the $\tilde{X}^1A'$ state of CF_3CHF^+, while the $\tilde{a}\,^3A$ state has a C_1 structure. The computed geometry changes upon ionisation from the $\tilde{X}^2A$ state of CF_3CHF to the $\tilde{X}^1A'$ and $\tilde{a}\,^3A$ states of the cation involve mainly increases of the r_e(CC) bond lengths (from 1.480 to 1.546 and 1.958 Å, respectively) and changes of the orientations of the F atoms in the CF_2 group (i.e. the FCC and FCCF angles). The vibrational frequency of the CC stretching mode of the $\tilde{X}^2A$ of CF_3CHF has computed harmonic values of 868 (MP2) and 854 (B3LYP) cm^{-1}. However, for the $\tilde{X}^1A'$ state of CF_3CHF^+, there are two a' modes with computed harmonic frequencies of 1191 and 869 cm^{-1} (MP2), which involve CC stretching. Similarly, for the $\tilde{a}\,^3A$ state of the cation, CC stretching is involved in two vibrational modes with computed harmonic frequencies of 733 and 979 cm^{-1} (MP2).

Computed AIE and VIE values to the $\tilde{X}^1A'$ and $\tilde{a}\,^3A$ states of CF_3CHF^+ obtained at different levels of calculations are summarised in Table 6.5. As restricted-spin open-shell Hartree-Fock (ROHF) calculations carried out on the $\tilde{a}\,^3A$ of CF_3CHF^+ at the optimised geometry of the neutral molecule faced SCF convergence problems, VIE values to the $\tilde{a}\,^3A$ state at the RCCSD(T) level could not be obtained. However, IE values could be obtained when the RCCSD(T) calculations were carried out at the optimised geometry of the $\tilde{a}\,^3A$ state. In addition, the perturbative triple excitations in the RCCSD(T) calculation employing the aug-cc-pVQZ basis set could not be completed with the computing resources available. Nevertheless, CBS values (CBS_1 in

Table 6.5) using RCCSD(T) results, which employed the aug-cc-pVDZ and aug-cc-pVTZ basis sets were obtained.

Methods	X^1A'		a^3A		Nb[a]
	AIE	VIE	AIE	VIE	
B3LYP/6-31++G**	9.83	10.56	12.69	13.77	120
MP2/6-31++G**	9.62	10.53	12.81	15.42	120
RCCSD/aug-cc-pVDZ//MP2/6-31++G**	9.619	10.549	12.787		147
RCCSD/aug-cc-pVTZ//MP2/6-31++G**	9.6	10.668	12.763		299
RCCSD/aug-cc-pVQZ/MP2/6-31++G**		10.719			526
RCCSD(T)/aug-cc-pVDZ//MP2/6-31++G**	9.58	10.444	12.732		147
RCCSD(T)/aug-cc-pVTZ//MP2/6-31++G**	9.571	10.562	12.719		299
CBS_1\{1/X^3:RCCSD(T)/aug-cc-pVDZ;aug-cc-pVTZ\}	9.568(4)	10.612(50)	12.714(5)		
CBS_2\{1/X^3:RCCSD/aug-cc-pVTZ,aug-cc-pVQZ\}		10.756(37)			
(T):{RCCSD;RCCSD(T)/aug-cc-pVTZ}		-0.1057			
CBS_2 + (T)		10.650(37)			
ΔZPE (MP2)	0.0029		-0.0424		
$AIE_0 = CBS_1 + \Delta ZPE$	9.571(4)		12.672(5)		

Table 6.5: *Computed AIEs and VIEs (eV) to the $X\ ^1A'$ and a^3A states of CF_3CHF^+ obtained at different levels of calculations.*

[a] The total number of contracted basis functions used in the calculation.

In addition, for the VIE to the $\tilde{X}^1A'$ state, CBS values (CBS_2 in Table 6.5) using RCCSD results, which employed the aug-cc-pVTZ and aug-cc-pVQZ basis sets have been obtained. Including a correction for perturbative triple excitations ((T) in Table 6.5), based on the RCCSD(T)/aug-cc-pVTZ results, it is seen that the CBS_2 + (T) value of (10.650 ± 0.037) eV agrees with the CBS_1 value of (10.612 ± 0.050) eV to within the estimated uncertainties. Including zero-point energy corrections (ΔZPE), the recommended first and second AIE_0 values to the $\tilde{X}^1A'$ and $\tilde{a}\ ^3A$ states are 9.571 and 12.672 eV respectively. In relation to the identification of the CF_3CHF radical in a photoelectron spectrum, computed *ab initio* results obtained in the present investigation suggest that the first photoelectron band has an onset at 9.57 eV and a band maximum at *ca.* 10.63 eV. Due to the large change in the predicted equilibrium geometry upon ionisation from the $\tilde{X}^2A$ state of the neutral molecule (with C_1 symmetry) to the $\tilde{X}^1A'$ of the cation (with C_s symmetry), the first photoelectron band is expected to be broad with complex vibrational structure. In addition, it is anticipated that higher IE bands are well separated from the first band, with the second photoelectron band corresponding to ionisation to the $\tilde{a}\ ^3A$ state starting at an IE of approximately 12.67 eV.

6.3.2.4 CF_3CF and its Cation

Decomposition of CF_3CHFCF_3 to give CF_3CF + CF_3H is another possible reaction channel (this is reaction 11 of Peterson and Francisco [6]). As mentioned previously, the photoelectron spectrum of CF_3H was recorded in this work. However, the photoelectron spectrum of CF_3CF is not available, so it was decided to compute AIE and VIE values to assist band assignment in the pyrolysis spectra. Previous *ab initio* calculations on CF_3CF focused mainly on the singlet – triplet gap of the carbene [34-36]. These calculations gave a singlet ground state for CF_3CF and the lowest triplet state was computed to be over 10 kcal.mol^{-1} higher in energy. However, no *ab initio* calculations have been carried out on the cation previously. Geometry optimisation and harmonic frequency calculations have been carried out in this work using MP2/6-31++G** and B3LYP/6-31++G** on the lowest singlet and triplet states of CF_3CF and the lowest doublet state of CF_3CF^+. The lowest triplet state of the neutral molecule is the $\tilde{a}\,^3A''$ state which has a C_s structure at both the MP2 and B3LYP levels. At the MP2 level, the $\tilde{X}^1A$ state has a C_1 structure, though a C_s saddle point (with a small computed a" imaginary frequency of 29.9i cm^{-1}) is only 13.6 cm^{-1} higher in energy. At the B3LYP level, there is also a similar C_s saddle point, but geometry optimisation with C_1 symmetry failed to converge after over 50 points. This is the case even when analytical second derivatives were computed explicitly at every point in the search, indicating that the B3LYP method is inadequate for the lowest singlet state of CF_3CF. The computed singlet-triplet separations at the MP2 and B3LYP levels (with respect to the C_s saddle point) are 10.0 and 12.6 kcal.mol^{-1}, respectively, in good agreement with results of previous calculations. The $\tilde{X}^2A$ state of CF_3CF^+ has a C_1 structure at both the MP2 and B3LYP levels. The computed r_e(CC) bond length in the ionic state is longer than that in the $\tilde{X}^1A$ state of the neutral molecule. At the MP2 level these bond lengths are 1.622 Å and 1.559 Å respectively. There are two vibrational modes with computed harmonic frequencies of 1330 and 683 cm^{-1} of the neutral, which involve CC stretching, and for the cation, these vibrations have computed harmonic vibrational frequencies of 788 and 513 cm^{-1}.

Computed first AIE and VIE values obtained at different levels of calculation are summarised in Table 6.6. The best estimated first AIE_0 value (CBS + ΔZPE in Table 6.6) and VIE value are (10.55 ± 0.02) and (11.49 ± 0.05) eV, respectively.

Method	AIE	VIE	Nb[a]
B3LYP/6-31++G**	10.52[b]		114
MP2/6-31++G**	10.32	11.08	114
IP-EOM-CCSD/aug-cc-pVDZ//MP2/6-31++G**		11.4	138
IP-EOM-CCSD/cc-pVTZ//MP2/6-31++G**		11.51	180
RCCSD/aug-cc-pVTZ//MP2/6-31++G**	10.472	11.455	276
RCCSD/aug-cc-pVQZ//MP2/6-31++G**	10.498	11.517	480
RCCSD(T)/aug-cc-pVTZ//MP2/6-31++G**	10.486	11.38	276
RCCSD(T)/aug-cc-pVQZ//MP2/6-31++G**	10.516	11.444	480
CBS{$1/X^3$:RCCSD(T)/aug-cc-pVTZ;aug-cc-pVQZ}	10.538 ± 0.022	11.491 ± 0.047	
ΔZPE(MP2)	0.012		
CBS + ΔZPE(MP2)	10.55 ± 0.02		

Table 6.6: *Computed first AIEs and VIEs (eV) to the $\tilde{X}^2A$ state of CF_3CF^+ obtained at different levels of calculation.*

[a] The total number of contracted basis functions used in the calculation.

[b] With respect to the C_S saddle point of CF_3CF; as with the B3LYP method, no true minimum of C_1 symmetry was obtained.

These values suggest that the first photoelectron band of CF_3CF is broad with a width of over 1 eV. When the best estimated first AIE_0 value of CF_3CF obtained in the present study is compared with the most reliable first AIE_0 value of CF_2 obtained recently from threshold photoelectron spectroscopy, (11.362 ± 0.005) eV [37], it can be seen that the CF_3 substituent has lowered the first AIE_0 of the fluorocarbene by *ca.* 0.8 eV, indicating that CF_3 is significantly less electron withdrawing than F. This is in line with the smaller group electronegativity of CF_3 (2.68) than F (4.00) [38, 39]. Computed VIE values to low-lying electronic states of CF_3CF^+ obtained at different levels of calculation are tabulated in Table 6.7.

$(m.o.)^{-1}$	HF-KT/ aug-cc-pVDZ	IP-EOM-CCSD/ aug-cc-pVDZ	IP-EOM-CCSD/ cc-pVTZ
24a	12.48	11.4	11.51
23a	17.68	15.67	15.78
22a	18.43	15.7	15.82
21a	18.79	16.28	16.39
20a	18.83	16.31	16.4
19a	19.79	17.21	17.3
18a	19.99	17.37	17.44
17a	20.6	18.2	18.3
16a	21.01	18.58	18.68
15a	23.09	20.73	20.77

Table 6.7: *Computed vertical ionisation energies (in eV) to low-lying cationic states of CF_3CF^+ obtained via Koopmans' Theorem (at the Hartree-Fock level; HF-KT), and from IP-EOM-CCSD calculations using two different basis sets at the MP2/6-31++G** geometry of the $\tilde{X}^2A$ state of CF_3CF^+.*

These values suggest that the first photoelectron band of CF_3CF is separated from the higher ionisation energy bands by *ca.* 4 eV. It should also be noted that C_2F_4 is expected to lie 18.0 kcal.mol^{-1} lower in energy than CF_3CF, from the energy of the isomerisation reaction determined by DiFelice and Ritter [40] by evaluation of available heats of formation, and calculations of forward and reverse rate coefficients and comparison with experimental evidence.

6.3.3 Thermal Decomposition Studies of CF_3CHFCF_3

Photoelectron spectra were recorded for flowing CF_3CHFCF_3 heavily diluted in argon in the temperature range 600-2000 °C. Typical spectra recorded at furnace temperatures of 1300 and 1800 °C are shown in Figure 6.4. Normalised product band intensities, as well as the normalised intensity of the first band of CF_3CHFCF_3, plotted as function of temperature are shown in Figure 6.5. Two of the favoured reactions from the computational study of Peterson and Francisco [6] are reactions (6.1) and (6.2). Reaction (6.2) was also suggested as the major initiation reaction in a shock tube study by Hynes *et al.* [1]. Clear evidence was obtained in the present work for reaction (6.1) as HF and $CF_3CF{=}CF_2$ were observed at pyrolysis temperatures in the region 600-1000 °C as initial decomposition products. However, no evidence was obtained for the products of reaction (6.2), CF_3CHF and CF_3 with expected first band VIE (and AIE) values of 10.63 (9.57) eV and 10.86 (9.05) eV respectively (see the previous section). Also, no evidence of C_2F_6, obtained from recombination of two CF_3 radicals, was obtained although there was evidence for production of CF_3H. In separate experiments in which the photoelectron spectra of C_2F_6 and CF_3H were recorded and calibrated, the VIEs of the first bands of these molecules were measured as (14.61 ± 0.01) eV and (14.78 ± 0.01) eV respectively in agreement with previous measurements [41-45]. Also, no evidence was obtained for production of CF_3CF, expected first AIE and VIE (10.55 ± 0.02) and (11.49 ± 0.05) eV respectively, although production of C_2F_4 was clearly observed. The molecules observed on pyrolysis of CF_3CHFCF_3, diluted in argon, are HF, $CF_3CF{=}CF_2$ (C_3F_6), C_2F_4, CF_2 and CF_3H. C_3F_6 could be readily identified as it has a characteristic first band in the 10.5-12.0 eV ionisation energy region (see Figure 6.2). HF is also readily observed as it has a sharp first band at 16.04 eV VIE [46]. C_2F_4 and CF_2 were also straightforward to identify as these show broad first bands at VIEs of 10.54 and 12.24 eV respectively [32, 37, 47-49]. The first band of CF_3H at 14.78 eV

could also be seen in pyrolysis spectra, and it was observed more clearly when contributions of C_3F_6 and CF_3CHFCF_3 had been subtracted off.

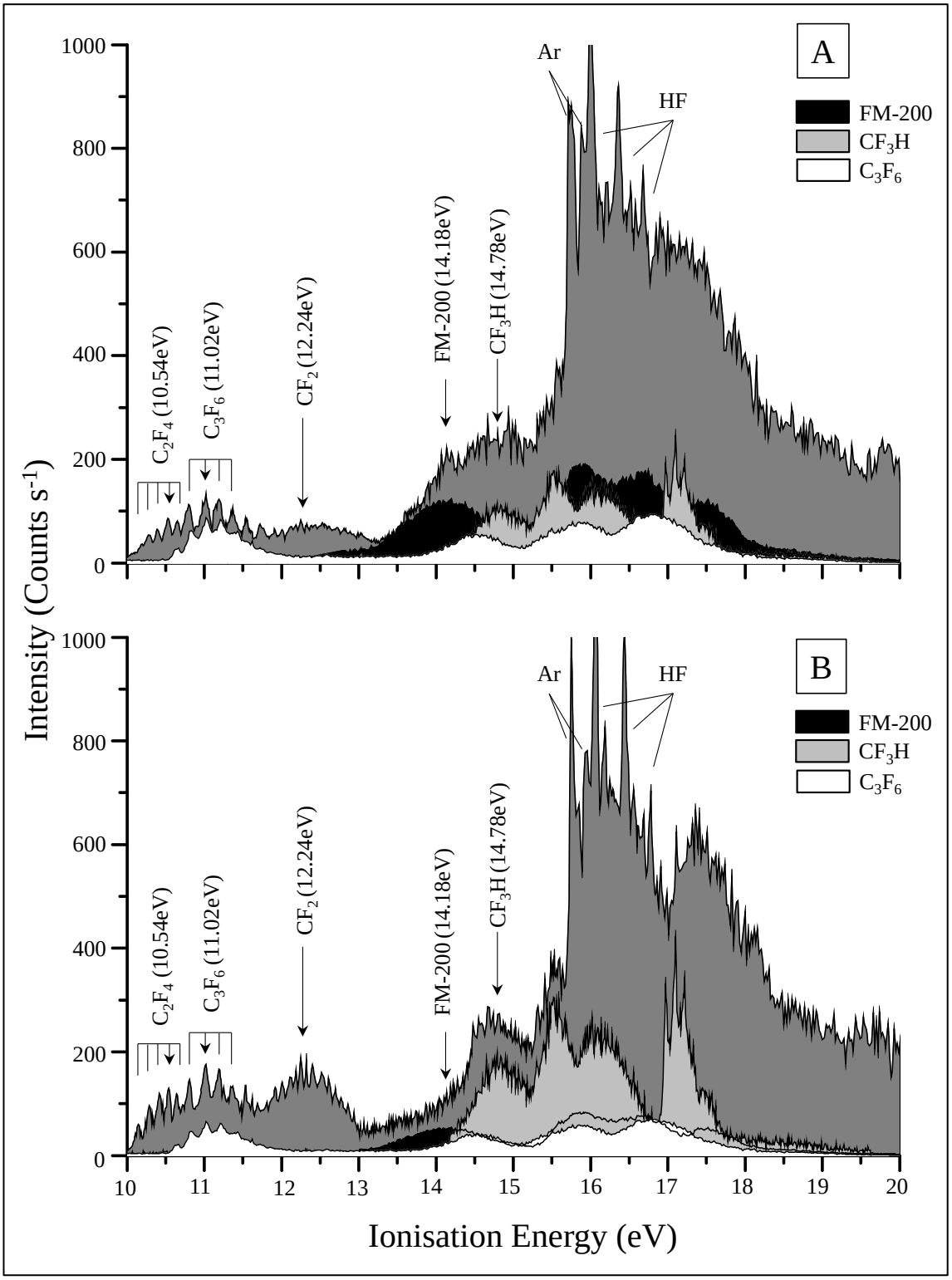

Figure 6.4: *PE spectra recorded from the thermal decomposition of CF_3CHFCF_3 at furnace temperatures of A, 1300 ℃ and B, 1800 ℃.*

The procedure used for analysis of the pyrolysis spectra involved first normalising the intensity of the first band in the photoelectron spectrum of C_3F_6 to the intensity of the corresponding band observed in the pyrolysis spectrum and then subtracting off its overall contribution. This procedure was then repeated for the first band of CF_3CHFCF_3 to subtract off the contributions of CF_3CHFCF_3 from the spectra. Then the calibrated spectrum of CF_3H was used to remove its contributions from the pyrolysis spectra by matching the intensity of the first PE band to the corresponding band seen in a pyrolysis spectrum. Estimating the observed photoelectron band intensities in this way at different furnace temperatures allowed a plot to be made of the normalised band intensities as a function of temperature. This is shown in Figure 6.5.

It should also be noted that in Figures 6.4A and 6.4B, in the ionisation energy region above 16.0 eV, as well as the bands shown from CF_3CHFCF_3, C_3F_6, CF_3H and HF, higher bands of CF_2 and C_2F_4 [47, 49] also contribute.

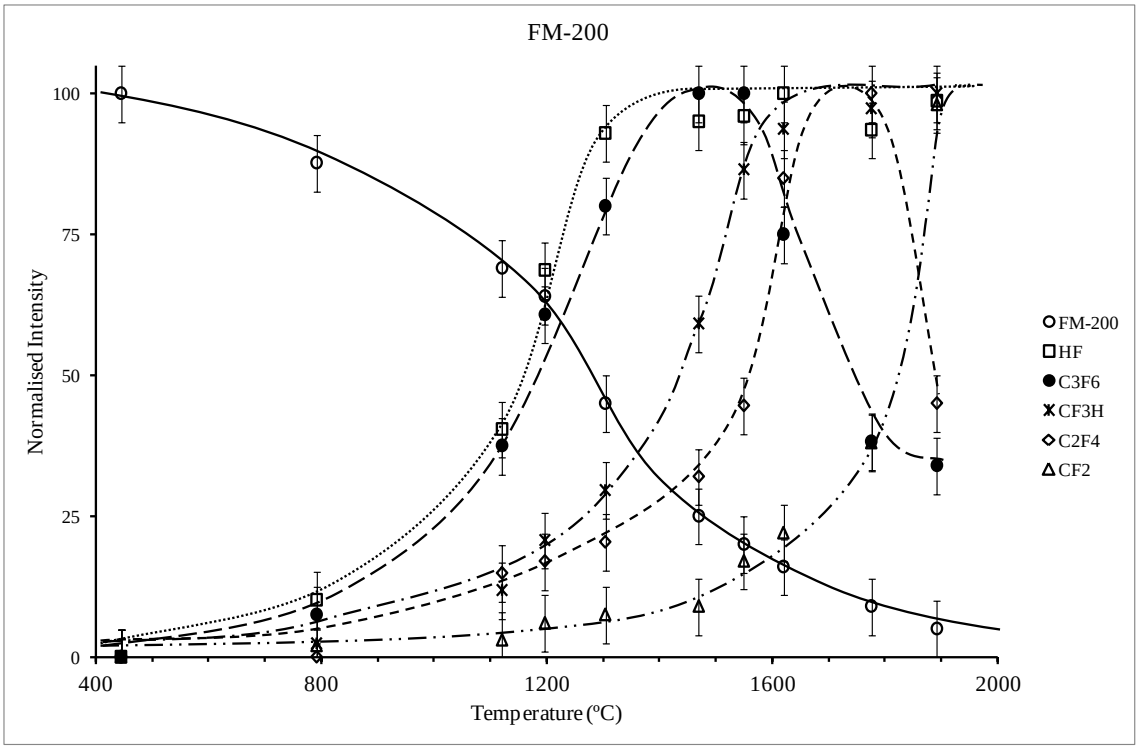

Figure 6.5: *Normalised experimental band intensities of CF_3CHFCF_3 and observed thermal decomposition products plotted as a function of temperature*

It is apparent from Figure 6.5 that CF_3CHFCF_3 undergoes initial thermal decomposition at approximately 600 °C and is fully decomposed by 2000 °C. C_3F_6 and HF are the first decomposition products observed in the region 600-900 °C. HF and C_3F_6 exhibit the

same temperature dependence until 1400 °C where C_3F_6 maximises and then, at higher temperatures, it decomposes to C_2F_4 and CF_2. CF_3H and C_2F_4 are observed from approximately 900 °C and in the temperature region 900-1400 °C appear to exhibit the same temperature dependence. CF_3H reached a plateau at approximately 1600 °C. C_2F_4 appears to maximise at slightly higher temperatures and then decreases as it is converted into CF_2. CF_2 increases steadily from 1200 °C and reaches a plateau at approximately 1850 °C.

On the basis of this evidence, it appears that at the lowest temperatures at which decomposition occurs 600-900 °C, C_3F_6 and HF are produced by reaction (6.1)

$$CF_3CHFCF_3 \rightarrow CF_3CF{=}CF_2 + HF \qquad (6.1)$$

This is then followed by reaction (6.3)

$$CF_3CHFCF_3 \rightarrow C_2F_4 + CF_3H \qquad (6.3)$$

and decomposition of C_3F_6 to give C_2F_4 and CF_2 via reaction (6.4)

$$CF_3CF{=}CF_2 \rightarrow C_2F_4 + CF_2 \qquad (6.4)$$

Heats of reactions for (6.1), (6.3) and (6.4) are $\Delta H_{f,298K}^{Ø}$ = (30.1 ± 3.6) kcal.mol^{-1}, $\Delta H_{f,298K}^{Ø}$ = (43.8 ± 3.6) kcal.mol^{-1} and $\Delta H_{f,298K}^{Ø}$ = (69.0 ± 2.2) kcal.mol^{-1} respectively. Reaction (6.3) appears to be more important than reaction (6.4) in the temperature range 900-1400 °C whereas reaction (6.4) is more important above 1400 °C. Above 1700 °C, C_2F_4 produced by both reactions (6.3) and (6.4) is decomposed to CF_2. Use of the most reliable $\Delta H_{f,298K}^{Ø}$ values leads to the reaction enthalpies shown above. In deriving these values, the heat of formation of CF_3CHFCF_3, obtained from a previous computational study $\Delta H_{f,298K}^{Ø}$ = (-370.6 ± 2.3) kcal.mol^{-1} [10] and the heat of formation of $CF_3CF{=}CF_2$ of $\Delta H_{f,298K}^{Ø}$ = (-275.3 ±1.1) kcal.mol^{-1} [50, 51] were used. The heats of formation of HF, CF_2, C_2F_4 and CF_3H used in these calculations were as used in previous earlier work (see Chapter 5).

In reference [6], a computational study of the thermal decomposition pathways of CF_3CHFCF_3 has been made. The enthalpies of twelve possible decomposition reactions have been calculated and the energy barriers for the five least endothermic reactions

have been evaluated. The enthalpies and energy barriers obtained for these five reactions are summarised in Table 6.8.

Reaction No; this work	Reaction No; Ref.[6]	Products	Reaction enthalpy kcal.mol^{-1} $\Delta H_{f,298K}^{\varnothing}$	Forward barrier height (0 K) kcal.mol^{-1}
2	1A	$CF_3CHF + CF_3$	92.3	not calculated
-	10	$CF_3CH + CF_4$	90.2	127.4
-	11	$CF_3CF + CF_3H$	81.9	97.6
-	2	$CF_3CF_3 + CHF$	79.2	127.4
-	12	$CF_3CF_2H + CF_2$	58.1	118.2
1	4	$CF_3CF=CF_2 + HF$	34.8	79.5

Table 6.8: *Reaction enthalpies and forward barrier heights computed using ab initio methods from the work of Peterson and Francisco [6], for the primary decomposition paths of CF_3CHFCF_3.*

As can be seen, the least endothermic reaction with the smallest activation energy is the dominant reaction observed in the present work. No evidence for the other reactions was obtained. For example, no evidence was obtained for production of $CF_3CF_2H + CF_2$, the next reaction expected on energetic grounds to participate. The photoelectron spectrum of CF_3CF_2H is well established from previous work (see Chapter 5), but no CF_3CF_2H was seen in the pyrolysis spectra. Also, there was no evidence of production of $CF_3CF + CF_3H$ ($\Delta H_{r,0K}^{\varnothing}$ calculated in reference [6] as 81.9 kcal.mol^{-1}). However, production of $C_2F_4 + CF_3H$ was observed. Using the energy of the reaction for conversion of C_2F_4 into CF_3CF of 18.0 kcal.mol^{-1} [40], the $\Delta H_{r,0K}^{\varnothing}$ value for production of $C_2F_4 + CF_3H$ can be calculated as 63.9 kcal.mol^{-1} i.e. the 81.9 kcal.mol^{-1} value of ref.[6] reduced by 18.0 kcal.mol^{-1}, which compares favourably with the enthalpy of reaction (6.3) of (69.0 ± 2.2) kcal.mol^{-1} evaluated using available heats of formation (see above). Decomposition of CF_3CFHCF_3 into $C_2F_4 + CF_3H$ rather than into $CF_3CF + CF_3H$ appears to be dominant under the experimental conditions used.

These studies have monitored the gas-phase products as a function of temperature in a flow system and are therefore valuable in providing information on how CF_3CHFCF_3 decomposes on heating. It should be noted, however, that they provide no information on the mechanism of the decomposition reactions. For example, some decomposition of CF_3CHFCF_3 on the heated furnace surface or decomposition via a free radical mechanism, involving for example CF_3 or CF_3CHF, could be taking place although no bands from these radicals were seen in the pyrolysis spectra.

In the earlier study on CF_3CHF_2, reported in Chapter 5, it was found that in the temperature range 700-1000 °C, under the conditions used, the dominant decomposition reaction is elimination of HF, as in the case of CF_3CFHCF_3 i.e.

$$CF_3CHF_2 \rightarrow C_2F_4 + HF \quad (5.5)$$

followed by

$$C_2F_4 \rightarrow 2CF_2 \quad (5.6)$$

Above 1000 °C, reaction (6.7) occurs

$$CF_3CHF_2 \rightarrow CF_2 + CF_3H \quad (5.7)$$

Tests of relative fire suppression efficiencies of a number of HFCs show that the suppression efficiency increases with the number of CF_3 groups in the suppressant, with CF_3CHFCF_3 being more efficient that CF_3CHF_2 [53]. HFCs suppress flames by two main mechanisms [54], physical cooling of the flame and associated solid surfaces, and chemical reaction of the suppressant and its decomposition products with key flame propagating reactive intermediates such as H, O, and OH. The molar specific heat capacity of CF_3CFHCF_3 is greater than that of CF_3CHF_2 [53] and therefore CF_3CHFCF_3 will be more effective at physically cooling a flame than CF_3CHF_2.

CF_2 is known to be a key intermediate in reacting with flame intermediates such as H, O and OH [54]. The results of this work indicate that it is produced in significant partial pressures earlier in the pyrolysis at lower temperatures from CF_3CHF_2 (see Chapter 5) than from CF_3CHFCF_3. However, H, O and OH will also react with $CF_3CF=CF_2$ and $CF_2=CF_2$ produced from decomposition of CF_3CHFCF_3, and $CF_2=CF_2$ produced from decomposition of CF_3CHF_2. As shown in this work, $CF_3CF=CF_2$ is produced early in the pyrolysis at relatively low temperatures from CF_3CHFCF_3. It is the combined effect of all these reactions, as well as the physical cooling effect, which will determine the efficiency of a fire suppressant in a particular flame. Further studies are clearly needed, involving both experimental work and flame modelling, to establish the relative importance of these and other reactions in a flame.

6.4 Conclusion

The pyrolysis products of CF_3CHFCF_3, diluted in argon at low pressure, have been studied as a function of temperature. The results have been interpreted in terms of two decomposition reactions, reaction (6.1) and (6.3), as well as the reaction $CF_3CF{=}CF_2 \rightarrow C_2F_4 + CF_2$.

The photoelectron spectrum of CF_3CHFCF_3 has been interpreted using state-of-the-art *ab initio* calculations and the first band has been shown to consist of ionisations from both of the outermost filled molecular orbitals, the 18a″ and 23a′ orbitals. Comparison has been made between the threshold photoelectron spectrum and the photoelectron spectrum of $CF_3CF{=}CF_2$. The first band in the threshold spectrum is a lot weaker than in the photoelectron spectrum, and the higher energy bands, above 13.5 eV, appear less well resolved in the TPE spectrum. This arises because autoionisation from high-lying Rydberg states, which are parts of a series converging to higher ionisation thresholds, contribute to the intensity in the higher ionisation energy region of the TPE spectrum. This effect has been observed before in two other fluorinated hydrocarbons, CF_3CHF_2 (see Chapter 5) and c-C_5F_8 [52].

The most favoured reaction, thermodynamically, to produce $CF_3CF{=}CF_2 + HF$, is found to be the main decomposition reaction at lower temperatures, 600-900 °C. At higher temperatures, 900-1200 °C, the decomposition reaction which gave $C_2F_4 + CF_3H$ was found to become important. No evidence for $CF_3CHFCF_3 \rightarrow CF_3CHF + CF_3$, a reaction expected to be important from a shock tube study, performed at much higher pressures, or for $CF_3CHFCF_3 \rightarrow CF_3CF + CF_3H$ was obtained, although for the latter reaction it is likely that CF_3CF converts into C_2F_4 under the conditions used before photoionisation in the ionisation region of the photoelectron spectrometer. At higher temperatures C_3F_6 decomposes to $C_2F_4 + CF_2$, and C_2F_4 decomposes to CF_2. *Ab initio* calculations have been performed of the adiabatic and vertical ionisation energies (VIE) of possible primary pyrolysis products to assist assignment of the photoelectron spectra recorded for heated flowing gas samples. A comparison is made between the threshold photoelectron (TPE) spectrum and the photoelectron spectrum (PE) of $CF_3CF{=}CF_2$.

References

[1] R. G. Hynes, J. C. Mackie and A. R. Masri, *J. Phys. Chem. A.*, 103, 1999, 54.

[2] T. Yamamoto, A. Yasuhara, F. Shiraishi, K. Kaya and T. Abe, *Chemosphere*, 35, 1997, 643.

[3] R. G. Hynes, J. C. Mackie and A. R. Masri, *Combustion Flame*, 113, 1998, 554.

[4] B. A. Williams, D. M. L'Esperance and J. W. Fleming, *Combustion Flame*, 120, 2000, 160.

[5] O. Sanogo, J. J. Delfrau, R. Akrich and C. Vovelle, *Comb. Sci. Technol.*, 122, 1997, 33.

[6] S. D. Peterson and J. S. Francisco, *J. Phys. Chem. A.*, 116, 2002, 3106.

[7] D. McNaughton and J. C. Evans, *Spectrochim. Acta. A.*, 55, 1999, 1177.

[8] E. D. Lancaster, K. L. McNesby, R. G. Daniel and A. W. Miziolek, *Applied Optics*, 38, 1999, 1476.

[9] S. H. Modiano, K. L. McNesby, P. E. Marsh, W. Bolt and C. Herud, *Applied Optics*, 35, 1996, 4004.

[10] E. P. F. Lee, J. M. Dyke, W. K. Chow, F. T. Chau and D. K. W. Mok, *Chem. Phys. Letts.*, 402, 2005, 32.

[11] E. P. F. Lee, J. M. Dyke, W. K. Chow, F. T. Chau and D. K. W. Mok, *Chem. Phys. Letts.*, 417, 2006, 256.

[12] E. P. F. Lee, J. M. Dyke, W. K. Chow, F. T. Chau and D. K. W. Mok, *J. Comp. Chem.*, 28, 2007, 1582.

[13] A. Morris, J. M. Dyke, G. D. Josland, M. P. Hastings, and P. D. Francis, *High Temp. Science*, 22, 1986, 95.

[14] D. Bulgin, J. M. Dyke, F. Goodfellow, N. Jonathan, E. P. F. Lee and A. Morris, *J. Elect. Spectrosc. Rel. Phenom.*, 12, 1977, 67.

[15] K. Kimura, S. Katsumata, Y. Achiba, T. Yamasaki and S. Iwata, Handbook of HeI Photoelectron Spectra, *Japan Scientific Press, Tokyo*, 1981.

[16] D. W. Turner, C. Baker, A. D. Baker and C. R. Brundle, Molecular Photoelectron Spectroscopy, *Wiley Interscience, London*, 1970.

[17] D. R. Lloyd, *J. Phys. E.*, 3, 1970, 269.

[18] M. J. Frisch, G. W. Trucks, H. B. Schlegel, G. E. Scuseria, M. A. Robb, J. R. Cheeseman, J. A. Montgomery Jr., T. Vreven, K. N. Kudin, J. C. Burant, J. M. Millam, S. S. Iyengar, J. Tomasi, V. Barone, B. Mennucci, M. Cossi, G.

Scalmani, N. Rega, G. A. Petersson, H. Nakatsuji, M. Hada, M. Ehara, K. Toyota, R. Fukuda, J. Hasegawa, M. Ishida, T. Nakajima, Y. Honda, O. Kitao, H. Nakai, M. Klene, X. Li, J. E. Knox, H. P. Hratchian, J. B. Cross, V. Bakken, C. Adamo, J. Jaramillo, R. Gomperts, K. Raghavachari, J. B. Foresman, J. V. Ortiz, Q. Cui, A. G. Baboul, S. Clifford, J. Cioslowski, B. B. Stefanov, G. Liu, A. Liashenko, P. Piskorz, I. Komaromi, R. L. Martin, D. J. Fox, T. Keith, M. A. Al-Laham, C. Y Peng, A. Nanayakkara, M. Challacombe, P. M. W. Gill, B. Johnson, W. Chen, M. W. Wong, C. Gonzalez and J. A. Pople, *Gaussian 03, Revision E.01, Gaussian, Inc., Wallingford CT*, 2004.

[19] H. J. Werner, P. J. Knowles, R. Lindh, F. R. Manby, M. Schütz, P. Celani, T. Korona, G. Rauhut, R. D. Amos, A. Bernhardsson, A. Berning, D. L. Cooper, M. J. O. Deegan, A. J. Dobbyn, F. Eckert, C. Hampel, G. Hetzer, A. W. Lloyd, S. J. McNicholas, W. Meyer, M. E. Mura, A. Nicklass, P. Palmieri, R. Pitzer, U. Schumann, H. Stoll, A. J. Stone, R. Tarroni and T. Thorsteinsson, *MOLPRO*, a package of *ab initio* programs, 2008.

[20] A. Halkier, T. Helgaker, W. Klopper, P. Jorgensen and A. G. Csaszar, *Chem. Phys. Letts.*, 310, 1999, 385.

[21] ACES II (version 2.6.0 release 2, Jan. 2006) is a program product of the Quantum Theory Project, University of Florida. Authors: J. F. Stanton, J. Gauss, J. D. Watts, M. Nooijen, N. Oliphant, S. A. Perera, P. G. Szalay, W. J. Lauderdale, S. A. Kucharski, S. R. Gwaltney, S. Beck, A. Balková, D. E. Bernholdt, K. K. Baeck, P. Rozyczko, H. Sekino, C. Hober and R. J. Bartlett, Integral packages included are VMOL (J. Almlöf and P. R. Taylor); VPROPS; (P. Taylor) ABACUS; (T. Helgaker, H. J. Aa, P. Jensen, P. Jørgensen, J. Olsen and P. R. Taylor).

[22] J. R. Nielsen and H. H. Claasen, *J. Chem. Phys.*, 20, 1952, 1916.

[23] W. R. Cullen, D. C. Frost and W. R. Leeder, *J. Fluorine Chem.*, 1, 1971/72, 227.

[24] B. S. Freiser and J. L. Beauchamp, *J. Am. Chem. Soc.*, 96, 1974, 6260.

[25] G. K. Jarvis, K. J. Boyle, C. A. Mayhew and R. P. Tuckett, *J. Phys. Chem. A.*, 102, 1998, 3230.

[26] C. Zazza, L. Bencivenni and M. Aschi, *Chem. Phys. Letts.*, 399, 2004, 184.

[27] K. Hirao, K. Takao, T. Iino, F. Nakagawa, H. Suyama, T. Mizuno and S. J. Yamabe, *J. Phys. Chem. A.*, 106, 2002, 603.

[28] G. A. Garcia, P. M. Guyon and I. Powis, *J. Phys. Chem. A.*, 105, 2001, 8296.

[29] R. L. Asher and B. Ruscic, *J. Chem. Phys.*, 106, 1997, 210.

[30] M. Horn, M. Oswald, R. Oswald and P. Botschwina, *Ber. Bunsenges Phys. Chem.*, 99, 1995, 323.

[31] J. M. Bowman, X. Huang, L. B. Harding and S. Carter, *Mol. Phys.*, 104, 2006, 33.

[32] G. K. Jarvis and R. P. Tuckett, *Chem. Phys. Letts.*, 295, 1998, 145.

[33] Y. Chen, A. Rauk and E. J. Tschuikow-Roux, *J. Chem. Phys.*, 94, 1991, 7299.

[34] J. E. O'Gara and W. P. Dailey, *J. Am. Chem. Soc.*, 114, 1992, 3582.

[35] V. M. Garcia, O. Castell, M. Reguero and R. Cabarallol, *Mol. Phys.*, 87, 1996, 1395.

[36] D. A. Dixon, D. Feller and G. J. Sandrone, *J. Phys. Chem. A.*,103, 1999, 4744.

[37] F. Innocenti, M. Eypper, E. P. F. Lee, S. Stranges, D. K. W. Mok, F. T. Chau, G. C. King G.C. and J.M. Dyke, *Chem. Eur. J.*, 14, 2008, 11452.

[38] R. J. Boyd and K. E. Edgecombe, *J. Am. Chem. Soc.*, 110, 1988, 4182 .

[39] L. Gong, M. A. McAllister and T. T. Tidwell, *J. Am. Chem. Soc.*, 113, 1991, 6021.

[40] J. J. DiFelice and E. R. Ritter, *Comb. Sci. Technol.*, 116, 1995, 5.

[41] I. G. Simm, C. J. Danby and J. H. D. Eland, *Int. J. Mass. Spectrom. Ion. Phys.*, 14, 1974, 285.

[42] I. G. Simm, C. J. Danby and J. H. D. Eland and P. I. Mansell, *J. C. S. Faraday II*, 72, 1976, 426.

[43] B. P. Pullen, T. A. Carlson, W. E. Moddeman, G. K. Schweitzer, W. E. Bull and F. A. Grimm, *J. Chem. Phys.*, 53, 1970, 768.

[44] C. R. Brundle, M. B. Robin and H. Basch, *J. Chem. Phys.*, 53, 1970, 2196.

[45] M. A. Parkes, R. Y. L. Chim, C. A. Mayhew, V. A. Mikhailov and R. P. Tuckett, *Mol. Phys.*, 104, 2006, 263.

[46] J. Berkowitz, *Chem. Phys. Letts.*, 11, 1971, 21.

[47] S. Eden, P. Limao-Vieira, P. A. Kendall, N. J. Mason, J. Delwiche, M. J. Hubin-Franskin, T. Tanaka, M. Kitajima, H. Tanaka, H. Cho and S. V. Hoffman, *Chemical Physics*, 297, 2004, 257.

[48] R. F. Lake and H. Thompson, *Proc. Roy. Soc. A*, 315, 1970, 323.

[49] J. M. Dyke, L. Golob, N. Jonathan, A. Morris and M. Okuda, *J.C.S.Faraday II*, 70, 1974, 1828.

[50] N. L. Haworth, M. H. Smith, G. B. Bacskay and J. C. Mackie, *J. Phys. Chem. A.*, 104, 2000, 7600.

[51] T. S. Papina, V. P. Kolesov and Y. G. Golovanova, *Russ. J. Phys. Chem.*, 61, 1987, 1168.

[52] M. A. Parkes, A. Sahangir, R. P. Tuckett, V. A. Mikhailov and C. A. Mayhew, *Phys. Chem. Chem. Phys.*, 9, 2007, 5222.

[53] E. J. P. Zegers, B. A. Williams, E. M. Fischer, J. W. Fleming and R. S. Shienson, *Combustion and Flame*, 121, 2000, 471.

[54] W. K. Chow, E. P. F. Lee, F. T. Chau and J. M. Dyke, *Architectural Science Review*, 47, 2004, 223.

Chapter 7

Study of the Ethene + Ozone Reaction with PES: Measurement of Product Branching Ratios and Atmospheric Implications

The reactions of ozone with alkenes have been the subject of numerous research investigations, largely because of their importance in atmospheric chemistry [1]. They are important in air pollution processes in urban areas and are significant loss processes for both ozone and alkenes in the atmosphere [2-4]. Globally alkenes account for most of the non-methane hydrocarbon emissions in the troposphere. Sources include automobile exhausts, industrial emissions and vegetation.

It is now generally accepted that ozonolysis of alkenes follows the mechanism proposed by Criegee [5, 6]. This involves three main steps [7],

1. Formation of a primary ozonide by addition of ozone to the double bond of the alkene.
2. Decomposition of the primary ozonide into a carbonyl compound and a carbonyl oxide (a Criegee intermediate).
3. A subsequent reaction of the Criegee intermediate with the reagents and products.

Whilst there is considerable experimental support for this mechanism, no Criegee intermediate has so far been observed and studied in the gas-phase with spectroscopic methods, although there is evidence for the presence of a Criegee intermediate in gas-

phase mass spectrometric studies and in infrared matrix isolation experiments [8-10]. In a recent study of the products of the reaction of CH_3SOCH_2 with O_2 with photoionisation mass spectrometry using synchrotron radiation [8], a signal was observed in the m/z = 46 mass channel. By measuring its intensity as a function of photon energy, a photoionisation onset was determined as (10.00 ± 0.02) eV. Supporting evidence was provided from electronic structure calculations that this arises from photoionisation of the Criegee intermediate CH_2OO and not its isomer dioxirane [8], which had been observed in earlier studies in the gas-phase by microwave spectroscopy and photoionisation mass spectrometry [11, 12]. In these experiments [11, 12], ozone and ethene were condensed on a surface cooled to liquid nitrogen temperature. The surface was then allowed to warm and the vapour above the solid was sampled by a mass spectrometer and a microwave spectrometer [11, 12]. Also, in matrix isolation infrared studies of ozone reactions with cis-2-butene, cyclopentene and cyclopentadiene, evidence was presented in each case for the formation and identification of a Criegee intermediate, as well as the associated primary ozonide [9, 10].

A number of studies of the ethene-ozone reaction have been made by electronic structure calculations [13-17]. The reaction is found to be highly exoergic with the formation of the primary ozonide calculated to be exothermic by 49 kcal.mol^{-1}. Decomposition of the primary ozonide into formaldehyde and the Criegee intermediate is 2 kcal.mol^{-1} endothermic with respect to the primary ozonide (exothermic by 47 kcal.mol^{-1} relative to the reagents) and conversion of the Criegee intermediate into formic acid is calculated to be exothermic by 102 kcal.mol^{-1} [13, 14].

Previous experimental studies of the ethene-ozone reaction include measurement of rate coefficients and branching ratios [18-33]. Product branching ratios have been measured using a number of methods, notably photoionisation mass spectrometry (PIMS) at low pressure [23, 24], and gas-phase and matrix isolation infrared spectroscopy [25-30], and chromatography [31, 32] of the reaction mixture heavily diluted in synthetic air at atmospheric pressure. It is clear from this work that while the rate coefficient has been measured experimentally at room temperature and over a temperature range, the reaction products and product branching ratios have only been partially established. Comparison of the experimental product branching ratios reported in different studies shows only modest agreement, probably because in each study the detection technique

used is only capable of detecting some but not all of the products. For example, formic acid has been observed in some of the studies and molecular oxygen, a major reaction product, has also been observed previously but there have been no measurements of the product yield [1].

Ultraviolet photoelectron spectroscopy is a method which can in principle be used to detect all reaction products, provided sufficient number densities are present in the photoionisation region. The aim of this work is to use this method to study the products of the ozone-ethene reaction as a function of time. The measured product yields will then be used in a global atmospheric model to estimate the annual global budgets of the observed products from this reaction.

7.1 Experimental

7.1.2 Photoelectron (PE) Spectra Recorded as a Function of Time

PE spectra were recorded for the ozone-ethene reaction at low pressure (~5 torr total pressure) at different reaction times (0-15 s) using a glass flow-tube, operated under laminar flow conditions, attached to the ionisation chamber of a PE spectrometer. The spectrometer used was a 10 cm mean radius hemispherical analyser instrument which uses a HeI photon source (21.22 eV), and has been described previously [34-36]. The ethene-ozone reaction is a slow reaction with a rate coefficient of 1.72×10^{-18} cm^3 $molecule^{-1}$ s^{-1} at 298 K [18]. As a result, a long flow-tube was used (30 m long; id 10 mm; open-ended into the spectrometer), with six equally spaced vacuum tap inlets along its length. During a typical experiment, ozone was passed along the length of the flow-tube and ethene (Aldrich 99.5%) was introduced through one of the equally spaced vacuum taps. In this way, PE spectra could be recorded as a function of mixing distance.

Ozone was made by a silent electric discharge of flowing oxygen and stored on non-indicating silica gel held at -78 °C in a dry-ice/acetone slush bath as described previously [37, 38]. The presence of O_3 on the gel was indicated by a deep blue colouration. In practice, ozone could be stored safely for as long as the slush bath was maintained. The U-tube containing the ozone on the silica gel was connected to the flow tube via a stainless steel needle valve. Initially the needle valve was opened slightly, to

remove residual oxygen from the U-tube. Removal of oxygen was checked by recording spectra at approximately 15 minute intervals. After about 1 hour, the needle valve was opened wider and a spectrum of ozone could be obtained with little or no contribution from oxygen. In a typical experiment, the pure ozone supply was maintained at constant pressure and this was checked at different stages during the experiment and at the end of the experiment. Pressure measurements were made every 5 m along the flow-tube using calibrated baratron pressure transducers. Using these measurements, the flow-rate and flow velocity could be calculated at each reaction mixing distance using the Poiseuille equation. In this way, a plot of PE band intensities of the reagents and products as a function of mixing distance could be converted to a plot of PE band intensities of the reagents and products as a function of reaction time. Calculations were also made of the Reynolds number, using the measured flow-rates, and these were consistent with laminar flow in the flow-tube.

7.2 Photoionisation Cross-Section Measurements

In order to convert plots of relative PE band intensities versus reaction time to plots of partial pressures versus reaction time, it is necessary to determine the photoionisation cross-sections of the reagents, ethene and ozone, and the observed products at the angle of detection of photoelectrons with respect to the unpolarised photon beam (90°) and at the photon energy used (21.22 eV). The method used has been developed from that used earlier to study the DMS + Cl_2 reaction [36, 39].

It involved making up a sample of known partial pressures of the molecule of interest and argon in a 7.3 L bulb in helium to a total pressure of 1 atm. (e.g. a mixture of ethylene (5%) and argon (5%) in helium). The sample was then admitted to a differentially pumped stainless-steel flow-tube, interfaced to a PE spectrometer (with a 20 cm mean radius analyser) at a known flow-rate (typically 100 sccm) using a calibrated mass flow-controller, as described previously [36, 39]. A second calibrated mass flow controller was used to admit the carrier gas (helium) to the flow-tube at a fixed flow-rate (typically 1 slm). PE spectra were then recorded with the objective of measuring the intensity of a selected PE band of the molecule of interest (the band monitored as a function of time in the ethene-ozone experiments; this was usually the first band of the selected molecule) relative to the argon $(3p)^{-1}$ PE bands. Also, the full PE spectrum of oxygen was recorded twice before sampling and twice after sampling.

These spectra were used in the analysis procedure to correct for any change in the transmission of the spectrometer during the sampling experiments. In most cases, the change in transmission during sampling was found to be small. From the experimental spectra, the area of the selected band of the molecule of interest, including all vibrational components, relative to the area of both spin-orbit components of the argon $(3p)^{-1}$ ionisation was measured. At least ten measurements were made in this way and the average value determined. This ratio was then corrected for the relative partial pressures of the sample and argon in the sample bulb. This is the photoionisation cross-section (PI-CS) on the spectrometer of the selected band of the molecule relative to the argon $(3p)^{-1}$ ionisation. The PI-CS values derived in this way and used in the analysis of the spectra recorded for the ethene-ozone reaction are shown in column 2 of Table 7.1. However, in order to obtain absolute photoionisation cross-sections from the known photoionisation cross-section of argon, a correction must be made for the transmission of the analyser (this is an electron kinetic energy correction) and for the angular distribution parameters of the selected bands of both the molecule and argon. These values are shown in columns 3 and 4 of Table 7.1 respectively. As can be seen, the electron kinetic energy correction is much bigger than the angular distribution correction.

Molecule	PI-CS on the Spectrometer	PI-CS Corrected for e.K.E	PI-CS Corrected for e.K.E and Angular Distribution (a)	Literature PI-CS (Mb) (b)	Literature PI-CS relative to argon (c)
Argon	1	1	1	37.1 [43]	1
Ethylene	0.49 ± 0.03	0.23 ± 0.02	0.21 ± 0.02	7.2 [44]	0.19
Oxygen	0.38 ± 0.02	0.20 ± 0.02	0.26 ± 0.02	7.42 [45,46]	0.2
Ozone, 3rd band	0.59 ± 0.10	0.34 ± 0.05	0.39 ± 0.0(d)	12.6 [42]	0.33
Carbon Monoxide	0.22 ± 0.01	0.15 ± 0.02	0.15 ± 0.02	7.0 [47]	0.19
Carbon Dioxide	0.22 ± 0.01	0.16 ± 0.01	0.20 ± 0.01	10.28 [48,49]	0.28
Acetaldehyde	0.63 ± 0.05	0.32 ± 0.02	0.36 ± 0.02	-	-
Formaldehyde	0.32 ± 0.02	0.15 ± 0.01	0.17 ± 0.01	8.47 [50,51]	0.19
Water	0.27 ± 0.07	0.18 ± 0.05	0.18 ± 0.05	6.61 [52]	0.18
Formic Acid	0.80 ± 0.10	0.40 ± 0.02	0.40 ± 0.02	15.0 [53]	0.4

Table 7.1*: Comparison of photoelectron band Photoionisation Cross-Sections (PI-CS) relative to argon. The first band of all the molecules has been used in the measurements, unless otherwise stated.*

(a) Photoionisation cross-sections measured relative to argon (this work).

(b) Available literature photoionisation cross-sections (measured in Mb, 10^{-18} cm^2).

(c) Literature photoionisation cross-sections measured relative to argon at 37.1 Mb [43] and normalised to 1.

(d) Total cross-section at hν = 16.0 eV taken as 31 Mb [42]; the cross-section for the third band was obtained by measuring its area relative to the total area (bands 1-3 in the He(I) spectrum).

This method to determine PE band cross-sections relative to argon was used for one of the reactants, ethene, and the products, oxygen, carbon monoxide, carbon dioxide, acetaldehyde, formaldehyde, and water. Formaldehyde was prepared, prior to this procedure, by heating paraformaldehyde to temperatures in excess of 383 K and collecting the gas in a liquid nitrogen trap as described elsewhere [40, 41]. It was then purified by passing it through traps at higher temperatures than 77 K before the argon/formaldehyde sample of known composition was prepared.

Problems were experienced with ozone and formic acid. In the ozone case, this procedure could not be used as it was not possible to make up a sample, mixed with argon, of known concentration and pass it through a mass flow controller without some decomposition into molecular oxygen occurring. In this case, an approximate procedure was used which involved using the measured cross-section of ozone at 16.0 eV photon energy taken from [42] (31.0 Mb; 1Mb = 10^{-18} cm^2). This was assumed to be the measured cross-section of the first three bands of ozone at $h\nu$ = 21.22 eV. This is reasonable as the higher PE bands of ozone from one-electron ionisation occur above 16.0 eV [37]. The experimental relative intensities of the first three bands of ozone were then used to give the photoionisation cross-section for the third band at $h\nu$ = 21.22 eV. The electron kinetic energy and angular distribution parameter correction was then made to give the photoionisation cross-section on the spectrometer, relative to argon, of the ozone third band. This is the value shown for ozone in Table 7.1 column 2. It is quoted with a larger error than the other values because of the approximate procedure used. In the case of formic acid, problems were experienced in obtaining reproducible results for mixtures made up with argon in a bulb, because of its relatively high vapour pressure at room temperature and its tendency to condense on the walls. In this case, an alternative, more approximate, procedure was used which involved admitting formic acid and argon into the PE spectrometer via the side of the ionisation chamber, at known partial pressures as measured by an ionisation gauge. The intensity of the first band of formic acid was then measured relative to the $(3p)^{-1}$ bands of argon. This method was felt to be reasonably reliable as the molecular weights of formic acid and argon are similar. However, the error in the formic acid relative cross-section on the spectrometer quoted in Table 7.1, column 2 is higher than the other values because this approximate method was used.

Also shown in Table 7.1, in column 5, are the available literature cross-sections for the relevant bands of the reagents and the observed reaction products at hν = 21.22 eV [43-53]. Column 6 of Table 7.1 shows the normalised values relative to argon. It can be seen in this table that on comparing column 6 with column 4 (the relative values derived in this work) that reasonably good agreement is obtained, supporting the values used in this work to convert relative PE band intensities into relative molecular partial pressures.

7.3 Description of the Global Model Used

Using the results from this study, the Global Chemistry Transport Model CRI-STOCHEM has been used to estimate the mass of products formed in the atmosphere. The CRI-STOCHEM model is described in detail in references [54, 55]. The model used is an updated version of the UK Meteorological Office tropospheric chemistry transport model (STOCHEM) described by Collins *et al.* [56], with updates reported in detail in the recent paper of Utembe *et al.* [54]. STOCHEM is a global 3-dimensional Chemical Transport Model (CTM) which uses a Lagrangian approach to advect 50,000 air parcels using a 4^{th} order Runge-Kutta scheme with advection time steps of 3 hours. The transport and radiation models are driven by archived meteorological data, generated by the Met office numerical weather prediction models as analysis fields with a resolution of 1.25° longitude and 0.83° latitude and on 12 vertical levels extending to 100 hPa. Full details of the model version employed are given elsewhere [57].

The common representative intermediates mechanism (CRIv2-R5) [58-60], which represents the chemistry of methane and 22 emitted non-methane hydrocarbons, was employed in the model. Each parcel contains the concentrations of 219 species involved in 618 photolytic, gas-phase and heterogeneous chemical reactions, with a 5 minute time step. The formation of secondary organic aerosol (SOA) is represented using 14 species, which are derived from the oxidation of aromatic hydrocarbons, monoterpenes, and isoprene [59].

The surface emissions (man-made, biomass burning, vegetation, oceans, soil and 'other' surface emissions) are distributed using two-dimensional source maps [61]. Emissions totals for the base case run for CO, NO_x and non-methane hydrocarbons are taken from the Precursor of Ozone and their Effects in the Troposphere (POET) inventory [62] for

the year 1998. The emission of the aromatic species ortho-xylene, benzene and toluene were taken from reference [63]. Biomass burning emission of ethyne, formaldehyde and acetic acid are produced using scaling factors from per mole of CO emitted, taken from reference [64]. NASA inventories are used for aircraft NO_x emissions for 1992 taken from [65]. The lightning and aircraft NO_x emissions are monthly averages and are 3-dimensional in distribution.

7.4 Results and Discussion

PE spectra of the ozone-ethene reaction, recorded in the 10.0-14.0 eV ionisation energy region, at constant initial reagent partial pressure at 5.0 and 30.0 m reactant mixing distance are shown in Figure 7.1. Bands associated with the reagents, ethene and ozone, as well as the products, oxygen, formaldehyde, carbon monoxide, carbon dioxide, formic acid and acetaldehyde, can be seen in this figure. A plot of their relative partial pressures as a function of reaction time, obtained from spectra recorded at different mixing distances at constant initial reagent partial pressures, are shown in Figure 7.2.

Because of overlap of the first two bands of ozone with the second band of ethene, the third band of ozone at 13.57 eV was used to monitor ozone partial pressures. Water was also observed as a reaction product but its intensity could not be measured reliably as its first band (at 12.62 eV; AIE = VIE) is overlapped by the ethene second band, the ozone first band and the oxygen first band. Methanol was not observed as a reaction product (first band 10.94 eV [66], AIE = VIE). As can be seen in Figure 7.2, the reagents decrease and the products increase smoothly with reaction time. It was found that for both ethene and ozone the decrease could be fitted to an exponential decay of the form,

$$a.exp^{(-bt)} + c \tag{7.1}$$

and the product increases could be fitted to an exponential increase of the form,

$$a.1 - exp^{(-bt)} \tag{7.2}$$

These fitted curves are shown as solid lines in Figure 7.2, 7.3 and 7.4. Comparison of the product yields measured at the longest mixing distance (reaction time) are shown in Table 7.2. These are expressed relative to the observed change in the reagent not in excess, which was ozone in all the experiments carried out. Also, shown in Table 7.2 is

a comparison with the product yields observed in other studies where product yields were measured [23, 25-28, 32].

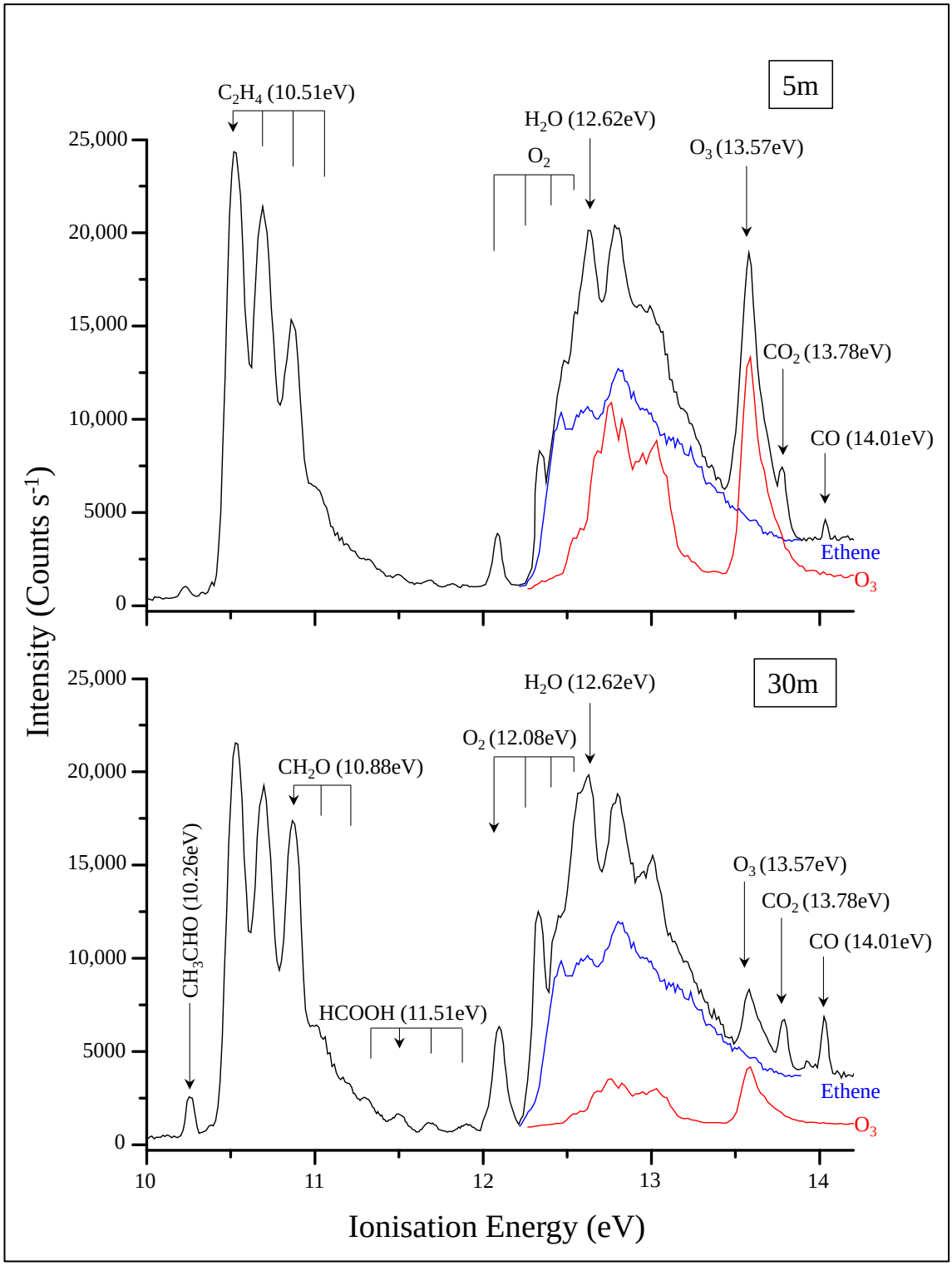

Figure 7.1: *Photoelectron spectra recorded for the ethene-ozone reaction at constant reagent partial pressure, at 298 K for reaction distances of 5 and 30 m.*

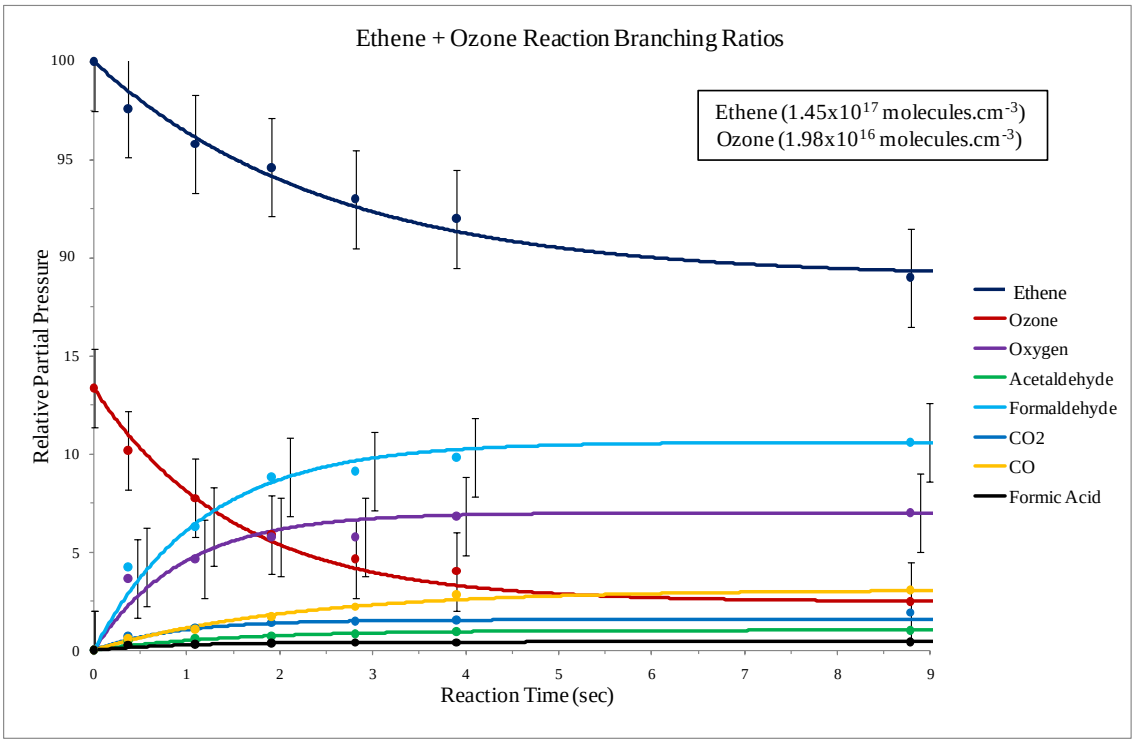

Figure 7.2: *Plot of reagent and product partial pressures as a function of reaction time at 298 K. Error bars have been derived from contributions of the experimental band intensities and experimental cross-sections (for convenience, the error bars on the oxygen and formaldehyde points have been displaced slightly horizontally; no error bars are shown on the minor products; they are shown in Figues 7.3 to 7.5)*

Molecule	This work m(a)	[23](b)	[25] (c)	[26] (d)	[27] (e)	[32] (f)	[28] (g)
H_2CO	0.89 ± 0.09	1.00	0.63 ± 0.11	0.87	0.66 ± 0.11	0.99 ± 0.06	0.92
CO	0.25 ± 0.02	-	0.37 ± 0.03	-	0.28 ± 0.04	-	0.29
CO_2	0.18 ± 0.02	0.27	0.19 ± 0.02	-	0.18 ± 0.03	-	0.20
H_2O	(observed but could not be reliably measured)	0.67	-	-	-	-	-
HCOOH	0.04 ± 0.01	0.06	0.04 ± 0.01	-	0.03 ± 0.01	-	0.04
HPMF(i)	-	-	0.10 ± 0.04	0.35 ± 0.05	dominant	-	0.18 (h)
$(CHO)_2O$	-	-	0.24 ± 0.05	-	< 0.001	-	-
O_2	0.60 ± 0.06	-	-	-	-	-	-
CH_3CHO	0.09 ± 0.01	-	-	-	-	-	-

Table 7.2: *Observed products and measured product yields of the ethene-ozone reaction in this work, compared to those of previous work.*

(a) expressed in terms of the observed change in the reagent not in excess
(b) Herron and Huie 1977 PIMS study; O_3 in O_2 reacted with ethene at low pressure (8 torr total)
(c) Su *et al.* 1980 IR study in air at close to 1 atm. pressure
(d) Niki *et al.* 1981 IR study in air at close to 1 atm. pressure
(e) Horie and Moortgat 1991 IR study in synthetic air close to 1 atm. pressure
(f) Grosjean and Grosjean 1996 study in air at 1 atm. pressure; analysis of carbonyl products with chromatography; cyclohexane scavenger added
(g) Neeb *et al.* (1998) IR study in air at close to 1 atm.
(h) HPMF + Formic Anhydride $(CHO)_2O$
(i) HPMF is hydroperoxy methylformate, $CH_2(OOH)CHO$

As can be seen, from this table, within experimental error, good agreement is obtained in this work with the results of other studies for the product yields of H_2CO, CO, CO_2 and HCOOH. However, no evidence was obtained for production of formic anhydride, $(HCO)_2O$, (1^{st} band expected at 11.32 eV; AIE = VIE [67]) or hydroperoxy methylformate (HPMF) , CH_2 (OOH)CHO which have been observed in other studies. The PE spectrum of HPMF does not appear to have been recorded previously but, based on the known spectrum of methyl formate [66]; it is expected to have a broad first band in the 10.0-11.0 eV ionisation energy region. The HPMF is thought to arise from reaction of the Criegee intermediate (H_2CO_2) with formic acid and decomposition of HPMF to $(HCO)_2O + H_2O$ occurs via a heterogeneous process [26, 28, 68]. Given the low yield of formic acid in this work, it is perhaps not surprising that HPMF and $(HCO)_2O$ are not observed. Two other products observed in this work were O_2 and CH_3CHO. Although both of these products have been observed in other studies, they were not observed in the references used for Table 7.2, studies where relative product yields were measured [23, 25-28, 32]. O_2, a significant product, will not be observed in infrared studies as it is infrared inactive [25-27] and acetaldehyde may not have been observed in the previous work summarised in Table 7.2 [23, 25-28, 32] as it is produced in low yield. In the first documented study of this reaction by Cvetanovic *et al.* [69], acetaldehyde was detected using gas-liquid chromatography to analyse the products (0.02 moles of acetaldehyde was observed for each mole of ozone consumed), and Kuhne *et al.* [70] observed both oxygen and acetaldehyde in a study of this reaction at low pressure (2 torr) using infrared matrix isolation spectroscopy, mass spectrometry and microwave spectroscopy.

7.5 Kinetics Simulations

In order to propose a series of reactions which are consistent with the observed product yields and temporal profiles, and provide explanations for the main production reactions of the observed products, a series of box model calculations have been carried out using ACUCHEM [71]. The three published reaction schemes were initially used to simulate the results obtained [23, 27 and 30]. In each case good agreement was obtained with the published simulations with the reaction scheme of Heron and Huie [23] giving the best agreement with the experimental results. Comparison of these simulations [23] with the experimental results is shown in Figure 7.3.

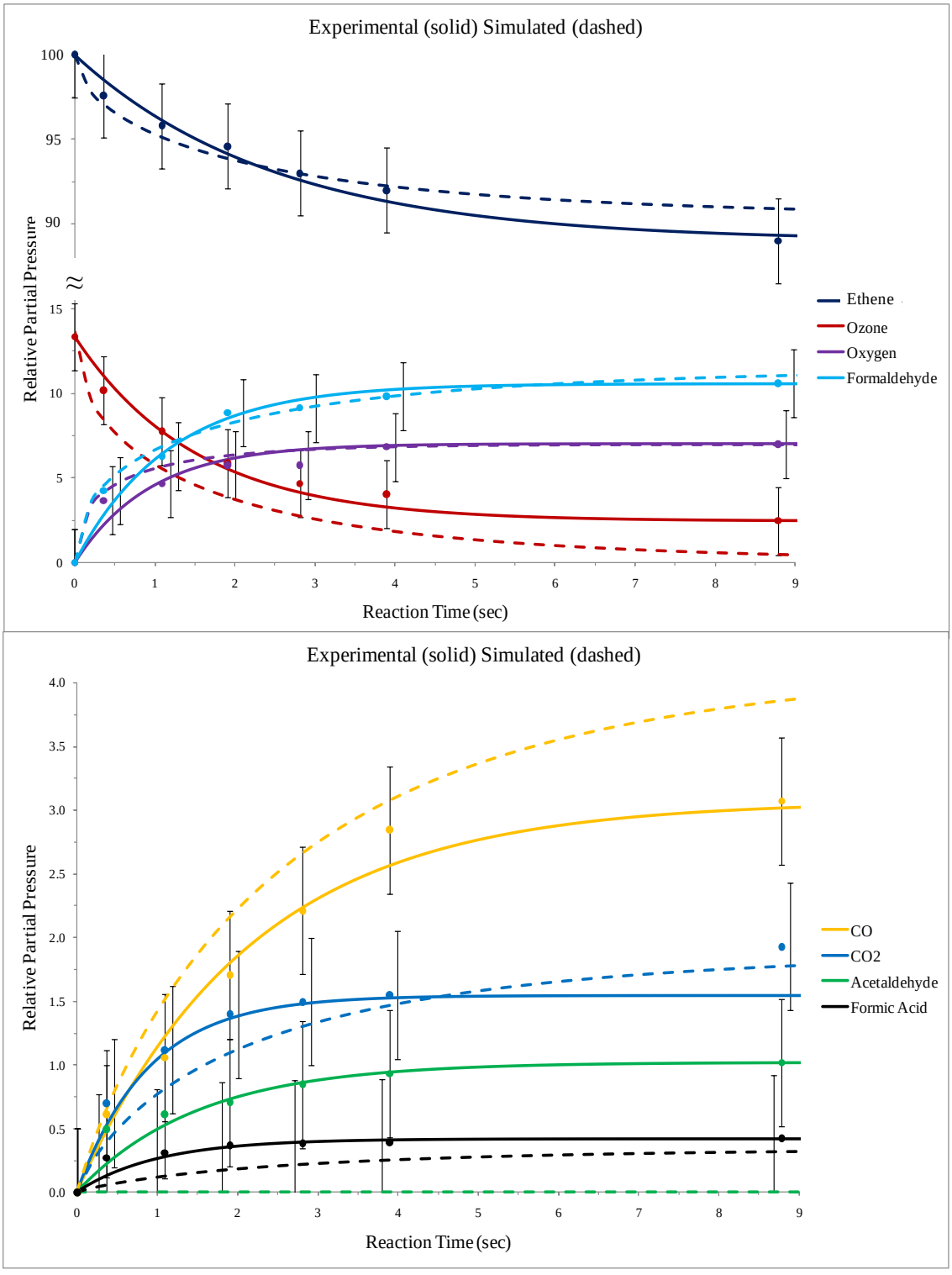

Figure 7.3: *Plot of reagent and product partial pressures as a function of reaction time at 298 K (solid lines) compared with the results of simulations using the reaction scheme of Herron and Huie [23]. The upper figure shows the reagents and the major products (O_2 and H_2CO) whereas the lower figure shows the minor products (CO, CO_2, CH_3CHO and HCOOH). Error bars have been derived from contributions of the experimental band intensities and experimental cross-sections, (for convenience, in some cases error bars have been displaced slightly horizontally).*

Taking into account the experimental errors in the data points, the agreement for the reagents (O_3 and C_2H_4), the dominant products (H_2CO and O_2), and the minor products (CO_2, CO, HCOOH) is reasonably good. However, no acetaldehyde is produced in the simulation as there are no acetaldehyde production reactions in the reaction scheme of reference [23]. In order to establish the main production routes of the products, particularly oxygen and acetaldehyde, which have not been studied as a function of reaction time previously, the reaction scheme has been broken down into three parts and simulations have been performed in stages using the different components. These parts, A, B and C, are shown in Table 7.3.

Section	Step	Reaction	Rate Coefficient (i)	Rate Coefficient (ii) [f]
A	Initial Reactions			
	1	$O_3 + C_2H_4 = H_2CO + H_2CO_2$	$1.72x10^{-18}$	$1.72x10^{-18}$
	2	$H_2CO_2 = CO_2 + H_2$	$5.76x10^{3}$ [a]	$\mathbf{8.0x10^{3}}$
	3	$H_2CO_2 = CO + H_2O$	$2.14x10^{4}$ [a]	$\mathbf{2.0x10^{4}}$
	4	$H_2CO_2 = H + HCO_2$	$2.88x10^{3}$ [a]	$\mathbf{1.2x10^{3}}$
	5	$H_2CO_2 = HCOOH$	$1.92x10^{3}$ [a]	$\mathbf{0.7x10^{3}}$
	6	$HCO_2 = H + CO_2$	$3.2x10^{4}$	$3.2x10^{4}$
	7	$H_2CO_2 + O_3 = H_2CO + O_2 + O_2$	$1.0x10^{-15}$ [b]	$\mathbf{1.0x10^{-13}}$
B	Other Reactions [c]			
	8	$O_3 + H = OH + O_2$	$2.66x10^{-11}$	$2.66x10^{-11}$
	9	$O_3 + C_2H_4OH = H_2CO + CH_2OH + O_2$	$9.13x10^{-13}$	$9.13x10^{-13}$
	10	$O_3 + CH_2OH = H_2CO + OH + O_2$	$9.13x10^{-13}$	$9.13x10^{-13}$
	11	$C_2H_4 + H = C_2H_5$	$3.82x10^{-13}$	$3.82x10^{-13}$
	12	$C_2H_4 + OH = C_2H_4OH$	$3.32x10^{-12}$	$3.32x10^{-12}$
	13	$OH + H_2CO = H_2O + HCO$	$1.39x10^{-11}$	$1.39x10^{-11}$
	14	$HO_2 + HO_2 = H_2O_2 + O_2$	$5.65x10^{-12}$	$5.65x10^{-12}$
C	Other reactions of the Criegee Intermediate			
	15	$H_2CO_2 + C_2H_4 = H_2CO + CH_3CHO$	$1.0x10^{-15}$ [d]	$\mathbf{5x10^{-14}}$
	16	$H_2CO_2 + H_2CO = H_2CO + HCOOH$	$4.0x10^{-13}$ [e]	$4.0x10^{-13}$
	17	$H_2CO_2 + H_2CO = H_2CO + CO_2 + H_2O$	$2.0x10^{-13}$ [e]	$2.0x10^{-13}$
	18	$H_2CO_2 + H_2CO = HCO + OH + HCO$	$2.0x10^{-13}$ [e]	$2.0x10^{-13}$
	19	$H_2CO_2 + H_2CO = CH_3CHO + O_2$	$1.0x10^{-13}$	$\mathbf{1.2x10^{-13}}$

Table 7.3: *Reaction scheme used to simulate the ozone-ethene reaction at room temperature (298 K).*

For calculations performed with rate coefficients (i), the rate coefficients were chosen as follows (see text);

(a) Set with the same ratios as used by Herron and Huie [23]; absolute values determined by simulation.

(b) Chosen because $HO_2 + O_3$ rate coefficient at room temperature is $2.0x10^{-15}$ cm^3 $molecule^{-1}$ s^{-1} [27].

(c) Apart from the reactions listed in A, the reactions listed in B were the reactions in the Herron and Huie [23] scheme which were found to make a significant, but small contribution, to the overall product yields. Other reactions listed in [23] were omitted.

(d) This was set to the value of $1x10^{-16}$ $cm^3molecule^{-1}s^{-1}$ [25] but increased to $1x10^{-15}$ $cm^3molecule^{-1}s^{-1}$ to increase the CH_3CHO yield.

(e) Initial values were taken from the relative rate coefficients of H_2CO_2 with C_2H_4 and H_2CO in reference [25] and the $H_2CO_2 + H_2CO$ reaction branching ratios in reference [28].

They were then increased to give acetaldehyde yields which agree within experimental errors with the observed yields.

(f) The coefficients shown in bold are those changed in (ii) compared to (i); these coefficients were optimised in (ii) to give better overall agreement for the experimental curves of the minor products (CO, CO_2, HCOOH, and CH_3CHO).

Part A consists of the initial O_3 + C_2H_4 reaction (reaction 1), which has a well established rate coefficient at room temperature [18], decomposition reactions of the Criegee intermediate (reactions 2-6), and reaction of the Criegee intermediate with ozone to give formaldehyde and oxygen (reaction 7). It was important to include this reaction as it is a possible source of O_2. Part B contains the reactions in the Herron and Huie scheme [23] which are not in part A, and were found in trial simulations to make significant contributions to the overall product yields. Of particular importance is reaction [8], $H + O_3 \rightarrow O_2 + OH$, which is a source of oxygen. In part C, other reactions of the Criegee intermediate are included, notably H_2CO_2 with C_2H_4 (reaction 15, which gives $CH_3CHO + H_2CO$), H_2CO_2 with H_2CO to give $H_2CO + HCOOH$, $H_2CO + CO_2 + H_2O$, HCO + OH + HCO, reactions (16), (17) and (18) respectively and H_2CO_2 with H_2CO to give $CH_3CHO + O_2$ (reaction 19). This reaction was added as a possible source, with reaction (15), of acetaldehyde. Values of the rate coefficients used are shown in column 4 of Table 7.3 (listed under (i) in this table) and the sources of these values are listed in the footnotes of Table 7.3. Unless otherwise stated, the rate coefficients were taken from Herron and Huie [23].

Three simulations were carried out using the rate coefficients listed under (i) in Table 7.3; A, A + B, and A + B + C. For A, for the reactants and major products (H_2CO and O_2), the ozone and ethene decrease and final values, and formaldehyde increase and final yield are reasonable compared to experiment, but very low yields of oxygen were calculated. For the minor products (CO, CO_2, CH_3CHO, HCOOH), carbon monoxide and carbon dioxide are over-predicted, formic acid is reasonably well predicted and, as expected, no acetaldehyde is produced in the simulation. For the A + B simulation, the ozone and ethene, and formaldehyde curves are improved compared to A and the oxygen yield curve is close to the experimental curve. For the minor products, the carbon monoxide and carbon dioxide curves are much better than in A and agree reasonably well with experiment, the formic acid is reasonably well predicted and no acetaldehyde is produced because there are no CH_3CHO producing reactions in A and B. For the A + B + C simulation (see Figure 7.4), the ozone and ethene curves and the major product increases and final yields are reasonably good and are virtually unchanged from the A + B simulation. For the minor products, the CO curve is in better agreement with experiment than in the A + B simulation, the CO_2 and HCOOH curves show similar agreement to the A + B simulation and the acetaldehyde curve and final

yield are lower than experiment and outside the experimental error of the measurement (see Figure 7.4). Acetaldehyde is produced by reactions [15] and [19] with both contributing to the overall yields. These calculations were also repeated using the rate coefficients listed in column 5 of Table 7.3 (in (ii) of this table). This model has the same rate coefficients as in (i), except for the rate coefficients shown in bold which were optimised to give better overall agreement for the experimental curves of the minor products (CO, CO_2, HCOOH, and CH_3CHO). The results are shown in Figure 7.5. The agreement with the experimental curves for the reactants, ethene and ozone, and the major products, formaldehyde and oxygen, was essentially the same as that obtained with the rate coefficients (i) in Table 7.3, and as expected the agreement of the curves for the minor products was better (see Figures 7.4 and 7.5).

As stated earlier, the objective of these simulations is to identify the main reactions responsible for formation of the observed products. Although the rate coefficients listed in Table 7.3, under (i) and (ii), are not uniquely determined, the main reaction products can be identified based on the results of the simulations (which were made with reasonable values for rate coefficients).

The main products determined from the simulations were, O_2, formaldehyde, CO, CO_2, acetaldehyde and HCOOH. The main O_2 production reaction is from reaction (8). Formaldehyde is produced mainly by reaction (1), however reactions (9) and (10) are also important production routes for formaldehyde. The minor products CO, CO_2 and HCOOH are produced mainly by decomposition of the Criegee intermediate (reactions 2-6),

reaction (2)	$H_2CO_2 \rightarrow CO_2 + H_2$
reaction (3)	$H_2CO_2 \rightarrow CO + H_2O$
reaction (4)	$H_2CO_2 \rightarrow H + HCO_2$
reaction (5)	$H_2CO_2 \rightarrow HCOOH$
reaction (6)	$HCO_2 \rightarrow H + CO_2$

Acetaldehyde is produced by reactions (15) and (19), with both reactions contributing to the overall acetaldehyde yield. This is demonstrated by simulations of the type (A + B + C) without reaction (19).

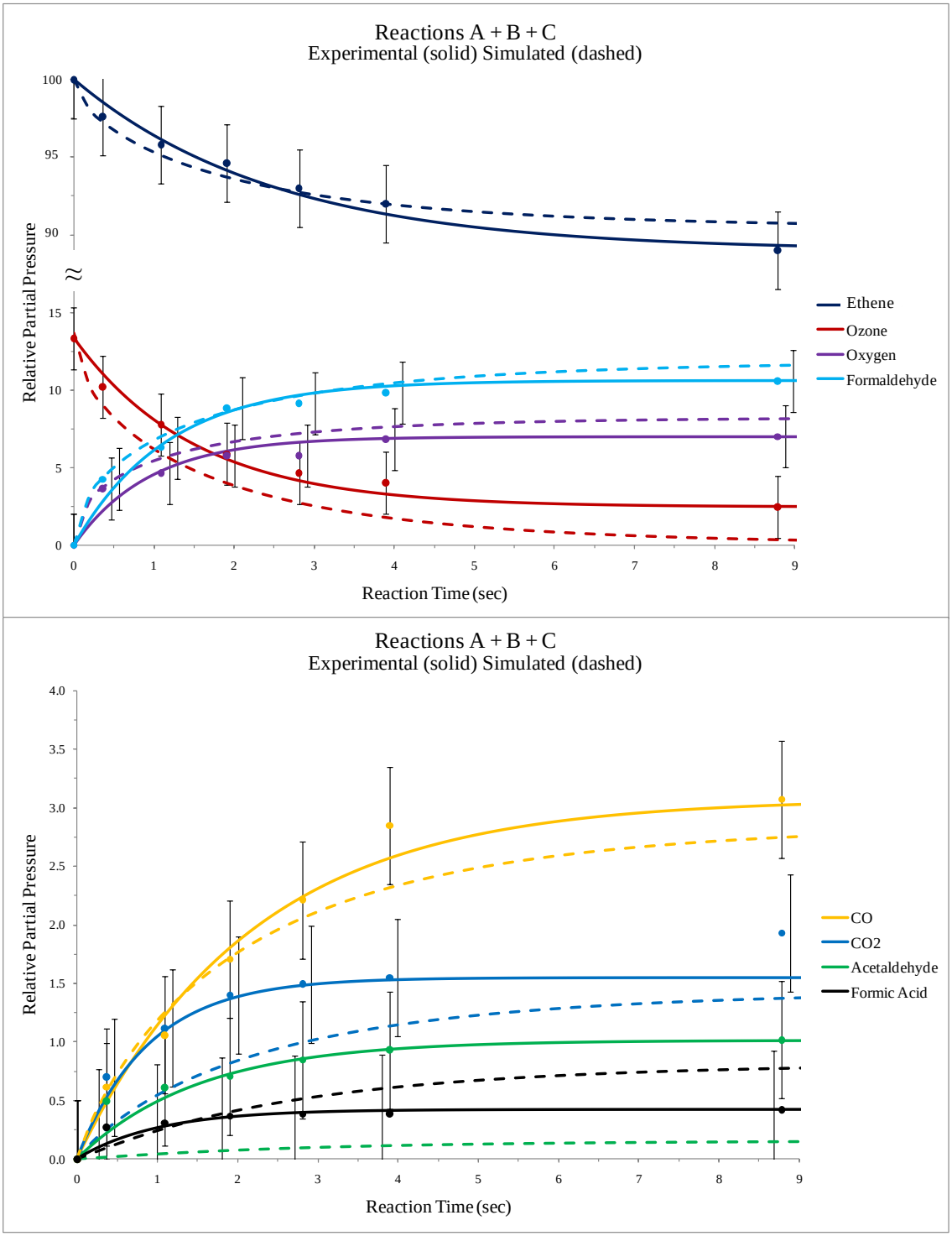

Figure 7.4: *Plot of reagent and product partial pressures as a function of reaction time at 298 K (solid lines) compared with the results of simulations using the reaction scheme A + B + C of Table 7.3, using rate coefficients (i) listed in column 4 of this table. The upper figure shows the reagents and the major products (O_2 and H_2CO) whereas the lower figure shows the minor products (CO, CO_2, CH_3CHO and HCOOH). (for convenience, in some cases error bars have been displaced slightly horizontally).*

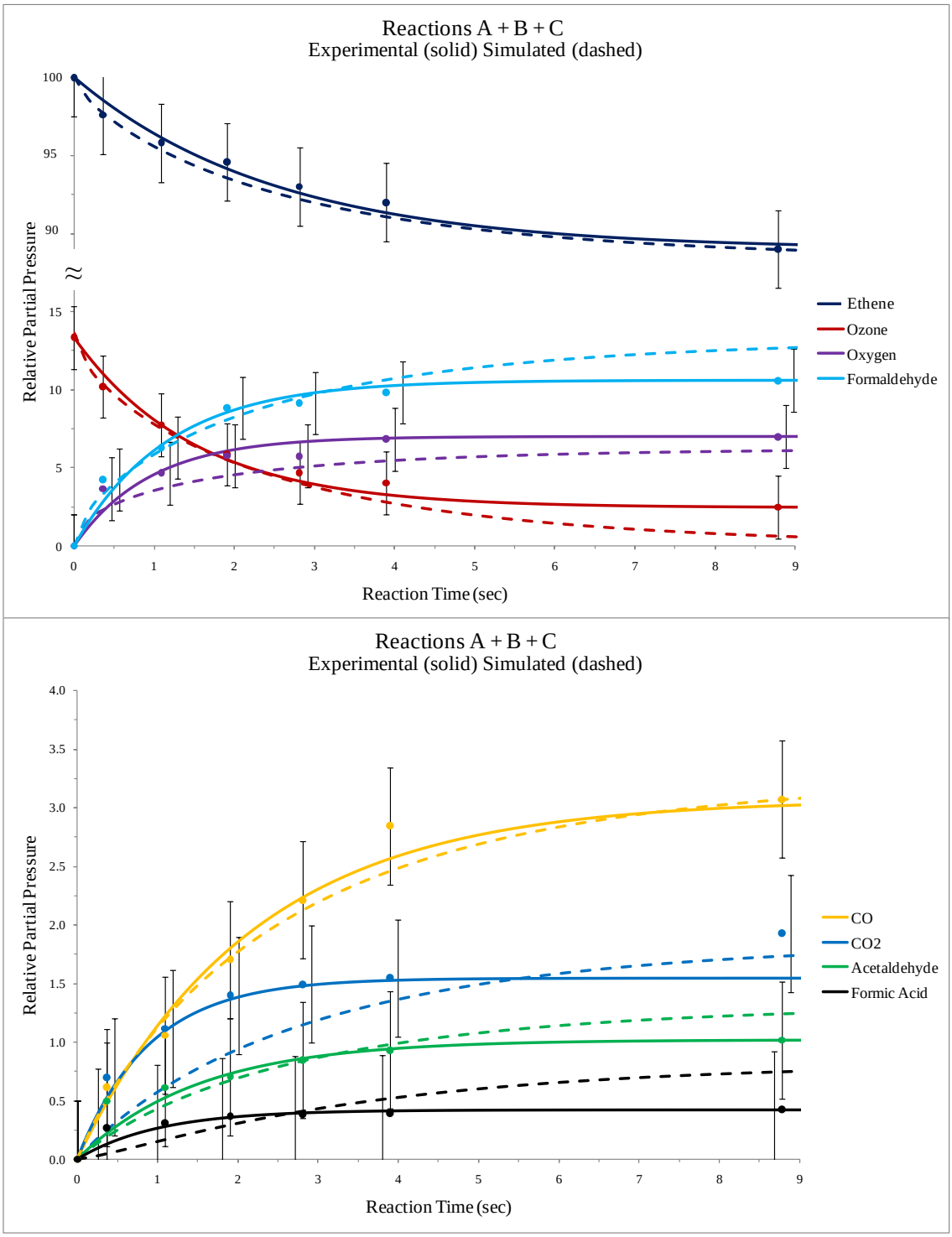

Figure 7.5: *Plot of reagent and product partial pressures as a function of reaction time at 298 K (solid lines) compared with the results of simulations using the reaction scheme A + B + C of Table 7.3, using rate coefficients (ii) listed in column 5 of this table. The upper figure shows the reagents and the major products (O_2 and H_2CO) whereas the lower figure shows the minor products (CO, CO_2, CH_3CHO and HCOOH). (for convenience, in some cases error bars have been displaced slightly horizontally).*

7.6 Results of Global Modelling

Based on global model simulations between 7.0-7.5 % of ethene oxidation occurs via reaction with ozone with the rest being initiated by OH (with NO_3 oxidation contributing less than 0.25% overall). Using the branching ratio data derived from this work the following annual global production totals for the various products were calculated as:- HCHO (0.96 ± 0.01 Tg), CO (0.22 ± 0.02 Tg), CO_2 (0.25 ± 0.02 Tg), HCOOH (0.052 ± 0.010 Tg), CH_3CHO (0.13 ± 0.01 Tg). These calculations assume that these products are primary products and therefore will be produced via these routes under atmospheric conditions. The kinetic modelling described in the previous section shows that this is true for H_2CO, CO, CO_2 and HCOOH. However, CH_3CHO is produced by the secondary reactions (15) and (19). These reactions will not be significant under atmospheric conditions and therefore the yield of CH_3CHO in the atmosphere is likely to be negligible.

In the global model used by Baboukas *et al.* [72], a yield of 42% was used for formic acid from the ozone-ethene reaction, taken from the work of Neeb *et al.* [29].

In this work the ozone-ethene reaction was studied using infrared spectroscopy and HPLC, in air at atmospheric pressure with water vapour added. Hydroxymethyl hydroperoxide (HMHP, $HOCH_2OOH$) was observed in reference [29] as an unstable product, which decomposes to HCOOH and H_2O on surfaces. The HMHP product yield was estimated in reference [29] as 42%. This is the figure quoted for formic acid production in reference [72]. On comparison of this value (0.42) with the values quoted in Table 7.4, of ≈ 0.04, the value of 0.42 is clearly too high by an order of magnitude. Also, it is evident that this figure does not apply to HCOOH production in the gas-phase, and therefore it is not appropriate to use this value in calculation of the global budget in the atmosphere. Therefore, the global production of HCOOH from the reaction of ozone with ethene has been significantly overestimated in this previous study [72].

The annual global emission levels of HCHO and HCOOH are approximately 4.8 and 7.3 Tg [54, 74]. The emission levels calculated in this work from the ozone-ethene reaction of (0.96 ± 0.01) and (0.052 ± 0.01) Tg for HCHO and HCOOH respectively, representing 20.0 and 0.7% of the total in each case. It is clear that the production of

HCHO from the ozone-ethene reaction, of 0.96 Tg per annum, is small but significant in terms of its global budget, which is dominated by production of HCHO from methane oxidation and oxidation of species such as isoprene (e.g. reference [73]).

The HCOOH yield from the ozone-ethene reaction is a much smaller fraction of the total emission. The other sources include other ozone-alkene reactions, photochemical oxidation of non-methane hydrocarbons, gas-phase reaction of H_2CO with HO_2, and vegetation and biogenic emissions. Global model simulations performed in this chapter were carried out by Prof. D. E. Shallcross of Bristol University.

7.7 Conclusion

The ozone-ethene reaction has been studied using a glass flow-tube interfaced to a photoelectron spectrometer, and the reagents and products have been monitored as a function of time. Kinetic simulations using an appropriate reaction scheme have been used to identify the main production reaction (or reactions) associated with each product and the measured product yields have been used in a global model to calculate the annual global emissions of the observed products in the atmosphere from this reaction.

The simulations indicate that of the observed products (H_2CO, CO, CO_2, HCOOH, CH_3CHO and O_2), H_2CO is mainly produced from decomposition of the primary ozonide formed in the first stage of the reaction and CO, CO_2 and HCOOH are mainly produced from decomposition of the Criegee intermediate which is also produced from decomposition of the primary ozonide. In contrast, CH_3CHO and O_2 are produced from subsequent reactions in the reaction scheme. As a result, the measured yields of H_2CO, CO, CO_2 and HCOOH are likely to be very similar to the corresponding yields from the ozone-ethene reaction in the atmosphere whereas the measured yields of CH_3CHO and O_2 will be very much lower under atmospheric conditions.

References

[1] J. G. Calvert, R. Atkinson, J. A.Kerr, S. Madronich, G. K. Moortgat, T. J. Wallington and G. Yarwood, The Mechanisms of Atmospheric Oxidation of the Alkenes, Oxford, *University Press Oxford*, 2000.

[2] R. Atkinson and S. M. Aschmann, *Environ. Sci. Technol.*, 27, 1993, 1357.

[3] W. P. L. Carter, *Atmos. Environ.*, 24A, 1990, 481.

[4] R. Atkinson, *Atmos. Environ.*, 24A, 1990, 1.

[5] R. Criegee and G. *Wenner, Chem. Ber.*, 564, 1949, 9.

[6] R. Criegee, Angew. *Chem. Int. Ed.*, 14, 1975, 745.

[7] W. H. Bunnelle, *Chem. Rev.*, 91, 1991, 335.

[8] C. A. Taatjes, G. Meloni, T. M. Selby, A. J. Trevitt, D. L. Osborn, C. J. Percival and D. E. Shallcross, *J. Am. Chem. Soc.*, 130, 2008, 11883.

[9] M. Clay and B. S. Ault, *J. Phys. Chem.*, 114, 2010, 2799.

[10] M. D. Hoops and B. S. Ault, *J. Am. Chem. Soc.*, 131, 2009, 2853.

[11] F. J. Lovas and R. D. Suenram, *Chem. Phys. Letts.*, 51, 1977, 453.

[12] R. I. Martinez, R. E. Huie and J. T. Herron, *Chem. Phys. Letts.*, 51, 1977, 457.

[13] J. M. Anglada, R. Creheut and J. M. Bofill, *Chem. Eur. J.*, 5, 1999, 1809.

[14] P. Aplincourt and M. F. Ruiz-Lopez, *J. Am. Chem. Soc.*, 122, 2000, 8990.

[15] T. Sato, S. Nishihara, Y. Kataoka, Y. Nakanishi, Y. Kitagawa, T. Kawakami, S. Yamanaka, M. Okumura and K. Yamaguchi, *J. Phys. Chem. A.*, 114, 2010, 12116.

[16] Y. Zhao, O. Tishchenko, J. R. Gour, W. Li, J. J. Lutz, P. Piecuch and D. G. Truhlar, *J. Phys. Chem. A.*, 113, 2009, 5786.

[17] R. Ponec, J. Roithova and Y. Hass, *Croatica. Chemica. Acta.*, 74, 2001, 251.

[18] R. Wegener, T. Brauers, R. Koppmann, S. R. Bares, F. Rohrer, R. Tillmann, A. Wahner, A. Hansel and A. Wisthaler, *J. Geophys. Res. Atmos.*, 112, 2007, 13301.

[19] H. T. Wang, Y. J. Zhang and Y. J. Mu, *J. Environ. Sci. Chi.*, 19, 2007, 641.

[20] R. Sondergaard, O. J. Nielsen, M. D. Hurley, T. J. Wallington and R. Singh, *Chem. Phys. Letts.*, 443, 2007, 199.

[21] W. T. Chan and I. P. Hamilton, *J. Chem. Phys.*, 118, 2003, 1688.

[22] R. Atkinson, D. L. Baulch, R. A. Cox, R. F. Hampson, J. A. Kerr, M. J. Rossi, and J. Troe, *J. Phys. Chem. Ref. Data*, 26, 1997, 521.

[23] J. T. Herron and R. E. Huie, *J. Am. Chem. Soc.*, 99, 1977, 5430.

[24] R. Atkinson, B. J. Finlayson and J. N. Pitts, *J. Am. Chem. Soc.*, 95, 1973, 7592.

[25] F. Su, J. G. Calvert and J. H. Shaw, *J. Phys. Chem.*, 84, 1980, 239.

[26] H. Niki, P. D. Maker, C. M. Savage and L. P. Breitenbach, *J. Phys. Chem.*, 85, 1981, 1024.

[27] O. Horie and G. K. Moortgat, *Atmos. Environ.*, 25A, 1991, 1881.

[28] P. Neeb, O. Horie and G. K. Moortgat, *J. Phys. Chem. A.*, 102, 1998, 6778.

[29] P. Neeb, F. Sauer, O. Horie and G. K. Moortgat, *Atmos. Environ.*, 31, 1997, 1417.

[30] B. Qi, K. Sato, T. Imamura, A. Takami, S. Hatakeyama and Y. Ma, *Chem. Phys. Letts.*, 427, 2006, 461.

[31] E. Grossjean and D. Grossjean, *Environmental Sci. Technol.*, 30, 1996, 859.

[32] E. Grossjean and D. Grossjean, *Environmental Sci. Technol.*, 30, 1996, 2036.

[33] D. Mihelcic, M. Heitlinger, D. Kley, P. Musgen and A. Volz-Thomas, *Chem. Phys. Letts.*, 301, 1999, 559.

[34] J. M. Dyke, N. Jonathan and A. Morris, *Int. Rev. Phys. Chem.*, 2, 1982, 3.

[35] M. C. R. Cockett, J. M. Dyke and H. Zamapourin, Vacuum Ultraviolet Photoionisation and Photodissociation of Molecules and Clusters, Edited by C. Y. Ng, *World Scientific Co.*, New Jersey, 1991.

[36] J. M. Dyke, M. V. Ghosh, M. Goubet, E. P. F. Lee, G. Levita, K. Miqueu and D. E. Shallcross, *Chem. Phys.*, 324, 2006, 85.

[37] J. M. Dyke, L. Golob, N. Jonathan, A. Morris and M. Okuda, *J.C.S Faraday II*, 70, 1974, 1828.

[38] S. Willitsch, F. Innocenti, J. M. Dyke, and F. Merkt, *J. Chem. Phys.*, 122, 2005, 024311.

[39] J. M. Dyke, M. V. Ghosh, D. J. Kinnison, G. Levita, A. Morris and D. E. Shallcross, *Phys. Chem. Chem. Phys.*, 7, 2005, 866.

[40] R. Spence and W. J. Wild, *J. Chem. Soc.*, 1, 1935, 338.

[41] F. D. Pope. C. A. Smith, M. N. R. Ashfold and A. J. Orr-Ewing, *Phys. Chem. Chem. Phys.*, 7, 2005, 79.

[42] J. Berkowitz, *Int. J. Mass. Spectrom.*, 271, 2008, 8.

[43] G. V. Marr, J. B. West, *Atomic Data Nuclear Data Tables*, 18, 1976, 497.

[44] J. G. Brennan, G. Cooper, J. C. Green, M. P. Payne and C. M. Redfern, *J. Elect. Spect. Rel. Phen.*, 43, 1987, 297.

[45] W. J. Van der Meer, P. Van der Meulen, M. Volmer and C. A. de Lange, *Chem. Phys.*, 126, 1988, 385.

[46] C. E. Brion, K. H. Tan, M. J. Van der Wiel and P. E. van der Leeuw, *J. Elect. Spect. Rel. Phen.*, 17, 1979, 101.

[47] E. W. Plummer, T. Gustafsson, W. Gudat and D. E. Eastman, *Phys. Rev. A.*, 15, 1977, 2339.

[48] C. E. Brion and K. H. Tan, *J. Elect. Spect. Rel. Phen.*, 15, 1979, 241.

[49] C. E. Brion and K. H. Tan, *Chem. Phys.*, 34, 1978, 141.

[50] G. Cooper, J. E. Anderson and C. E. Brion, *Chem. Phys.*, 209, 1996, 61.

[51] I. Cacelli, R. Moccia and R. Montuoro, *Chem. Phys. Letts.*, 347, 2001, 261.

[52] C. E. Brion and F. Carnovale, *Chem. Phys.*, 100, 1985, 291.

[53] T. A. Cool, J. Wang, K. Nakajima, C. A. Taatjes and A. Mcllroy, *Int. J. Mass. Spec.*, 247, 2005, 18.

[54] S. R. Utembe, M. C. Cooke, A. T. Archibald, M. E. Jenkin, R. G. Derwent, and D. E. Shallcross, *Atmos. Environ.*, 44, 2010, 1609.

[55] A. T. Archibald, M. C. Cooke, S. R. Utembe, D. E. Shallcross, R. G. Derwent and M. E. Jenkin, *Atmos. Chem. Phys.*, 10, 2010, 1.

[56] W. Collins, D. Stevenson, C. Johnson and R. Derwent, *J. Atmos. Chem.*, 26, 1997, 223.

[57] R. G. Derwent, D. S. Stevenson, R. M. Doherty, W. J. Collins, M. G. Sanderson and C. E. Johnson, *Climatic Change*, 88, 2008, 385.

[58] M. E. Jenkin, L. A. Watson, S. R. Utembe and D. E. Shallcross, *Atmos. Environ.*, 427185, 2008, 7195.

[59] S. R. Utembe, L. A. Watson, D. E. Shallcross and M. E. Jenkin, *Atmos. Environ.*, 43, 2009, 1982.

[60] L. A. Watson, D. E. Shallcross, S. R. and M. E. Jenkin, *Atmos. Environ.*, 42, 2008, 7196.

[61] J. G. Olivier, A. F. Bouwman, J. J. Berdowski, C. Veld J. P. Bloos, A. J. Visschedijk, P. Y. Zandveld and J. L. Haverlag, Description of EDGAR Version 2.0: A set of global emission inventories of greenhouse gases and ozone depleting substances for all anthropogenic and most natural sources on a per country basis and on a 1deg. x 1deg. grid. Technical Report, Netherlands Environmental Assessment Agency 1996.

[62] C. Granier, J. Lamarque, A. Mieville, J. Muller, J. Olivier, J. Orlando, J. Peters, G. Petron, S. Tyndall and S. Wallens, 2005, POET, (database of surface emissions of ozone precursors). http://www.aero.jussieu.fr/projet/ACCENT/POET.php'.

[63] D. Henze, J. Seinfeld, N. Ng, J. Kroll, T. Fu, D. Jacob and C. Heald, *Atmos Chem. Phys.*, 82405, 2008, 2420.

[64] M. Andreae and P. Merlet, *Global Biogeochemical Cycles*, 15, 2001, 955.

[65] J. E. Penner, D. H. Lister, D. J. Griggs, D. J. Dokken and M. McFarland, IPCC Special Report on Aviation and Global Atmosphere, *Technical report: the Intergovernmental Panel on Climate Change*, 1999.

[66] K. Kimura, S. Katsumata, Y. Achiba, T. Yamasaki and S. Iwata, Handbook of HeI Photoelectron Spectra, *Japan Scientific Press*, Tokyo 1981.

[67] D. M. de Leeuw, R. Mooyman and C. A. de Lange, *Chem. Phys. Letts.*, 63, 1979, 57.

[68] C. S. Kan, F. Su, J. G. Calvert and J. H. Shaw, *J. Phys. Chem.*, 85, 1981, 2359.

[69] T. Vrbaski and R. J. Cvetanovic, *Can. J. Chem.*, 38, 1960, 1053.

[70] H. Kuhne, S. Vaccani, T. K. Ha, A. Bauder and H. H. Gunthard, *Chem. Phys. Letts.*, 39, 1976, 449.

[71] W. Braun, J. T. Herron and D. K. Kahaner, *Int. J. Chem. Kinetics.*, 20, 1988, 51.

[72] E. D. Baboukas, M. Kanakidou and N. Mihalopoulos, *J. Geophys. Res.*, 105, 2000, 14459.

[73] M. C. Cooke, S. R. Utembe, P. G. Carbajo, A. T. Archibald, A. J. Orr-Ewing, R. G. Derwent, M. E. Jenkin, D. J. Lary and D. E. Shallcross, *Atmos. Sci. Lett.*,11, 2010, 33.

[74] M. C. Cooke, Ph,D Thesis, Univeristy of Bristol, 2010.

Chapter 8

A Study of 2-Methylpropene + Ozone and 2, 3 Dimethyl-2-butene + Ozone Reactions using PES

Alkenes from both biogenic and anthropogenic sources constitute an important class of volatile organic compounds (VOCs) in the troposphere and their reactions with ozone are key removal processes. These reactions produce OH radicals and results of modelling calculations indicate that they may be important sources of HO_x species in the troposphere [1-3]. Their atmospheric importance has led to a significant number of experimental studies of their kinetics and mechanisms [1, 4-17]. Rate coefficients and products have been determined for a number of ozone-alkene reactions. However, while in general room temperature rate coefficients are well established, there are uncertainties concerning product branching ratios. In fact, no complete product branching ratio data are available for any alkene-ozone reaction apart from the ethene-ozone reaction. This reaction was investigated by our group recently at low pressure in a flow-tube using u.v. photoelectron spectroscopy and the product branching ratios were measured for all the main products. This present study extends this work by studying the reaction of O_3 with 2, 3-dimethyl-2-butene (DMB) and O_3 with 2-methylpropene (2MP).

The general mechanism for ozone-alkene reactions, first proposed by Criegee [18], is now widely accepted. It involves addition of ozone across the double bond of the alkene

to form a primary ozonide. This reaction is quite exothermic and results in decomposition of the primary ozonide into a carbonyl compound and a Criegee intermediate (R_1R_2COO) which may decompose, or react with the reagents or other products. Quantum chemical calculations [19-25] have shown that the activation barrier connecting the primary ozonide to the Criegee intermediate is ~20 kcal.mol^{-1}. The primary ozonide is formed with nearly 50 kcal.mol^{-1} excess energy and it can easily pass over the barrier to form the Criegee intermediate and a carbonyl compound. Matrix isolation infrared spectroscopy has been used to study the reactions of ozone with 2, 3 dimethyl-2-butene, cis-2-butene, cyclopentene and cyclopentadiene [26-28]. In each case, the observed spectra, obtained for different stages of the reaction, are consistent with the reaction proceeding via the Criegee mechanism, with spectral absorptions being recorded for the primary ozonide and Criegee intermediate.

Previous experimental studies of the reaction of O_3 with DMB and O_3 with 2MP have included measurement of rate coefficients and branching ratios [4-17]. Product branching ratios have been measured using a number of methods, notably photoionisation mass spectrometry (PIMS) at low pressure [7], and gas-phase infrared spectroscopy and chromatography [11, 14-17] of the reaction mixture heavily diluted in synthetic air at atmospheric pressure. The reaction product branching ratios derived in these investigations show only moderate agreement. Also the available product branching ratio data are incomplete as the yields of some of the known reaction products such as O_2 have not been measured and the yields of products such as CO, CO_2 and HCOOH have not been measured in all published investigations, as the detection methods used are capable of detecting some, but not all, of the products.

The reaction of O_3 with DMB and O_3 with 2MP were selected for study as a logical extension of our work on the reaction of O_3 with ethene. The reaction of O_3 with 2MP was felt to be particularly interesting as, unlike the reactions of O_3 with ethene and DMB, where a symmetrical primary ozonide is formed which can decompose in only one way, the primary ozonide in the reaction of O_3 with 2MP can decompose in two ways to give H_2CO and the Criegee intermediate Me_2COO, and Me_2CO and the Criegee intermediate H_2COO. The relative importance of these pathways will control the final product yields. The same detection technique was used in this investigation as that used for the reaction of O_3 with ethene (described in Chapter 7) to study the products of the reaction of O_3 with DMB and O_3 with 2MP as a function of time. The measured product

yields will be compared with product yields measured for these reactions in earlier work by other researchers. For each reaction, the measured product yields will be used in a global atmospheric model to estimate the annual global budgets of the observed products. Kinetics simulations will also be carried out for both reactions in order to establish the main pathway for production of each observed product.

8.1 Experimental

8.1.1 Photoelectron (PE) Spectra Recorded as a Function of Time

PE spectra were recorded for the reactions of O_3 with DMB and O_3 with 2MP at low pressure (~1-2 torr) at different reaction times using a flow-tube attached to the ionisation chamber of a PE spectrometer. The procedure used followed that adopted for the reaction of O_3 with ethene, with the main difference being that because the reactions of O_3 with DMB and O_3 with 2MP are faster than the reaction of O_3 with ethene, the glass flow-tube used was shorter. (Rate coefficients at 298 K for reactions of O_3 with DMB and O_3 with 2MP are 1.13×10^{-15} and 1.13×10^{-17} $cm^3.molecule^{-1}$ s^{-1} respectively [4]). No carrier gas was used. The flow-tube (length 50 cm) consisted of two concentric glass tubes, with the inner tube being moveable with respect to the outer tube. A schematic diagram of this inlet system has been shown previously in reference [29], Figure 3(d), where it was used to study the reaction of DMS with Cl_2.

For both reactions, the alkene was passed down the inner tube and ozone was passed down the outer tube via a side arm near the top. The lower end of the flow-tube, which was positioned just above the photon beam of the PE spectrometer, has a constricted end with a small hole in it which allowed gas to be sampled by the PE spectrometer. The hole size was 1.5 mm for the reaction of O_3 with DMB and 0.5 mm for the reaction of O_3 with 2MP. Spectra were recorded for both reactions for mixing distances along the flow-tube in the range 0-50 cm at 5 cm intervals. Studies were made for both [alkene] > [O_3] and [alkene] < [O_3].

Two baratron pressure transducers, positioned at 10 cm and 48 cm from the lower end of each inlet, were used to monitor the pressure change along the flow-tube under experimental conditions. By taking pressure measurements at these two points during a reaction, the flow-rate and linear flow velocity could be calculated using the Poiseuille

equation. Knowing the linear flow velocity, reaction distances could be converted into reaction times. Calculations were also made of the Reynolds number, using the measured flow-rates and the values obtained, which were less than 2000, were consistent with laminar flow in the flow-tube.

The PE spectrometer used was a 10 cm mean radius hemispherical analyser instrument with a He(I) photon source (21.22 eV) [30-32]. Ozone was made by a silent electric discharge of flowing oxygen and stored on non-indicating silica gel held at -78 °C in a dry-ice/acetone slush bath as described previously [33, 34]. Samples of the alkenes used were obtained from a commercial source (Aldrich, 99% for both DMB and 2MP).

8.1.2 Photoionisation Cross-Section Measurements

The experimental PE spectra recorded at different reaction times were used to obtain plots of partial pressures of reagents and products as a function of time. This was done by selecting a suitable band for a reagent or product, usually the first band, and using its intensity with the photoionisation cross-section for that band determined in this work to obtain its partial pressure. The procedure for determining molecular photoionisation cross-sections involved measuring the intensity of a selected band of a reagent or product relative to the intensity of the $(3p)^{-1}$ ionisation of argon from a sample containing known partial pressures of the molecule of interest and argon.

The method can be summarised as follows:-

A sample of known partial pressures of the molecule of interest and argon in a 7.3 L bulb is made up to a total pressure of 1 atm. with helium (e.g. a mixture of 2MP (5%) and argon (5%) in helium). The sample was then admitted to a differentially pumped stainless-steel flow-tube, interfaced to a PE spectrometer (with a 20 cm mean radius analyser) at a known flow-rate (typically 100 sccm) using a calibrated mass flow-controller, as described previously [29, 30]. A second calibrated mass flow controller was used to admit the carrier gas (helium) to the flow-tube at a fixed flow-rate (typically 1 slm). PE spectra were then recorded with the objective of measuring the intensity of a selected PE band of the molecule of interest (the band monitored as a function of time in the ozone-alkene experiments) relative to the argon $(3p)^{-1}$ PE bands. Also, the full PE spectrum of oxygen was recorded twice before sampling and twice after sampling. These spectra were used in the analysis procedure to correct for any change in the

transmission of the spectrometer during the sampling experiments. In most cases, the change in transmission during sampling was found to be small. From the experimental spectra, the area of the selected band of the molecule of interest, including all vibrational components, relative to the area of both spin-orbit components of the argon $(3p)^{-1}$ ionisation was measured. At least ten measurements were made in this way and the average value determined. This ratio was then corrected for the relative partial pressures of the sample and argon in the sample bulb. This is the photoionisation cross-section (PI-CS) on the spectrometer of the selected band of the molecule relative to the argon $(3p)^{-1}$ ionisation.

The PI-CS values derived in this way, which were used in the analysis of the spectra recorded for the alkene-ozone reactions of O_3 with DMB and O_3 with 2MP, are shown in column 2 of Table 8.1.

Molecule	PI-CS on the Spectrometer	PI-CS Corrected for e.K.E	PI-CS Corrected for e.K.E and Angular Distribution (a)	Literature PI-CS (b) Mb	Literature PI-CS relative to argon (c)
Argon	1	1	1	37.1 [36]	1
2MP	0.75 ± 0.04	0.33 ± 0.02	0.33 ± 0.02	10.7 [37]	0.29
DMB	0.98 ± 0.08	0.42 ± 0.03	0.44 ± 0.03	-	-
Oxygen	0.38 ± 0.02	0.20 ± 0.02	0.26 ± 0.02	7.42 [38, 39]	0.20
Ozone, 3rd band	0.59 ± 0.10	0.34 ± 0.05	0.39 ± 0.0(d)	12.6 [35]	0.33
Carbon Monoxide	0.22 ± 0.01	0.15 ± 0.02	0.15 ± 0.02	7.0 [40]	0.19
Carbon Dioxide	0.22 ± 0.01	0.16 ± 0.01	0.20 ± 0.01	10.28 [41, 42]	0.28
Acetaldehyde	0.63 ± 0.05	0.32 ± 0.02	0.36 ± 0.02	-	-
Formaldehyde	0.32 ± 0.02	0.15 ± 0.01	0.17 ± 0.01	8.47 [43, 44]	0.19
Acetone	0.54 ± 0.07	0.26 ± 0.03	0.30 ± 0.03	11.2 [46]	0.30
Water	0.27 ± 0.07	0.18 ± 0.05	0.18 ± 0.05	6.61 [45]	0.18
Formic Acid	0.80 ± 0.10	0.40 ± 0.02	0.40 ± 0.02	15.0 [46]	0.40

Table 8.1: *Comparison of photoelectron band Photoionisation Cross-Sections (PI-CS) relative to argon. The first band of all the molecules has been used in the measurements, unless otherwise stated.*

(a) Photoionisation cross-sections measured relative to argon (this work).

(b) Available literature photoionisation cross-sections (measured in Mb, $10^{-18}cm^2$).

(c) Literature photoionisation cross-sections measured relative to argon at 37.1Mb [36] and normalised to 1.

(d) Total cross-section at hν = 16.0 eV taken as 31 Mb [35]; the cross-section for the third band was obtained by measuring its area relative to the total area (bands 1-3 in the He(I) spectrum).

However, in order to obtain absolute photoionisation cross-sections from the known photoionisation cross-section of argon, a correction must be made for the transmission of the analyser (this is an electron kinetic energy correction) and for the angular distribution parameters of the selected bands of both the molecule and argon. These

corrected values are shown in columns 3 and 4 of Table 8.1 respectively. As can be seen, the electron kinetic energy correction is much bigger than the angular distribution correction. (Independent experiments showed that the transmission functions of the two spectrometers used in this work, which had 10 cm and 20 cm mean radius analysers, were within experimental errors the same).

Also shown in Table 8.1, in column 5, are the available literature cross-sections for the relevant bands of the reagents and the observed reaction products at hν = 21.22 eV [35-46]. Column 6 of Table 8.1 shows the normalised values relative to argon. It can be seen in this table that on comparing column 6 with column 4 (the relative values derived in this work) that reasonably good agreement is obtained, supporting the values used in this work to convert relative PE band intensities into relative molecular partial pressures.

8.2 Description of the Global Model used

In order to use the results of this study to estimate the mass of products formed in the atmosphere, the Global Chemistry Transport Model CRI-STOCHEM, described in references [47, 48], has been used. The model used is an updated version of the UK Meteorological Office tropospheric chemistry transport model (STOCHEM) described by Collins *et al.* [49], with updates reported in detail in the recent paper of Utembe *et al.* [47]. STOCHEM is a global 3-dimensional Chemical Transport Model (CTM) which uses a Lagrangian approach to advect 50,000 air parcels using a 4^{th}-order Runge-Kutta scheme with advection time steps of 3 hours. The transport and radiation models are driven by archived meteorological data, generated by the Met office numerical weather prediction models as analysis fields with a resolution of 1.25° longitude and 0.83° latitude, and on 12 vertical levels extending to 100 hPa. Full details of the version of the model that was employed are given elsewhere [50].

The common representative intermediates mechanism (CRIv2-R5) [51-53], which represents the chemistry of methane and 22 emitted non-methane hydrocarbons was employed in the model. Each parcel contains the concentrations of 219 species involved in 618 photolytic, gas phase and heterogeneous chemical reactions, with a 5 minute time step. The formation of secondary organic aerosol (SOA) is represented using 14

species, which are derived from the oxidation of aromatic hydrocarbons, monoterpenes, and isoprene [52].

The surface emissions (man-made, biomass burning, vegetation, oceans, and soil) are distributed using two-dimensional source maps [54]. Emissions totals for the base case run for CO, NO_x and non methane hydrocarbons are taken from the Precursor of Ozone and their Effects in the Troposphere (POET) inventory [55] for the year 1998; more recent databases exist but do not cover as wide a range as POET and so we have used POET in this work.

The emissions of the aromatic species ortho-xylene, benzene and toluene were taken from reference [56]. Biomass burning emission of ethyne, formaldehyde and acetic acid are produced using scaling factors from per mole of CO emitted, taken from reference [57]. NASA inventories are used for aircraft NO_x emissions for 1992 taken from reference [58]; again more recent estimates for regional emissions are available, but we prefer to use the previous global totals. The lightning and aircraft NO_x emissions are monthly averages and are 3-dimensional in distribution.

8.3 Results and Discussions

For convenience, the results for DMB + ozone are described first, as DMB is more symmetrical than 2MP.

For each reaction, separate studies were made as a function of time with initial concentrations (i) [alkene] > [O_3] and (ii) [alkene] < [O_3]. Typical spectra recorded in the low ionisation region (8.0-14.0 eV) are shown in Figures 8.1 and 8.3.

Figure 8.1, obtained for O_3 + DMB, shows two spectra obtained at 5 and 20 cm mixing distances with the initial concentrations [alkene] < [O_3]. The plot of the relative partial pressure of the reagents and products as a function of reaction time obtained from this experiment is shown in Figure 8.2.

Similarly, Figure 8.3, obtained for O_3 + 2MP, shows two spectra obtained at 5 and 40 cm mixing distances with the initial concentrations [alkene] > [O_3], with the plots of relative partial pressures as a function of time shown in Figure 8.4.

Figure 8.1, recorded for the reaction of O_3 with DMB, shows bands associated with the products formaldehyde, oxygen, acetone, carbon monoxide, and carbon dioxide as well as bands associated with the reagents DMB and ozone. No formic acid was seen from this reaction.

Figure 8.2 and 8.4 show that the reagents decrease and the products increase smoothly with reaction time. It was found that both the decrease of DMB and ozone could be fitted to an exponential decay of the form,

$$a.exp^{(-bt)} + c \tag{8.1}$$

and the product increases could be fitted to an exponential increase of the form,

$$a.1 - exp^{(-bt)} \tag{8.2}$$

These fitted curves are shown as solid lines in Figure 8.2. Because of overlap of the first two bands of ozone with the third band of DMB, the third band of ozone at 13.57 eV was used to monitor the ozone partial pressure. Water was also observed as a reaction product but its intensity could not be measured reliably as its first band is overlapped by the third band of DMB, the ozone first band and the oxygen first band.

Comparison of the product yields measured at the longest mixing distance (reaction time) is shown in Table 8.2. These are expressed relative to the observed change in the reagent not in excess. The observed product yields recorded with excess alkene and with excess ozone are in good agreement with each other, taking into account experimental error.

Also, listed in Table 8.2 are product yields measured in other studies [7, 14-17]. As can be seen, for the products, H_2CO, $(CH_3)_2CO$, CO, and CO_2, the product yields in this work agree reasonably well with those of other studies. O_2, a major product observed in this work, appears not to have been observed previously from the O_3 + DMB reaction. Its yield is reported here for the first time. Minor products observed in some of the other studies, but not observed in this work, with known vertical ionisation energies (VIEs) in brackets [59, 60], are CH_3OH (10.94 eV), CH_3COCHO (10.0 eV), and $HOCH_2COCH_3$ (10.0 eV).

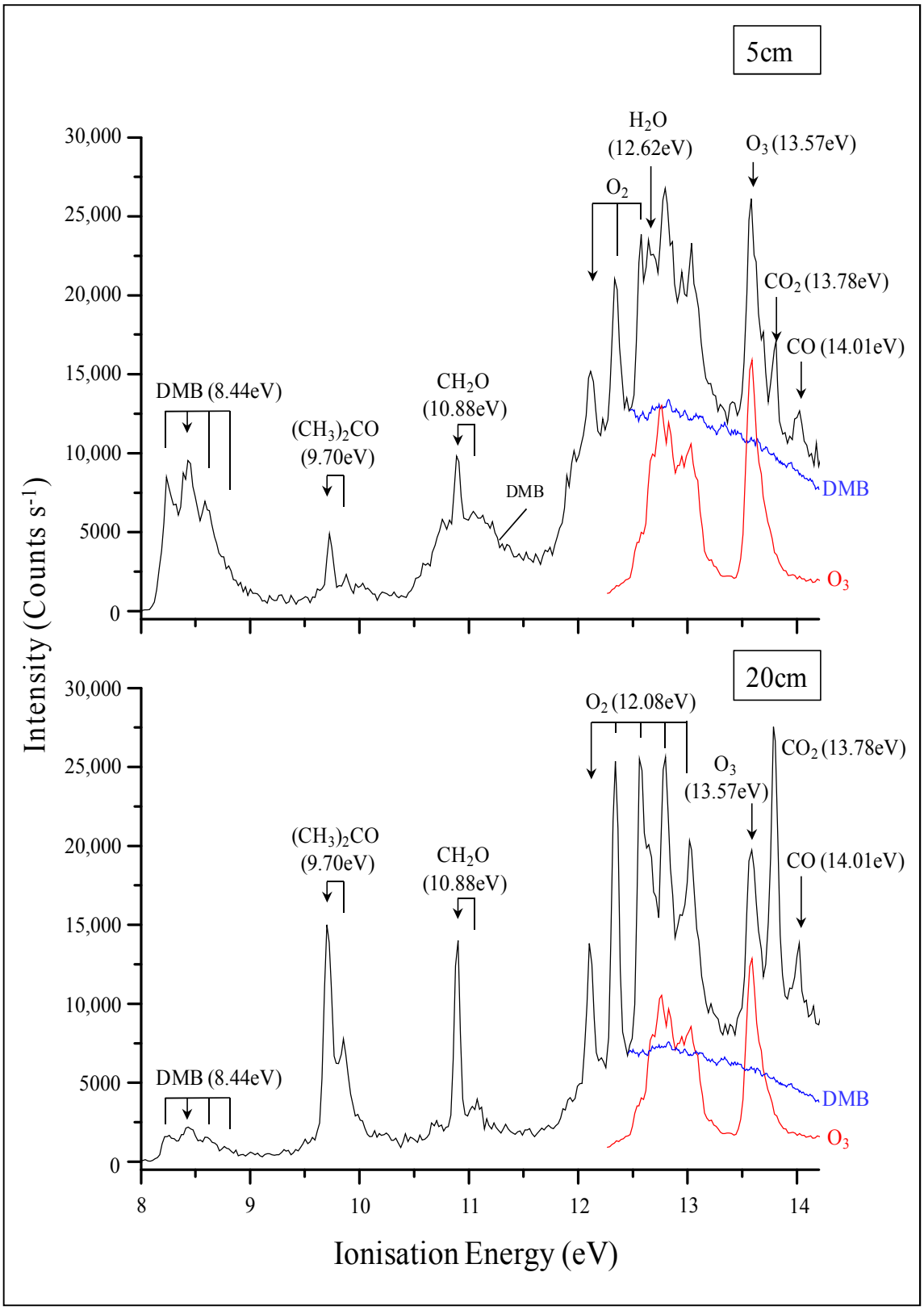

***Figure 8.1**: Photoelectron spectra recorded for the O_3 + DMB reaction at constant initial reagent partial pressures, [DMB] < [O_3], at 5 and 20 cm reaction distance.*

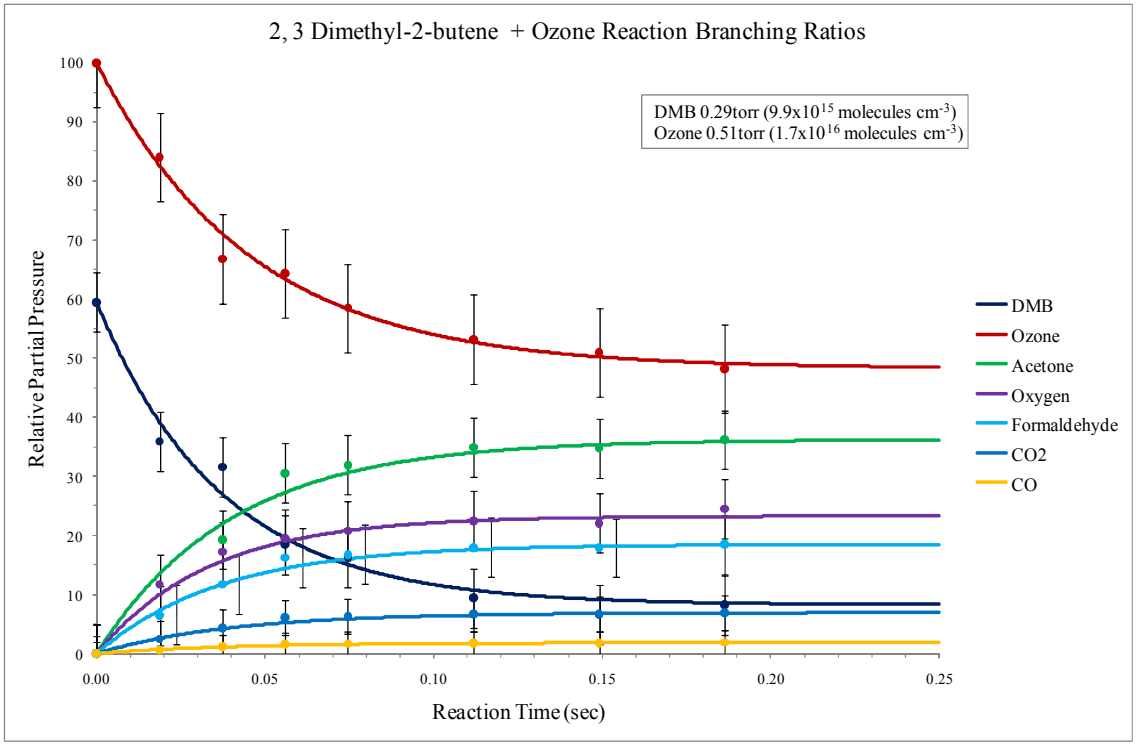

Figure 8.2: *Plot of reagent and product partial pressures as a function of reaction time, obtained from the experiment carried out to obtain Figure 8.1. Error bars have been derived from contributions of the experimental band intensities and experimental cross-sections, (for convenience, in some cases error bars have been displaced slightly horizontally).*

Reference	This work Excess alkene (a)	This work Excess Ozone (a)	[11] (b)	[14] (c)	[15] (d)	[16] (e)
H_2CO	0.385 ± 0.04	0.361 ± 0.04	0.33 ± 0.02	0.119 ± 0.008	0.288 ± 0.023	0.426 ± 0.081
$(CH_3)_2CO$	0.647 ± 0.10	0.707 ± 0.10	1.02 ± 0.13	0.88 ± 0.04	1.006 ± 0.049	1.14 ± 0.19
CO	0.052 ± 0.01	0.036 ± 0.01	0.07 ± 0.02	-	-	-
CO_2	0.194 ± 0.01	0.135 ± 0.01	0.21 ± 0.02			0.275 ± 0.040
H_2O	*	*	-	-	-	-
CH_3OH	-	-	0.04 ± 0.001	-	-	0.055 ± 0.014
CH_3COCHO	-	-	-	0.314 ± 0.071	0.284 ± 0.010	-
$HOCH_2COCH_3$	-	-	0.05 ± 0.01	-	(f)	-
O_2	0.433 ± 0.03	0.455 ± 0.04	-	-	-	-

Table 8.2: *Observed products and measured product yields in this work for the ozone plus 2, 3-dimethyl-2-butene (DMB) reaction, compared to those of previous work.*

(*) observed but could not be reliably measured.

(a) expressed in terms of the observed change in the reagent not in excess.

(b) Niki *et al*. 1987 IR study in air at close to 1 atm pressure.

(c) Grosjean *et al.* 1994 study in air at 1 atm pressure; analysis of carbonyl and carboxylic acid products with chromatography; cyclohexane scavenger added

(d) Grosjean and Grosjean 1996 study in air at 1 atm pressure; analysis of carbonyl products with chromatography in dry and humid air; cyclohexane scavenger added.

(e) Tuazon *et al.* 1997 gas chromatography and IR study in air close to 1 atm pressure; cyclohexane scavenger added.

(f) No differentiation between CH_3COCHO and $HOCH_2COCH_3$ could be made.

Figure 8.3 recorded for the O_3 + 2MP reaction, shows bands associated with the products formaldehyde, oxygen, acetone, carbon monoxide, carbon dioxide and formic acid as well as bands associated with the reagents 2MP and ozone. The corresponding plot of the relative partial pressures of reagents and observed products as a function of reaction time is shown in Figure 8.4, with their exponential fits shown as solid lines. Again water was observed as a reaction product but its intensity was not measured because of band overlap problems.

The product yields measured at the longest mixing distance (reaction time) are shown in Table 8.3 for both [alkene] > [O_3] and [alkene] < [O_3]. As with the DMB reaction, the product yields, expressed relative to the observed change in the reagent not in excess, are in good agreement for both [alkene] > [O_3] and [alkene] < [O_3]. As shown in Table 8.3, the product yields measured in this work for H_2CO, $(CH_3)_2CO$, CO, CO_2 and HCOOH are in reasonably good agreement with those measured earlier [11, 14-16].

Also, as with the O_3 + DMB reaction, the O_2 product yield has not been measured previously and the O_2 yields quoted are the first to be reported. Methanol, methylglyoxal, hydroxyacetone, acetic acid, acetaldehyde and glyoxal have been reported as minor products in some other studies, but they were not observed in this work.

Also, no methyl acetate (1^{st} and 2^{nd} VIEs expected at 10.48 and 11.16 eV [61]) was observed in the spectra recorded for the O_3 + DMB and the O_3 + 2MP reactions, indicating that, as is well known [4], the "ester channel" for decomposition of the Criegee intermediate $(CH_3)_2COO$ ($(CH_3)_2COO \rightarrow CH_3COOCH_3$) is not occurring, although from the results obtained for O_3 + 2MP and O_3 + ethene, it appears that the smaller Criegee intermediate H_2COO, decomposes via this route ($H_2COO \rightarrow HCOOH$) to give formic acid. It has been proposed, based on high level electronic structure calculations that H_2COO isomerises to form a dioxirane intermediate which further isomerises to formic acid [62, 63].

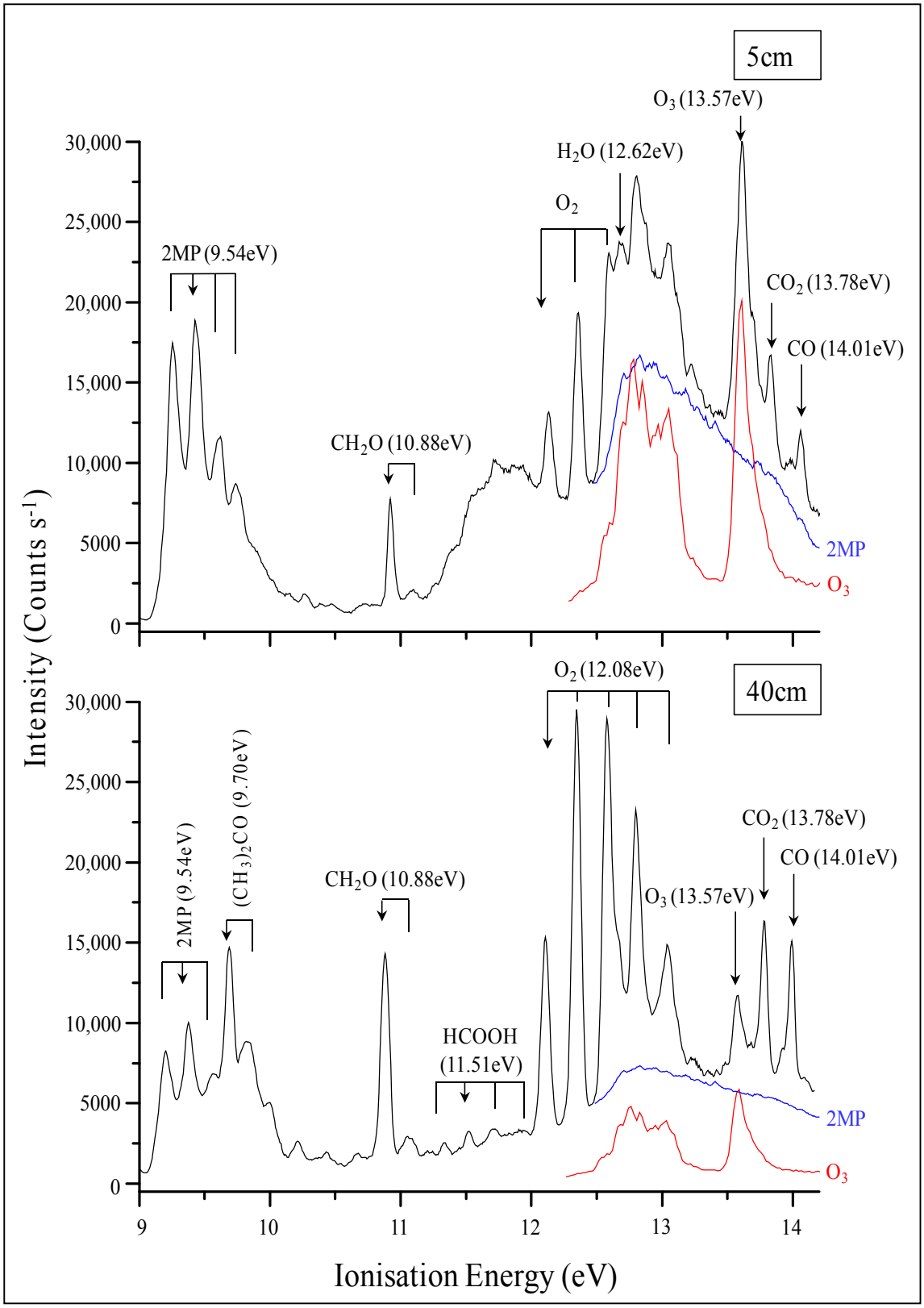

Figure 8.3: *Photoelectron spectra recorded for the O_3 + 2MP reaction at constant initial reagent partial pressures, [2MP] > [O_3], at 5 and 40 cm reaction distance.*

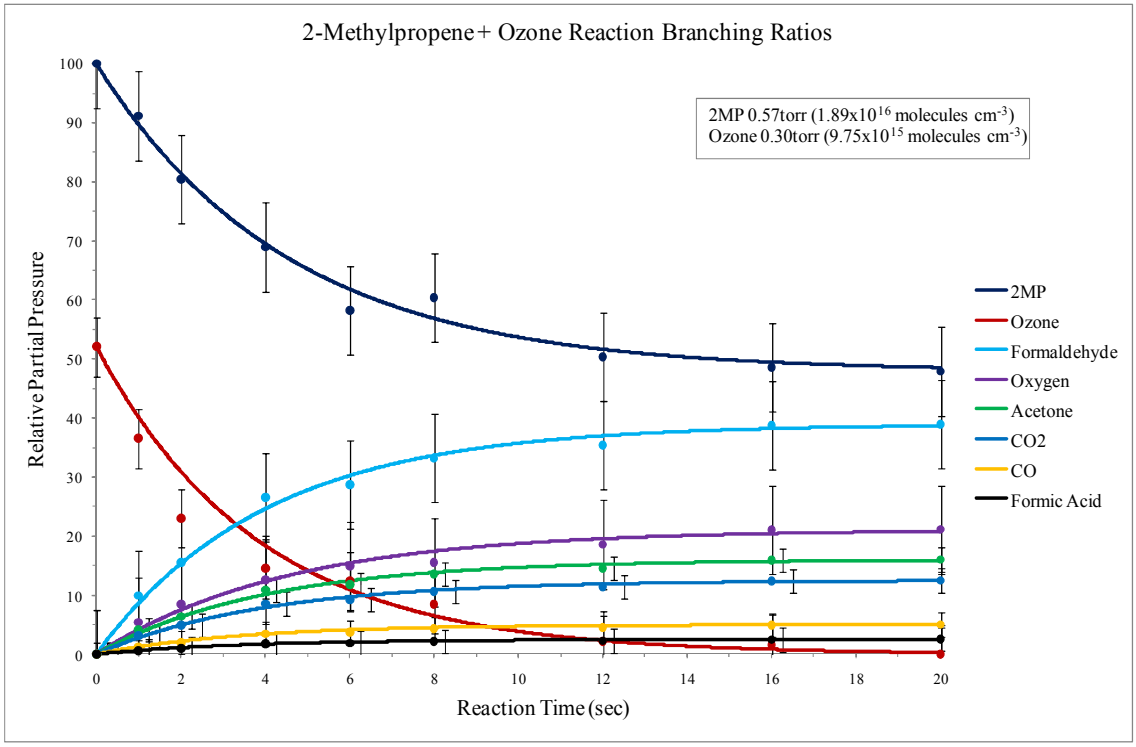

***Figure 8.4**: Plot of reagent and product partial pressures as a function of reaction time, obtained from the experiment carried out to obtain Figure 8.3.*

Reference	This work Excess alkene (a)	This work Excess ozone (a)	[7](b)	[14](c)	[15](d)	[16](e)	[17](f)
H_2CO	0.75 ± 0.08	0.75 ± 0.08	1	0.31 ± 0.03	0.95 ± 0.098	1.01 ± 0.07	0.85 ± 0.03
$(CH_3)_2CO$	0.31 ± 0.03	0.29 ± 0.03	0.41	0.27 ± 0.01	0.340 ± 0.031	0.294 ± 0.031	0.32 ± 0.02
CO	0.10 ± 0.01	0.09 ± 0.01	-	-	-	0.093 ± 0.011	0.06 ± 0.01
CO_2	0.24 ± 0.02	0.22 ± 0.02	0.16	-	-	0.277 ± 0.023	0.23 ± 0.02
H_2O	*	*	0.35	-	-	-	-
HCOOH	0.05 ± 0.01	0.05 ± 0.01	0.06	0.156 ± 0.040	-	-	0.03 ± 0.01
CH_3OH	-	-	0.03	-	-	0.054 ± 0.007	0.04
CH_3COOH	-	-	0.02	-	-	-	-
CH_3COCHO	-	-	-	0.434 ± 0.044[g]	0.190 ± 0.016[g]	-	0.1
$HOCH_2COCH_3$	-	-	-	g	g	-	0.06
CH_3CHO	-	-	-	0.024 ± 0.008	0.02 ± 0.007	-	-
HCOCHO	-	-	-	0.004 ± 0.003[h]	0.006 ± 0.001[h]	-	-
O_2	0.40 ± 0.04	0.50 ± 0.04	-	-	-	-	-

***Table 8.3:** Observed products and measured product yields in this work for the ozone plus 2-methyl propene (2MP) reaction, compared to those of previous work.*

(*) observed but could not be reliably measured.

(a) expressed in terms of the observed change in the reagent not in excess.

(b) Herron and Huie 1978 PIMS study; O_3 in O_2 reacted with 2MP at low pressure (4 torr total).

(c) Grosjean *et al.* 1994 study in air at 1 atm. pressure; analysis of carbonyl and carboxylic acid products with chromatography; cyclohexane scavenger added.

(d) Grosjean and Grosjean 1996 study in air at 1 atm pressure; analysis of carbonyl products with chromatography in dry and humid air; cyclohexane scavenger added.

(e) Tuazon *et al.*1997 gas chromatography and IR study in air close to 1 atm pressure; cyclohexane scavenger added.

(f) Sauer *et al.* 1998 IR, gas chromatography and HPLC study in air close to 1 atm pressure.

(g) No differentiation between CH_3COCHO and $HOCH_2COCH_3$ could be made.

(h) No differentiation between glyoxal and hydroxyacetaldehyde could be made

8.3.1 Kinetics Simulations

Box model kinetics simulations were performed with ACUCHEM [64]. The objective was to propose a series of reactions for use in these simulations which give results which are consistent with the observed product yields and temporal profiles, and provide explanations for the main production reactions of the observed products. For O_3 + DMB, as with the ozone + ethene reaction, in order to establish the main production routes of the products, a reaction scheme has been constructed of three parts (A, B and C shown in Table 8.4), and simulations have been performed in steps using the different components.

Part A consists of the initial O_3 + DMB reaction (reaction 1 in Table 8.4) which has a well established rate coefficient [4] and decomposition reactions of the Criegee intermediate $(CH_3)_2COO$ with rate coefficients taken from references [7, 8, 13 and 65]. In part C, reactions of the Criegee intermediate with O_3, DMB and CH_3 were included with rate coefficients taken from the rate coefficients used for the reactions H_2COO + ethene, (see Chapter 7), H_2COO + O_3, (used for the $(CH_3)_2COO$ + DMB and $(CH_3)_2COO$ + O_3 reactions respectively), and the known rate coefficient for $HO_2 + CH_3 \rightarrow CH_3O + OH$ [66] (used for the $(CH_3)_2CO_2 + CH_3 \rightarrow CH_3O + (CH_3)_2CO$ reaction). Reactions in part B were other reactions in the DMB + O_3 reaction scheme of reference [8] which were found in trial simulations to make significant contributions to the product yields. Rate coefficients for these reactions were taken from reference [8]. Four simulations were carried out for both of the two experimental conditions [DMB] > [O_3] and [DMB] < [O_3] using the rate coefficients listed in Table 8.4.

These were (A), (A + B), (A + C) and (A + B + C). The results of these simulations (the A + B + C plots) compared to experiment are shown in Figures 8.5 and 8.6. As can be seen for [DMB] < [O_3] (Figure 8.5), the decrease of the reagents and the increase of the major products H_2CO, $(CH_3)_2CO$ and O_2 is fitted within experimental error as are the plots obtained for the minor products CO and CO_2. Similar agreement is obtained for the results obtained with [DMB] > [O_3] (Figure 8.6), with the CO_2 curve computed to be lower than the experimental curve. The rate coefficients listed in Table 8.4 are not uniquely determined and so reasonable values for the rate coefficients were made for the simulations. These were valuable in that they allowed the main reactions to be identified for the production of the observed products.

The main reaction products observed were acetone, formaldehyde, O_2, CO_2, CO and H_2O. Acetone is mainly produced by reaction (1), formaldehyde is produced mainly by reaction (17), O_2 is mainly produced by reactions (16) and (22), CO_2 is mainly produced via reaction (2), a decomposition reaction of the Criegee intermediate which is also the main production channel for CH_3. The main channel for CO production is reaction (5), another decomposition channel of the Criegee intermediate, and H_2O is produced mainly by reaction (11),

Section	Step	Reaction	*Rate Coefficient
A			
	1[(a)]	$C_6H_{12} + O_3 = (CH_3)_2CO + (CH_3)_2COO$	$1.13x10^{-15}$
	2[(b)]	$(CH_3)_2COO = CH_3 + CH_3 + CO_2$	$2.50x10^{+05}$
	3	$(CH_3)_2COO = CH_3COCH_2 + OH$	$7.80x10^{+05}$
	4	$(CH_3)_2COO = CH_3C(O)OCH_3$	$5.00x10^{+04}$
	5[(c)]	$(CH_3)_2COO = CH_3O + CH_3 + CO$	$1.70x10^{+05}$
	6	$(CH_3)_2COO = CH_3O + CH_3CO$	$4.40x10^{+05}$
	7	$(CH_3)_2COO = CH_3C(O)O + CH_3$	$1.10x10^{+05}$
B			
	8	$H + C_6H_{12} = C_6H_{13}$	$3.82x10^{-13}$
	9	$H + O_3 = OH + O_2$	$2.66x10^{-11}$
	10	$OH + C_6H_{12} = C_6H_{12}OH$	$1.19x10^{-10}$
	11[(d)]	$OH + CH_2O = H_2O + HCO$	$1.39x10^{-11}$
	12	$OH + CO = CO_2 + H$	$1.49x10^{-13}$
	13	$HO_2 + HO_2 = H_2O_2 + O_2$	$5.65x10^{-12}$
	14	$HO_2 + OH = H_2O + O_2$	$7.97x10^{-11}$
	15	$HO_2 + CH_3O = CH_3OH + O_2$	$1.66x10^{-12}$
	16[(e)]	$CH_3 + O_3 = CH_2O + H + O_2$	$9.13x10^{-13}$
	17[(f)]	$CH_3 + CH_3O = CH_4 + CH_2O$	$4.50x10^{-11}$
	18	$CH_3O + O_2 = CH_2O + HO_2$	$1.49x10^{-15}$
	19	$CH_3O + CH_3O = CH_2O + CH_3OH$	$2.49x10^{-11}$
	20	$CH_3O + OH = CH_2O + H_2O$	$4.98x10^{-11}$
C			
	21	$(CH_3)_2COO + C_6H_{12} = (CH_3)_2CO + C_6H_{12}O$	$5.00x10^{-14}$
	22[(g)]	$(CH_3)_2COO + O_3 = (CH_3)_2CO + O_2 + O_2$	$1.00x10^{-13}$
	23	$(CH_3)_2COO + CH_3 = (CH_3)_2CO + CH_3O$	$3.01x10^{-11}$

Table 8.4: *Reaction scheme used to simulate the Ozone-DMB reaction.*

(*) rate coefficients (in units $cm^3\ molecule^{-1}\ s^{-1}$) were selected as described in the text.

(a) Main $(CH_3)_2CO$ production route.

(b) Main CO_2 and CH_3 production route.

(c) Main CO production route.

(d) Main H_2O production channel.

(e) Main O_2 and H atom production route.

(f) Main CH_2O production route.

(g) O_2 production route for [DMB] > [O_3].

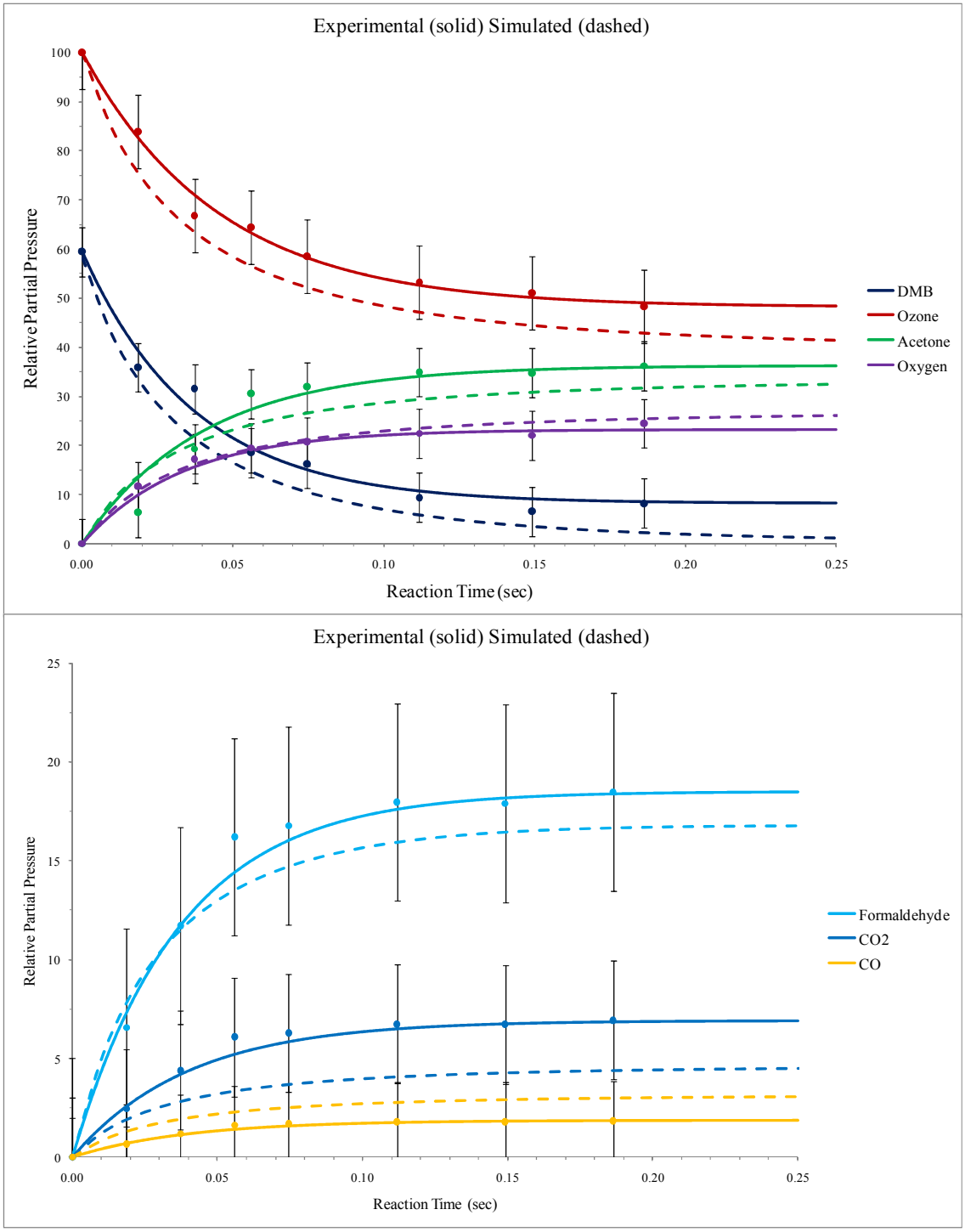

Figure 8.5: *Plot of reagent and product partial pressures as a function of reaction time (solid lines) for O_3 + DMB, with [DMB] < [O_3], compared with the results of simulations using the reaction scheme A + B + C of Table 8.4, using rate coefficients listed in this table. The upper figure shows the reagents and the products (O_2 and $(CH_3)_2CO$) whereas the lower figure shows the products (CO, CO_2, and H_2CO). (for convenience, in some cases error bars have been displaced slightly horizontally). The initial partial pressures are those shown in Figure 8.2; DMB 0.29 torr, Ozone 0.51 torr.*

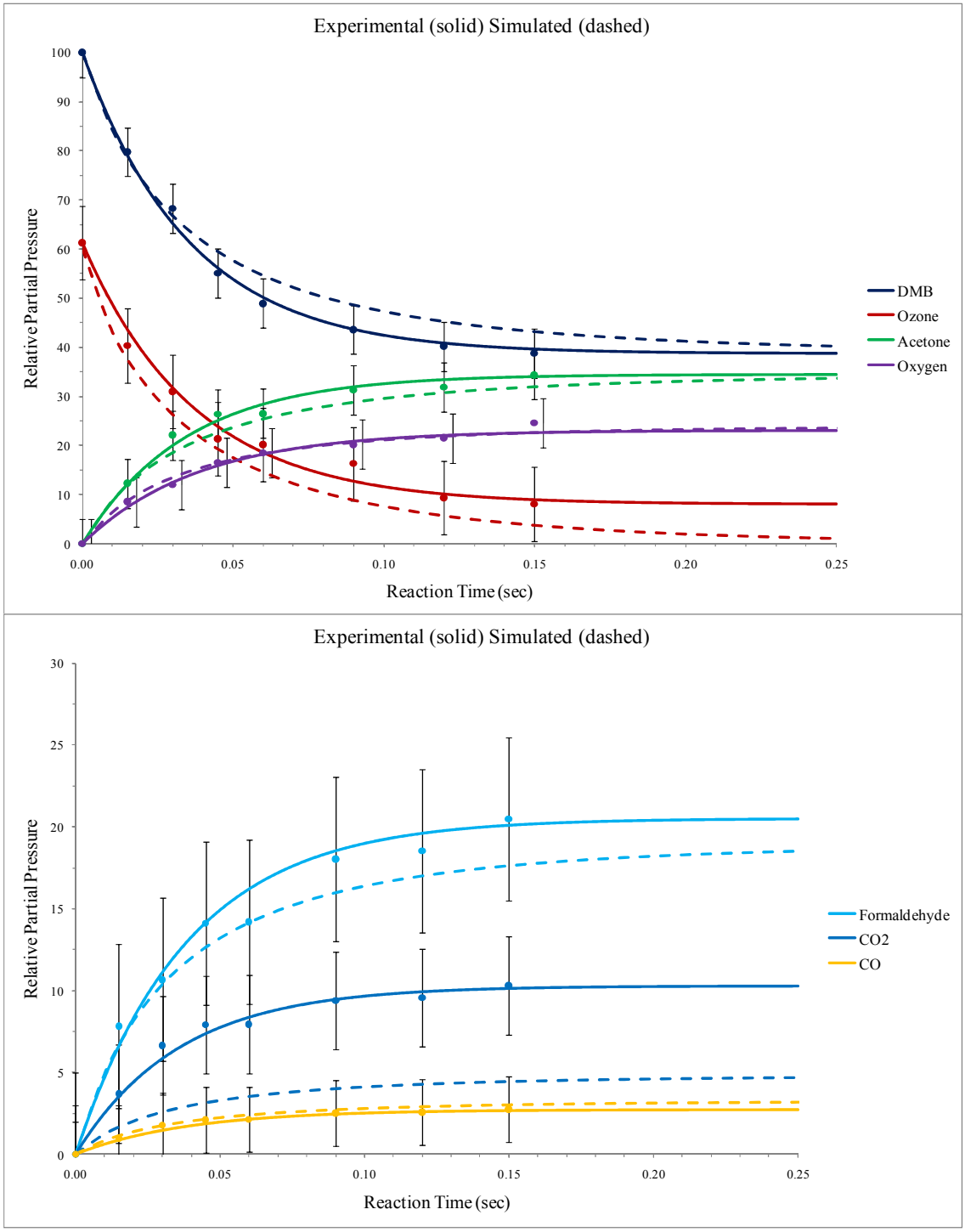

Figure 8.6: *Plot of reagent and product partial pressures as a function of reaction time (solid lines) for O_3 + DMB, with [DMB] > [O_3], compared with the results of simulations using the reaction scheme A + B + C of Table 8.4, using rate coefficients listed in this table. The upper figure shows the reagents and the products (O_2 and $(CH_3)_2CO$) whereas the lower figure shows the products (CO, CO_2, and H_2CO). (for convenience, in some cases error bars have been displaced slightly horizontally). The initial partial pressures were DMB 0.51 torr, Ozone 0.29 torr.*

Section	Step	Reaction	*Rate Coefficient
A			
	1[(a)]	$O_3 + C_4H_8 = CH_2O + (CH_3)_2COO$	$7.31x10^{-18}$
	2[(b)]	$O_3 + C_4H_8 = CH_2OO + (CH_3)_2CO$	$4.31x10^{-18}$
	3[(c)]	$CH_2OO = CO_2 + H_2$	$5.76x10^{+03}$
	4	$CH_2OO = CO_2 + H + H$	$2.88x10^{+03}$
	5[(d)]	$CH_2OO = CO + H_2O$	$2.14x10^{+04}$
	6	$CH_2OO = H + HCO_2$	$2.88x10^{+03}$
	7[(e)]	$CH_2OO = HCOOH$	$1.92x10^{+03}$
	8	$HCO_2 = H + CO_2$	$3.20x10^{+04}$
	9[(f)]	$(CH_3)_2COO = CH_3 + CH_3 + CO_2$	$2.50x10^{+05}$
	10	$(CH_3)_2COO = CH_3COCH_2 + OH$	$7.80x10^{+05}$
	11	$(CH_3)_2COO = CH_3C(O)OCH_3$	$5.00x10^{+04}$
	12	$(CH_3)_2COO = CH_3O + CH_3 + CO$	$1.70x10^{+05}$
	13	$(CH_3)_2COO = CH_3O + CH_3CO$	$4.40x10^{+05}$
	14	$(CH_3)_2COO = CH_3C(O)O + CH_3$	$1.10x10^{+05}$
	15	$CH_2OO + O_3 = CH_2O + O_2 + O_2$	$1.00x10^{-15}$
	16	$(CH_3)_2COO + O_3 = (CH_3)_2CO + O_2 + O_2$	$1.00x10^{-13}$
B			
	17	$H + C_4H_8 = C_4H_9$	$3.82x10^{-12}$
	18	$H + O_3 = OH + O_2$	$2.66x10^{-11}$
	19	$OH + C_4H_8 = C_4H_8OH$	$1.49x10^{-11}$
	20	$OH + CH_2O = H_2O + HCO$	$1.39x10^{-11}$
	21	$OH + CO = CO_2 + H$	$1.49x10^{-13}$
	22	$HO_2 + HO_2 = H_2O_2 + O_2$	$5.65x10^{-12}$
	23	$HO_2 + OH = H_2O + O_2$	$7.97x10^{-11}$
	24	$HO_2 + CH_3O = CH_3OH + O_2$	$1.66x10^{-12}$
	25[(g)]	$CH_3 + O_3 = CH_2O + H + O_2$	$9.13x10^{-13}$
	26	$CH_3 + CH_3O = CH_4 + CH_2O$	$4.50x10^{-11}$
	27	$CH_3O + O_2 = CH_2O + HO_2$	$1.49x10^{-15}$
	28	$CH_3O + CH_3O = CH_2O + CH_3OH$	$2.49x10^{-11}$
	29	$CH_3O + OH = CH_2O + H_2O$	$4.98x10^{-11}$
C			
	30	$CH_2OO + CH_2O = CH_2O + HCOOH$	$4.00x10^{-13}$
	31	$CH_2OO + CH_2O = CH_2O + CO_2 + H_2O$	$2.00x10^{-13}$
	32	$CH_2OO + CH_2O = HCO + HCO + OH$	$2.00x10^{-13}$
	33	$CH_2OO + CH_2O = CH_3CHO + O_2$	$1.00x10^{-13}$
	34	$(CH_3)_2COO + CH_3 = (CH_3)_2CO + CH_3O$	$3.01x10^{-11}$
	35	$CH_2OO + C_4H_8 = (CH_3)_2CO + CH_3CHO$	$1.00x10^{-15}$
	36	$(CH_3)_2COO + C_4H_8 = (CH_3)_2CO + C_4H_8O$	$5.00x10^{-14}$

Table 8.5: *Reaction scheme used to simulate the Ozone-2MP reaction.*

(*) rate coefficients (in units $cm^3\,molecule^{-1}\,s^{-1}$) were selected as described in the text.

(a) Main CH_2O production route.

(b) Main $(CH_3)_2CO$ production route.

(c) Main CO_2 production route with step (9).

(d) Main CO production route; this is also the main H_2O production channel.

(e) Main HCOOH production route.

(f) Main CO_2 production route with step (3).

(g) Main O_2 production route.

A reaction scheme, made from a combination of the reactions used in the reaction schemes for O_3 + ethene and O_3 + DMB, was constructed for the O_3 + 2MP reaction and is shown in Table 8.5. The reaction rate coefficients were kept the same as those used in the O_3 + ethene and O_3 + DMB simulations. As with the O_3 + ethene and O_3 + DMB reaction schemes it was constructed in three parts (A), (B), and (C).

Simulations of the type (A), (A + B), (A + C) and (A + B + C) were also performed and a comparison of the experimental and simulated (A + B + C) plots are shown in Figures 8.7 and 8.8. For [2MP] > [O_3], the decrease of the reagents and the increase of the major products formaldehyde, acetone and oxygen is fitted within experimental error, as is the plot for the minor product formic acid. However, CO_2 is under predicted and CO is over predicted (see Figure 8.7). For [2MP] < [O_3], similar trends are observed, as can be seen in Figure 8.8. From these simulations, the main reactions for the production of the observed products could be identified.

The main reaction products were formaldehyde which is mainly formed from reaction (1), acetone which is formed mainly from reaction (2), O_2 which is produced mainly by reaction (25) with reaction (18) also contributing, CO_2 is produced by reactions (3) and (9) with, reaction (9) being the dominant channel (these reactions are decomposition reactions of the Criegee intermediates H_2COO and $(CH_3)_2COO$ respectively), CO is produced mainly by reaction (5) which is also the main production route for water and reaction (7) which is the main production route for formic acid.

When comparing the yields obtained in this work with those obtained in previous studies, see Tables 8.2 and 8.3, it is important to bear in mind the different experimental conditions used. Apart from the work of reference [7], which is a PIMS study of the O_3 + 2MP reaction at low pressure in the presence of O_2, comparison is made in these tables between the results of this work, which is performed at low pressure, with other studies made in air at atmospheric pressure [11, 14-17].

For the O_3 + DMB reaction, the main production routes of $(CH_3)_2CO$, CO and CO_2 in this work involved decomposition of the Criegee intermediate $(CH_3)_2COO$. This is also true in the higher pressure studies of references [11, 14-16] and hence the product yields $(CH_3)_2CO$, CO and CO_2 in Table 8.2 of this work and references [11, 14-16] can be directly compared.

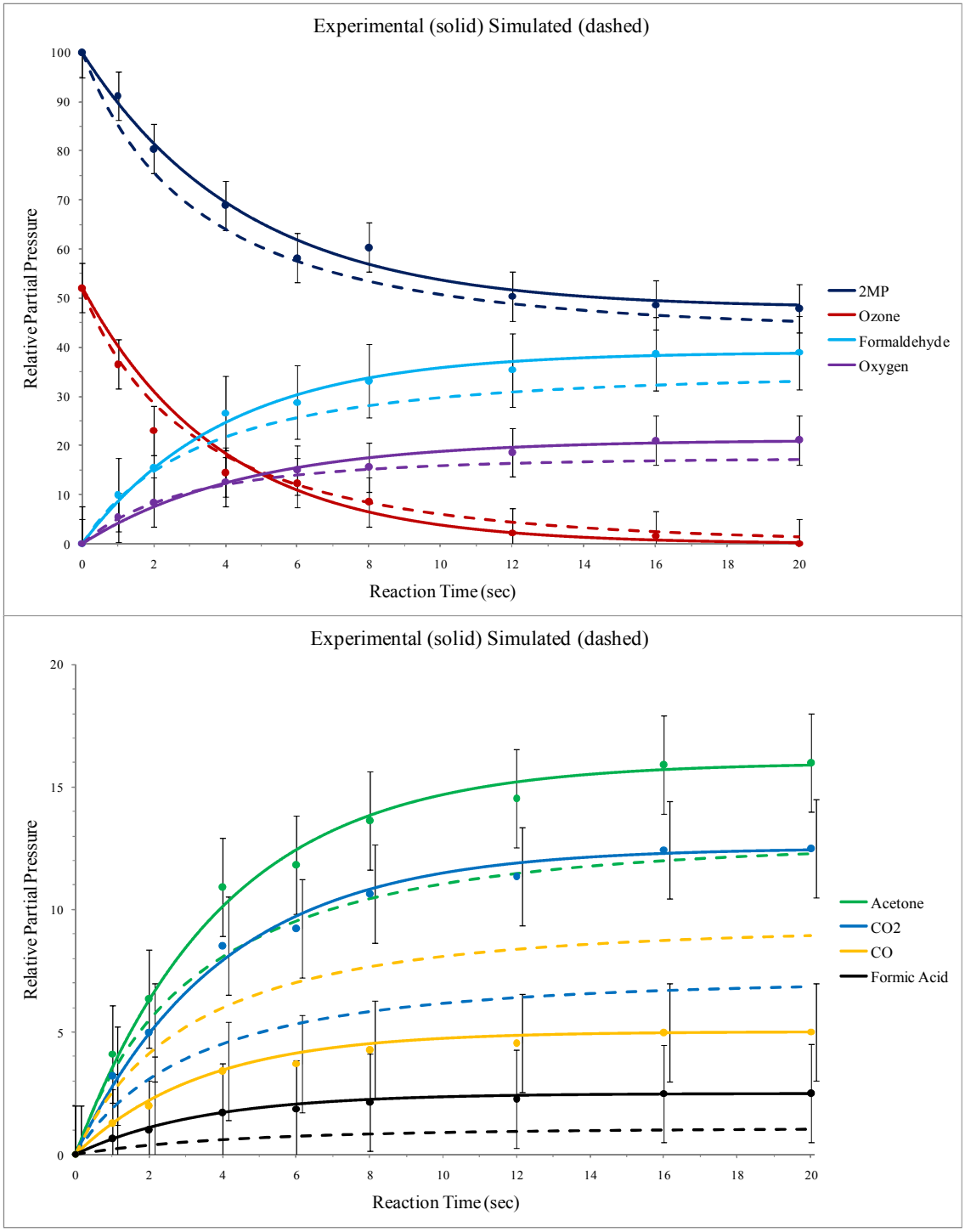

Figure 8.7: *Plot of reagent and product partial pressures as a function of reaction time (solid lines) for O_3 + 2MP, with [2MP] > [O_3], compared with the results of simulations using the reaction scheme A + B + C of Table 8.5, using rate coefficients listed in this table. The upper figure shows the reagents and the products (O_2 and (H_2CO) whereas the lower figure shows the products (CO, CO_2, $(CH_3)_2CO$ and HCOOH). (for convenience, in some cases error bars have been displaced slightly horizontally). The initial partial pressures were as used for Figure 8.4.*

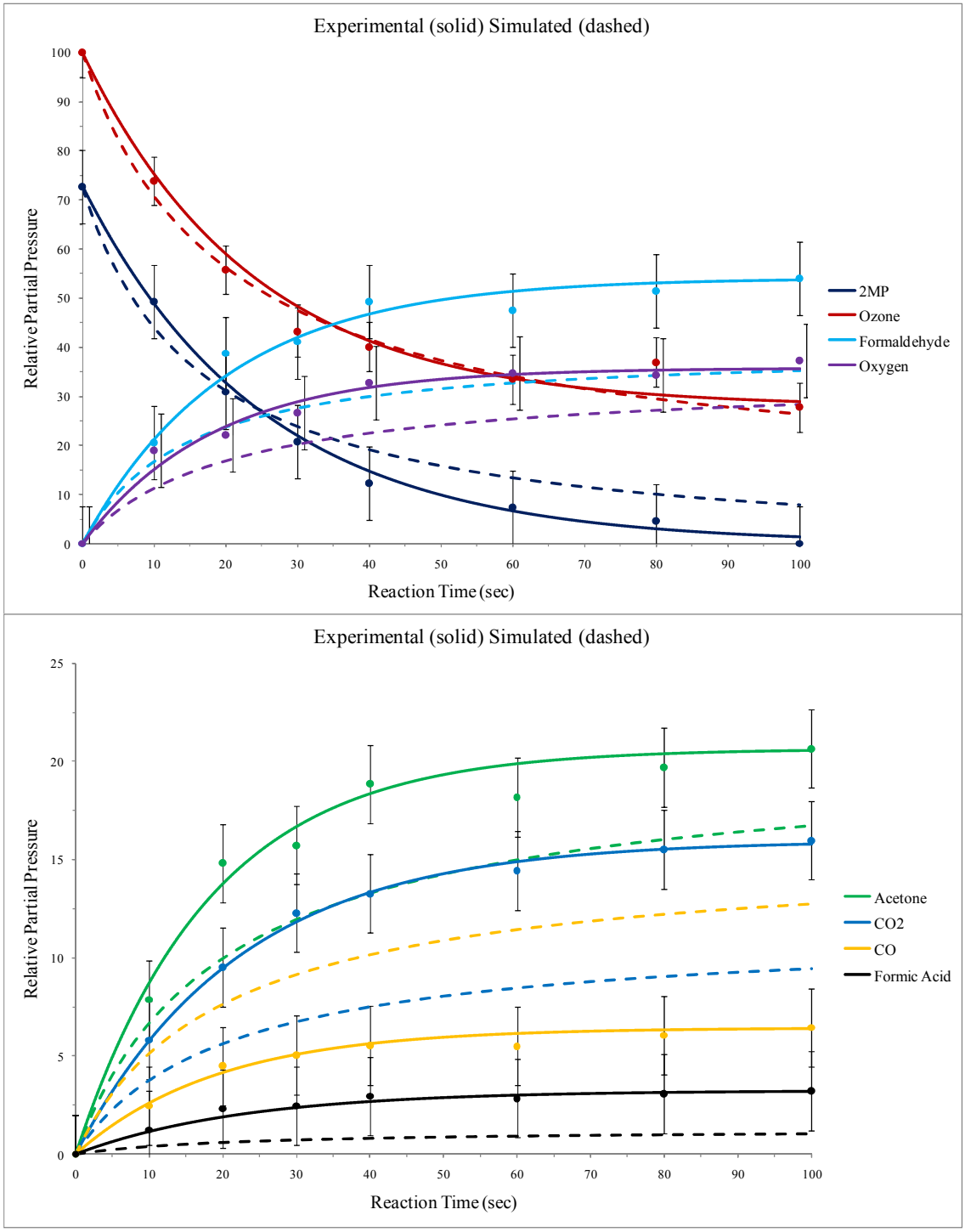

Figure 8.8: *Plot of reagent and product partial pressures as a function of reaction time (solid lines) for O_3 + 2MP, with [2MP] < [O_3], compared with the results of simulations using the reaction scheme A + B + C of Table 8.5, using rate coefficients listed in this table. The upper figure shows the reagents and the products (O_2 and (H_2CO) whereas the lower figure shows the products (CO, CO_2, $(CH_3)_2CO$ and HCOOH). (for convenience, in some cases error bars have been displaced slightly horizontally). The initial partial pressures were 2MP 0.07 torr and Ozone 0.09 torr.*

However, for H_2CO, the main reaction responsible for production of H_2CO in this work is reaction (17) of Table 8.4 (i.e. $CH_3 + CH_3O \rightarrow CH_4 + H_2CO$) whereas under the conditions used in references [11, 14-16] H_2CO arises from rearrangement of $(CH_3)_2COO$ to form a hydroperoxide, $CH_3C(OOH)=CH_2$ followed by subsequent reaction with O_2, i.e.

$$(CH_3)_2COO^* \rightarrow (CH_3C(OOH)=CH_2^* \rightarrow CH_3COCH_2 + OH \quad (8.1)$$

$$CH_3COCH_2 + O_2 \rightarrow CH_3C(O)CH_2OO \quad (8.2)$$

$$CH_3C(O)CH_2OO + OH \rightarrow CH_3C(O)CH_2O + HO_2 \quad (8.3)$$

$$CH_3C(O)CH_2O \rightarrow CH_3CO + H_2CO \quad (8.4)$$

Because of this, the yield of H_2CO measured in this work and the H_2CO yields quoted in Table 8.2 [7, 14-16] cannot be directly compared. Because H_2CO arises in this work from a secondary reaction, listed in Table 8.4 section B (reaction (17) $CH_3 + CH_3O \rightarrow CH_4 + H_2CO$), it is not appropriate to use the H_2CO yield from the O_3 + DMB reaction of this work to estimate the global yield of H_2CO.

In contrast, for the O_3 + 2MP reaction, in the present study H_2CO was found to arise mainly from reaction (1) in Table 8.5 (O_3 + 2MP $\rightarrow H_2CO + (CH_3)_2COO$). Of the previous studies quoted in Table 8.3, references [14-17] were carried out in air at 1 atm. pressure and reference [7] was carried out at low pressure with added oxygen. In these studies, [7, 14-17] extra H_2CO should be produced by the route outlined above (involving formation of a hydroperoxide and reaction with O_2), and hence the H_2CO yields quoted in Table 8.3 in references [7, 14-17] might be expected to be greater than that measured in this work.

This appears to be the case for the results of references [7, 15, 16 and 17] (which are larger by ~30% than the yield of this work) but not for the H_2CO yields of references [14] (see Table 8.3). We therefore conclude that the H_2CO yield measured in this present work for the O_3 + 2MP reaction can be used in global model calculations but is expected to yield a value which is an underestimate (by ~30%).

8.3.2 Results of Global Modelling

Based on global model simulations, approximately 20% of DMB oxidation occurs via reaction with ozone, with oxidation initiated by OH being approximately 4% and oxidation by NO_3 contributing 76%. Determining the annual global emission total for DMB is difficult, but based on the POET [55] emission database for butane, an upper limit of 7.0 Tg is estimated. Using the branching ratio data derived from this work, the following upper limits for the observed products per annum, excluding oxygen, are H_2CO (0.52 Tg), CO (0.06 Tg), CO_2 (0.24 Tg), and $(CH_3)_2CO$ (0.90 Tg). These calculations assume that these products are primary products and therefore will be produced via these routes under atmospheric conditions.

The kinetic modelling described in the previous section shows that this is true for $(CH_3)_2CO$, CO and CO_2. However, H_2CO is produced mainly by the secondary reaction (17) in Table 8.4. This reaction will not be significant under atmospheric conditions and therefore the yield of H_2CO measured in this work cannot be used to determine an annual global yield. However, if the results of reference [11], an infrared study in air at ~1 atm pressure, are taken as representative of the higher pressure studies in air, an annual global yield of ~10% lower than 0.56 Tg is to be expected, where the main source of H_2CO in this case is formation of a hydroperoxide from the Criegee intermediate, $(CH_3)_2COO$, followed by subsequent reaction with oxygen (see the reactions written above). The annual global emission level of acetone is estimated as approximately 78 Tg (17.1 Tg as direct emission and the rest *in-situ* production) [47] and therefore the expected upper limit of 0.9 $Tg.year^{-1}$ of $(CH_3)_2CO$ determined for the O_3 + DMB reaction represents 1% of the *in-situ* source.

Similar global simulations were carried out for 2MP. It was found that approximately 7.5% of 2MP oxidation occurs via reaction with ozone, with OH initiated oxidation being approximately 75% and NO_3 oxidation contributing 17%. An upper limit of about 7.0 $Tg.year^{-1}$ is estimated for the global emission total of 2MP. Using the branching ratio values derived in this work, the following upper limits for the annual yields of the observed products, excluding oxygen, are H_2CO (0.50 Tg), CO(0.05 Tg), CO_2 (0.13 Tg), HCOOH(25.0 Gg) and $(CH_3)_2CO$ (0.16 Tg), where the H_2CO yield has been increased by 30% as noted above to give an upper limit estimate. Inspection of Table 8.5 shows that CO, CO_2, HCOOH and $(CH_3)_2CO$ are primary products which will be

produced under atmospheric conditions. Estimated annual global production levels of H_2CO, HCOOH and $(CH_3)_2CO$ are 2200, 7.3 and 78 Tg [55, 67], and the annual production levels of H_2CO, HCOOH and $(CH_3)_2CO$ derived in this work from the reaction of O_3 with 2MP represent 0.02, 0.30 and 0.20% of the totals respectively.

These results emphasise that the structure of the alkene is critical. For DMB, atmospheric oxidation is dominated by NO_3 whereas for 2MP atmospheric oxidation is mainly via reaction with OH, with ozone oxidation playing a minor role for 2MP but a more prominent role for DMB. In terms of acetone production, this work shows that ozonolysis of short-lived alkenes cannot be ignored. Global model simulations performed in this chapter were carried out by Prof. D. E. Shallcross of Bristol University.

8.4 Conclusions

The O_3 + DMB and O_3 + 2MP reactions have been studied as a function of time using a flow-tube interfaced to a photoelectron spectrometer. Photoelectron band intensities for the reactants and observed products were converted to partial pressures using photoionisation cross-sections which were measured as part of this work. For each reaction, kinetic simulations were used to simulate the observed time-dependences of the reactants and products, and to identify the dominant reactions in a reaction scheme, which are responsible for the observed products. Also global model simulations were used to convert the observed product yields into upper limits produced from these reactions in the atmosphere.

The main result of this work is that for the first time for the two ozone-alkene reactions studied the yields of all the main reaction products, including oxygen, have been measured by the same experimental method.

References

[1] D. Johnson and G. Marston, *Chem. Soc. Rev.*, 37, 2008, 699.

[2] S. E. Paulson and J. J. Orlandi, *Geophys. Res. Letts.*, 23, 1996, 3727.

[3] P. A. Ariya, R. Sander and P. J. Crutzen, *J. Geophys. Res.*, 105, 2000, 17721.

[4] J. G. Calvert, R. Atkinson, J. A. Kerr, S. Madronich, G. K. Moortgat, T. J. Wallington and G. Yarwood, The Mechanisms of Atmospheric Oxidation of the Alkenes, *Oxford University Press*, Oxford, 2000.

[5] R. Wegener, T. Brauers, R. Koppmann, S. T. Bares, F. Rohrer, R. Tilmann, A. Wahner, A. Hansel and A. Wisthaler, *J. Geophys. Res. Atm.*, 112, 2007, 13301.

[6] C. R. Greene and R. Atkinson, *Int. J. Chem. Kinetics.*, 24, 1992, 803.

[7] J. T. Herron and R. E. Huie, *Int. J. Chem. Kinetics.*, 10, 1978, 1019.

[8] R. I. Martinez and J. T. Herron, *J. Phys. Chem.*, 91, 1987, 946.

[9] R. I. Martinez, J. T. Herron and R. E. Huie, *J. Am. Chem. Soc.*, 103, 1981, 3807.

[10] G. E. Orzechowska and S. E. Paulson, *J. Phys. Chem. A.*, 109, 2005, 5358.

[11] H. Niki, P. D. Maker, C. M. Savage, L. P. Breitenbach and M. D. Hurley, *J. Phys. Chem.*, 91, 1987, 941.

[12] R. Atkinson, E. C. Tuazon, and S. M. Aschmann, *Environ. Sci. Technol.*, 29, 1995, 1860.

[13] P. Neeb and G. K. Moortgat, *J. Phys. Chem. A.*, 103, 1999, 9003.

[14] D. Grosjean, E. Grosjean and E. L. Williams, *Environ. Sci. Technol.*, 28, 1994, 186.

[15] D. Grosjean and E. Grosjean, *Environ. Sci. Technol.*, 30, 1996, 859.

[16] E. C. Tuazon, S. M. Aschmann, J. Arey and R. Atkinson, *Environ. Sci. Technol.*, 31, 1997, 3004.

[17] F. Sauer, C. Schafer, P. Neeb, O. Horie and G. K. Moortgat, *Atmos. Environ.*, 33, 1998, 229.

[18] R. Criegee and G. Wenner, *Chem. Ber.*, 564, 1949, 9.

[19] W. T. Chan and J. P. Hamilton, *J. Chem. Phys.*, 118, 2003, 1688.

[20] M. F. Henricks and C. Vinckier, *J. Chem. Phys. A.*, 107, 2003, 7574.

[21] I. Ljubic and A. Sabljic, *J. Chem. Phys. A.*, 106, 2002, 4745.

[22] J. M. Anglada, R. Creheut, and J. M. Bofill, *Chem. Eur. J.*, 5, 1999, 1809.

[23] T. Saito, S. Nishihara, Y. Kataoka, Y. Nakanishi, Y. Kitagawa, T. Kawakami, S. Yamanaka, M. Okumura and K. Yamaguchi, *J. Phys. Chem. A.*, 114, 2010, 12116.

[24] Y. Zhao, O. Tishchenko, J. R. Gour, W. Li, J. J. Lutz, P. Piecuch and D. G. Truhlar, *J. Phys. Chem. A.*, 113, 2009, 5786.

[25] R. Ponec, J. Roithiva and Y. Haas, *Croat. Chem. Acta.*, 74, 2001, 251.

[26] M. Clay and B. S. Ault, *J. Phys. Chem. A.*, 114, 2010, 2799.

[27] M. D. Hoops and B. S. Ault, *J. Am. Chem. Soc.*, 131, 2009, 2853.

[28] B. E. Coleman and B. S. Ault, *J. Phys. Chem. A.*, 114, 2010, 12667.

[29] J. M. Dyke, M. V. Ghosh, M. Goubet, E. P. F. Lee, G. Levita, K. Miqueu and D. E. Shallcross, *Chem. Phys.*, 324, 2006, 85.

[30] J. M. Dyke, M. V. Ghosh, D. J. Kinnison, G. Levita, A. Morris and D. E. Shallcross, *Phys. Chem. Chem. Phys.*, 7, 2005, 866.

[31] J. M. Dyke, N. Jonathan and A. Morris, *Int. Rev. Phys. Chem.*, 2, 1982, 3.

[32] M. C. R. Cockett, J. M. Dyke and H. Zamanpour, Vacuum Ultraviolet Photoionisation and Photodissociation of Molecules and Clusters.

[33] J. M. Dyke, L. Golob, N. Jonathan, A. Morris and M. Okuda, *J. C. S. Faraday II*, 70, 1974, 1828.

[34] S. Willitsch, F. Innocenti, J. M. Dyke, and F. Merkt, *J. Chem. Phys.*, 122, 2005, 024311.

[35] J. Berkowitz, *Int. J. Mass. Spec.*, 271, 2008, 8.

[36] G. V. Marr and J. B. West, *Atomic Data Nuclear Data Tables*, 18, 1976, 497.

[37] J. Wang, B. Yang, T. A. Cool, N. Hansen and T. Kasper, *Int. J. Mass. Spec.*, 269, 2008, 210.

[38] W. J. Van der Meer, P. Van der Meulen, M. Volmer and C. A. de Lange, *Chem. Phys.*, 126, 1988, 385.

[39] C. E. Brion, K. H. Tan, M. J. Van der Wiel and P. E. van der Leeuw, *J. Elec. Spec. Rel. Phen.*, 17, 1979, 101.

[40] E. W. Plummer, T. Gustafsson, W. Gudat and D. E. Eastman, *Phys. Rev. A.*, 15, 1977, 2339.

[41] C. E. Brion and K. H. Tan, *J. Elec. Spec. Rel. Phen.*, 15, 1979, 241.

[42] C. E. Brion and K. H. Tan, *Chem. Phys.*, 34, 1978, 141.

[43] G. Cooper, J. E. Anderson and C. E. Brion, *Chem. Phys.*, 209, 1996, 61.

[44] I. Cacelli, R. Moccia and R. Montuoro, *Chem. Phys. Letts.*, 347, 2001, 261.

[45] C. E. Brion and F. Carnovale, *Chem. Phys.*, 100, 1985, 291.

[46] T. A. Cool, J. Wang, K. Nakajima, C. A. Taatjes and A. Mcllroy, *Int. J. Mass. Spec.*, 247, 2005, 18.

[47] S. R. Utembe, M. C. Cooke, A. T. Archibald, M. E. Jenkin, R. G. Derwent and D. E. Shallcross, *Atmos. Environ.*, 44, 2010, 1609.

[48] A. T. Archibald, M. C. Cooke, S. R. Utembe, D. E. Shallcross, R. G. Derwent and M. E. Jenkin, *Atmos. Chem. Phys.*, 10, 2010, 1.

[49] W. Collins, D. Stevenson, C. Johnson and R. Derwent, *J. Atmos. Chem.*, 26, 1997, 223.

[50] R. G. Derwent, D. S. Stevenson, R. M. Doherty, W. J. Collins, M. G. Sanderson and C. E. Johnson, *Climatic Change*, 88, 2008, 385.

[51] M. E. Jenkin, L. A. Watson, S. R. Utembe and D. E. Shallcross, *Atmos. Environ.*, 427185, 2008, 7195.

[52] S. R. Utembe, L. A. Watson, D. E. Shallcross and M. E. Jenkin, *Atmos. Environ.*, 43, 2009, 1982.

[53] L. A. Watson, D. E. Shallcross, S. R. and M. E. Jenkin, *Atmos. Environ.*, 42, 2008, 7196.

[54] J. G. Olivier, A. F. Bouwman, J. J. Berdowski, C. Veld, J. P. Bloos, A. J. Visschedijk and J. L. Haverlag, Description of EDGAR Version 2.0: A set of global emission inventories of greenhouse gases and ozone depleting substances for all anthropogenic and most natural sources on a per country basis and on a 1deg. x 1deg. grid, Technical Report, *Netherlands Environmental Assessment Agency*, 1996.

[55] C. Granier, J. Lamarque, A. Mieville, J. Muller, J. Olivier, J. Orlando, J. Peters, G. Petron, S. Tyndall and S. Wallens, 2005 POET, *database of surface emissions of ozone precursors*. http://www.aero.jussieu.fr/projet/ACCENT/POET.php'.

[56] D. Henze, J. Seinfeld, N. Ng, J. Kroll, T. Fu, D. Jacob and C. Heald, *Atmos. Chem. Phys*., 82405, 2008, 2420.

[57] M. Andreae and P. Merlet, *Global Biogeochemical Cycles.*, 15, 2001, 15, 955.

[58] J. E. Penner, D. H.Lister, D. J. Griggs, D. J. Dokken and M. McFarland, IPCC Special Report on Aviation and Global Atmosphere, Technical report, *Intergovernmental Panel on Climate Change*, 1999.

[59] K. Kimura, S. Katsumata, Y. Achiba, T. Yamasaki and S. Iwata, Handbook of HeI Photoelectron Spectra, *Japan Scientific Press*, Tokyo, 1981.

[60] R. Arakawa, *Bull. Chem. Soc. Jap.*, 64, 1991, 1022.

[61] D. A. Sweigart and D. W. Turner, *J. Am. Chem. Soc.*, 94, 1972, 5592.

[62] D. Cremer, E. Kraka and P. G. Szalay, *Chem. Phys. Lett.*, 292, 1998, 97.

[63] H. E. O'Neal and C. A. Blumstein, *Int. J. Chem. Kinet.*, 5, 1973, 397.

[64] W. Braun, J. T. Herron and D. K. Kahaner, *Int. J. Chem. Kinetics.*, 20, 1988, 51.

[65] M. Siese, K. H. Becker, K. J. Brockman, H. Geiger, A. Hofzumahuas, F. Holland, D. Mihelcic and K. Wirtz, *Environ. Sci. Technol.*, 35, 2001, 4660.

[66] D. L. Baulch, C. J. Cobos, R. A. Cox, C. Esser, P. Frank, J. A. Kerr, M. J. Pilling, J. Troe, R. W. Walker and J. Warnatz, *J. Phys. Chem. Ref. Data*, 21, 1992, 411.

[67] M. C. Cooke, PhD Thesis, University of Bristol, 2010.

Chapter 9

A Study of Selected Triatomics using TPES and PES

During the course of this project, four weeks were allocated at the Elettra synchrotron radiation facility in Trieste, Italy, to study three non-linear triatomic molecules, SF_2, HOCl and HO_2 using threshold photoelectron spectroscopy (TPES). Three experiments were carried out with the following objectives,

1. To record a well resolved first TPE band of the molecule SF_2 with reduced contributions from S_2, from the consecutive reactions,

$$F + OCS \rightarrow SF + CO \quad (9.1)$$

$$SF + SF \rightarrow SF_2 + S \quad (9.2)$$

$$S + S + M \rightarrow S_2 + M \quad (9.3)$$

2. To record the TPE spectrum of the first two bands of the unstable intermediate hypochlorous acid (HOCl), where HOCl is produced from the reactions,

$$Cl_2 + HgO_{(s)} \rightarrow Cl_2O + Hg_{(s)} \quad (9.4)$$

$$Cl_2O + H_2O \rightarrow 2HOCl \quad (9.5)$$

3. To record a TPE spectrum of HO_2 from the reaction,

$$F + H_2O_2 \rightarrow HO_2 + HF \quad (9.6)$$

in the photon energy region 10.5-13.5 eV, to observe the first band of HO_2.

HO_2 has been widely studied because of its importance in atmospheric and combustion chemistry [1-3]. The He(I) PE spectrum, recorded by Dyke *et al.* [4], shows vibrational structure associated with a progression in the O-O symmetric stretching mode with a measured first AIE of (11.35 ± 0.01) eV and a measured vibrational frequency of (1560 ± 50) cm^{-1} (0.19 eV). The aim of the present work was to record a high resolution TPE spectrum of the vibrational structure observed from PES studies of HO_2 in the photon energy range 11.3 to 12.2 eV.

In this work, HO_2 was prepared for a TPES study using reaction (9.6), which has an estimated room temperature rate coefficient of $4.98x10^{-11}$ $cm^3.molecules^{-1}$ s^{-1} [5]. H_2O_2 was prepared in the gas-phase for this reaction by warming a hydrogen peroxide urea complex mixed in sand (SiO_2, Sigma Aldrich), using a weight ratio of 1:2, to 35 ºC in a round bottom flask. The H_2O_2 vapour was then flowed through a teflon coated glass inlet (as described in Chapter 3 section 3.2.1) where it reacted with F atoms (produced from discharging F_2) forming HO_2 + HF. A secondary reaction also occurs using this experimental method, which gives O_2 from reaction (9.7),

$$F + HO_2 \rightarrow O_2 + HF \qquad (9.7)$$

This has an estimated room temperature rate coefficient of $8.30x10^{-11}$ $cm^3.molecules^{-1}s^{-1}$ [5]. The recorded TPE spectrum of HO_2 shows three vibrational components at (11.35 ± 0.01) eV, (11.55 ± 0.01) eV and (11.75 ± 0.01) eV. O_2 and H_2O were also observed from the recorded TPE spectra with O_2 arising from reaction (9.7) and H_2O occurring during heating of H_2O_2. Large fluctuations in band intensities were observed when recording TPE spectra of HO_2. These fluctuations were due to poor temperature control on the heating mantle used to warm the urea complex resulting in an unsteady flow of H_2O_2 vapour. As a consequence of this generally poor spectra were obtained. This experiment needs to be repeated using a heating mantle with a more reliable thermostat which will give a constant vapour pressure of H_2O_2. Because of this, the work on HO_2 is still ongoing and so will not be presented in this thesis.

The first experiment performed at Elettra was to record the TPE spectrum of SF_2. SF_2 had previously been investigated at Elettra, using reactions (9.1) to (9.2) to prepare SF_2. TPE spectra were recorded with a low $[SF_2]$:$[S_2]$ ratio. In order to obtain a higher $[SF_2]$:$[S_2]$ ratio the production method was first optimised at Southampton using PES before being studied at Elettra. To achieve a higher $[SF_2]$:$[S_2]$ ratio the reaction mixing

distance was reduced in order to minimise the contribution of reaction (9.3) thereby reducing the S_2 signal observed in the TPE spectra. The results obtained from this work are compared with results of recent *ab initio* calculations and are described in section 9.1 of this chapter.

The second experiment performed at Elettra was to attempt to record a well resolved TPE spectrum of the unstable intermediate hypochlorous acid (HOCl), prepared from reactions (9.4) and (9.5) by bubbling Cl_2 through an aqueous solution of mercuric oxide (HgO). Initial PE spectra of this molecule were recorded in Southampton using a He(I) photon source on the *synchrotron* PE spectrometer (described in section 3.4.2 of Chapter 3), before it was transported to Elettra to be used for TPES measurements, in order to optimise the method to produce HOCl. HOCl was observed reproducibly from recorded PE spectra in Southampton. However, attempts made to reproduce these results at the synchrotron facility using the proposed method proved unsuccessful, with HOCl being produced in small amounts for short periods of time. This meant that the method used to prepare HOCl for TPES study had to be developed further in order to allow HOCl PE spectra, where HOCl is prepared from reactions (9.4) and (9.5), to be obtained for extended periods of time (~4 hours). These conditions were necessary in order to be able to record TPE spectra at Elettra.

A reliable method has now been developed to record TPE spectra of HOCl consistently for upwards of 4 hours and is discussed in the second part of this chapter (see section 9.5) with the first section of this chapter describing the results of the SF_2 investigation carried out at Elettra.

9.1 A Study of SF_2 using TPES

SF_x reactive intermediates have received considerable attention both experimentally and theoretically because of their importance in the semiconductor industry [6], where they play a major role in plasma etching.

The He(I) PE spectrum of SF_2 was recorded in 1978 by de Leeuw *et al.* [7] where SF_2 was prepared using the reaction of OCS with discharged SF_6 (or CF_4). Five PE bands were observed in the He(I) PE spectrum with vibrational structure only observed in the first PE band. This showed a regular series in the symmetric stretching mode of the ion, with an average separation of 935 cm^{-1} (116 meV) [7]. The first adiabatic and vertical

first ionisation energy, AIE and VIE, were experimentally determined in this study as (10.08 ± 0.02) eV and (10.31 ± 0.02) eV respectively. Using Resonance Enhanced Multi-Photon Ionisation (REMPI), Li *et al.* [8] assigned eight Rydberg series showing structure in vibrational frequencies, ν_1 and ν_2. A first AIE for SF_2 of 10.021 eV was also determined in this study from Rydberg series extrapolation.

Electronic structure calculations have also been performed on SF_2. Irikura *et al.* [9] carried out *ab initio* calculations to determine the molecular structure and the thermochemistry of the SF_n (n = 1 to 5) molecules and their respective cations in the gas-phase, determining a first AIE of (10.15 ± 0.19) eV and vibrational frequencies of ν_1 = 840 cm^{-1}, ν_2 = 339 cm^{-1} and ν_3= 827 cm^{-1} for the ground state of SF_2 and ν_1 = 956 cm^{-1}, ν_2 = 389 cm^{-1} and ν_3 = 976 cm^{-1} for the ground state of SF_2^+. Lee *et al*. [10] simulated the He(I) PE spectrum of SF_2 using *ab initio* calculations on SF_2 and SF_2^+ followed by Franck-Condon factor calculations allowing for anharmonicity. Good agreement was observed for the first PE band when comparing the simulated PE spectrum to that recorded by de Leeuw *et al*. [7]. Computed vibrational frequencies were also obtained in this work as, ν_1 = 846.6 cm^{-1}, ν_2 = 357.0 cm^{-1} and ν_3 = 823.9 cm^{-1} for the ground state of SF_2 and ν_1 = 985.6 cm^{-1}, ν_2 = 413.4 cm^{-1} and ν_3 = 1012.5 cm^{-1} for the ground state of SF_2^+ with a determined first AIE of 10.075 eV [10]. A summary of the vibrational frequencies, AIEs and VIEs determined is shown in Table 9.1.

Source	Vibrational Frequency (cm^{-1})			Ionisation Energy (eV)	
	ν_1	ν_2	ν_3	AIE	VIE
Kirchhoff *et al.*[11]	840 ± 20	357 ± 2	809 ± 10	-	-
Deroche *et al.*[12]	838.5299 ± 0.0015	-	813.0413 ± 0.0005	-	-
Glinsky *et al.*[13,14]	838 ± 2	355 ± 2	817 ± 6	-	-
Irikura *et al.*[9]	840	339	827	10.15 ± 0.19	-
(SF_2^+)[9]	956	389	976	-	-
Lee *et al.*[10]	846.6	357.0	823.9	10.075 ± 0.011	10.319
(SF_2^+)[10]	985.6	413.4	1012.5	-	-
de Leeuw *et al.*[7]	935 ± 40	-	-	10.08	10.31
Li *et al.*[8]	-	-	-	10.021	-
This Work	(See Table 9.3)			10.076 ± 0.005	10.320 ± 0.005

Table 9.1: *Summary of the vibrational frequencies, AIEs and VIEs recorded experimentally and theoretically.*

In the present work, the first PE band of SF_2 has been investigated by TPES measurements with the aim of obtaining a high resolution PE spectrum of the first band of SF_2 to determine the first AIE, VIE and ionic state vibrational constants.

9.2 Experimental

All the experiments reported in this chapter were carried out on the Circularly Polarised Beamline (4.2R, Polar) at the Elettra synchrotron radiation source using the photoelectron spectrometer described in section 3.4.2 of Chapter 3. SF_2 was produced from reactions (9.1) to (9.2). These reactions have room temperature rate coefficients of $1.8x10^{-11}$ $cm^3.molecule^{-1}$ s^{-1} and $2.5x10^{-11}$ $cm^3.molecule^{-1}$ s^{-1} respectively [15]. F atoms were made in this work by discharging F_2 as described in Chapter 3 section 3.2.1. Before carrying out any TPE measurements at Elettra, the experimental method was first optimised in Southampton, to determine the optimum partial pressures and reactant mixing distance required to yield the highest $[SF_2]$:$[S_2]$ ratio, from PES measurements. These were found to be Δp (Ar) = $5.40x10^{-7}$ mbar, Δp (OCS) = $2.80x10^{-6}$ mbar and Δp (5% F_2/He) = $6.00x10^{-6}$ mbar. The optimum reaction mixing distance which gave the highest $[SF_2]$:$[S_2]$ ratio was found to be 0 cm above the photon beam. Argon was introduced with the reagents to optimise the voltages when recording TPE spectra, as described in Chapter 3 section 3.4.3.

9.3 Results and Discussion

He(I) PE spectra recorded for the F + OCS reaction, at mixing distances of 8 cm and 0 cm above the photon beam, are shown in Figure 9.1. It can be seen in both PE spectra that SF_2 shows a regular vibrational progression between 10.0 eV and 11.0 eV [9, 14], with a first AIE and VIE of (10.076 ± 0.005) eV and (10.320 ± 0.005) eV respectively (determined from this work). Secondary products of reaction (9.1) are observed in both spectra, i.e. S atoms, which have a first IE of 10.36 eV [16] and S_2, which has four bands in the energy region of interest, at 9.41 eV, 11.82 eV, 12.33 eV and 13.20 eV (VIE) [17]. CO and CO_2 are also observed in the spectra with first VIEs of 14.01 eV and 13.78 eV respectively [18].

Previous TPE measurements at Elettra on SF_2 (2007) were recorded at a mixing distance of 8 cm and revealed a low $[SF_2]$:$[S_2]$ ratio. PE spectra recorded at this mixing distance also revealed a low $[SF_2]$:$[S_2]$ ratio, as shown in the upper PE spectrum in Figure 9.1, with significantly more S_2 than S atoms being observed. A higher S_2 production is expected at longer mixing distances as this allows an increased recombination time of S atoms than that at shorter mixing distances. However, the yield

of SF_2 appears reasonable and the vibrational progression is clearly visible with very little excess OCS observed, under the reaction conditions used. However, a TPE study of O_2 by Ellis *et al.* [19] revealed that in TPE experiments, the vibrational structure associated with the first band of O_2 extended beyond that observed from PE spectra (12.08 eV to 12.98 eV) showing vibrational structure between the first two bands (13 eV to 16 eV). This extra structure arises from autoionisation in the TPE work. Because S_2 has a very similar PE spectrum to O_2 (they have the same valence electronic structure) and assuming that the same autoionisation effect occurs in S_2 as in O_2, extra vibrational structure would be observed in the TPE spectrum from that seen in the PE spectrum through the ionisation region of interest (9.7 eV to 10.7 eV). This was apparent in this IE region in the previous TPE spectra recorded at a mixing distance of 8 cm.

It was therefore necessary to obtain conditions for recording TPE spectra of SF_2 with a lower yield of S_2 production and this was the aim of this investigation. It was found that using shorter mixing distances (0 cm) provided a higher yield of SF_2 relative to S_2 from initial PES measurements. This is observed from Figure 9.1 (bottom PE spectrum) which shows significantly smaller quantities of S and S_2 production. At shorter mixing distances S atoms have considerably less time in which to recombine to form S_2 which makes these conditions, where a high $[SF_2]$:$[S_2]$ ratio is observed, more suitable for recording TPE spectra than those at longer mixing distances. Lee *et al.* have carried out *ab initio* calculations on the ground states of SF_2 and SF_2^+ to simulate the He(I) spectrum of SF_2 including effects of anharmonicity [20]. The simulated He(I) PE spectrum of SF_2 is shown below in Figure 9.2 with a FWHM resolution of each component of 1meV. This spectrum was simulated at a Boltzmann temperature of 600 K. The bands observed at *ca.* 9.98 eV are attributed to "hot" bands as there features are not seen from spectra (experimental and simulated) obtained at room temperature. Additional "hot" bands are also observed, associated with the main vibrational components and are labelled in red in Figure 9.2.

The TPE spectrum of SF_2 recorded under the optimum conditions, determined from PES measurements, which gives the highest $[SF_2]$:$[S_2]$ ratio obtained from the F + OCS reaction at Elettra is shown in Figure 9.3.

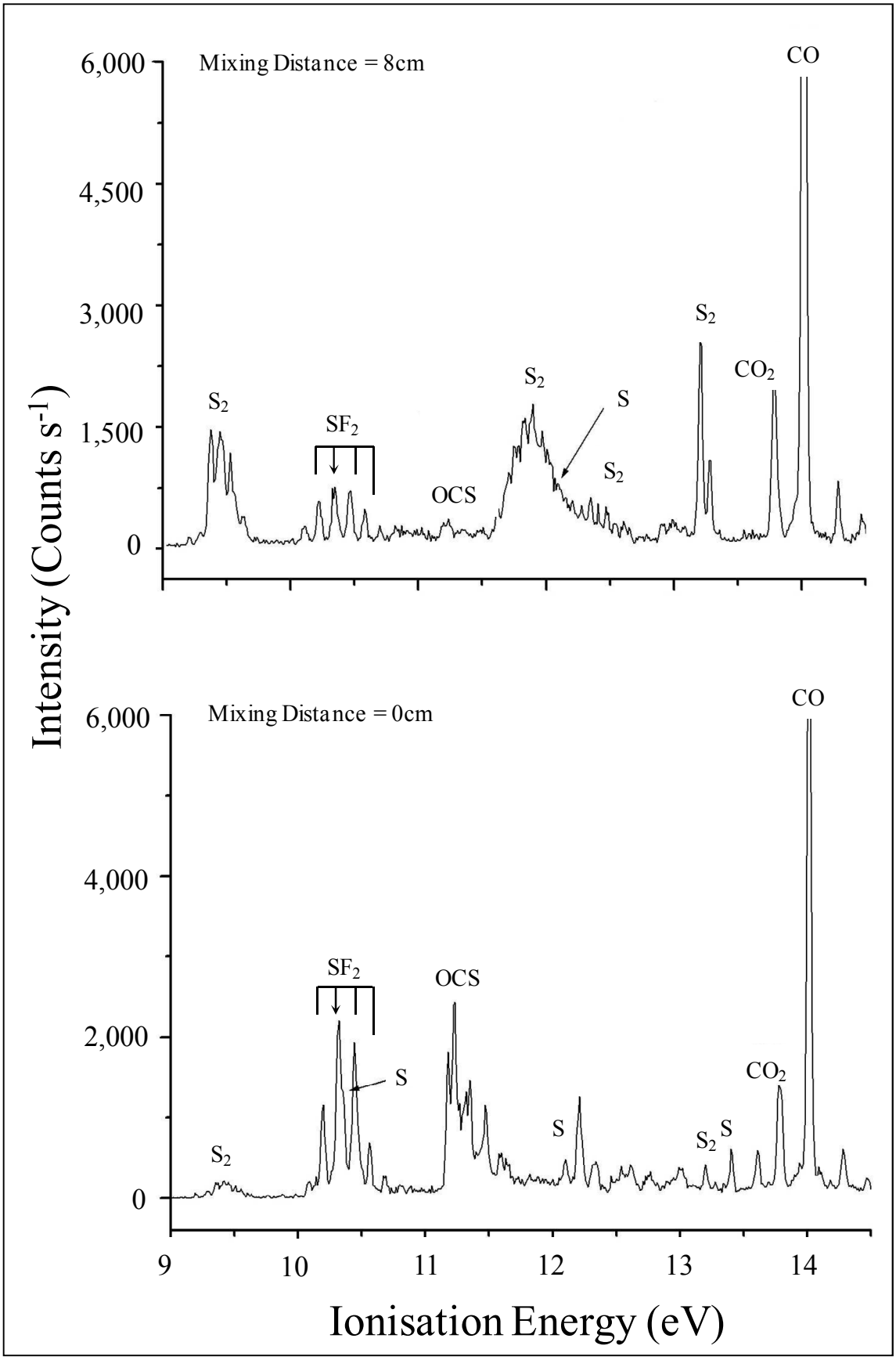

Figure 9.1: *He(I) PE spectra recorded for the reaction F + OCS (recorded at room temperature, 298 K) showing a low $[SF_2]:[S_2]$ ratio (top spectrum) and a high $[SF_2]:[S_2]$ ratio (bottom spectrum).*

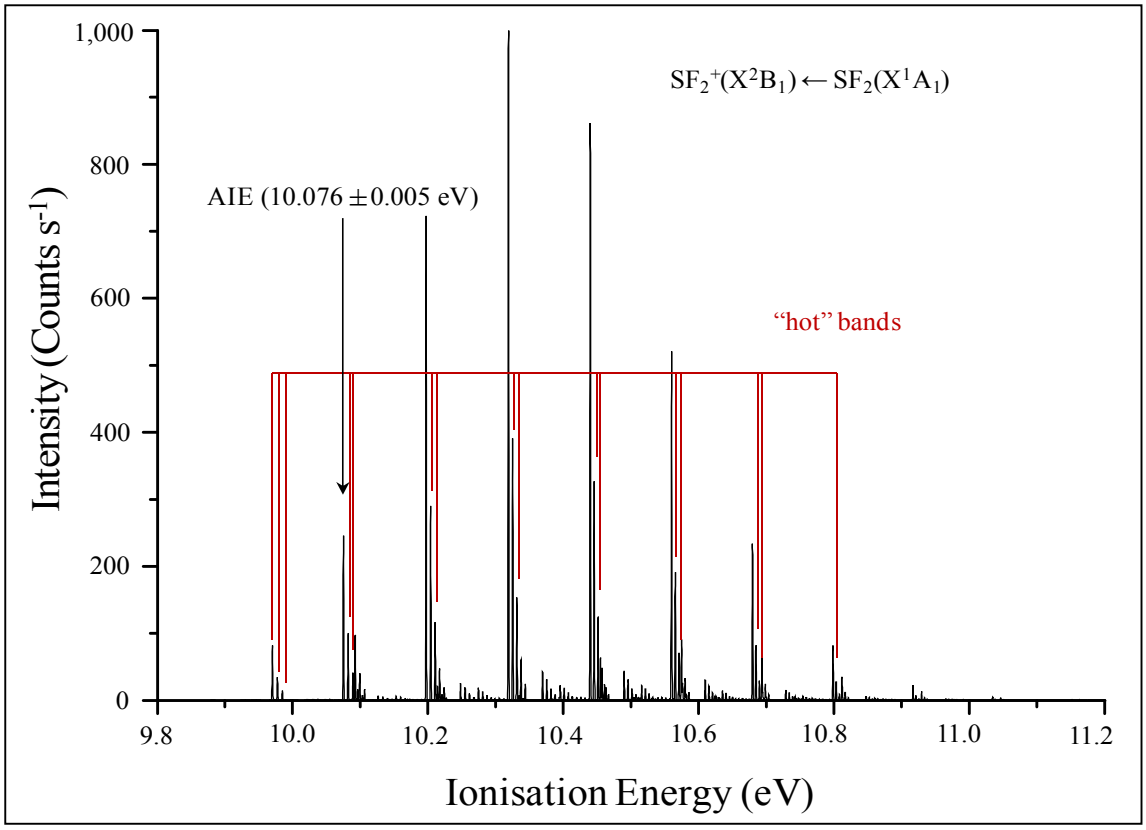

Figure 9.2: *Simulated He(I) PE spectrum of SF_2 at a vibrational Boltzmann temperature of 600 K.*

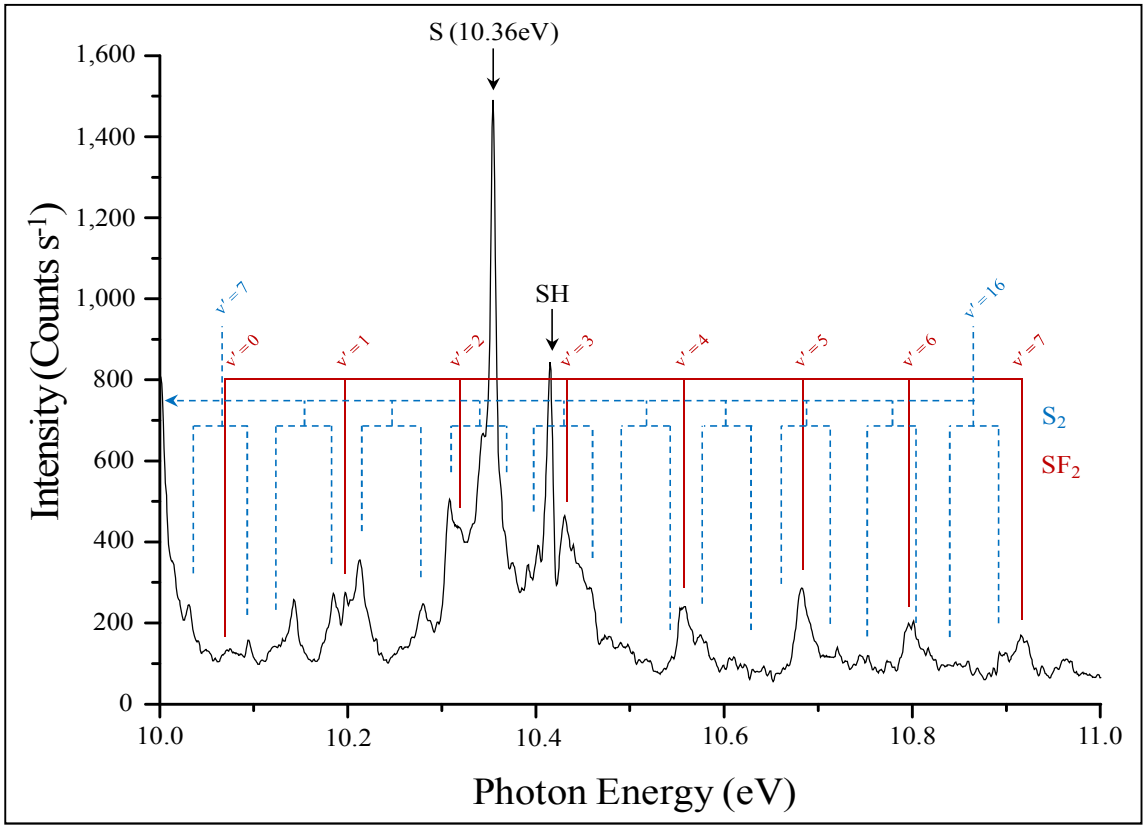

Figure 9.3: *TPE spectrum of SF_2 (recorded at room temperature, 298 K) obtained at the Elettra synchrotron radiation facility using a high [SF_2]:[S_2] ratio in the photon energy region 10 eV to 11 eV.*

More vibrational structure is observed in the TPE spectrum for SF_2, shown in Figure 9.3, than from that seen in the PE spectrum, (bottom spectrum in Figure 9.1). Additional structure arises because TPE spectra are subject to autoionisation processes (see Chapter 2), which can lead to non-Franck-Condon distributions as well as the observation of ionic vibrational levels which are not observed in the normal Franck-Condon distribution. The main SF_2 features in the TPE spectrum in Figure 9.3 have been assigned with the help of the PE spectra shown in Figure 9.1. It is apparent from the PE spectrum that even when recorded under the optimum conditions (high $[SF_2]$:$[S_2]$ ratio), there is still a residual amount of S_2 produced.

However from the PES results, it was expected that the SF_2 band would be clear from any S_2 contamination, due to the low quantities of S_2 observed, with the exception of the S atom band which occurs at 10.36 eV. Unfortunately, residual amounts of S_2 formed from the recombination of S atoms were seen in all recorded TPE spectra and proved difficult to remove completely. The vibrational bands attributed to autoionisation of S_2 overlap those of SF_2 and are labelled in blue with the main SF_2 bands labelled red in Figure 9.3. S_2 band positions shown in Figure 9.3 ($v = 7$ to 16) have been extrapolated forward from vibrational spacings measured for intense S_2 bands ($v = 0$ to 6, which are not overlapped) occurring lower in ionisation energy. Each S_2 vibrational component consists of two spin-orbit components and these are shown for $v = 7$ to 16 in Figure 9.3. SH and S are also visible in the TPE spectrum and arise from secondary reactions.

Vibrational Component	Band Position (eV)	Spacing ΔE_{vib} (cm^{-1})
$v = 0$	10.076 ± 0.002	-
$v = 1$	10.198 ± 0.003	984 ± 10
$v = 2$	10.320 ± 0.004	976 ± 10
$v = 3$	10.441 ± 0.003	976 ± 10
$v = 4$	10.559 ± 0.002	976 ± 9
$v = 5$	10.680 ± 0.001	976 ± 8
$v = 6$	10.799 ± 0.002	958 ± 8
$v = 7$	10.919 ± 0.001	958 ± 8

Table 9.2: *Band positions of the SF_2 vibrational components obtained from fitting the experimental bands using Gaussian functions.*

The contribution of S_2 bands in this energy region prevented the observation of any additional structure in the SF_2 vibrational progression, i.e. contributions from "hot" bands, as seen in the simulated PE spectrum of SF_2 in Figure 9.2, or progressions in another vibrational mode (other than ν_1). In order to determine band positions for SF_2,

each component observed was fitted using an asymmetric Gaussian function. This was carried out for all the recorded TPE spectra in this region and the results were averaged. The determined band positions for SF_2 are shown in Table 9.2. The spacings, ΔE_{vib}, between the bands are also given in the Table 9.2.

Vibrational components v = 4, 5, 6 and 7 are clearly observed from Figure 9.3, and as a result the associated band positions were straightforward to determine. However, the vibrational components v = 1, 2 and 3 are overlapped by additional bands, and had to be deconvoluted in order to determine their positions. The first vibrational component, v = 0, is not overlapped however, is very low in intensity. Therefore fitting the bands in this energy region (10.00 eV to 10.25 eV) is approximate due to the reduced intensities and amount of overlap observed. Knowing the positions of the last four vibrational components (v = 4, 5, 6 and 7), and the spacing between them, allowed an approximate position of the first four vibrational (v = 0, 1, 2 and 3) components to be determined by extrapolation.

Vibrational constants, ω_e and $\omega_e\chi_e$, could therefore be determined in the symmetric stretching mode of the ionic state of SF_2 by plotting the measured ΔE_{vib} against as a function of (v +1) yielding a line of slope $-2\omega_e\chi_e$ and intercept ω_e (see Chapter 2 for details). The results are shown in Table 9.3.

Vibrational Constants	This Work	Lee *et al.*[10]	de Leeuw *et al.*[7]
ω_e (cm^{-1})	988 ± 7	985.6	935 ± 40
$\omega_e\chi_e$ (cm^{-1})	2 ± 1	-	-

Table 9.3: *Comparison of recently and previously determined vibrational constants for the ionic state of SF_2.*

The results obtained in the present work compare well with those determined previously, particularly those obtained by Lee *et al*. from *ab initio*/Franck-Condon factor calculations [10]. The agreement between the results obtained in the present TPES work and those of Lee *et al.* demonstrate the significance of the high resolution obtained from TPES compared to conventional PES despite the presence of S_2 in TPE spectra.

9.4 Conclusion

TPE spectra were recorded at the Elettra synchrotron facility for the triatomic molecules HO_2 and SF_2. Problems occurred in both experiments, with vapour pressure

fluctuations, arising from a heating mantle with poor temperature control preventing stable conditions needed to record TPE spectra of HO_2, and S_2 contamination from SF_2 measurements. Initial TPE spectra of HO_2 show vibrational components in the symmetric stretching mode at 11.35 eV, 11.55 eV and 11.75 eV. However, only a modest improvement in the resolution between the PE and TPE spectra was observed, which prevented the observation of any underlying structure. The fourth vibrational component of HO_2 was not reproducible under the reaction conditions and therefore could not be confidently assigned. The poor resolution observed when recording TPE spectra was due to the inability to maintain a constant temperature, to within ± 0.1°C, of the heated complex used to prepare H_2O_2 in the vapour phase from the apparatus used. As a result, the TPE spectra obtained, all suffered from fluctuations due to the temperature instability, which gave rise to a H_2O_2 vapour pressure variation. This experiment needs to be carried out again with an accurate temperature control on the heating system in order to maintain a constant vapour pressure of H_2O_2 with the aim of resolving any underlying structure in the HO_2 first PE band and to obtain a clear spectrum of the second band which is expected to have its first component in the 11.5 eV to 12.0 eV region [21-23].

From the SF_2 investigation, good agreement was observed between the AIE and VIE values, obtained in the present work and with results of state-of-the-art *ab initio* calculations [8, 10] (within 1 meV). The vibrational constant (ω_e) for the first symmetric stretching mode in the ground ionic state was also in good agreement with that quoted by Lee *at al*. [10]

Unfortunately, the presence of an S_2 vibrational progression, arising from autoionisation in the TPE measurements, prevented the observation of any additional structure, and although better resolution was achieved with respect to previous experimental work, it was not possible to obtain more information from the SF_2 spectra. For this reason, another experimental approach is currently being investigated to produce SF_2. This involves discharging either SF_4 [24] or SF_6 [25] heavily diluted in argon in attempt to minimise the production of S_2 observed from autoionisation processes in the energy region of interest. Similarly, an improved experimental protocol is needed to repeat the TPE measurements on HO_2, which will provide stable conditions for H_2O_2 production, in the hope of resolving the underlying structure associated with the first two PE bands of HO_2.

9.5 A Study of HOCl and Cl_2O using TPES and PES

The stratospheric chemistry of halogenated compounds has been the subject of numerous studies due to potential perturbations in the ozone layer which result from release of anthropogenic halogenated hydrocarbons [26-31]. Hypochlorous acid (HOCl) is an atmospherically important chlorine containing reservoir molecule. HOCl is produced in the stratosphere as a result of the reaction (9.8) [26-31],

$$HO_2 + ClO \rightarrow HOCl + O_2 \qquad (9.8)$$

This has a measured room temperature rate coefficient of (4-6) $x10^{-12}$ $cm^3.molecules^{-1}s^{-1}$ [32-36]. It is also produced heterogeneously on ice surfaces in polar stratospheric clouds via the reaction [37],

$$ClONO_2 + H_2O \rightarrow HOCl + HNO_3 \qquad (9.9)$$

HOCl is destroyed in the atmosphere by various processes, e.g. photolysis and reaction with the OH radical [38]. Its importance is that it acts as a reservoir for OH and Cl species which are involved in the catalytic destruction of ozone.

Experimental ionisation energies have been obtained for HOCl and chlorine monoxide (Cl_2O), prepared by reactions (9.4) and (9.5), from photoelectron spectroscopic studies using He(I) radiation (21.22 eV) by Frost and McDowell [39, 40]. Two vibrationally resolved PE bands were observed for HOCl. The adiabatic ionisation energy (AIE) and vertical ionisation energy (VIE) of the first PE band were measured as (11.12 ± 0.01) eV and (11.23 ± 0.01) eV respectively and the VIE of the second PE band was measured as (12.29 ± 0.01) eV. VIEs for the first four PE bands for Cl_2O were determined to be (11.02 ± 0.02) eV, (12.37 ± 0.02) eV, (12.65 ± 0.02) eV and (12.79 ± 0.02) eV [40].

Potential energy surfaces for ground and excited electronic states of HOCl have been calculated using *ab initio* molecular orbital (MO) configuration interaction (CI) methods [41, 42]. On the basis of these calculations two transitions were calculated at 335 nm and 245 nm (vertical transition wavelengths) which are in close agreement with the experimental band maxima in the ultraviolet absorption spectra recorded by Molina *et al.* [26] and Mishalanie *et al.* [29]. Another theoretical study has performed *ab initio* electronic structure calculations to calculate the ionisation energies of HOCl through

perturbation corrections to Koopmans' theorem, obtaining a first VIE of 11.21 eV [43]. The first two PE bands of HOCl have also been simulated at the MP2 level using the aug-cc-pVTZ basis set and assuming a harmonic model for the vibrational frequencies [44]. In this study, the AIE of the first PE band was determined to be 11.07 eV. A theoretical investigation by Glukhovstev *et al.* [45] using *ab initio* calculations at the G2 level reports the first AIE of HOCl to be 11.08 eV which is in good agreement with the result of an earlier study of Lee *et al.* [44].

Initially the aim of this project was to measure the threshold photoelectron (TPE) spectrum of the first two bands of HOCl, where HOCl is produced from the reactions (9.4) and (9.5), at the Elettra synchrotron radiation facility. However, during the time at Elettra, the method used to prepare HOCl, which followed that of Bell *et al.* [46] proved to be unsuccessful and not reproducible in obtaining an intense, clean HOCl PE spectrum for a sufficiently long time. The aim of this project was therefore to develop a reproducible method to obtain and record the PE spectrum of HOCl, and ultimately to optimise the method in order to record its TPE spectrum at Elettra. The PE spectrum of chlorine monoxide (Cl_2O), produced from reaction (9.4), has already been recorded by Frost and McDowell [40]. However there appears no evidence in the literature that its TPE spectrum has ever been recorded. Therefore a related objective was to develop a method to record a pure PE spectrum for Cl_2O produced from reaction (9.4) with the intention of recording its TPE spectrum at Elettra.

9.6 Experimental

The initial method used at Elettra to produce HOCl involved bubbling Cl_2 through a suspension of mercuric oxide (HgO) in water, contained in a round bottom flask, for several hours before introducing the HOCl vapour formed in solution directly to the ionisation chamber of the spectrometer. Although HOCl had been observed by PES from this preparation method previously in Southampton, in most cases at Elettra, HOCl was not observed in PE spectra, (PE spectra were recorded before recording TPE spectra to ensure that the sample preparation was successful) and when HOCl was observed, the spectra obtained were either not of sufficient quality and/or HOCl was only produced over a short period of time. This meant that TPE spectrum of HOCl could not be recorded, as a stable source which is steady over a period of at least several hours.

A variety of different methods have been used to prepare HOCl and Cl_2O previously. The most commonly used methods are the Bell method [46, 47] (as described above), the Klemm (or bulb) method [46], the Cady method [49, 50] and the column method [51, 52], all of which employ subtle variations of the reactions (9.4) and (9.5). The Bell, Klemm and Cady methods all involve making a sample of HOCl away from the spectrometer and bringing it to the spectrometer where it is then sampled, whereas the column method has the advantage of being online where HOCl can be detected and investigated spectroscopically as it is formed during the reaction.

The Klemm method, also referred to as the bulb method, uses a large (e.g. 2L) glass sample bulb containing solid HgO which is exposed to Cl_2, forming Cl_2O from reaction (9.4). Cl_2O is then converted to HOCl using the ambient moisture already adsorbed on the HgO. The Cady method, however, forms Cl_2O in a separate reaction. Firstly Cl_2 is bubbled through a flask containing dry carbon tetrachloride (CCl_4) and then HgO is added to the mixture, when a sufficiently high concentration of Cl_2 in CCl_4 has been obtained, to form Cl_2O. The solution is then filtered to remove the reacted HgO powder and mixed with H_2O. The CCl_4 is then pumped away to yield a relatively pure sample of HOCl.

The column method involves creating HOCl *in-situ*, by passing Cl_2 gas and H_2O vapour through a column system containing HgO powder. Variations of the column method have been used, with Barnes *et al.* [31, 51, 52] using a mixture of HgO and 6 mm glass beads (glass beads are used to ensure loose packing of the HgO powder within the column) and Fujiwara *et al.* [30] adopting a column packed solely with neat HgO powder. The column method has the advantage of being a continuous process, making it possible to introduce the HOCl directly to the spectrometer as it is formed, minimising any decomposition which can occur from wall losses or surface reactions which may take place whilst admitting the sample to the spectrometer, as might be the case in the off-line methods of Bell, Klemm or Cady.

In this work a different experimental approach was taken from that used previously at the synchrotron source (Bell method) in order to record a PE spectrum of sufficient quality over long periods of time (at least 4 hours) which is suitable to allow the TPE spectrum of HOCl to be recorded. The method used involved producing HOCl *in-situ* using an online column set-up rather than preparing a sample off the spectrometer. This

was also the favoured method chosen for preparing a Cl_2O source which will in future be used to record TPE spectra.

9.6.1 Sample Preparation

The column used in this work was a glass tube, 350 mm long with inner and outer diameters of 10 mm and 12 mm respectively. This contained a glass frit ~5 mm long, of porosity grade 0, to enable maximum sample throughput whilst preventing any HgO powder entering the ionisation region of the spectrometer. The frit was positioned in the glass column 150 mm above the point of photoionisation. Cl_2 and H_2O were admitted separately at the top of the inlet via a T-junction. The inlet was mounted on the ionisation chamber of the *small* spectrometer. Needle valves were used to regulate the flow rates of Cl_2 and H_2O.

The column was packed off-line in all sample preparations and brought to the spectrometer. Various packing regimes were used during this work and these are shown schematically as (A), (B) and (C) in Figure 9.4. All sample preparations in the column used a ~5 mm bed of glass wool which was packed on top of the glass frit to ensure that no HgO powder entered the ionisation chamber of the spectrometer.

Method (A)

Initial tests with the column method used a glass inlet which was packed with 10 mm of HgO powder on top of a ~5 mm bed of glass wool positioned on the glass frit. This is shown in Figure 9.4 as inlet (A). Good yields of HOCl were observed from the PE spectra recorded using this column. Chlorine monoxide (Cl_2O) was also observed in the spectra using inlet (A), as were the reagents Cl_2 and H_2O; however, further testing revealed that this system was not suitable for measurements lasting longer than an hour. After passing Cl_2 and H_2O through this column for 30 mins to 1 hour, the HgO powder began to discolour as it was consumed in the reaction and it provided lower yields of HOCl with increased reaction time. Poor reproducibility was also experienced when attempting to replicate the method under the same conditions. This indicated that the distribution of the HgO packing within the column and the availability of surface reaction sites were important for this experiment. This method did however provide good preliminary results with high yields of HOCl being produced over short periods of time, with the amount of HgO in the column being the rate determining factor for the

overall lifetime of the HOCl source. To increase the reaction lifetime, more HgO powder was added to the column. However it was found that packing the column with a ≥ 15 mm length of HgO powder prevented a uniform flow of Cl_2 and H_2O vapour. Due to the poor flow conditions when using a ≥ 15 mm length of HgO powder within the column, discolouration of the HgO appeared to only take place on the top surface indicating that the bulk of HgO remained unreacted. From these results it was concluded that using more HgO powder would provide the reaction longevity required when recording TPE spectra (4-6 hours) and that distributing the HgO, i.e. increasing its surface area within the inlet, would provide the reagents being admitted with a more uniform flow and allow them easier access to the HgO surfaces.

Method (B)

In order to improve the reaction lifetime and ensure a steady reagent throughput within the inlet, the surface area and the amount of HgO used was therefore increased. Initially, the inlet was filled with a loose packing of glass wool (on top of a compact 10 mm glass wool bed). HgO powder was then finely dispersed throughout the inlet, covering the loosely packed glass wool, to increase its surface area. However, this proved to be a more difficult column preparation to replicate than that described in method (A). Each column could never be prepared in exactly the same way, and as a consequence inconsistent results were obtained. In order to produce an even dispersion of HgO powder, the inlet was filled with 3 mm glass beads. The glass beads provided a fixed surface area to disperse the HgO powder on and this approach was deemed to be a more robust method when preparing the inlet than using glass wool. The use of glass beads also helped to maintain steady flow conditions for both the reactants (Cl_2 and H_2O) [31, 51, 52]. This column is shown schematically in Figure 9.4 as inlet (B).

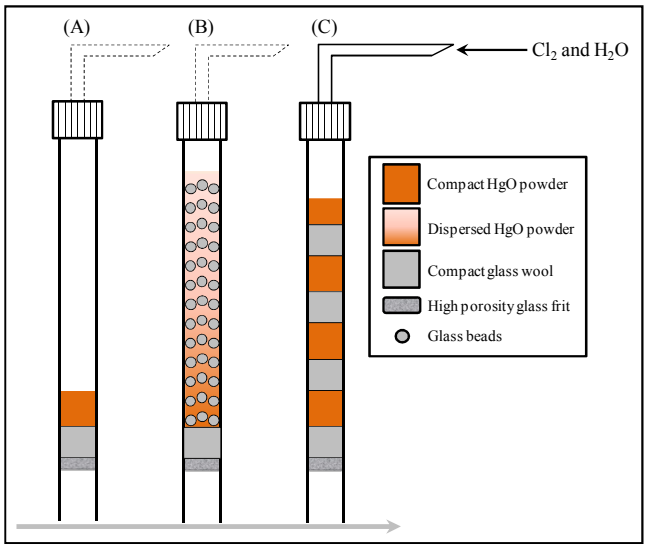

Figure 9.4: *Schematic diagram of the inlet (columns) systems showing the different HgO packing regimes used in methods (A), (B) and (C).*

In both variations of sample preparation (with glass wool and with glass beads), dispersing HgO evenly and consistently proved to be very difficult, and hence it was difficult to obtain a reproducible source of HOCl. In some cases, HOCl was produced for short periods of time with intense PE spectra of HOCl being observed; however in contrast some preparations of the column provided too great a reagent flow rate and resulted in no HOCl being observed in the PE spectra with all the HgO in the inlet appearing to remain unreacted (i.e. no discolouration of the HgO powder was observed during the run) with just Cl_2 and H_2O being observed in the PE spectra.

Method (C)

The best column set-up, which continually provided consistent results with an extended reaction lifetime, involved stacking successive layers of HgO powder, each 10 mm long, on alternating 10 mm long compacted glass wool stacks which covered the length of the inlet tube, i.e. from the glass frit positioned near the base of the inlet, (150 mm above the photoionisation region), to the top of the inlet where the Cl_2 and H_2O were admitted (~200 mm). This column is shown as inlet (C) in Figure 9.4. Stacking layers of HgO powder on top of glass wool, as shown in Figure 9.4, initially provided poor reagent flow conditions; however it was found that the reagent flow rates gradually settled down over time (usually taking no more than a few minutes). An advantage found in using this method was that adding more HgO powder to the inlet tube in stages (in stacks of $\leq$ 10mm deep) increased the reaction lifetime without compromising the flow rate of the reagents. The increased lifetime of the reaction is beneficial for recording TPE spectra at the synchrotron radiation facility at Elettra, Trieste, where spectra may need to be recorded continuously over long periods of time (4-6 hours). Preparing the column by stacking the HgO in layers provided good results which were consistent over several hours. However, it was discovered that this method, although generally reproducible, was not always fully reproducible in terms of producing a good source of HOCl every time. This appeared to be related to the time that HgO was exposed to the air between preparing the column, mounting it and pumping it down on the spectrometer. The best results were obtained when the column was coupled to the spectrometer directly after being prepared with a short exposure time of HgO to ambient conditions. This is possibly due to moisture in the air being adsorbed on the HgO reducing the number of active sites available for reaction.

It was noted from the work of Secoy and Cady [49] that in some cases pre-heating HgO for extended periods of time (an hour or longer) before carrying out experiments may be an important factor. Therefore the inlet system was coupled to the PE spectrometer using a water cooled flange and heated using heating tape to 300ºC for 2-3 hours before the experiment. A K-type (Ni-Cr/Ni-Al) thermocouple, in contact with the external wall of the inlet, was used to measure the temperature whilst heating. The tube was left to cool to ambient temperature before carrying out the reaction. It was found that pre-heating the inlet in this way provided more reproducible reaction conditions. This may be because by pre-heating the inlet to such temperatures removes adsorbed species, e.g. H_2O, from the surface of HgO providing more active sites for the reaction to take place. Stacking the HgO powder in sections in this way, separated by glass wool, and pre-heating the HgO contained in the tube, provided a stable and reproducible set of reaction conditions, which ultimately gave reproducible results. A PE spectrum of HOCl, recorded in this work, is shown in Figure 9.5. The PE spectrum shown in Figure 9.5 was recorded after 4 hours of reaction time using inlet (C). Reproducible spectra could be obtained over this time.

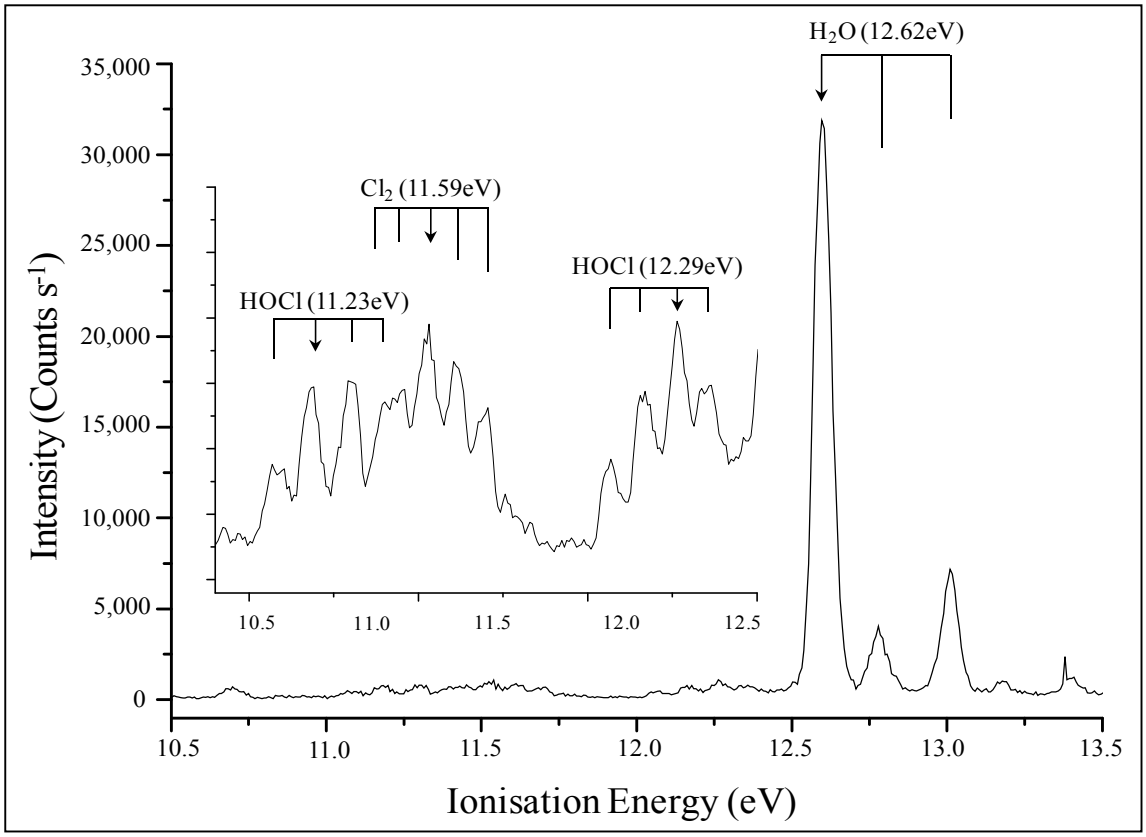

Figure 9.5: *PE spectrum showing the first and second PE bands of HOCl and residual Cl_2 (inset) and the first PE band of H_2O. The experiment was performed using method (C) shown in Figure 9.4.*

When recording the PE spectra of HOCl, H_2O was initially added to the column. Once the flow conditions were stable Cl_2 was then added. When optimising the reagent partial pressures to maximise the HOCl signal by adjusting flow rates of H_2O and Cl_2, Cl_2O was observed with low intensity when the flow rates of H_2O and Cl_2 were approximately equal. It was seen that the first and second PE bands of Cl_2O overlapped with the first and second bands of HOCl. In order to identify the extent of band overlap of HOCl with Cl_2O, a method was developed to record a clean PE spectrum of Cl_2O which can be sustained for long periods of time with the aim of recording its TPE spectrum. Preliminary experiments were carried out, using the same column set-up as that described above, for producing HOCl, by passing Cl_2 over dry HgO. These initial experiments showed that Cl_2O could not be formed by passing Cl_2 over dry HgO, as has been described previously by Molina *et al.* [26] and that the reaction required H_2O to be present throughout, revealing that H_2O was necessary for the formation of Cl_2O.

For the optimum experimental conditions for recording the PE spectrum of HOCl, it was found that, H_2O was required to be in excess throughout the reaction and Cl_2 was slowly added until an intense HOCl signal was observed. As the reaction conditions favoured excess H_2O, an intense first PE band of H_2O was always observed in the spectra. However, this is not a problem when recording PE spectra for HOCl as the bands of interest are lower in ionisation energy than those of H_2O and as a result the first two bands of HOCl are not overlapped by H_2O. However removal of H_2O from the PE spectrum is important when recording the PE spectrum of Cl_2O, as the third and fourth PE bands of Cl_2O which occur at 12.65 eV and 12.79 eV are heavily overlapped by the first PE band of H_2O which occurs at 12.62 eV. Therefore a method was developed to record the PE spectrum of Cl_2O by trapping H_2O, after the reaction, to prevent it reaching the ionisation region of the spectrometer. This was achieved using a U-tube as part of the inlet system, which was positioned on the end of the column.

The U-tube was immersed in a crushed ice/salt mixture which trapped H_2O after the reaction preventing any excess, unreacted H_2O from reaching the ionisation region of the spectrometer. The set-up shown as inlet (C) in Figure 9.4, along with the cold trap, produced relatively clean PE spectra of Cl_2O. HOCl and H_2O were not observed in the recorded PE spectra and only a small contribution of excess Cl_2 was observed. Cl_2O spectra could be recorded for upwards of 6 hours using this trapping method so long as the low temperature required in the cold trap was maintained. When recording the PE

spectrum of Cl_2O, H_2O was the first reagent admitted to the column and after a few minutes Cl_2 was gradually introduced. This was found to provide the optimum reaction conditions (this protocol was also adopted when recording HOCl spectra). This method was reproducible over a sufficiently long period of time as spectra were obtained over a 6 hour period. Figure 9.6 shows the PE spectrum of Cl_2O obtained with this method after 6 hours of continuous reaction. The absence of HOCl suggests that the small amounts of H_2O used and the large amounts of HgO in the column greatly increase the rate of formation of Cl_2O, whilst limiting the formation of HOCl. In all experimental methods it was found that gradually adding H_2O to the inlet before introducing Cl_2 provided the optimum reaction conditions. All reactions were performed at room temperature.

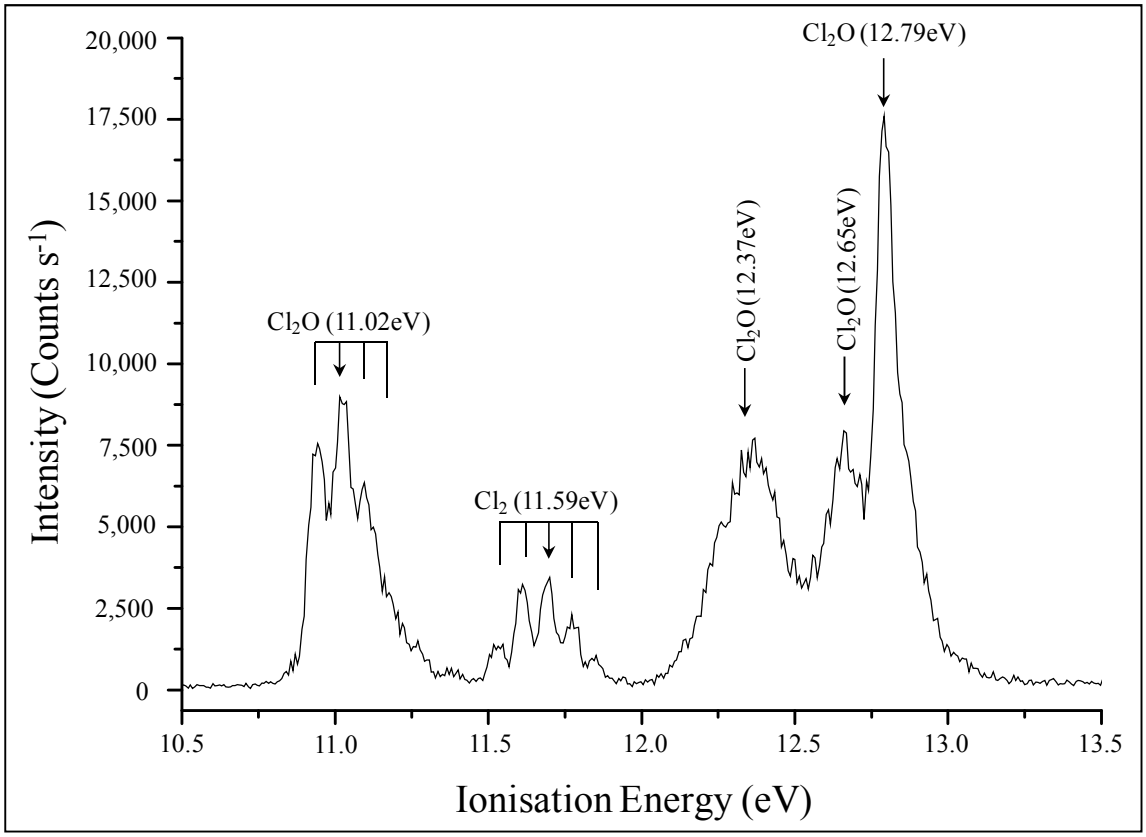

Figure 9.6: *PE spectrum of Cl_2O also showing the first band of Cl_2. The experiment was performed using method (C) shown in Figure 9.4, with trapping of excess H_2O (see text).*

9.7 Conclusion

HOCl and Cl_2O have both been observed by PES using the column method by flowing Cl_2 saturated in H_2O vapour through successive layers of dried HgO powder as

described in method (C). As a result of this work, the recommended methods for producing HOCl and Cl_2O for TPES measurements at Elettra are as follows:

For HOCl production, the column was packed as shown in Figure 9.4, inlet (C). The column was then coupled to the spectrometer using a water cooled flange and heated for upwards of 2 hours to a temperature of 300 ºC using heating tape to remove any species which may have adsorbed on the HgO during the preparation of the column. The heating tape was removed and the column was left to cool to room temperature. Once the column was at room temperature, H_2O was slowly admitted until the flow conditions stabilised (usually this was after a few minutes). Cl_2 was then gradually added to the column. PE spectra were recorded as Cl_2 was admitted to the column to monitor the production of HOCl. Once an intense HOCl PE spectrum was obtained the conditions were noted and PE spectra were recorded every 15 mins for upwards of 4 hours. It was found from pressure measurements that a $[H_2O]$:$[Cl_2]$ ratio of ~2:1 provided the optimum and most consistent conditions for recording HOCl over a 4-6 hour period.

The recommended method used to produce Cl_2O for TPES measurements at Elettra followed the HOCl method, in that the same packing regime was used and the column was pre-heated for ~2 hours to a temperature of 300ºC using heating tape. Once the heating tape was removed and the inlet had cooled to ambient temperature, H_2O was gradually admitted. Once a steady flow of H_2O had been established, Cl_2 was then slowly introduced. PE spectra were then recorded as the Cl_2 was admitted to monitor the reaction products. When HOCl was observed in the spectra, the flow rate of H_2O was reduced and the Cl_2 flow-rate was increased until HOCl was no longer the dominant reaction product in the spectra with Cl_2O being the most intense species observed. It was found that the reagent partial pressures used to achieve an intense PE spectrum of Cl_2O were, in contrast to those used for HOCl production, in the ratio $[H_2O]$:$[Cl_2]$ ~1:2.

Spectra recorded using this technique are shown as (A) and (B) in Figure 9.7. The PE spectrum (A), shown in Figure 9.7, was recorded after approximately 3 hours reaction time and the spectrum shown as (B) was recorded after 4 hours reaction time. Although H_2O was required during the reaction in order to produce Cl_2O, it was only required in minimal amounts, unlike HOCl where H_2O was required to be in excess to obtain

favourable results. When recording PE spectra, for both HOCl and Cl_2O, Cl_2 was always observed in small amounts.

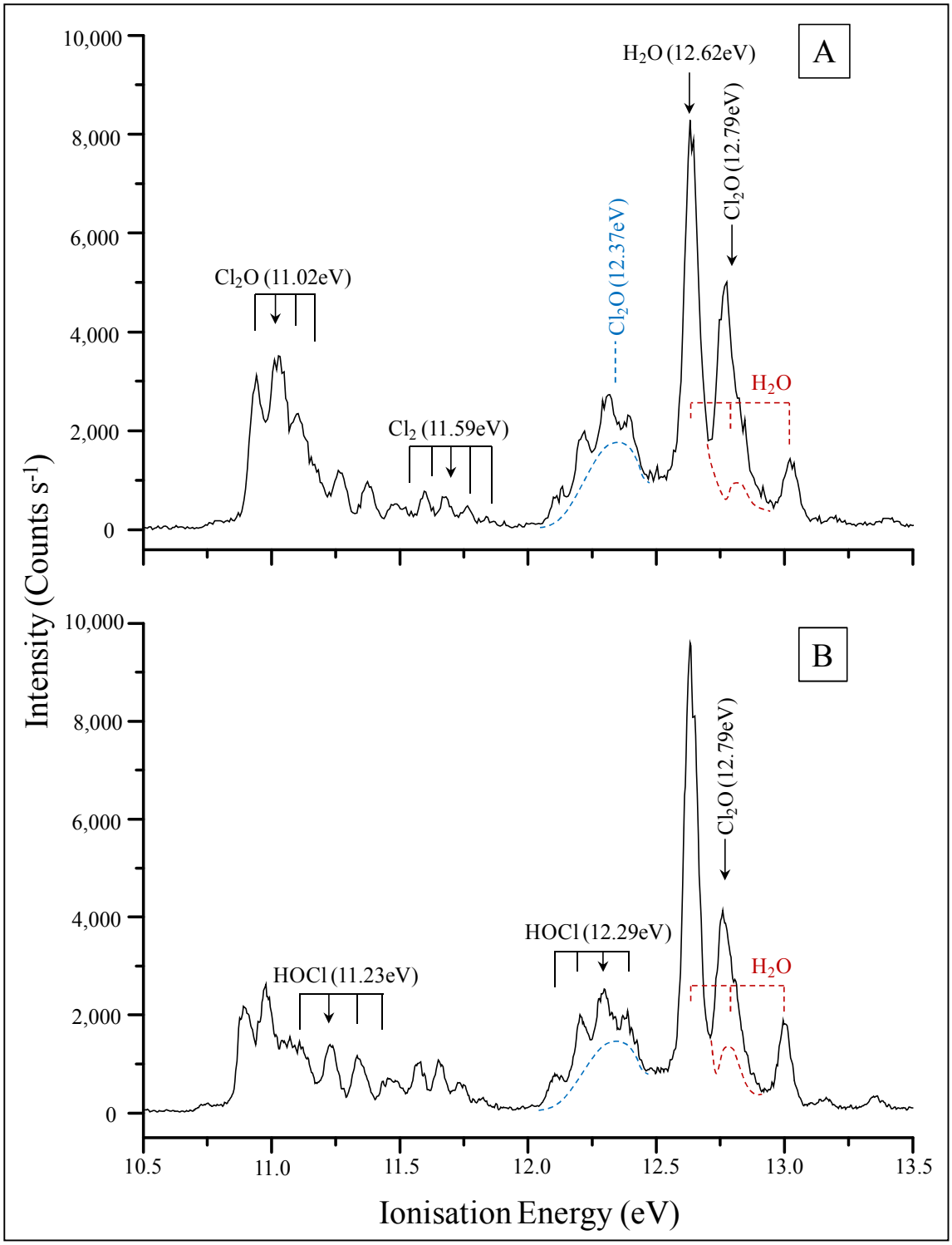

Figure 9.7: *PE spectra of Cl_2O showing the vibrational structure of the first band of HOCl and Cl_2. Spectrum (A) was recorded after 3 hours and Spectrum (B) was recorded after approximately 4 hours. PE spectra were obtained using a $[H_2O]:[Cl_2]$ ratio of ~1:2.*

In order to record a clean PE spectrum of Cl_2O in Southampton, a cold trap was used in order to remove excess H_2O from the spectrum (as the first band of H_2O and third and fourth bands of Cl_2O overlap at an ionisation energy of around 12.6 eV as shown in Figure 9.7) in order to observe four Cl_2O PE bands, as shown in Figure 9.6. However using a cold trap in this way is not advisable for experiments in Elettra as a leak may cause problems with the synchrotron storage ring. The first two bands of Cl_2O occur in the same ionisation region as the first two bands of HOCl. However, by adjusting the reagent mixing ratios, as mentioned above, conditions should be obtained in which HOCl or Cl_2O can be suitably resolved by TPES. The methods developed in this work will provide a good starting point for recording TPE spectra of HOCl and Cl_2O at the Elettra synchrotron source, which is the next step in this project.

References

[1] D. W. Smith and L. Andrews, *J. Chem. Phys.*, 60, 1974, 81.

[2] C. J. Howard, *J. Chem. Phys.*, 67, 1977, 5258.

[3] J. W. C. Johns, A. R. W. McKellar and M. Riggin, *J. Chem. Phys.*, 68, 1978, 3957.

[4] J. M. Dyke, N. Jonathan, A. Morris and M. J. Winter, *Mol. Phys.*, 44, 1981, 1059.

[5] C. D. Walther and H. G. Wagner, *Ber. Bunsenges. Phys. Chem.*, 87, 1983, 403.

[6] D. R. Johnson and F. X. Powell, *Science*, 164, 1969, 950.

[7] D. M. de Leeuw, R. Mooyman and C. A. de Lange, *Chem. Phys.*, 34, 1978, 287.

[8] Q. Li, J. Shu, Q. Zhang, S. Yu, L. Zhang, C. Chen and X. Ma, *J. Phys. Chem. A.*, 102 1998, 7233.

[9] K. K. Irikura, *J. Chem. Phys.*, 102, 1995, 5357.

[10] E. P. F. Lee, D. K. W. Mok, F. Chau and J. M. Dyke, *J. Chem. Phys.*, 125, 2006, 104304.

[11] W. H. Kirchoff, D. R. Johnson, and F. X. Powell, *J. Mol. Spectrosc.*, 48, 1973, 157.

[12] J. C. Deroche, H. Bűrger, P. Schulz and H. Willner, *J. Mol. Spectrosc.*, 89, 1981, 269.

[13] R. J. Glinski and C. D. Taylor, *Chem. Phys. Lett.*, 155, 1989, 511.

[14] R. J. Glinski, C. D. Taylor, and F. Kutzler, *J. Phys. Chem.*, 94, 1990, 6196.

[15] J. Brunning and M. A. A. Clyne, *J.C.S. Faraday II*, 80, 1984, 1001.

[16] C. E Moore, Atomic Energy Levels, *National Bureau of Standards*, Washington, 1949.

[17] J. M. Dyke, L. Golob, N. Jonathan, A. Morris and M. Okuda, *J. S. C. Faraday*, 70, 1974, 1828.

[18] K. Kimura, S Katsumata, Y. Achiba, T. Yamazaki and S. Iwata, *Japan Scientific Societies Press*, Tokyo, 1981.

[19] K. Ellis, R. I. Hall, L. Avaldi, G. Dawber, A. McConkey, L. Andric and G. C. King, *J. Phys. B.*, 27, 1994, 3415.

[20] E. P. F. Lee, *Private Communication*, 2011.

[21] C. D. Walther and H. G. Wagner, *Ber. Bunsenges. Phys. Chem.*, 87, 1983, 403.

[22] G. J. Vazquez, R. J. Buenker and S. D. Peyerimhoff, *Mol. Phys.*, 29, 1986, 291.

[23] M. L. Senent, *Mol. Phys.*, 96, 1999, 1587.

[24] A. H. Cowley, M. Lattman and M. L. Walker, *J. Am. Chem. Soc.*, 101, 1979, 4074.

[25] D. C. Frost, C. A. McDowell, J. S. Sandhu and D. A. Vroom, *Advan. Mass Spectrom.*, 4, 1968, 781.

[26] L. T. Molina and M. J. Molina, *J. Phys. Chem.*, 82, 1978, 2410.

[27] F. S. Rowland and M. J. Molina, *J. Rev. Geophys. Space. Phys.*, 13, 1975, 1.

[28] P. Z. Warneck, *Naturforsch. A.*, 32, 1977, 1254.

[29] E. A. Mishalanie, C. J. Rutkowski, R. S. Hutte and J. W. Birks, *J. Chem. Phys.*, 90, 1986, 5578.

[30] H. Fujiwara and T. Ishiwata, *J. Chem. Phys. A.*, 102, 1998, 3856.

[31] R. J. Barnes, A. Sinha and A. H. Michelson, *J. Chem. Phys. A.,* 102, 1998, 8855.

[32] B. Reimann and F. Kaufman, *J. Chem. Phys.*, 69, 1978, 2925.

[33] R. Stimpfle, R. Perry and C. J. Howard, *J. Chem. Phys.*, 71, 1979, 5183.

[34] T. J. Leck, J. L. Cook and J. W. Birks, *J. Chem. Phys.*, 72, 1980, 2364.

[35] J. P. Burrows, R. A. Cox and R. G. Derwent., *J. Photochem.*, 16, 1981, 147.

[36] M. J. Molina, T. Ishiwata and L. T. Molina, *J. Phys. Chem.*, 84, 1980, 821.

[37] K. V. Chance, D. G. Johnson and W. A. Traub, *J. Geophys. Res.*, 94, 1989, 11059.

[38] J. P. Abbatt and M. J. Molina, *J. Phys. Chem.*, 96, 1992, 7674.

[39] D. Colbourne, D. C. Frost, C. A. McDowell and N.C. P. Westwood, *J. Chem. Phys.*, 68, 1978, 3574.

[40] A. B. Cornford, D. C. Frost, C. A. McDowell, J. L. Ragle and I. A. Stenhouse, *J. Chem. Phys.*, 55, 1971, 2820.

[41] S. Nambu, K. Nakata and S. Iwata, *Chem. Phys.*, 135, 1989, 75.

[42] S. Nambu and S. Iwata, *J. Phys. Chem.*, 96, 1992, 2103.

[43] D. P. Chong, F. G. Herring and Y. Takahata, *J. Elec. Spec. Rel. Phen.*, 13, 1978, 39.

[44] E. P. F. Lee, *Private Communication*, 2011.

[45] M. N. Glukhovstev, A. Pross and L. Radom, *J. Phys. Chem.*, 100, 1996, 3498.

[46] A. J. Bell, S. A. Boggis, J. M. Dyke, J. G. Frey, R. Ritchter, N. Shaw and M. Tabrizchi, *J. Chem. Soc. Faraday Trans.*, 90, 1994, 17.

[47] B. J. Drouin, *J. Quant. Spec. Rad. Trans.*, 103, 2007, 558.

[48] R. P. Thorn, Jnr., L. J. Stief, S. Kuo and R. B. Klemm, *J. Phys. Chem.*, 103, 1999, 812.

[49] C. H. Secoy and G. H. Cady, *J. Am. Chem. Soc.*, 62, 1940, 1036.

[50] G. H. Cady, *Inorg. Synth.*, 5, 1957, 156.

[51] R. J. Barnes and A. Sinha, *J. Chem. Phys.*, 107, 1997, 3730.

[52] R. J. Barnes, G. Dutton and A. Sinha, *J. Phys. Chem. A.*, 101, 1997, 8374.

Chapter 10

A Determination of the Photolysis Rate Coefficient of Monochlorodimethyl Sulphide (CH_3SCH_2Cl) in the Atmosphere

Dimethylsulphide (DMS, CH_3SCH_3) is a naturally emitted compound produced as a by-product from the biodegradation of organosulphur compounds from phytoplankton throughout the marine environment. It is predicted that 10-50 Mtons of DMS are emitted annually into the atmosphere via this pathway. The presence of DMS in maritime air was first demonstrated in 1972 by Lovelock *et al.* using gas-chromatography with a flame photometric detector [1]. Current estimates show that DMS contributes between 20-30% of the total global sulphur budget and is the single largest source of atmospheric sulphur in the southern hemisphere [2]. Oxidation of DMS is the main reaction process in the atmosphere which leads to the production of oxidised sulphur compounds, particularly sulphur dioxide (SO_2), methanesulphonic acid (MSA) (CH_3SO_3H), dimethylsulphoxide (DMSO) ($(CH_3)_2SO$), methylsulphonylmethane ($(CH_3)_2SO_2$) and sulphuric acid (H_2SO_4) [3, 4, 5], which serve as cloud condensation nuclei (CCN), contributing to the natural acidity of precipitation. DMS oxidation is also thought to provide a negative feedback mechanism to the Earth's radiative balance. This was first proposed by Charlson, Lovelock, Andreae and Warren and is known as the CLAW hypothesis [6]. It is for this reason that DMS removal processes in the atmosphere have been the subject of numerous investigations over the

years. There have been many field and laboratory studies involving DMS oxidation in the last decade [7, 8, 9], although there are still considerable uncertainties concerning the oxidation of DMS in the atmosphere [10]. It appears from field studies that DMS oxidation in the atmosphere is more rapid than can be accounted for using existing models: notably, the production of SO_2 (assumed to be derived from DMS) is more rapid than expected. The dominant oxidant for DMS was first considered to be the OH radical with evidence that the NO_3 radical is an important oxidant at night in coastal areas [11]; the significance of NO_3 in open ocean areas is thought to be very small. Modelling studies using oxidation of DMS with OH gives rise to lower levels of SO_2 than actually observed and oxidation of DMS with halogens has been suggested as a way of increasing the computed SO_2 yields.

The rate coefficient of the reaction, DMS + Cl_2 → Products, has been measured in the Southampton PES group with the discharge flow method (see Chapter 3 for details) as $(3.4 \pm 0.7)x10^{-14}$ $cm^3.molecules^{-1}$ s^{-1} at (294 ± 2) K using a flow-tube interfaced to a PE spectrometer [12, 13]. The reaction products from this reaction were CH_3SCH_2Cl and HCl. This work has shown that although the interaction between DMS and Cl_2 is moderately slow, it is of significance as it ultimately leads to extra SO_2 in the atmosphere. There are field observations which show that Cl_2 levels can reach 150 ppt at night [14]. If it is assumed that the average Cl_2 level at night is 50 ppt then the lifetime of DMS with respect to reaction with Cl_2 is expected to be approximately 6 hours. Shallcross *et al.* [15] estimate that the average DMS level is 50 ppt at night (field measurements suggest that this is perfectly reasonable in the southern ocean for example) and that the DMS and Cl_2 levels are replenished at night, maintaining these levels over a 6 hour period, around 40 ppt of CH_3SCH_2Cl would be generated (this is assuming that CH_3SCH_2Cl does not react and simply builds up) at night. In the morning, photolysis of Cl_2 will be rapid and the reaction of DMS + Cl_2 → products will be ineffective, as Cl_2 levels fall rapidly as Cl_2 is photolysed. Therefore CH_3SCH_2Cl, which has built up during the night, can either react with OH or be photolysed. The relative rates of these processes are unknown. However, both routes are expected to ultimately lead to SO_2 production. Therefore the night-time interaction between DMS and Cl_2 may well provide a mechanism to speed up SO_2 production rates during the day and go some way towards explaining the discrepancy between observed and computed

SO_2 production rates during the day. The main issue addressed in this chapter is: what are the lifetimes of CH_3SCH_2Cl with respect to photolysis and reaction with OH?

The lifetime of CH_3SCH_2Cl with respect to reaction with OH can be estimated because the rate coefficient of CH_3SCH_2Cl + OH has been measured with the discharge-flow kinetic technique using resonance fluorescence to measure the relative concentration of OH as a function of time on reaction with CH_3SCH_2Cl. The rate coefficient obtained was $(2.5 \pm 1.3)x10^{-12}$ cm^3 $molecules^{-1}$ s^{-1}. In this work an estimate was also made of the room temperature rate coefficient of CH_3SCH_2Cl + Cl as $1x10^{-10}$ cm^3 $molecules^{-1}$ s^{-1} (estimated from known rate coefficients of Cl and OH reactions with related molecules with the known CH_3SCH_2Cl + OH rate coefficient) [15-20]. Assuming average values of [OH] = $1x10^6$ molecules cm^{-3} and [Cl] = $1x10^5$ molecules cm^{-3} in the marine boundary layer [21], lifetimes of CH_3SCH_2Cl with respect to reaction with [OH] and [Cl] were calculated as 4.6 and 1.2 days respectively. This was determined as 1/k[X] where X = [OH] or [Cl]. It is therefore important to estimate the lifetime of CH_3SCH_2Cl with respect to photolysis and compare it with the estimated lifetimes of CH_3SCH_2Cl with respect to reaction with OH and Cl are known. This is the main objective of this chapter.

The production of SO_2 from photolysis of CH_3SCH_2Cl is thought to arise from the following reactions, which are initiated by photodissociation of CH_3SCH_2Cl, i.e.

$$CH_3SCH_2Cl + h\nu \rightarrow CH_3S + CH_2Cl \qquad (10.1a)$$

$$CH_3S + NO_2\ (O_3) \rightarrow CH_3SO_2 + NO\ (O_2) \qquad (10.2)$$

$$CH_3SO_2 + h\nu \rightarrow CH_3 + SO_2 \qquad (10.3)$$

It is thought that the C-S bond cleaves, producing CH_3S and CH_2Cl from reaction (10.1a). CH_3S is then oxidised by O_3 and/or NO_2 in the atmosphere to form CH_3SO_2. This produces SO_2 on photolysis and/or from thermal decomposition during the day. Other dissociative routes for CH_3SCH_2Cl which must also be considered on photolysis are,

$$CH_3SCH_2Cl + h\nu \rightarrow CH_3 + SCH_2Cl \qquad (10.1b)$$

$$CH_3SCH_2Cl + h\nu \rightarrow CH_3SCH_2 + Cl \qquad (10.1c)$$

It would be very valuable to determine (i) if CH_3SCH_2Cl is dissociative on photoexcitation in the atmosphere and, if so (ii) which photolysis channel is the dominant photodissociation channel. If the photolysis rate coefficient can be determined from the electronic absorption spectrum of CH_3SCH_2Cl, the photolysis lifetime of CH_3SCH_2Cl can be determined and compared to the lifetimes of CH_3SCH_2Cl for the reactions $CH_3SCH_2Cl + OH$ and $CH_3SCH_2Cl + Cl$. This would then determine the main channel for SO_2 production in the atmosphere from CH_3SCH_2Cl.

In this work ultraviolet (UV) absorption spectroscopy has been used to record the absorption spectrum of CH_3SCH_2Cl in the solar actinic region at known sample pressures. This then allowed photoabsorption cross-sections to be obtained in the actinic region. This information has been used with the known actinic solar flux to calculate the photolysis rate coefficient, on the assumption that photodissociation occurs in the actinic region.

10.1 Experimental

All experimental measurements reported in this chapter were conducted at the Molecular Spectroscopy Facility at the Rutherford Appleton Laboratories (RAL) using a Bruker IFS 66v/S Fourier Transform Spectrometer (FTS). This spectrometer provides a spectral coverage from the infrared to the near-ultraviolet region, i.e. 500 cm^{-1} (20,000 nm) to 50,000 cm^{-1} (200 nm), and has a maximum unapodized resolution of 0.12 cm^{-1}.

In this spectrometer a collimated beam of radiation, with a diameter of 25 mm, reflected from a gold-coated 90° off-axis parabolic mirror (focal length 121 mm) inside the FTS, is directed through a KBr optical window into an evacuated stainless-steel tube connected to the cell. The KBr window allows the transmission of radiation over a wide spectral range from 500 cm^{-1} to 50,000 cm^{-1}. The optical beam is transmitted through the cell towards another KBr window where it enters an evacuated tube connected to a vacuum chamber which contains the detector. The chamber can contain up to three detectors at any one time and the optical beam can be remotely steered onto each of the detectors using a second gold-coated 90° off-axis parabolic mirror (focal length 43 mm) which images the collimated beam onto the detector elements.

For the u.v.-visible experiments a xenon lamp was used as the source which covers the range (50,000 cm^{-1} to 18,000cm^{-1}). This was replaced with a glowing filament made of

silicon carbide (SiC) for the infrared measurements. A photomultiplier was used as the detector for the u.v. visible experiments with two different detectors used for the IR experiments; an indium antimonide (InSb) detector, which is suitable over the energy region 1800-6000 cm^{-1} and a mercury cadmium telluride (MCT) detector for covering the energy region 500-8000 cm^{-1}.

The CH_3SCH_2Cl sample (liquid) used in this work was obtained from a commercial source (Aldrich > 95%). The liquid sample was admitted to a glass ampule which was coupled to the reaction cell of the FTS (two reaction cells were used in this work; for the UV measurements a cell with a path length of (0.228 ± 0.002) m was used and for the infrared measurements a cell with a path length of (1.030 ± 0.002) m was used). The freeze-pump-thaw method was used to degas and improve the purity of the sample on a vacuum line before admitting the sample to the cell. CH_3SCH_2Cl vapour was then admitted to the cell using a needle valve. Pressures inside the cell were measured using a baratron pressure gauge.

Absolute photoabsorption cross-sections were obtained (at known wavelength), using the Beer-Lambert law,

$$I = I_0 exp^{(-\sigma lc)} \tag{10.4a}$$

where I is the radiation intensity transmitted through the gas sample, I_0 is the incident radiation intensity on the cell, l is the absorption path length, c is the molecular number density of the sample and σ is the absolute photoabsorption cross-section. This can be re-written for absorbance as,

$$Absorbance\ (Abs) = \ln\left(\frac{I_0}{I}\right) = \sigma lc \tag{10.4b}$$

The experimental error in the photoabsorption cross-sections measured in this work is estimated at (± 5%).

10.2 Computational Details

Electronic structure calculations were performed by Dr E. P. F. Lee of the Southampton PES group in support of this experimental work. The results are included here for completeness.

Geometry optimisation and harmonic frequency calculations were carried out for the dissociation products, CH_3S, CH_2Cl, SCH_2Cl and CH_3SCH_2 from the photolysis reactions (10.1a), (10.1b) and (10.1c), using the Gaussian09 suite of programs [22], employing the time dependent density functional theory (TD-DFT) method and the MP2 method with the B3LYP functional. Single energy calculations for improved relative electronic energies were performed at the RHF/UCCSD(T) level using the MOLPRO program [23]. All single energy higher level calculations have employed the MP2/6-311++G** geometries. At the RHF/UCCSD(T)/F-12x (x = a or b) level, the VTZ-F12 and the VQZ-F12 basis sets, which have been optimised for F12 calculations, have been used together with corresponding default RI (F12 optimised) and DF basis sets as implemented by MOLPRO. AVTZ and AVQZ quality basis sets were used with the RCCSD(T) method, which employed the aug-cc-pV(X+d)Z basis sets for S and Cl atoms. The complete basis set (CBS) limit values of the reaction energies were obtained using the $1/X^3$ extrapolation formula. Reaction enthalpies were evaluated within the rigid rotor harmonic oscillator model using computed MP2 geometries and vibrational frequencies.

10.3 Results and Discussion

10.3.1 The UV Absorption Spectrum of CH_3SCH_2Cl

Absorption spectra were recorded of CH_3SCH_2Cl at four different pressures, 0.80, 1.25, 1.60 and 2.00 mbar, over the range 28,000 cm^{-1} to 50,000 cm^{-1} using a cell of path length (0.228 ± 0.002) m. As far as is known no electronic absorption spectra of CH_3SCH_2Cl have been reported before this work.

The UV absorption spectra of CH_3SCH_2Cl are shown in Figure 10.1 (top). They show two main absorption bands, a weak absorption band, observed between 30,000 cm^{-1} and 38,000 cm^{-1}, and a second, much larger, absorption band observed from 38,000 cm^{-1} to 45,000 cm^{-1}. The lower spectrum in Figure 10.1 shows the first, weaker, absorption band of CH_3SCH_2Cl more clearly. The first absorption band has an onset at (28,000 ± 100) cm^{-1} and a band maximum at (34,500 ± 100) cm^{-1}. The larger absorption band has a measured band maximum of (42,800 ± 50) cm^{-1}. The first absorption band overlaps the region of the solar actinic flux (shown in red in Figure 10.1).

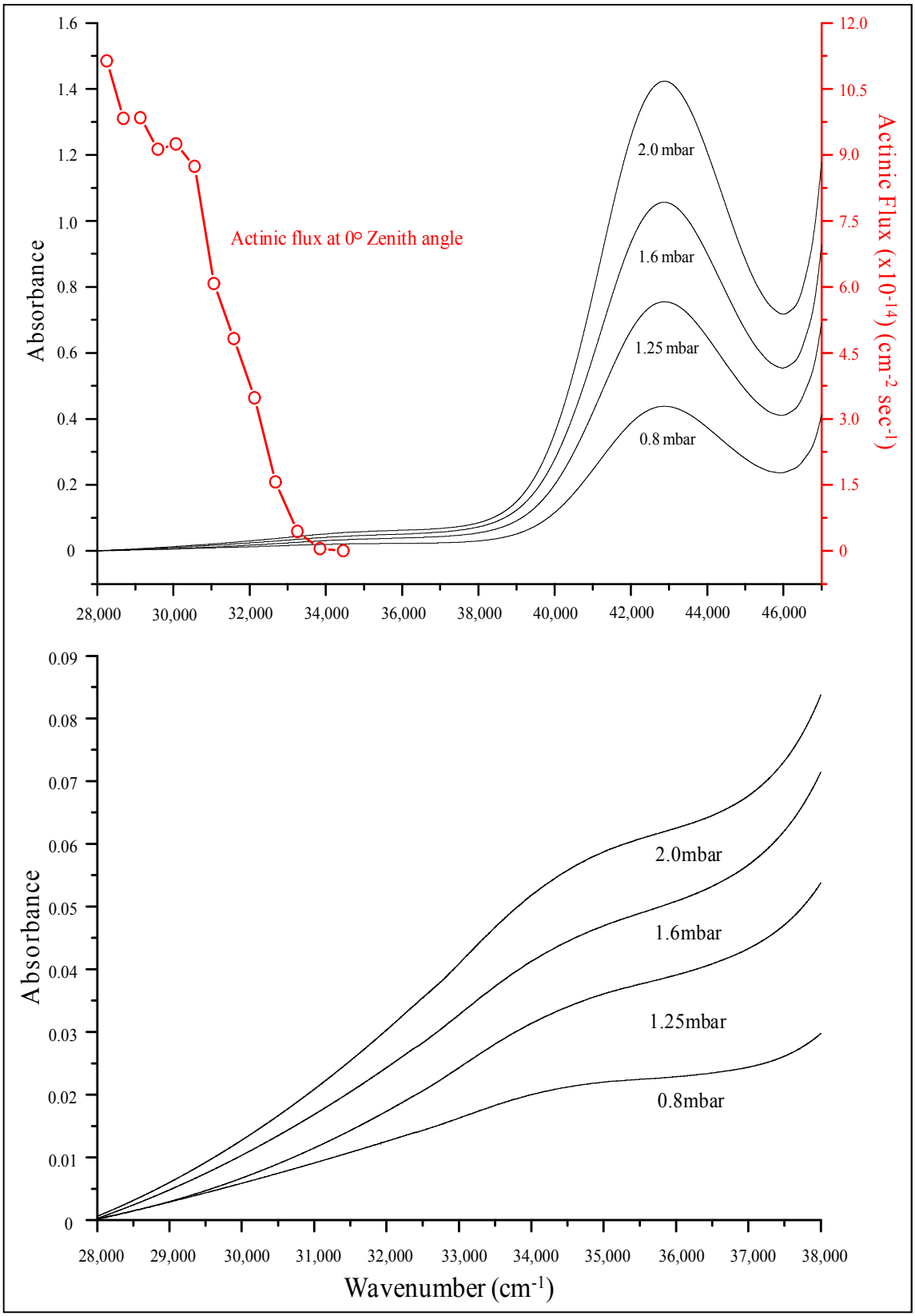

Figure 10.1: *The UV absorption spectrum of CH_3SCH_2Cl recorded at four different pressures showing the absorption in the actinic flux region (shown in red in the upper spectrum).The bottom spectra show the first absorption band at each pressure recorded. The cell path length used to obtain these spectra was (0.228 ± 0.002) m.*

The solar actinic flux is the intensity of radiation in a given wavelength window (usually given as the sum over 5 nm) available to molecules at a particular height in the atmosphere. Solar actinic flux values, listed in reference [24], have been plotted for the solar zenith angles (SZA) of, 0°, 10°, 20°, 30°, 40°, 50°, 60°, 70°, 78° and 86°, over the range 14,000 cm^{-1} to 34,000 cm^{-1}, and are shown in Figure 10.2 (the SZA is defined with respect to the earth's surface; 0° means directly above).

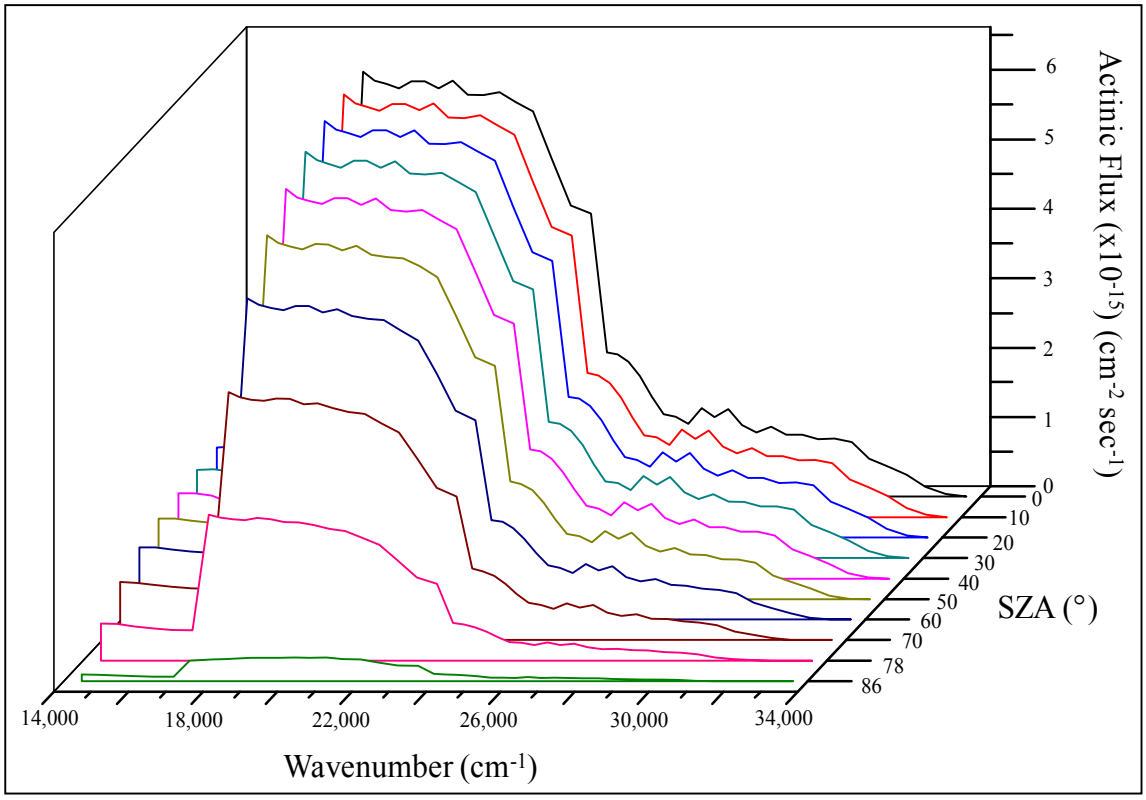

Figure 10.2: *Solar actinic solar flux values determined at different solar zenith angles over the range 14,000cm^{-1} to 34,000cm^{-1} plotted as a function of wavenumber [24].*

Solar actinic flux values in the region of interest, i.e. the region which overlaps with the first absorption band seen in the recorded UV spectrum of CH_3SCH_2Cl, which is *ca.* 28,000 cm^{-1} to *ca.* 34,200 cm^{-1} or 290 nm to 355nm, (see Figure 10.1) will be used in order to determine the photolysis rate coefficient of CH_3SCH_2Cl.

Photoabsorption cross-sections of CH_3SCH_2Cl, calculated from recorded UV absorption spectra, were used along with the solar actinic flux values taken from the literature [24] and quantum yields of CH_3SCH_2Cl, to determine its photolysis rate coefficient and hence photolysis lifetime in the atmosphere. This involved taking experimental absorbance values, $\ln(I_0/I)$, at each wavenumber value, with known values of l and c to determine σ, the photoabsorption cross-section. In order to determine photoabsorption

cross-sections of CH_3SCH_2Cl at a known wavelength, (λ), equation 10.4b can be rearranged to give,

$$\sigma_{MClDMS}(\lambda) = \frac{Abs}{l\,.\,c} \tag{10.5}$$

Using the known photoabsorption cross-sections at each wavelength, using equation 10.5, the photolysis rate coefficient, $J_{(MClDMS)}$, can be calculated using equation 10.6,

$$J_{(MClDMS)} = \int_{\lambda_A}^{\lambda_B} F(\lambda)\sigma_{MClDMS}(\lambda)\Phi(\lambda)\,d\lambda \tag{10.6}$$

where $F(\lambda)$ is the spherically integrated actinic solar photon flux at the earth's surface for a given wavelength, $\sigma_{MClDMS}(\lambda)$ is the photoabsorption cross-section determined at known (λ) from equation 10.5 and Φ(λ) is the absolute quantum yield of CH_3SCH_2Cl (assumed to be unity in this work). To evaluate equation 10.6, $J_{(MClDMS)}$ was approximated as a sum of $F(\lambda)\sigma_{MClDMS}(\lambda)\Phi(\lambda)$ in small wavelength intervals over the wavelength range (*ca.* 28,000 cm^{-1} to *ca.* 34,000 cm^{-1} or 290 nm to 355nm). To determine the photolysis rate coefficient equation 10.6 then becomes,

$$J_{(MClDMS)} = \sum_{290}^{355} F(\lambda)\sigma_{MClDMS}(\lambda)\Phi(\lambda) \tag{10.7}$$

Inspection of equation 10.4b shows that absorbance must scale linearly with molecular number density. To check this, absorbance values were measured at different wavenumber values for the first and second absorption bands and plotted as a function of pressure. Wavenumber values chosen for the first absorption band were 32,000 cm^{-1}, 34,000 cm^{-1} and 36,000 cm^{-1}. Wavenumber values chosen for the second absorption band were 41,000 cm^{-1}, 42,000 cm^{-1} and 43,000 cm^{-1}.

Absorbance values plotted as a function of pressure are shown in Figure 10.3. Absorbance values at 32,000 cm^{-1} and 34,000cm^{-1} were chosen as these values reside within the solar actinic flux region. Wavenumber values are shown to scale linearly with pressure obeying the Beer-Lambert relationship (Figure 10.3). Error bars are shown for uncertainties in measured absorbance and pressure. An uncertainty of (± 0.2) mbar is used for pressure and (± 0.01) is used for measured absorbance values in both linear plots.

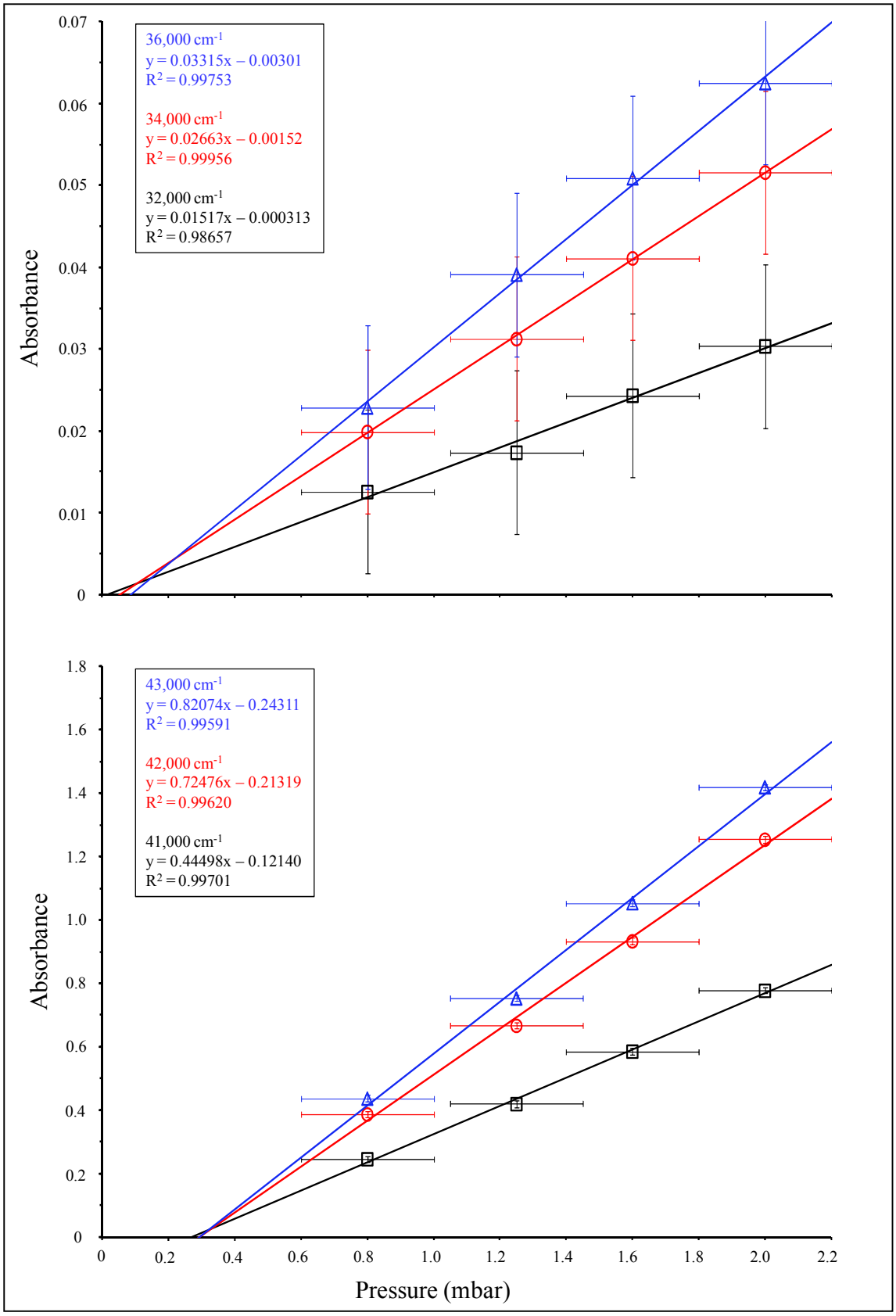

Figure 10.3: *Absorbance values determined from UV absorption spectra of CH_3SCH_2Cl for the first and second absorption bands (upper and lower plots respectively) plotted against pressure.*

It can be seen from the plots shown in Figure 10.3 that for the first band (upper plot) the linear fits can be extrapolated back to intercept the origin. It is observed for the second absorption band (lower plot) that the linear fits for each wavenumber value do not go through the origin; however, given the error bars involved, notably in the pressure (± 0.2) mbar, this was not considered a serious problem.

Photoabsorption cross-sections were determined in 5 nm bins from 290 nm to 355 nm (28,369 cm^{-1} to 34,188 cm^{-1}) as $F(\lambda)$ values are listed as a total per 5 nm bin in reference [24]. The results are shown in Table 10.1.

Wavelength (nm)	Wavenumber (cm^{-1})	Photoabsorption Cross-Sections (cm^2) (± 5%)
290 to 295	34483 to 33898	$(4.78 \pm 0.24) \times 10^{-20}$
295 to 300	33898 to 33333	$(4.30 \pm 0.21) \times 10^{-20}$
300 to 305	33333 to 32787	$(3.74 \pm 0.19) \times 10^{-20}$
305 to 310	32787 to 32258	$(3.21 \pm 0.16) \times 10^{-20}$
310 to 315	32258 to 31746	$(2.73 \pm 0.14) \times 10^{-20}$
315 to 320	31746 to 31250	$(2.30 \pm 0.11) \times 10^{-20}$
320 to 325	31250 to 30769	$(1.90 \pm 0.95) \times 10^{-20}$
325 to 330	30769 to 30303	$(1.53 \pm 0.77) \times 10^{-20}$
330 to 335	30303 to 29851	$(1.21 \pm 0.60) \times 10^{-20}$
335 to 340	29851 to 29412	$(9.17 \pm 0.46) \times 10^{-21}$
340 to 345	29412 to 28986	$(6.54 \pm 0.33) \times 10^{-21}$
345 to 350	28986 to 28571	$(4.19 \pm 0.21) \times 10^{-21}$
350 to 355	28571 to 34188	$(2.20 \pm 0.11) \times 10^{-21}$

Table 10.1: *Photoabsorption cross-sections calculated in 5 nm bins from absorption spectra of CH_3SCH_2Cl.*

The sum of the $J_{(MClDMS)}$ values over the entire wavelength range (290 nm to 355 nm) yields the photolysis rate coefficient at ground level for a given SZA, using equation 10.7, at each pressure measured. It must be noted that solar actinic flux values used in the determination of the CH_3SCH_2Cl photolysis rate coefficient have been determined for the earth's surface i.e. approximately a few metres above ground level and that each actinic flux value used per 5 nm bin is a summation of actinic fluxes over that wavelength interval [24].

The photoabsorption cross-sections, shown in Table 10.1, were used in equation 10.7 to determine the photolysis rate coefficient of CH_3SCH_2Cl at each SZA. As photodissociation of CH_3SCH_2Cl is a first order process, the photolysis rate coefficients at a given SZA can be used to determine the photolysis lifetime ($t_{½}$) of CH_3SCH_2Cl at the corresponding SZA using equation 10.8.

$$t_{1/2} = {}^{1}/_{k} \qquad (10.8)$$

where k is the photolysis rate coefficient of CH_3SCH_2Cl determined from equation 10.8. For a first order reaction process, $\ln(2)/k$ should be used to determine (t½) values, however $1/k$ is used here purely to provide an estimate and to be consistent with the equation used to determine the photolysis lifetimes with respect to OH and Cl reactions. The photolysis rate coefficients at each SZA and photolysis lifetimes of CH_3SCH_2Cl are given in Table 10.2.

Solar Zenith Angle	Rate Coefficient (sec^{-1}) (± 5%)	Photolysis Lifetime (t½) (hours)
0°	$(7.67 \pm 0.38) \times 10^{-5}$	3.62
10°	$(7.57 \pm 0.38) \times 10^{-5}$	3.67
20°	$(7.23 \pm 0.36) \times 10^{-5}$	3.84
30°	$(6.65 \pm 0.33) \times 10^{-5}$	4.17
40°	$(5.83 \pm 0.29) \times 10^{-5}$	4.77
50°	$(4.72 \pm 0.24) \times 10^{-5}$	5.88
60°	$(3.36 \pm 0.17) \times 10^{-5}$	8.27
70°	$(1.85 \pm 0.92) \times 10^{-5}$	15.05
78°	$(7.77 \pm 0.39) \times 10^{-6}$	35.76
86°	$(1.50 \pm 0.08) \times 10^{-6}$	185.06

Table 10.2: *Photolysis rate coefficients determined in this work for CH_3SCH_2Cl at different solar zenith angles. Photolysis lifetimes of CH_3SCH_2Cl have been estimated using1/k.*

It is clear from the results shown in Table 10.2 that, during the day, where the photon flux is at its most intense, at ground level at SZA values of 0° to 30°, the photolysis rate of CH_3SCH_2Cl is at its highest, with rate coefficients in the range 6.79×10^{-5} to 7.83×10^{-5} sec^{-1} with an expected photolysis lifetime in the range of a few hours (*ca.* 3-4 hours). A further increase in SZA shows the lifetime to increase from 5 to 10 hours with photolysis rate coefficients decreasing from 5.95×10^{-5} to 1.88×10^{-5} sec^{-1}. The photolysis rate decreases significantly at higher zenith angles of 78° and 86°, which would correspond to sunset, (where the solar actinic flux is at its lowest), with determined rate coefficients of 7.92×10^{-6} and 1.53×10^{-6} sec^{-1} respectively. Photolysis lifetimes at these angles have been determined to be from approximately > 1 day to > 7 days. It is evident that the photolysis rate coefficients decrease with increasing SZA and the photolysis lifetime of CH_3SCH_2Cl increases with increasing SZA. Photolysis rate coefficients determined in this work, plotted as a function of SZA, are shown in Figure 10.4. Solar actinic flux values used in this work are given in Table 10.3. From the calculations it shows that apart from when the sun is low in the sky, at zenith angles greater than

approximately 70°, the lifetime of CH_3SCH_2Cl with respect to photolysis is much lower than the lifetime with respect to reaction with OH and Cl.

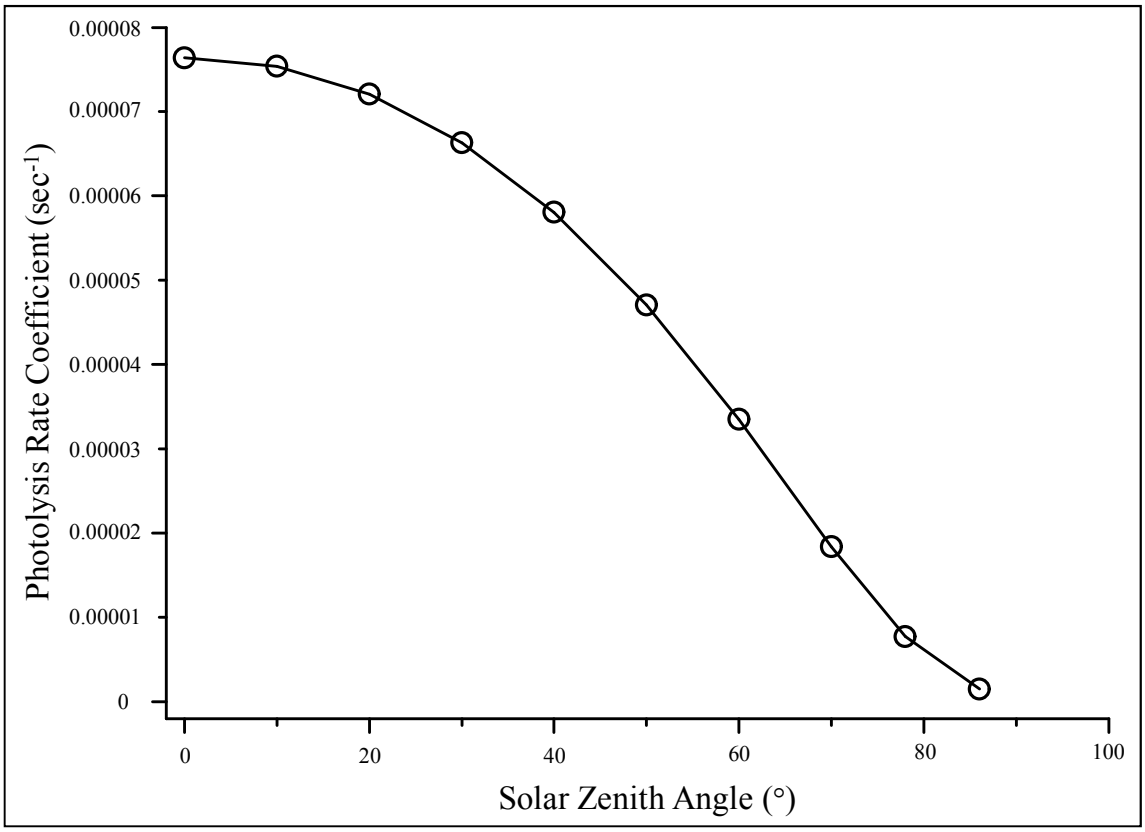

Figure 10.4: *Photolysis rate coefficients determined in this work, from photoabsorption cross-section measurements, plotted as a function of solar zenith angle (see Table 10.2 for errors associated with determine rate coefficients).*

Wavenumber (cm^{-1})	Solar Zenith Angle (°)									
	0	10	20	30	40	50	60	70	78	86
34483 to 33898	1	1	0	0	0	0	0	0	0	0
33898 to 33333	41	38	30	19	9	3	0	0	0	0
33333 to 32787	398	381	331	255	167	84	27	4	1	0
32787 to 32258	1410	1370	1250	1050	800	513	244	64	11	2
32258 to 31746	3140	3100	2910	2580	2130	1560	922	357	90	9
31746 to 31250	4350	4310	4100	3740	3210	2520	1670	793	264	30
31250 to 30769	5480	5410	5190	4800	4230	3430	2430	1290	502	73
30769 to 30303	7890	7790	7510	7010	6270	5210	3830	2170	928	167
30303 to 29851	8350	8250	7980	7500	6760	5720	4300	2540	1150	241
29851 to 29412	8240	8160	7910	7460	6780	5790	4430	2690	1250	282
29412 to 28986	8890	8800	8540	8090	7380	6360	4930	3040	1440	333
28986 to 28571	8870	8790	8540	8110	7430	6440	5040	3150	1510	352
28571 to 34188	10050	9960	9700	9220	8480	7390	5830	3690	1770	414

Table 10.3: *Solar actinic flux values ($x10^{11}$), (cm^{-2} sec^{-1}) calculated at the earth's surface, in reference [24], as a function of wavenumber and solar zenith angle, for best estimated surface albedos. Each value is given as the sum over a 5 nm wavelength window.*

10.3.2 The Infrared Absorption Spectrum of CH_3SCH_2Cl

Infrared absorption spectra were recorded of CH_3SCH_2Cl at five different pressures, 0.5, 1.0, 3.0, 5.0 and 10.0 mbar in the range 400 cm^{-1} to 4,000 cm^{-1} using a cell of path length (1.030 ± 0.002) m.

CH_3SCH_2Cl is a non-linear molecule with 9 atoms and 21 vibrational modes. The vibrational wavenumber values and intensities, computed for the optimised geometry at the MP2/6-311** level, are shown in Table 10.4. A description of each normal mode is also given in Table 10.4. The computed infrared spectrum is shown in Figure 10.5 where each absorption is represented using a Lorentz function with a half-width of 5 cm^{-1}. The experimental infrared absorption spectrum, shown in Figure 10.6 (top), shows 17 major infrared bands, labelled A-J. Absorption bands E, F, H and J show grouped absorption bands, shown in Figure 10.6 (bottom), and have been labelled E_{1-2}, F_{1-2}, H_{1-3} and J_{1-4}. A total of 17 infrared bands are observed from the spectrum of CH_3SCH_2Cl. The spectrum shown in Figure 10.6 was recorded at room temperature and at a pressure of 5.0 mbar.

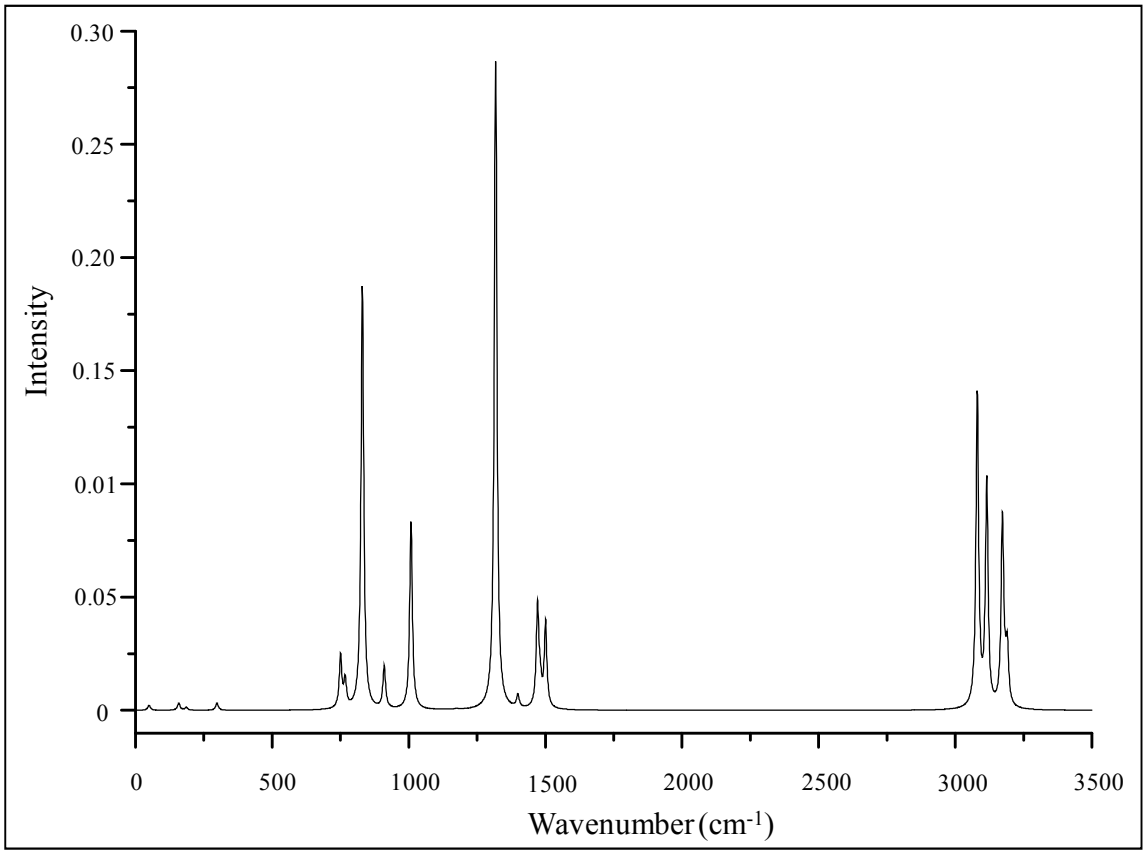

Figure 10.5: *Infrared spectrum of CH_3SCH_2Cl computed at the MP2/6-311** level.*

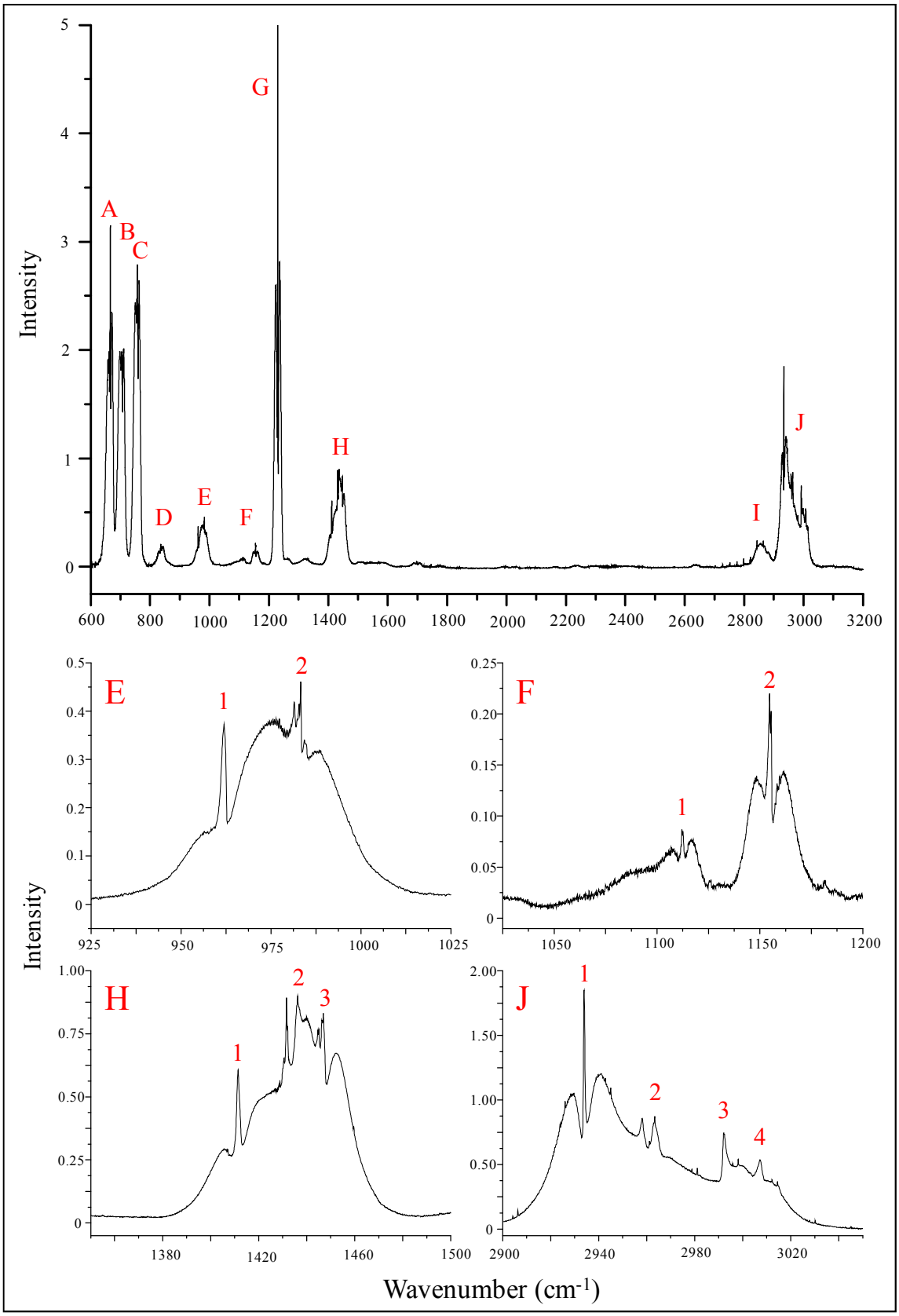

Figure 10.6: *The infrared absorption spectrum of CH_3SCH_2Cl recorded at a pressure of 5.0 mbar.*

Experimental infrared absorption bands (labelled A-J, shown in Figure 10.6) have been compared with the vibrational wavenumbers and absolute intensities of the calculated spectrum and are shown in Table 10.4.

Mode	Calculated			Experimental		
	Wavenumber (cm^{-1})	Intensity ($km.mol^{-1}$)	Description	Band	Wavenumber (cm^{-1})	Intensity
1	50	0.45	C-H_2 Rocking/ C-H_2 (in CH_3) Rocking			
2	159	0.62	C-H_2 Rocking/ C-H_2 (in CH_3) Rocking			
3	186	0.26	Cl-C-S-C Bending			
4	298	0.63	C-S-C Bending			
5	751	4.65	Cl-C-S-C Stretching	A	666.20	Strong
6	767	2.37	C-S-C Stretching	B	704.35	Strong
7	830	37.44	Cl-C-S Stretching	C	756.65	Strong
8	911	3.71	C-H_2 Rocking	D	836.46	Moderate
9	1008	7.93	C-H_3 Rocking	E_1	961.97	Moderate
				E_2	983.92	Weak
10	1009	8.85	C-H_2 (in CH_3) Rocking	F_1	1112.48	Weak
11	1175	0.08	C-H_2 Twisting	F_2	1155.99	Weak
12	1318	57.69	C-H_2 Wagging	G	1229.47	Strong
13	1400	1.12	C-H_3 Bending			
14	1471	9.03	C-H_2 (in CH_3) Twisting	H_1	1411.39	Moderate
15	1482	1.73	C-H_2 Stretching/ C-H_3 Bending	H_2	1436.15	Moderate
16	1501	7.56	C-H_3 Bending	H_3	1445.73	Moderate
17	3081	27.72	C-H_3 Stretch	I	2855.39	Moderate
18	3115	19.86	C-H_2 Stretch	J_1	2933.08	Moderate
19	3173	16.67	C-H_3 Stretch	J_2	2963.65	Moderate
20	3183	1.09	C-H_2 Stretch	J_3	2992.28	Moderate
21	3191	4.79	C-H_3 Stretch	J_4	3007.42	Moderate

Table 10.4: *Vibrational wavenumbers calculated at the MP2/6-311G** level for CH_3SCH_2Cl compared with the corresponding values for the absorption bands from the experimental infrared spectrum of CH_3SCH_2Cl.*

Reasonable agreement is observed between the experimental and computed infrared spectra of CH_3SCH_2Cl. Intense absorption bands are observed for C-H_2 wagging and Cl-C-S stretching at 1318 cm^{-1} and 830 cm^{-1} in the calculated spectrum with the corresponding experimental infrared absorption bands observed at (1229.47 ± 0.50) cm^{-1} and (756.65 ± 0.50) cm^{-1}.

In order to show that absorbance scales linearly with molecular number density, absorbance values were measured at different wavenumber values, 836 cm^{-1} (D), 1411 cm^{-1} (H_1) and 2933 cm^{-1} (J_1) and plotted as a function of pressure. Absorbance values plotted as a function of pressure are shown in Figure 10.7.

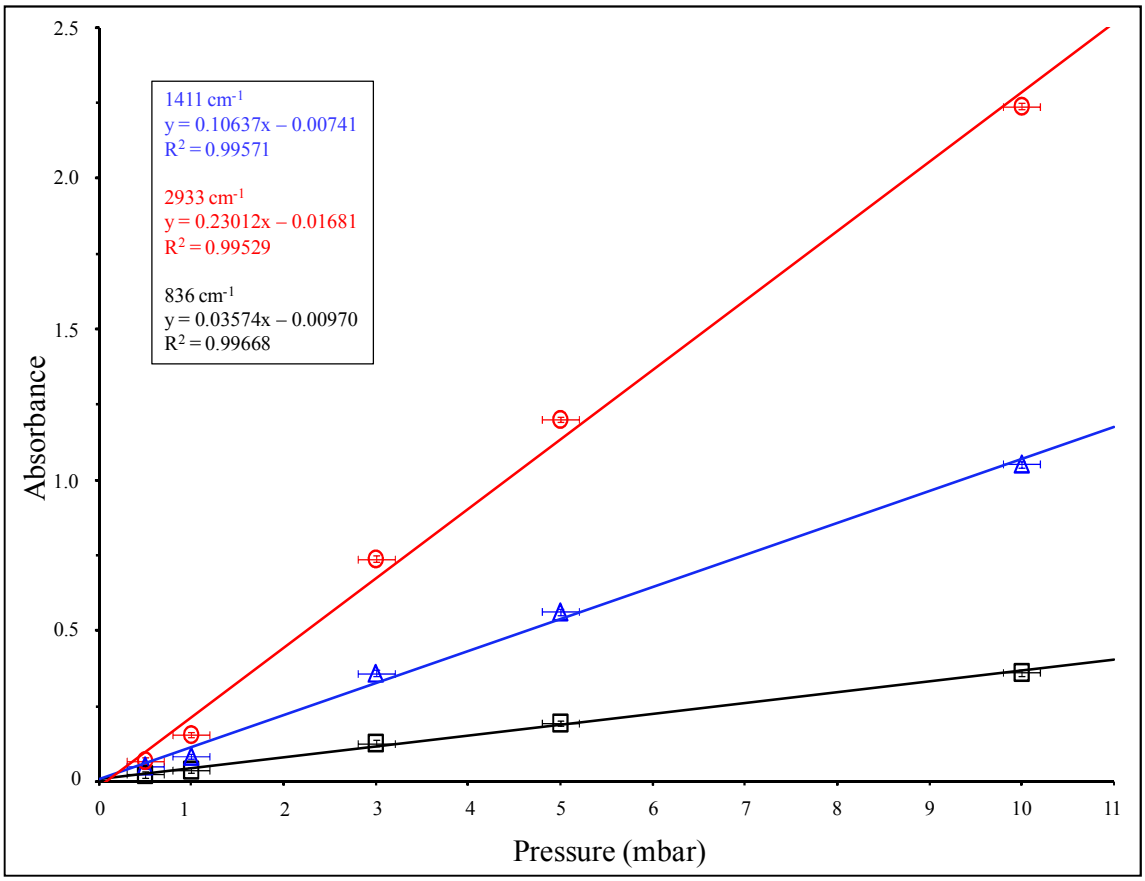

Figure 10.7: *Absorbance values determined from infrared absorption spectra of CH_3SCH_2Cl at the wavenumber values of 836 cm^{-1}, 1411 cm^{-1} and 2933 cm^{-1} plotted against pressure.*

Wavenumber values are shown to scale linearly with pressure obeying the Beer-Lambert relationship. Error bars are shown for uncertainties in measured absorbance and pressure. An uncertainty of (± 0.2) mbar is used for pressure and an uncertainty of (± 0.01) is used for measured absorbance values.

Infrared photoabsorption cross-sections were determined in this work, the same way as those described above for UV photoabsorption cross-sections, for the 17 key absorptions (A to J), shown in Figure 10.6. However, photoabsorption cross-sections were not used for any further analysis of CH_3SCH_2Cl. The infrared photoabsorption cross-sections of CH_3SCH_2Cl are given in Table 10.5.

Absorption Band	Wavenumber (cm^{-1})	Intensity	Photoabsorption Cross-Sections (cm^2) (± 5%)
A	666	Strong	$(5.16 \pm 0.26) \times 10^{-21}$
B	704	Strong	$(1.78 \pm 0.09) \times 10^{-21}$
C	756	Strong	$(2.10 \pm 0.11) \times 10^{-19}$
D	836	Moderate	$(1.50 \pm 0.07) \times 10^{-20}$
E_1	961	Moderate	$(2.49 \pm 0.12) \times 10^{-20}$
E_2	983	Weak	$(2.81 \pm 0.14) \times 10^{-20}$
F_1	1112	Weak	$(6.24 \pm 0.31) \times 10^{-21}$
F_2	1155	Weak	$(1.29 \pm 0.06) \times 10^{-20}$
G	1229	Strong	$(3.12 \pm 0.16) \times 10^{-19}$
H_1	1411	Moderate	$(4.35 \pm 0.22) \times 10^{-20}$
H_2	1436	Moderate	$(6.72 \pm 0.34) \times 10^{-20}$
H_3	1445	Moderate	$(5.55 \pm 0.28) \times 10^{-20}$
I	2855	Moderate	$(1.67 \pm 0.08) \times 10^{-20}$
J_1	2933	Moderate	$(9.27 \pm 0.46) \times 10^{-20}$
J_2	2963	Moderate	$(6.37 \pm 0.32) \times 10^{-20}$
J_3	2992	Moderate	$(5.46 \pm 0.27) \times 10^{-20}$
J_4	3007	Moderate	$(3.99 \pm 0.20) \times 10^{-20}$

Table 10.5: *Photoabsorption cross-sections determined from infrared absorption spectra of CH_3SCH_2Cl.*

Infrared cross-section data are important in atmospheric chemistry as they allow for improved retrieval and quantification of certain species which are monitored at various heights in the atmosphere. Knowing where these species are in the atmosphere and having the ability to quantify them, i.e. to determine number densities or concentration profiles, is invaluable for atmospheric chemistry. Also infrared spectra with known photoabsorption cross-sections can be used to determine the global warming potentials (GWP) for a given species.

Global warming potentials of greenhouse gases depend on the number of absorption bands in the infrared region, the intensity of those bands and more importantly the position of the absorption bands. Several studies have been carried out to determine radiative efficiencies and global warming potentials of greenhouse gases using measured infrared absorption cross-sections [25, 26, 27].

The radiative efficiency is an experimentally determined quantity derived from the radiative forcing, which is the amount of energy per unit area per unit time that a greenhouse gas absorbs, of a species along with its infrared photoabsorption cross-sections. The global warming potential, which is the radiative forcing capacity of the greenhouse gas weighted by its atmospheric lifetime, of a given species can be determined using the radiative efficiencies [28, 29, 30].

10.3.3 Heat of Formation ($\Delta H_{f,\,298K}^{Ø}$) of CH_3SCH_2Cl

In order to calculate the bond energies associated with the photolysis processes (10.1a), (10.1b) and (10.1c), the heat of formation ($\Delta H_{f,298K}^{Ø}$) of CH_3SCH_2Cl is required. The experimental $\Delta H_{f,298K}^{Ø}$ of CH_3SCH_2Cl has been determined in this work using values taken from the literature. Dissociation energies (D_0) of CH_3SCH_3 and CH_3SCH_2Cl have been calculated for $CH_3SCH_3 \rightarrow CH_3SCH_2 + H$ and $CH_3SCH_2Cl \rightarrow CH_3SCH_2 + Cl$ (photolysis channel (10.1c)) to be (91.8 ± 0.2) kcal.mol^{-1} and (72.0 ± 0.6) kcal.mol^{-1} respectively [31]. These values were obtained by photoionisation mass spectroscopy (PIMS) [31] by measuring the IE of CH_3SCH_3 and the appearance energy of $CH_3SCH_2^+$ from,

$$CH_3SCH_3 + h\nu \rightarrow CH_3SCH_2^+ + H + e^- \qquad (10.9)$$

and by measuring the IE of CH_3SCH_2Cl and the appearance energy of $CH_3SCH_2^+$ from,

$$CH_3SCH_2Cl + h\nu \rightarrow CH_3SCH_2^+ + Cl + e^- \qquad (10.10)$$

Dissociation energies of the $CH_3SCH_2 + H$ and the $CH_3SCH_2 + Cl$ decomposition channels must therefore be,

$$D_A\,(CH_3SCH_3) = \Delta H_f\,(H) + \Delta H_f\,(CH_3SCH_2) - \Delta H_f\,(CH_3SCH_3) \qquad (10.11)$$

$$D_B\,(CH_3SCH_2Cl) = \Delta H_f\,(Cl) + \Delta H_f\,(CH_3SCH_2) - \Delta H_f\,(CH_3SCH_2Cl) \qquad (10.12)$$

The $\Delta H_{f,298K}^{Ø}$ of CH_3SCH_2Cl can therefore be determined from,

$$(D_A - D_B) = (H) - (Cl) - (CH_3SCH_3) + (CH_3SCH_2Cl) \qquad (10.13)$$

If the $\Delta H_{f,298K}^{Ø}$ are known for, H, Cl and CH_3SCH_3 then the $\Delta H_{f,298K}^{Ø}$ of CH_3SCH_2Cl can be determined as (D_A - D_B) is known [31]. Experimentally determined $\Delta H_{f,298K}^{Ø}$ values, H (52.1 ± 0.0014) kcal.mol^{-1} [32], Cl (28.992 ± 0.002) kcal.mol^{-1} [32] and CH_3SCH_3 (91.8 ± 0.2) kcal.mol^{-1} [33] were used in (10.13) to determine the $\Delta H_{f,298K}^{Ø}$ of CH_3SCH_2Cl as (-12.32 ± 1.00) kcal.mol^{-1}. The dissociation energies can then be calculated, using the $\Delta H_{f,298K}^{Ø}$ determined for CH_3SCH_2Cl, for photolysis channels (10.1a) and (10.1b) using a similar methodology.

Of the three photolysis routes, experimental $\Delta H_{f,298K}^{Ø}$ of the reaction products from photolysis reaction (10.1a) are known and have been used in this work to determine its

dissociation energy. The dissociation energy of (10.1b) cannot be determined as no experimental $\Delta H_{f,298K}^{Ø}$ value was available for the photolysis product SCH_2Cl. This value has, however, been calculated by Dr E. P. F. Lee. The dissociation energy of (10.1c) has already been determined as (72.0 ± 0.6) kcal.mol^{-1} in reference [31].

The $\Delta H_{f,298K}^{Ø}$ values used for photolysis products CH_3S and CH_2Cl of reaction (10.1a) were (29.87 ± 0.47) kcal.mol^{-1} and (27.96 ± 0.74) kcal.mol^{-1} respectively [34, 35, 36]. Using experimental $\Delta H_{f,298K}^{Ø}$ values quoted in the literature with the $\Delta H_{f,298K}^{Ø}$ of CH_3SCH_2Cl of (-12.32 ± 1.00) kcal.mol^{-1}, the dissociation energies of channel (10.1a) was determined as $D_{(S-C)}$ (70.15 ± 2.2) kcal.mol^{-1}. Results of the available dissociation energies for (10.1a) and (10.1c) are compared with those computed by Dr E. P. F. Lee in Table 10.6.

Methods	Reaction (10.1a)			Reaction (10.1b)			Reaction (10.1c)		
	ΔE_e	ΔE_{0K}	ΔH_{298K}	ΔE_e	ΔE_{0K}	ΔH_{298K}	ΔE_e	ΔE_{0K}	ΔH_{298K}
B3LYP/6-31++G**	62.95	57.39	58.54	68.57	65	66.08	67.33	60.18	62.54
MP2/6-31++G**	70.09	64.76	65.82	77.6	74.14	75.12	73.87	67.97	69.15
F12a/VTZ-F12	73.52	68.24	69.3	76.94	73.48	74.46	77.55	71.66	72.83
F12b/VTZ-F12	73.34	68.06	69.12	76.75	73.29	74.27	77.38	71.48	72.66
F12a/VQZ-F12	73.44	68.16	69.23	76.93	73.47	74.45	77.48	71.58	72.76
F12b/VQZ-F12	73.35	**68.07**	**69.13**	76.83	**73.36**	**74.34**	77.38	**71.49**	**72.66**
RCCSD(T)/AVTZ	72.17	66.89	67.95	75.45	71.99	72.96	75.75	69.85	71.03
RCCSD(T)/AVQZ	73.06	67.78	68.85	76.57	73.11	74.09	76.86	70.97	72.14
RCCSD(T)/CBS	73.72	**68.44**	**69.5**	77.39	**73.93**	**74.91**	77.68	**71.78**	**72.95**
Experimental Value			70.15 ± 2.2[a]						72.0 ± 0.6[b]

Table 10.6: *Computed reaction energies (ΔE_e and ΔE_{0K}) and enthalpies (ΔH_{298K}) in kcal.mol^{-1} for reactions (10.1a), (10.1b) and (10.1c) obtained at different levels of calculations.*

[a] This work.
[b] reference [31].

In Table 10.6, the RCCSD(T)/CBS value of 69.50 kcal.mol^{-1} compares well with (70.15 ± 0.22) kcal.mol^{-1} for channel (10.1a) derived in this work and the RCCSD(T)/CBS value of 72.95 kcal.mol^{-1} compares well with (72.0 ± 0.6) kcal.mol^{-1} for channel (10.1c) obtained in reference [31] indicating that the computed reaction energy for (10.1b) (RCCSD(T)/CBS value of 74.91 kcal.mol^{-1}) is reliable to within (± 1.0) kcal.mol^{-1}. This provides strong evidence to suggest that on photolysis of CH_3SCH_2Cl the lowest energy dissociation channel involves cleavage of the CH_3S-CH_2Cl bond to give CH_3S + CH_2Cl.

10.3.4 Dissociation of CH_3SCH_2Cl in the Excited State

For absorption in the region 28,000 cm^{-1} to 38,000 cm^{-1} the excited state is likely to be dissociative or predissociative as (i) the onset of the band (28,000 ± 100) cm^{-1} (80.06 ± 0.15) $kcal.mol^{-1}$ (see Figure 10.1) is above the expected dissociation energy of CH_3S-CH_2Cl bond ((70.15 ± 2.2) $kcal.mol^{-1}$) (see Table 10.6) and (ii) the first allowed absorption band in DMS, corresponding to the $a^1B_1 \leftarrow \tilde{X}^1A_1$ transition, is known to be predissociative [37, 38]. For DMS, the observed absorption bands, which are in the region 35,000 cm^{-1} to 50,000 cm^{-1} and higher, can be classified as members of valence-valence transitions, of the $n_s \rightarrow \sigma^*$ type, and valence-Rydberg transitions [39]. Nevertheless as the quantum yield for photodissociation of CH_3SCH_2Cl at wavelengths in the actinic region could be less than 1.0, the photodissociation rate coefficients determined in this work must be viewed as upper limits and the derived lifetime lower limits.

As can be seen from Figure 10.1, the absorption spectrum of CH_3SCH_2Cl shows a very weak band centred at (34,500 ± 100) cm^{-1} and a stronger band centred at (42,800 ± 50) cm^{-1}. These bands were assigned on the basis of the results of the time-dependant density functional theory (TD-DFT) calculations shown in Table 10.7.

States	Excitations	*f*	ΔE_{ex}	Wavenumber (cm^{-1})	Optimisation
$(1)^3A''$	25→27, 0.587	0	4.647	37475.81	Break S-CH_2Cl
$(2)^3A''$	25→26, 0.626	0	4.977	40137.1	Break C-Cl
$(1)^1A''$	25→26, 0.630	0.0001	5.031	40572.58	Break C-Cl
$(2)^1A''$	25→27, 0.612	0	5.211	42024.19	Break S-CH_2Cl
$(3)^3A''$	25→28, 0.646	0	5.552	44774.19	Minimum
$(3)^1A''$	25→28, 0.684	0.0013	5.634	45435.48	Break S-CH_2Cl
$(4)^3A''$	25→30, 0.567	0	5.922	47758.06	-
$(1)^3A'$	25→29, 0.699	0	6.175	49798.39	-
$(2)^1A'$	25→29, 0.705	0.033	6.213	50104.84	-

Table 10.7: *Computed vertical excitation energies (ΔE_{ex}) and oscillator strengths (f) of some low-lying states of CH_3SCH_2Cl obtained at the TD-B3LYP/6-311++G**//B3LYP/6-311++G**.*

This table shows vertical excitation energies to the four lowest singlet excited states and the five lowest triplet excited states computed (by Dr. E. P. F. Lee) at the TD-B3LYP/6-311++G** level with the B3LYP/6-311++G** optimised geometry of the $\tilde{X}^1A'$ state of CH_3SCH_2Cl. Geometry optimisation was also performed on the six lowest excited states and they were all found to be dissociative apart from the $(3)^3A''$ state, with a computed

excitation energy of 5.552 eV (44,782 cm^{-1}). Comparison of Figure 10.1 with Table 10.7 indicates that excitations to the six excited states probably all contribute to the absorption spectrum shown in Figure 10.1.

The weak band centred at (34,500 ± 100) cm^{-1} is assigned to the formally forbidden $(1)^3A'' \leftarrow \tilde{X}^1A'$ transition with a computed excitation energy of 4.647 eV (37,483 cm^{-1}). It presumably gains some intensity via spin-orbit interaction of the $(1)^3A''$ state with neighbouring $^1A''$ states.

The strong band centred at (42,800 ± 50) cm^{-1} is assigned to the spin allowed transition $(3)^1A'' \leftarrow \tilde{X}^1A'$ with a computed vertical excitation energy of 5.634 eV (45,169 cm^{-1}) (computed oscillator strength, *f*, 0.0013). The experimental separation of these two bands is (8300 ± 150) cm^{-1} compared to the computed separation of 7686 cm^{-1}. As shown in Table 10.7, the main contributors to the $(1)^3A'' \leftarrow \tilde{X}^1A'$ and the $(3)^1A'' \leftarrow \tilde{X}^1A'$ transitions are the one electron excitations from molecular orbitals 25 to 27 and 25 to 28 respectively. These are both excitations from an S3p non-bonding lone pair with some small C2pπ anti-bonding contributions to a delocalised σ anti-bonding orbital.

It is also noted that in both cases the excited state, the $(1)^3A''$ state and the $(3)^1A''$ state, is dissociative in character with dissociation occurring by breaking the CH_3S-CH_2Cl bond (see Table 10.6). Other bands will contribute to the spectrum with the $(1)^1A'' \leftarrow \tilde{X}^1A'$ transition, with a computed vertical excitation energy of 5.031 eV (40,580 cm^{-1}) and a computed oscillator strength, *f*, 0.0001, being the most significant contributor (the main contributor to this excitation is the 25 → 26 transition, see Table 10.7, which is from an S3p non-bonding lone pair, with small anti-bonding contributions, from C2pπ orbitals, to a delocalised σ anti-bonding orbital).

The two bands observed in the absorption spectrum of CH_3SCH_2Cl have therefore been assigned on the basis of the TD-DFT calculations to valence-valence transitions. In order to estimate the position of the lower valence-Rydberg transitions in CH_3SCH_2Cl, the first adiabatic ionisation energy (AIE) is required. The first band in the PE spectrum of CH_3SCH_2Cl is a sharp non-bonding type band with the adiabatic ionisation energy (AIE) equal to the vertical ionisation energy (VIE) at (9.17 ± 0.01) eV [13]. It corresponds to removal of an S3p lone pair electron. The lowest transitions to Rydberg orbitals are expected to be S3p → 3d and S3p → 4s transitions. As the quantum defects

of nd and ns Rydberg orbitals in atomic sulphur are ~0.3 and ~2.0 respectively [40, 41], the transition energies to the 3d and 4s Rydberg orbitals are expected at 58,913 cm^{-1} and 46,532.7 cm^{-1} respectively, calculated using equation 10.14 (see section 1.3 of Chapter 1),

$$E_n = IE - \frac{R}{(n-\delta)^2} \qquad (10.14)$$

These transitions are above the region shown in Figure 10.1 (28,000 – 46,000 cm^{-1}) and are not expected to contribute to the spectrum in this region.

10.4 Conclusion

The u.v. absorption spectrum of CH_3SCH_2Cl has been recorded in the region 28,000 cm^{-1} to 47,000 cm^{-1} at four different pressures and reported for the first time. The infrared absorption spectrum was recorded of CH_3SCH_2Cl at five different pressures in the region 500 cm^{-1} to 3500 cm^{-1}. Quantum chemical calculations have been used to assign the absorption bands observed in the UV and infrared spectra. The photolysis rate coefficient of CH_3SCH_2Cl in the atmosphere has been determined using photoabsorption cross-section measurements at ten different solar zenith angles. A photolysis rate coefficient of 7.83×10^{-05} s^{-1}, which yields a photolysis lifetime of *ca.* 3-4 hours, has been determined at 0° zenith at ground level in the atmosphere.

It has been shown in this work that photolysis of CH_3SCH_2Cl occurs at a much higher rate with respect to attack by OH radicals and reaction with Cl atoms in the atmosphere. The photolysis lifetime of CH_3SCH_2Cl is *ca.* 3-4 hours compared with a lifetime of 4.6 and 1.2 days with respect to reaction with OH and Cl respectively. It has also been shown using experimentally derived reaction energies, with supporting quantum chemical calculations, that the dominant photo-dissociation route of CH_3SCH_2Cl is breaking of the C-S bond to produce the products CH_3S and CH_2Cl. Both these results are of significant value as this strongly supports the hypothesis that if DMS and Cl_2 react to form CH_3SCH_2Cl at night, the CH_3SCH_2Cl formed is photolysed the following morning to produce CH_3S and CH_2Cl. CH_3S is then oxidised by O_3 and/or NO_2 in the atmosphere to form CH_3SO_2 which produces SO_2 from photolysis and/or from thermal decomposition during the day.

References

[1] J. E. Lovelock, R. J. Maggs and R. A. Rasmussen, *Nature*, 237, 1972, 452.

[2] T. J. Wallington, T. Ellerman and O. J. Nielsen, *J. Phys. Chem.*, 97, 1993, 8442.

[3] D. Grosjean, *Environ. Sci. Technol.*, 18, 1984, 460.

[4] S. M. Hatakeyama, K. Izumi and H. Akimoto, *Atmos. Environ.*, 19, 1985, 135.

[5] I. Barnes, V. Bastian and K. H. Becker, *Int. J. Chem. Kin.*, 20, 1988, 415.

[6] R. J. Charlson, J. E. Lovelock, M. O. Andreae and S. G. Warren, *Nature*, 326, 1987, 655.

[7] W. J. de Bruyn, M. Harvey, J. M. Cainey and E. S. Saltzman, *J. Atmos. Chem.*, 41, 2002, 189.

[8] J. Sciare, E. Baboukas and N. Mihalopoulos, *J. Atmos. Chem.*, 39, 2001, 281.

[9] G.P. Knight and J.N. Crowley, *Phys. Chem. Chem. Phys*, 3, 2001, 393.

[10] D. D. Lucas and R. G. Prinn, *J. Geophys. Res.*, 107, 2002, 12.

[11] H. Bardouki, H. Berresheim, M. Vrekoussis, J. Sciare, G. Kouvarakis, K. Oikonomou, J. Schneider and N. Mihalopoulos, *Atmos. Chem. and Phys.*, **3,** 2003, 1871.

[12] J. M. Dyke, M. V. Ghosh, D. J. Kinnison, G. Levita, A. Morris and D. E. Shallcross, *Phys. Chem. Chem. Phys.*, **7**, 2005, 866.

[13] J. M. Dyke, M. V. Ghosh, M. Goubet, E. P. F. Lee, and G. Levita, *Chem. Phys.*, 85, 2006, 324.

[14] C. W. Spicer, E. G. Chapman, B. J. Finlayson-Pitts, R. A. Plastridge, J. M. Hubbe, J. D. Fast and C. M. Berkowitz, *Nature*, 394, 1998, 353.

[15] D. E. Shallcross, S. Vaughan, D. R. Trease, C. E. Canosa-Mas, M. V. Ghosh, J. M. Dyke and R. P. Wayne, *Atmos. Environ.*, 40, 2006, 6899.

[16] Y. Diaz-de-Mera, A. Aranda, D. Rodrigues, R. Lopez, B. Cabanas and E. Martinez, *J. Phys. Chem. A*., 106, 2002, 8627.

[17] R. E. Stickel, J. M. Nicovich, S. Wang, Z. Zhao and P. H. Wine, *J. Phys. Chem.*, 96, 1992, 9875.

[18] S. Enami, Y. Nakano, S. Hashimoto, M. Kawasaki, S. Aloisio and J. S. Francisco, *J. Phys. Chem. A.*, 108, 2004, 7785.

[19] M. Albu, I. Barnes, K. H. Becker, I. Patroescu-Klotz, R. Mocanu and T. Benter, *Phys. Chem. Chem. Phys.*, 8, 2006, 728.

[20] A. A. Turnipseed, S. B. Barone and A. R. Ravishankara, *J. Phys. Chem.*, 100, 1996, 14703.

[21] B. J. Finnlayson-Pitts and J. N. Pitts, Chemistry of the Upper and Lower Atmosphere:Theory, Experiments and Applications, *Academic Press, London*, 2000 (Page 181).

[22] M. J. Frisch, G. W. Trucks, H. B. Schlegel, G. E. Scuseria, M. A. Robb, J. R. Cheeseman, G. Scalmani, V. Barone, B. Mennucci, G. A. Petersson, H. Nakatsuji, M. Caricato, X. Li, H. P. Hratchian, A. F. Izmaylov, J. Bloino, G. Zheng, J. L. Sonnenberg, M. Hada, M. Ehara, K. Toyota, R. Fukuda, J. Hasegawa, M. Ishida, T. Nakajima, Y. Honda, O. Kitao, H. Nakai, T. Vreven, J. A. Montgomery, Jr., J. E. Peralta, F. Ogliaro, M. Bearpark, J. J. Heyd, E. Brothers, K. N. Kudin, V. N. Staroverov, R. Kobayashi, J. Normand, K. Raghavachari, A. Rendell, J. C. Burant, S. S. Iyengar, J. Tomasi, M. Cossi, N. Rega, J. M. Millam, M. Klene, J. E. Knox, J. B. Cross, V. Bakken, C. Adamo, J. Jaramillo, R. Gomperts, R. E. Stratmann, O. Yazyev, A. J. Austin, R. Cammi, C. Pomelli, J. W. Ochterski, R. L. Martin, K. Morokuma, V. G. Zakrzewski, G. A. Voth, P. Salvador, J. J. Dannenberg, S. Dapprich, A. D. Daniels, Ö. Farkas, J. B. Foresman, J. V. Ortiz, J. Cioslowski, and D. J. Fox, Gaussian 09, Revision A.1, Gaussian, Inc., Wallingford CT, 2009.

[23] H. J. Werner, P. J. Knowles, G. Knizia, F. R. Manby, M. Schütz, P. Celani, T. Korona, R. Lindh, A. Mitrushenkov, G. Rauhut, K. R. Shamasundar, T. B. Adler, R. D. Amos, A. Bernhardsson, A. Berning, D. L. Cooper, M. J. O. Deegan, A. J. Dobbyn, F. Eckert, E. Goll, C. Hampel, A. Hesselmann, G. Hetzer, T. Hrenar, G. Jansen, C. Köppl, Y. Liu, A. W. Lloyd, R. A. Mata, A. J. May, S. J. McNicholas, W. Meyer, M. E. Mura, A. Nicklass, D. P. O'Neill, P. Palmieri, K. Pflüger, R. Pitzer, M. Reiher, T. Shiozaki, H. Stoll, A. J. Stone, R. Tarroni, T. Thorsteinsson, M. Wang, and A. Wolf, MOLPRO, version 2010, 1, a package of *ab initio* programs.

[24] J. T. Peterson, Calculated Actinic Fluxes for Air Pollution Photochemistry Applications, *National Technical Information Service*, U.S. Environmental Protection Agency EPA-600/4-76-025, Springfield VA, 1976.

[25] K. Sihra, M. D. Hurley, K. P. Shine and T. J. Wallington, *J. Geophys. Res.*, 106, 2001, 20,493.

[26] I. Bravo, Y. Diaz-de-Mera, A. Aranda, E. Moreno, D. R. Nutt and G. Marston, *Phys. Chem. Chem. Phys.*, 13, 2011, 17185.

[27] O. Boucher, C. Moulin, S. Belviso, O. Aumont, L. Bopp, E. Cosme, R. von Kuhlmann, M. G. Lawrence, M. Pham, M. S. Reddy, J. Sciare, and C. Venkataraman, *Atmos. Chem. Phys. Discuss.*, 2, 2002, 1181.

[28] I. Bravo, G. Marston, D. R. Nutt and K. P. Shine, *J. Quant. Spec. Rad. Trans.*, 112, 2011, 1967.

[29] I. Bravo, A. Aranda, M. D. Hurley, G. Marston, D. R. Nutt, K. P. Shine, K. Smith and T. J. Wallington, *J. Geophys. Res.*, 115, 2010, D24317.

[30] I. Bravo, Y. Diaz-de-Mera, A. Aranda, K. Smith, , K. P. Shine and G. Marston, *Phys. Chem. Chem. Phys.*, 12, 2010, 5115.

[31] Bing-Ming Cheng, Eh Piew Chew, Jen-Shiang K and Chin-hui Yu, *J. Chem. Phys.*, 114, 2001, 4817.

[32] J. D. Cox, D. D. Wagman and V. A. Medvedev, CODATA Key Values for Thermodynamics, *Hemisphere Publishing Corp.*, New York, 1984, 1.

[33] H. Y. Afeefy, J. F. Liebman and S. E. Stein, In NIST Chemistry WebBook, NIST Standard Reference Database, Number 69, 2005.

[34] S. M. Resende and F. R. Ornellas, *Chem. Phys. Lett.*, 367, 2003, 489.

[35] I. A. Gargurevich, *Ind. Eng. Chem. Res.*, 44, 2005, 7706.

[36] J. A. Seetula, *J. Soc. Faraday. Trans.*, 92, 1996, 3069.

[37] P. Quintana, R. F. Delmdahl, D. H. Parker, B. Martinez-Haya, F. J. Aoiz, L. Banares and E. Verdasco, *Chem. Phys. Lett*. 325, 2000, 146.

[38] B. Martinez-Haya, P. Qiuntana, L. Banares, P. Samartzis, D. J. Smith and T. N. Kitsopoulos, *J. Chem. Phys.*, 114, 2001, 4450.

[39] P. Limao-Vieira, S. Eden, P. A. Kendall, N. J. Mason and S. V. Hoffman, *Chem. Phys. Lett.*, 366, 2002, 343.

[40] C. E. Moore, Atomic energy levels as derived from the analyses of optical spectra, U.S. Dept. of Commerce, *National Bureau of Standards*, Vol 1, 1949.

[41] L. Zuin, Ph.D Thesis, Southampton University, 2004.

Chapter 11

Conclusions and Future Work

During this research the main investigations carried out were: an investigation of the pyrolysis behaviour of two hydrofluorocarbon (HFC) fire suppression agents, 2-H heptafluoropropane (CF_3CHFCF_3) and pentafluoroethane (CF_3CHF_2) in order to determine their thermal decomposition pathways, a study of three ozone-alkene reactions (O_3 + ethene, O_3 + 2-methylpropene (2MP) and O_3 + 2, 3 dimethyl-2-butene (DMB)) in order to measure their product branching ratios, a feasibility study of the TPE spectra of the first bands of four selected triatomics, (SF_2, HO_2, HOCl and Cl_2O), and determination of the photolysis rate coefficient in the u.v. visible region of the atmospherically important molecule monochlorodimethyl sulphide (CH_3SCH_2Cl). The first three investigations were carried out using photoelectron spectroscopy, whereas the fourth investigation was carried out with u.v. absorption spectroscopy.

The results obtained from monitoring the pyrolysis products of flowing CF_3CHF_2, diluted with argon, as a function of temperature, have been interpreted in terms of two main thermal decomposition reactions,

$$CF_3CHF_2 \rightarrow C_2F_4 + HF \qquad (11.1a)$$

$$C_2F_4 \rightarrow 2CF_2 \qquad (11.1b)$$

and

$$CF_3CHF_2 \rightarrow CF_2 + CF_3H \qquad (11.2)$$

as well as the reaction, $C_2F_4 \rightarrow 2CF_2$. A study of the pyrolysis products of CF_3CHFCF_3, diluted in argon, as a function of temperature, have also been interpreted in terms of two main thermal decomposition reactions,

$$CF_3CHFCF_3 \rightarrow CF_3CF{=}CF_2 + HF \qquad (11.3)$$

and

$$CF_3CHFCF_3 \rightarrow C_2F_4 + CF_3H \qquad (11.4)$$

as well as the reaction $CF_3CF{=}CF_2 \rightarrow C_2F_4 + CF_2$. PE spectra of CF_3CHF_2 and CF_3CHFCF_3 were each assigned using state-of-the-art *ab initio* calculations.

Comparison of the PE spectrum of CF_3CHF_2 with the published TPE spectrum [1] showed good agreement for the first band but the higher energy bands appear less well resolved in the TPE spectrum. The PE spectrum of CF_3CHFCF_3 was also compared with the corresponding TPE spectrum [2] and showed that the first band seen in the TPE spectrum was a lot weaker than that observed in the PE spectrum, and the higher energy bands (above 13.5 eV) appeared to be less well resolved in the TPE spectrum. The apparent loss of resolution observed in the TPE spectra in the higher energy regions for both CF_3CHF_2 and CF_3CHFCF_3 is due to autoionisation from high-lying Rydberg states which converge to higher ionisation thresholds (see Chapters 5 and 6).

Three ozone-alkene reactions were studied (O_3 + ethene, O_3 + 2MP and O_3 + DMB) using a glass flow-tube interfaced to a PE spectrometer, and the reagents and products were monitored as a function of reaction time. PE band intensities for the reactants and observed products were converted to partial pressures using measured photoionisation cross-sections. These experiments allowed the determination of all the main product yields from each reaction by the same experimental technique for the first time.

The experimental product yields measured for each reaction agreed reasonably well when compared to those measured in other studies [3-13]. For O_3 + ethene, the observed products were H_2CO, CO, CO_2, HCOOH, CH_3CHO and O_2. For the reactions O_3 + 2MP and O_3 + DMB, H_2CO, CO, CO_2, $(CH_3)_2CO$ and O_2 were observed as reaction products. HCOOH was observed from the O_3 + 2MP reaction but not from the O_3 + DMB reaction. The yield of O_2, (a main reaction product observed in all three alkene-ozone reactions studied), was measured for the first time for these reactions. Methyl acetate

(CH_3COOCH_3) was not observed in the spectra recorded for the O_3 + 2MP and the O_3 + DMB reactions, indicating that, as in the well known, the "ester channel" [14] for decomposition of the Criegee intermediate, $(CH_3)_2COO \rightarrow CH_3COOCH_3$, is not occurring, although from the results obtained for O_3 + 2MP and O_3 + ethene, it appears that the smaller Criegee intermediate, H_2COO, rearranges to give HCOOH. For each reaction kinetic simulations were used to identify the main production reaction (or reactions) associated with each observed product and the measured product yields were used in a global model to calculate the annual global emissions of the observed products in the atmosphere.

A plan to record TPE spectra of SF_2, HO_2, HOCl and Cl_2O at the Elettra synchrotron facility was only partially successful. Preliminary TPE spectra were obtained for SF_2 and HO_2, but no attempts were made to record the TPE spectra of HOCl and Cl_2O because initial PE experiments performed at Elettra showed that the source used for producing HOCl and Cl_2O was not sufficiently stable to allow TPE spectra to be recorded. PES experiments have since been performed in Southampton to develop sufficiently stable sources of HOCl and Cl_2O for subsequent synchrotron TPES measurements. This involved flowing Cl_2 saturated in H_2O vapour through successive layers of dried HgO powder in a column attached to the inlet of a PE spectrometer. The recommended methods for producing HOCl and Cl_2O for TPES measurements at the Elettra synchrotron source have been described (Chapter 9). The methods developed in this work will provide a good starting point for recording TPE spectra of HOCl and Cl_2O at Elettra, which is the next step in this project.

TPE spectra were recorded at Elettra for the triatomic molecules HO_2 and SF_2. However, problems occurred in both experiments. Vapour pressure fluctuations, arising from a heating mantle with poor temperature control, prevented stable conditions needed to record TPE spectra of HO_2 and because the reaction chosen to produce SF_2 also produces S atoms, which recombined to make S_2, the first TPE band of SF_2 contained contributions from the first band of S_2.

The photolysis rate coefficient of atmospherically important molecule monochlorodimethyl sulphide (CH_3SCH_2Cl) was investigated as an extension of the work performed for the reactions of dimethyl sulphide (DMS) plus Cl_2 and DMS plus OH (see Chapter 10) [15, 16, 17]. The absorption spectrum of CH_3SCH_2Cl was

recorded and reported in this work for the first time. Photoabsorption cross-sections were measured for recorded absorption spectra at different pressures and were used along with solar actinic flux values to determine the photolysis rate coefficient of CH_3SCH_2Cl at various solar zenith angles. It was found that of the three removal routes for CH_3SCH_2Cl in the atmosphere (CH_3SCH_2Cl + OH, CH_3SCH_2Cl + Cl and photolysis of CH_3SCH_2Cl) that photolysis was the dominant removal route with CH_3SCH_2Cl having a photolysis rate coefficient of 7.83×10^{-05} s^{-1}, which yields a photolysis lifetime of *ca.* 3-4 hours (at 0° zenith at ground level in the atmosphere) compared to attack by OH and reaction with Cl atoms with expected reaction lifetimes of 4.6 and 1.2 days respectively. Quantum chemical calculations were performed of the photo-dissociation channel,

$$CH_3SCH_2Cl + h\nu \rightarrow CH_3S + CH_2Cl \qquad (11.5)$$

to determine reaction energies for each channel. It was found that the photolysis channel (11.5) had the lowest computed $\Delta H_{f,298K}^{Ø}$ of 69.50 kcal.mol^{-1} and had a band onset of (28,000 ± 100) cm^{-1}, (80.06 ± 0.15) kcal.mol^{-1}, which was above the expected dissociation energy of (70.15 ± 2.2) kcal.mol^{-1}. From these results it can be concluded that the dominant removal route for CH_3SCH_2Cl in the atmosphere is photolysis with CH_3S and CH_2Cl being the favoured products formed.

11.1 Future Work

The results obtained in this work demonstrate that a number of valuable experiments could be performed in future.

During the pyrolysis of HFCs it was noted that the experimental first VIE of CF_3CHF_2 is lower than the computed first VIE by 0.3 eV. This was explained in terms of dissociation of $CF_3CHF_2^+$ in the vertical ionisation region from the neutral. The recommended first AIE of CF_3CHF_2 is also 0.5 eV below the measured band onset in both the PE and TPE spectra. A more reliable experimental determination of this AIE could be achieved by recording a high-resolution zero-electron kinetic energy pulsed field ionisation (ZEKE-PFI) spectrum of this molecule by a two-colour process involving initial excitation to an excited state with an equilibrium geometry closer to that of the ion than that of the neutral ground state [18]. The structure obtained in the ZEKE-PFI first band should also enable an understanding of the ionic state dissociation

to be obtained. An extension of the pyrolysis work described in Chapters 5 and 6 would be to study the reactive intermediates, CHF, CH_2F, CHF_2, CH_3CF, CF_3CF and CFCHF by PES, TPES and ZEKE-PFI spectroscopy to determine their first ionisation energies and investigate their low lying ionic states.

As noted in Chapter 9, in order to record the TPE spectrum of HO_2 in the region 10.5-13.5 eV, the experiment needs to be carried out with an accurate temperature control on the heating system used to heat the urea-hydrogen peroxide complex in order to maintain a constant vapour pressure of H_2O_2. The aim is to resolve vibrational structure in the HO_2 first PE band and to obtain a vibrationally resolved spectrum of the second band which is expected to have its first component in the 11.5 eV to 12.0 eV ionisation energy region.

From the SF_2 investigation described in Chapter 9, good agreement was observed between the AIE and VIE values for the first TPE band, obtained in the present work, with results of state-of-the-art *ab initio* calculations. The vibrational constant (ω_e) for the symmetric stretching mode in the ground ionic state, derived from the vibrationally resolved TPE spectra, was also in good agreement with the value calculated by Lee *at al*. (using the RCCSD(T) method with basis sets up to aug-cc-pV(5+*d*)Z quality) [19]. Unfortunately, the presence of an S_2 vibrational progression, arising from autoionisation of S_2, in the TPE first band of SF_2, prevented the observation of any additional structure, and although better resolution was achieved with respect to previous experimental work, it was not possible to obtain more information from the SF_2 spectra. For this reason, another experimental approach is currently being investigated to produce SF_2. This involves discharging either flowing SF_4 or SF_6 heavily diluted in argon in an attempt to make SF_2 with minimal S_2 production. In collaborative experiments with the Southampton PES group, the method of discharging flowing SF_6 diluted in argon has been tested in Elettra by Dr S. Stranges (University of Rome) with encouraging results obtained from recorded PE spectra.

An improvement to the synchrotron PE spectrometer is currently being carried out by the Southampton PES group in collaboration with Dr S. Stranges and Dr G. Cautero at Elettra. This involves replacing the channeltron electron detector with a 2D position sensitive detector. This will allow PE and TPE spectra to be recorded at shorter times with improved signal-to-noise ratios [20].

As well as future projects which arise from this work, a number of longer term developments can be anticipated. For example, a common problem when studying the photoelectron spectra of reactive intermediates is that of overlapping bands produced by different species present in the ionisation region e.g. the photoelectron spectrum recorded for Cl_2O in Figure 9.7 (Chapter 9) shows the overlap between the second bands of HOCl (VIE 12.29 eV) and Cl_2O (VIE 12.37 eV). If the electrons and ions produced in a photoionisation event can be correlated, then the PE signal attributed to each species present in the mixture can be separated and the overlapping band problem can be avoided. This would mean incorporation of an ion detector, such as a time-of-flight mass analyser. Suitably timed extraction voltages would be needed to allow Photoelectron-Photoion-Coincidence (PEPICO) measurements to be performed.

Threshold Photoelectron-Photoion-Coincidence (TPEPICO) experiments could also be performed and these are likely to have higher signal-to-noise ratios for reactive intermediates than PEPICO experiments because of the high collection efficiency of the threshold method [21]. This technique has been successfully used by Alcaraz *et al.* and Ueda *et al.* [22, 23]. Alcaraz *et al.* recorded TPE spectra of the methyl radical (CH_3) and its deuterated isotopomers CH_2D, CHD_2 and CD_3 produced at the same time in the same reaction mixture from flash pyrolysis of CH_xD_yONO (where $x + y = 3$) in the energy region 9.5 - 10.5 eV. From TPE spectra of each isotopomer the ground ionic states of CH_3, CH_2D, CHD_2 and CD_3 were investigated and resonant autoionisation process were studied. An example of a reactive intermediate which could be studied using this technique, relevant to the work described in Chapters 7 and 8, is the Criegee intermediate, CH_2OO. This could be made for initial study with PES and then more detailed study by TPES from the following reactions,

$$F + CH_3OCH_3 \rightarrow CH_3OCH_2 + HF \qquad (11.5)$$

$$O_2 + CH_2OCH_2 \rightarrow CH_3O + CH_2OO \qquad (11.6)$$

Reaction (11.5) has been used to study CH_3OCH_2 by PES [24]. Another method which could be used to produce the Criegee intermediate for PES and TPES study is that used by Taatjes *et al.* [25];

$$Cl + (CH_3)_2SO \rightarrow CH_3S(O)CH_2 + HCl \qquad (11.7)$$

$$O_2 + CH_3S(O)CH_2 \rightarrow CH_3SO + CH_2OO \qquad (11.8)$$

This was the first gas-phase study of this radical (by photoionisation mass spectrometry). Clearly TPEPICO studies would be very valuable here to obtain a clean TPE spectrum of CH_2OO, (it should be noted that CH_2S, a possible by-product of the above reactions, has the same mass as CH_2OO). Once CH_2OO has been studied by TPEPICO spectroscopy other Criegee intermediates could be studied in this way. Other small reactive intermediates such as HONO (AIE 10.97 ± 0.03 eV) [26], CH_3O_2 (AIE 10.33 ± 0.05 eV) [25, 27, 28] and $C_2H_5O_2$ (AIE 9.61 ± 0.08 eV) [28, 29, 30, 31] are possibilities for future PE and TPE work.

Initial experiments were made to prepare CH_3O_2 for PES study in this work from the reactions,

$$CH_4 + F \rightarrow CH_3 + HF \qquad (11.9)$$

$$CH_3 + O_2 + M \rightarrow CH_3O_2 + M \qquad (11.10)$$

The experimental setup needed for reaction (11.9), to produce F atoms, involved discharging 5% F_2 in helium. This was achieved by using the same experimental setup as that described in section 3.2.1 of Chapter 3 (as used in the SF_2 investigation) which involved using an open-ended inlet system. The first step of this experiment was to optimise the conditions used to produce CH_3 from reaction (11.9) by determining the optimum reactant partial pressures of CH_4 and F_2, as a function of mixing distance, needed to provide high number densities of CH_3 in the flow-tube i.e. to optimise conditions to allow CH_3O_2 production from the secondary reaction of CH_3 with O_2. Preliminary results of the first reaction step of this experiment were encouraging, producing relatively high yields of CH_3.

The optimised conditions for producing CH_3 were found to use a 1.5:1 ratio of F_2:CH_4 (Δp F_2 6.2×10^{-5} mbar and Δp CH_4 4.1×10^{-5} mbar) at a reaction mixing distance of 6mm from the point of ionisation. Attempts at making CH_3O_2 from reaction (11.10), by the addition of O_2 to the reaction mixture proved to be less successful. Once an intense first PE band of CH_3 was observed, O_2 was slowly admitted to the top of the movable injector along with CH_4 using a T-piece. However, CH_3O_2 was never observed from recorded PE spectra in this work (only CH_3 and O_2 were observed along with the reactants CH_4 and F/F_2). One reason that CH_3O_2 was not observed may be because O_2 was admitted via the top of the injector along with CH_4 and not at the point where CH_3

was produced (at the bottom of the injector). In a previous flow-tube investigation by Bacak *et al.* [27], chemical ionisation mass spectrometry (CIMS) was used to determine the rate coefficient for the reaction CH_3O_2 + NO → Products. In this study, reactions (11.9) and (11.10) were used to successfully produce CH_3O_2. The flow-tube used was very similar in design to that described in section 3.22 of Chapter 3. However it contained two additional inlets on the side arm (equivalent in position to inlet *a* shown Figure 3.7).

A microwave cavity was attached to the side arm to produce F atoms, with CH_4 being admitted via the first inlet to produce CH_3. The second inlet, positioned downstream of the first, meant that O_2 could be admitted directly at the point where CH_3 was produced, maximising the production of CH_3O_2 from reaction (11.10). Concentrations of CH_3O_2 obtained in this way were of the order 1-10x10^{10} molecules cm^{-3} [27].

A PE spectrum obtained from reaction (11.9), with added O_2, from this work is shown in Figure 11.1. It shows the bands of CH_3 (VIE 9.84 eV) [32], CH_4 (VIE 13.60 eV) [33], F_2 (VIE 15.70 eV) [34] and F (VIE 17.42 eV) [35] along with the He(I)α and He(I)β bands of the first PE band of O_2 (red). The arrow, shown in blue, is the expected position of the first PE band of CH_3O_2 (AIE 10.33 ± 0.05 eV) [25]. CH_3O_2 is not observed in this spectrum because of insufficient mixing between CH_3 and O_2. Also, as reaction (11.10) is a third body reaction, (k = 4.49 x 10^{-31} cm^6.$molecules^{-2}$ s^{-1}) [36] the pressures need to be increased to increase the yield of CH_3O_2.

Possible modifications to the experimental set-up would be to try and improve the reaction efficiency in order to maximise the CH_3 production by providing improved mixing at the outlet of the injector. One way to do this would be to use a "tubuliser", like that described in reference [27], positioned at the end of the moveable injector. This would provide efficient mixing at short mixing distances and help to minimise secondary reactions. Also the use of an inlet with a tapered end and a smaller hole, like those used for the O_3 + alkene experiments described in Chapters 7 and 8, would allow greater local pressures and more collisions between CH_3 and O_2 to occur.

Recent studies by the Southampton PES group have carried out in depth investigations into reactions of the atmospherically important molecule dimethyl sulphide (DMS, CH_3SCH_3) with the molecular halogens Cl_2, Br_2, BrCl and ICl using PES and IR matrix isolation techniques (see Chapter 10) [15, 16, 37, 38].

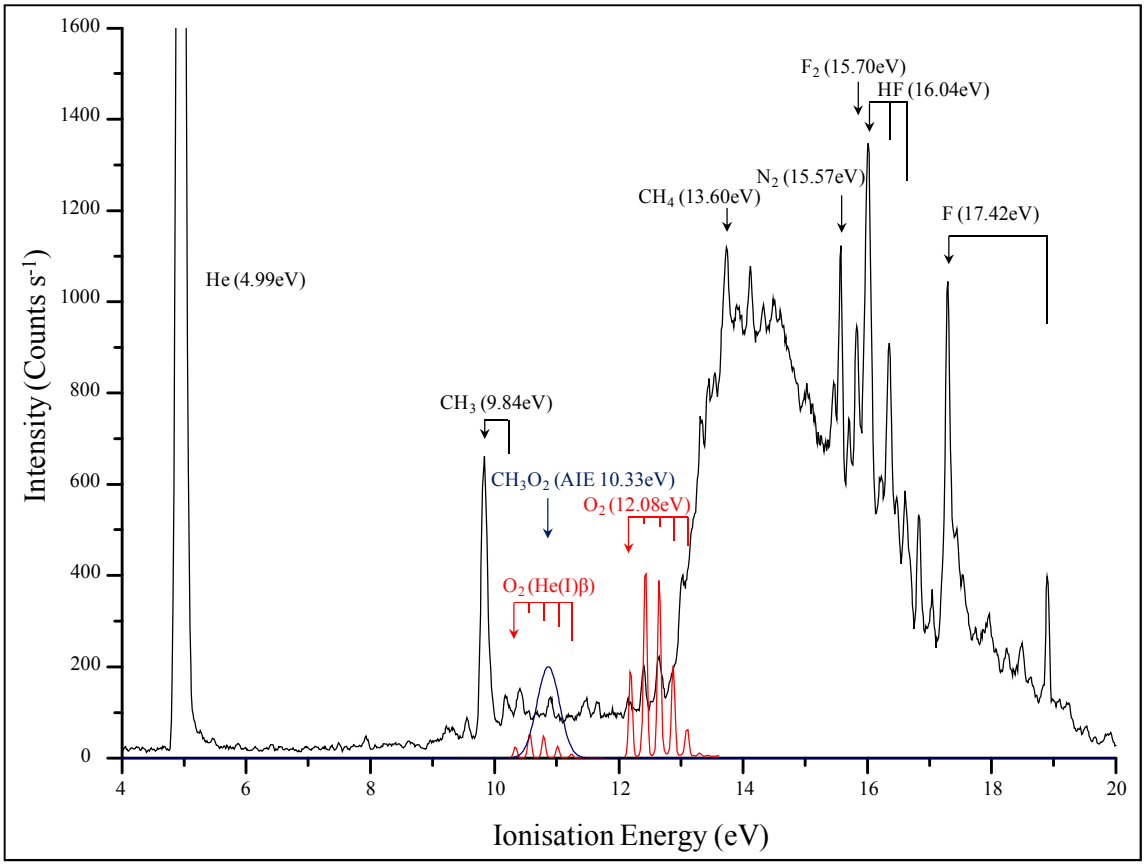

Figure 11.1: *PE spectrum of reaction scheme (11.9) and (11.10) showing a high yield of CH_3.*

A logical extension of this work (and that of Chapter 10) would be to carry out a flow-tube investigation of these reactions in order to measure the photoionisation cross-sections of the reactants and observed products to ultimately measure reaction branching ratios using the method described in Chapters 7 and 8. Future experiments, including reactions of CH_3SCH_3 (and possibly other sulphur containing species such as $CH_3S(O)CH_3$ and $(CH_3)_2SO_2$) with reactive species present in the marine boundary layer (MBL) such as OH, NO_3 and IO may also be considered for such an investigation. A reaction of particular interest is OH with CH_3SCH_3, as this is the main oxidation reaction of CH_3SCH_3 in the atmosphere during the day. Two reaction channels are possible,

$$CH_3SCH_3 + OH \rightarrow CH_3S(OH)CH_3 \qquad (11.11)$$

$$CH_3SCH_3 + OH \rightarrow CH_3SCH_2 + H_2O \qquad (11.12)$$

The overall room temperature rate coefficient for $CH_3SCH_3 + OH \rightarrow$ Products has been measured as 5.38×10^{-12} $cm^3.molecules^{-1}$ s^{-1} [39]. However, no complete branching ratio data of the possible reaction channels (11.11) and (11.12) have been determined for this

reaction. Also, oxidation of CH_3SCH_3 in the atmosphere occurs at night via the reaction CH_3SCH_3 with O_3/NO_3. This reaction has an estimated room temperature rate coefficient of 9.7 x 10^{-13} $cm^3.molecules^{-1}$ s^{-1} [40] and may occur via the two channels,

$$CH_3SCH_3 + NO_3 \rightarrow CH_3SCH_2 + HNO_3 \quad (11.13)$$

$$CH_3SCH_3 + NO_3 \rightarrow CH_3S(NO_3)CH_3 \quad (11.14)$$

PES could be used to observe the products of both reactions and hence estimate the reaction branching ratios. Currently photoabsorption cross-sections and photolysis rate coefficients obtained in this work from absorption measurements of CH_3SCH_2Cl (Chapter 10) are being used in atmospheric kinetics simulations and global models involving CH_3SCH_3 reactions with Cl_2, Cl and OH to predict the estimated annual SO_2 global budget and determine atmospheric mixing ratios of CH_3SCH_3 and SO_2 at the marine boundary layer (MBL). Reaction branching ratio data of CH_3SCH_3 reactions would be of use in order to improve such models.

References

[1] W. Zhou, D. P. Seccombe, R. P. Tuckett and M. K. Thomas, *Chem. Phys.*, 283, 2002, 419.

[2] G. K. Jarvis, K. J. Boyle, C. A. Mayhew and R. P. Tuckett, *J. Phys. Chem.*, 102, 1998, 3230.

[3] W. H. Bunnelle, *Chem. Rev.*, 91, 1991, 335.

[4] P. Aplincourt and M. F. Ruiz-Lopez, *J. Am. Chem. Soc.*, 122, 2000, 8990.

[5] T. Sato, S. Nishihara, Y. Kataoka, Y. Nakanishi, Y. Kitagawa, T. Kawakami, S. Yamanaka, M. Okumura amd K. Yamaguchi, *J. Phys. Chem. A.*, 114, 2010, 12116.

[6] Y. Zhao, O. Tishchenko, J. R. Gour, W. Li, J. J. Lutz, P. Piecuch, and D. G. Truhlar, *J. Phys. Chem. A.*, 113, 2009, 5786.

[7] R. Ponec, J. Roithova and Y. Hass Croatica, *Chemica. Acta.*, 74, 2001, 251.

[8] J. T. Herron and R. E. Huie, *J. Am. Chem. Soc.*, 99, 1977, 5430.

[9] F. Su, J. G. Calvert and J. H. Shaw, *J. Phys. Chem.*, 84, 1980, 239.

[10] H. Niki, P. D. Maker, C. M. Savage and L. P. Breitenbach, *J. Phys. Chem.*, 85, 1981, 1024.

[11] O. Horie and G. K. Moortgat, *Atmospheric Environment*, 25A, 1991, 1881.

[12] P. Neeb, O. Horie and G. K. Moortgat, *J. Phys. Chem. A.*, 102, 1998, 6778.

[13] E. Grossjean and D. Grossjean, *Environmental Sci. Technol.*, 30, 1996, 2036.

[14] J. G. Calvert, R. Atkinson, J. A. Kerr, S. Madronich, G. K. Moortgat, T. J. Wallington and G. Yarwood, The Mechanisms of Atmospheric Oxidation of the Alkenes, *Oxford University Press*, Oxford, 2000.

[15] J. M. Dyke, M. V. Ghosh, D. J. Kinnison, G. Levita, A. Morris and D. E. Shallcross, *Phys. Chem. Chem. Phys.*, 7, 2005, 866.

[16] J. M. Dyke, M. V. Ghosh, M. Goubet, E. P. F. Lee, and G. Levita, *Chem. Phys.*, 85, 2006, 324.

[17] D. E. Shallcross, S. Vaughan, D. R. Trease, C. E. Canosa-Mas, M. V. Ghosh, J. M. Dyke and R. P. Wayne, *Atmos. Environ.*, 40, 2006, 6899.

[18] F. Merkt and T. P. Softley in High Resolution Laser Photoionisation and Photoelectron Studies, *edited by I. Powis, T. Baer and C. Y. Ng*, article entitled "VUV-ZEKE Photoelectron Spectroscopy: Final State Interactions in Small Molecular Systems", *John Wiley and Sons Ltd.*, Oxford, 1995.

[19] E. P. F. Lee, D. K. W. Mok, F. Chau and J. M. Dyke, *J. Chem. Phys.*, 125, 2006, 104304.

[20] A. Morris, N. Jonathan, J. M. Dyke, P. D. Francis, N. Keddar and J. D. Mills, *Rev. Sci. Instrum.*, 55, 1984, 172.

[21] K. Ueda and J. H. D. Eland, *J. Phys. B. At. Mol. Opt. Phys.*, 38, 2005, S839.

[22] G. Prumper and K. Ueda, *Nuc. Instr. Meth. Phys. Res. A.*, 574, 2007, 350.

[23] B. K. Cunha de Miranda, C. Alcaraz, M. Elhanine, B. Noller, P. Hemberger, I. Fischer, G. A. Garcia, H. Soldi-Lose, B. Gans, L. A. V. Mendes, S. Boye - Peronne, S. Douin, J. Zabka and P. Botschwina, *J. Phys. Chem. A.*, 114, 2010, 4818.

[24] M. H. Zamanpour, Ph.D Thesis, *University of Southampton*, 1989.

[25] C. A. Taatjes, G. Meloni, T. M. Selby, A. J. Trevitt, D. L. Osborn, C. J. Percival and D. E. Shallcross, *J. Am. Chem. Soc.*, 130, 2008, 11883.

[26] C. A. Taatjes, D. L. Osborn, T. A. Cool and K. Nakajima, *Chem. Phys. Lett.*, 394, 2004, 19.

[27] A. Bacak, M. W. Bardwell, M. T. Raventos, C. J. Percival, G. S. Reyna and D. E. Shallcross, *J. Phys. Chem. A.*, 108, 2004, 10681.

[28] G. S. Tyndall, R. A. Cox, C. Grainer, R. Lesclaux, G. K. Moortgat, M. J. Pilling, A. R. Ravishankara and T. J. Wallington, *J. Geophys. Res.*, 106, 2001, 12157.

[29] G. Meloni, P. Z. Stephen, S. J. Klippenstein, M. Ahmed, S. R. Leone, C. A. Taatjes and D. L. Osborn, *J. Am. Chem. Soc.*, 128, 2006, 13559.

[30] M. T. Raventos, C. J. Percival, M. R. McGillen, P. D. Hamer and D. E. Shallcross, *Phys. Chem. Chem. Phys.*, 9, 2007, 4338.

[31] P. Dagaut, T. J. Wallington and M. J. Kurylo, *J. Phys. Chem.*, 92, 1988, 3836.

[32] J. A. Blush, P. Chen, R. T. Wiedmann and M. G. White, *J. Chem. Phys.*, 98, 1993, 3557.

[33] K. Kimura, S. Katsumata, Y. Achiba, T. Yamasaki and S. Iwata, Handbook of HeI Photoelectron Spectra, *Japan Scientific Press*, *Tokyo*, 1981.

[34] A. B. Cornford, D. C. Frost, C. A. McDowell, J. L. Ragle and I. A. Stenhouse, *J. Chem. Phys.*, 54, 1970, 2651.

[35] C. E. Moore, *Natl. Stand. Ref. Data Ser.*, NSRDS-NBS 3, Sect. 3, 1970.

[36] W. B. DeMore, S. P. Sander, D. M. Golden, R. F. Hampson, M. J. Kurylo, C. J. Howard, A. R. Ravishankara, C. E. Kolb and M. J. Molina, Chemical Kinetics

and Photochemical Data for use in Stratospheric Modeling: Evaluation Number 12, *JPL Publication,* 97-4, 1997.

[37] S. Beccaceci, J. S. Ogden and J. M. Dyke, *Phys. Chem. Chem. Phys.*, 12, 2010, 2075.

[38] S. Beccaceci, J. S. Ogden and J. M. Dyke, *Unpublished Work*, 2011.

[39] M. Albu, I. Barnes, K. H. Becker, I. Patroescu-Klotz, R. Mocanu and T. Benter, *Phys. Chem. Chem. Phys.*, 8, 2006, 728.

[40] R. Atkinson, J. N. Pitts Jnr and S. M. Aschmann, *J. Phys. Chem.*, 88, 1984, 1584.